frontiers | Research Topics

# Multidisciplinary approaches to the FLASH radiotherapy

**Edited by**
Fabio Di Martino, Vincenzo Patera, Pierre Montay-Gruel, Valentina Tozzini, Emanuele Scifoni, Francesco Romano and Arash Darafsheh

**Published in**
Frontiers in Physics
Frontiers in Oncology

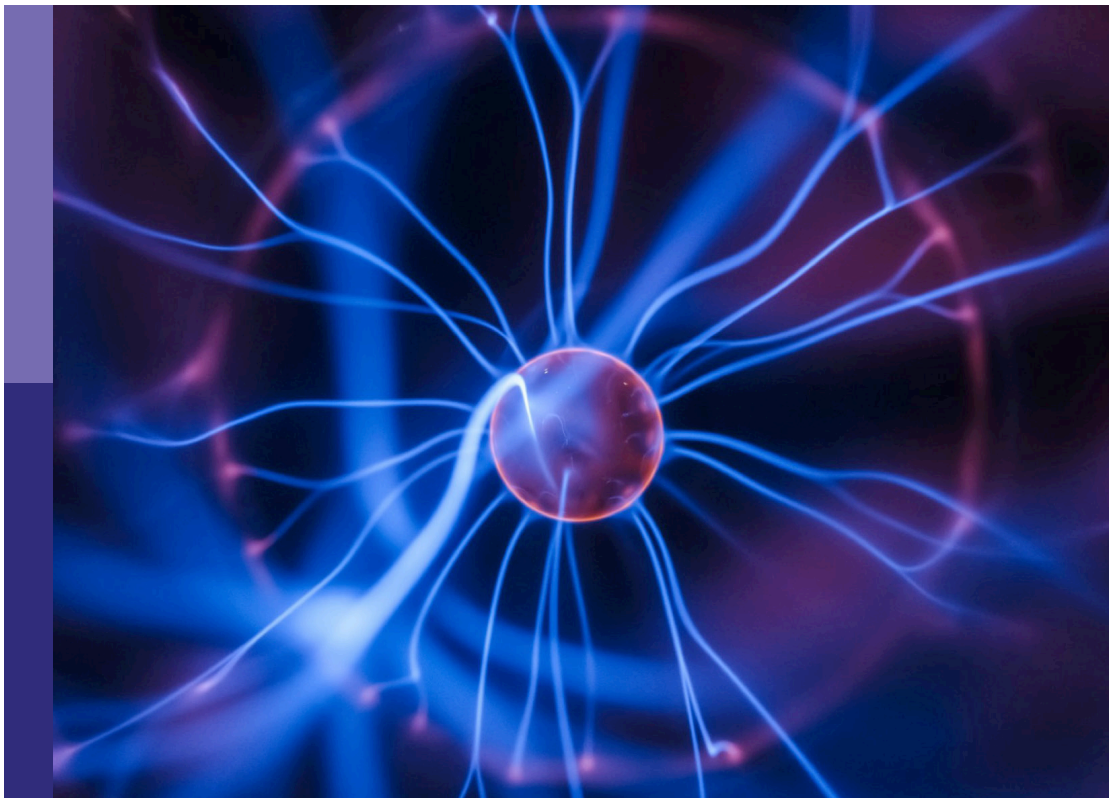

ISSN 1664-8714
ISBN 978-2-8325-5094-6
DOI 10.3389/978-2-8325-5094-6

## About Frontiers

Frontiers is more than just an open access publisher of scholarly articles: it is a pioneering approach to the world of academia, radically improving the way scholarly research is managed. The grand vision of Frontiers is a world where all people have an equal opportunity to seek, share and generate knowledge. Frontiers provides immediate and permanent online open access to all its publications, but this alone is not enough to realize our grand goals.

## Frontiers journal series

The Frontiers journal series is a multi-tier and interdisciplinary set of open-access, online journals, promising a paradigm shift from the current review, selection and dissemination processes in academic publishing. All Frontiers journals are driven by researchers for researchers; therefore, they constitute a service to the scholarly community. At the same time, the *Frontiers journal series* operates on a revolutionary invention, the tiered publishing system, initially addressing specific communities of scholars, and gradually climbing up to broader public understanding, thus serving the interests of the lay society, too.

## Dedication to quality

Each Frontiers article is a landmark of the highest quality, thanks to genuinely collaborative interactions between authors and review editors, who include some of the world's best academicians. Research must be certified by peers before entering a stream of knowledge that may eventually reach the public - and shape society; therefore, Frontiers only applies the most rigorous and unbiased reviews. Frontiers revolutionizes research publishing by freely delivering the most outstanding research, evaluated with no bias from both the academic and social point of view. By applying the most advanced information technologies, Frontiers is catapulting scholarly publishing into a new generation.

## What are Frontiers Research Topics?

Frontiers Research Topics are very popular trademarks of the *Frontiers journals series*: they are collections of at least ten articles, all centered on a particular subject. With their unique mix of varied contributions from Original Research to Review Articles, Frontiers Research Topics unify the most influential researchers, the latest key findings and historical advances in a hot research area.

Find out more on how to host your own Frontiers Research Topic or contribute to one as an author by contacting the Frontiers editorial office: frontiersin.org/about/contact

# Multidisciplinary approaches to the FLASH radiotherapy

**Topic editors**

Fabio Di Martino — Pisana University Hospital, Italy
Vincenzo Patera — Sapienza University of Rome, Italy
Pierre Montay-Gruel — UCI Health, United States
Valentina Tozzini — Nanoscience Institute, National Research Council (CNR), Italy
Emanuele Scifoni — Universities and Research, Italy
Francesco Romano — National Institute of Nuclear Physics of Catania, Italy
Arash Darafsheh — Washington University in St. Louis, United States

**Citation**

Di Martino, F., Patera, V., Montay-Gruel, P., Tozzini, V., Scifoni, E., Romano, F., Darafsheh, A., eds. (2024). *Multidisciplinary approaches to the FLASH radiotherapy*. Lausanne: Frontiers Media SA. doi: 10.3389/978-2-8325-5094-6

# Table of contents

05 Editorial: Multidisciplinary approaches to the FLASH radiotherapy
Fabio Di Martino, Emanuele Scifoni, Vincenzo Patera, Pierre Montay-Gruel, Francesco Romano, Arash Darafsheh and Valentina Tozzini

08 A stochastic reaction–diffusion modeling investigation of FLASH ultra-high dose rate response in different tissues
Ramin Abolfath, Alexander Baikalov, Alberto Fraile, Stefan Bartzsch, Emil Schüler and Radhe Mohan

19 An insight into hypothesized biological mechanisms contributing to the Flash effect
Francesca Del Debbio, Maria Sofia Bertilacchi, Alessandra Gonnelli, Eleonora Da Pozzo, Valentina Tozzini, Claudia Martini, Simone Capaccioli and Barbara Costa

26 Passive SOBP generation from a static proton pencil beam using 3D-printed range modulators for FLASH experiments
Felix Horst, Elke Beyreuther, Elisabeth Bodenstein, Sebastian Gantz, Diego Misseroni, Nicola M. Pugno, Christoph Schuy, Francesco Tommasino, Uli Weber and Jörg Pawelke

38 Treatment planning of intracranial lesions with VHEE: comparing conventional and FLASH irradiation potential with state-of-the-art photon and proton radiotherapy
A. Muscato, L. Arsini, G. Battistoni, L. Campana, D. Carlotti, F. De Felice, A. De Gregorio, M. De Simoni, C. Di Felice, Y. Dong, G. Franciosini, M. Marafini, I. Mattei, R. Mirabelli, S. Muraro, M. Pacilio, L. Palumbo, V. Patera, A. Schiavi, A. Sciubba, M. Schwarz, S. Sorbino, V. Tombolini, M. Toppi, G. Traini, A. Trigilio and A. Sarti

50 Intertrack interaction at ultra-high dose rates and its role in the FLASH effect
Alexander Baikalov, Ramin Abolfath, Emil Schüler, Radhe Mohan, Jan J. Wilkens and Stefan Bartzsch

65 Monitoring beam charge during FLASH irradiations
Borivoj Vojnovic, Iain D. C. Tullis, Robert G. Newman and Kristoffer Petersson

81 New insights on clinical perspectives of FLASH radiotherapy: from low- to very high electron energy
Stefano Ursino, Giovanni Gadducci, Noemi Giannini, Alessandra Gonnelli, Taiushia Fuentes, Fabio Di Martino and Fabiola Paiar

87 Across the stages: a multiscale extension of the generalized stochastic microdosimetric model (MS-GSM$^2$) to include the ultra-high dose rate
Marco Battestini, Marta Missiaggia, Andrea Attili, Francesco Tommasino, Chiara La Tessa, Francesco G. Cordoni and Emanuele Scifoni

101 Realization and dosimetric characterization of a mini-beam/flash electron beam
Jake Harold Pensavalle, Francesco Romano, Mariagrazia Celentano, Damiano Del Sarto, Giuseppe Felici, Gaia Franciosini, Luigi Masturzo, Giuliana Milluzzo, Vincenzo Patera, Yolanda Prezado and Fabio Di Martino

116 Architecture, flexibility and performance of a special electron linac dedicated to Flash radiotherapy research: electronFlash with a triode gun of the centro pisano flash radiotherapy (CPFR)
F. Di Martino, D. Del Sarto, G. Bass, S. Capaccioli, M. Celentano, D. Coves, A. Douralis, M. Marinelli, M. Marrale, L. Masturzo, G. Milluzzo, M. Montefiori, F. Paiar, J. H. Pensavalle, L. Raffaele, F. Romano, A. Subiel, E. Touzain, G. Verona Rinati and G. Felici

130 First experimental validation of silicon-based sensors for monitoring ultra-high dose rate electron beams
Elisabetta Medina, Arianna Ferro, Mohammad Abujami, Aurora Camperi, Matteo Centis Vignali, Emanuele Data, Damiano Del Sarto, Umberto Deut, Fabio Di Martino, Mohammad Fadavi Mazinani, Marco Ferrero, Veronica Ferrero, Simona Giordanengo, Oscar A. Martì Villarreal, Mohammad Amin Hosseini, Felix Mas Milian, Luigi Masturzo, Diango M. Montalvan Olivares, Marco Montefiori, Giovanni Paternoster, Jake Harold Pensavalle, Valentina Sola, Roberto Cirio, Roberto Sacchi and Anna Vignati

frontiers | Frontiers in Physics

TYPE Editorial
PUBLISHED 20 June 2024
DOI 10.3389/fphy.2024.1439081



OPEN ACCESS

EDITED AND REVIEWED BY
Federico Giove,
Centro Fermi—Museo storico della fisica e Centro studi e ricerche Enrico Fermi, Italy

*CORRESPONDENCE
Fabio Di Martino,
f.dimartino@ao-pisa.toscana.it
Emanuele Scifoni,
emanuele.scifoni@tipfa.infn.it

RECEIVED 27 May 2024
ACCEPTED 30 May 2024
PUBLISHED 20 June 2024

CITATION
Di Martino F, Scifoni E, Patera V, Montay-Gruel P, Romano F, Darafsheh A and Tozzini V (2024), Editorial: Multidisciplinary approaches to the FLASH radiotherapy. *Front. Phys.* 12:1439081. doi: 10.3389/fphy.2024.1439081



# Editorial: Multidisciplinary approaches to the FLASH radiotherapy

Fabio Di Martino[1,2,3]*, Emanuele Scifoni[4,5]*, Vincenzo Patera[6,7], Pierre Montay-Gruel[8,9], Francesco Romano[10], Arash Darafsheh[11] and Valentina Tozzini[2,12]

[1]Azienda Ospedaliera Universitaria Pisana, Pisa, Italy, [2]INFN Sezione di Pisa, Pisa, Italy, [3]Centro Pisano Multidisciplinare sulla Ricerca e Implementazione Clinica della Flash Radiotherapy (CPFR), Pisa, Italy, [4]INFN-TIFPA, Trento Institute for Fundamental Physics and Applications, Trento, Italy, [5]Department of Physics, University of Trento, Trento, Italy, [6]Dipartimento di Scienze di Base e Applicate all'Ingegneria, Università di Roma La Sapienza, Roma, Italy, [7]INFN, Sezione Roma-1, Roma, Italy, [8]Antwerp Research in Radiation Oncology (AReRO), Centre for Oncological Research (CORE), University of Antwerp, Antwerp, Belgium, [9]Radiation Oncology Department, Iridium Netwerk, Wilrijk, Belgium, [10]INFN Sezione Catania, Catania, Italy, [11]Department of Radiation Oncology, Washington University School of Medicine in St. Louis, St. Louis, MO, United States, [12]Istituto Nanoscienze—CNR, Lab NEST-SNS, Pisa, Italy

KEYWORDS

**radiotherapy, dosimetry, radiobiology, radiobiological modeling, FLASH radiotherapy, ultra high dose rate irradiation, ultra high dose-per-pulse, clinical translation**

Editorial on the Research Topic
Multidisciplinary approaches to the FLASH radiotherapy

Radiotherapy (RT) is extensively used in cancer treatment, although its toxicity often limits the treatment of radioresistant tumors. In this context, it has been recently shown, that irradiation at ultra-high dose rate (UHDR) (mean dose rate ≥40 Gy/s, with specific beam characteristics), called "FLASH-RT" may significantly reduce radiation-induced toxicity on normal tissues, while keeping similar antitumor effect as conventional RT [1]. This so called "FLASH effect" has been demonstrated *in vivo* on different animal models and various tumor types, using different radiations types (electrons, protons, carbon ions, and photons [2]) and pulse structures.

While these rapidly accumulating results indicate bright prospects, the clinical translation is still in its early phase, due to different challenges. First, several technological issues must be addressed to design new stable radiation sources capable of delivering beams with fluences orders of magnitude higher than those of conventional RT, and with a reliable real time beam monitoring system. This also implies the need of new dosimetric protocols, since most of the active dosimeters used for conventional beams do not respond accurately to UHDR and ultra high dose-per-pulse (UHDP) [3, 4]. Accurate dosimetry is not only needed for clinical implementation, but also for more robust and reproducible pre-clinical experiments [5]. The second challenge is understanding the biological mechanism underlying the FLASH effect, to explain the differential response of cancer vs. normal tissues. Several hypotheses have been considered, involving the whole cascade from the early radiation chemistry events to the classical radiation-induced molecular and cellular mechanisms and tissue recovery processes, also including a role for (epi)-genetics, stem cells or the immune system. While many results support different hypotheses, no compelling evidence exists that can yet confirm any of them.

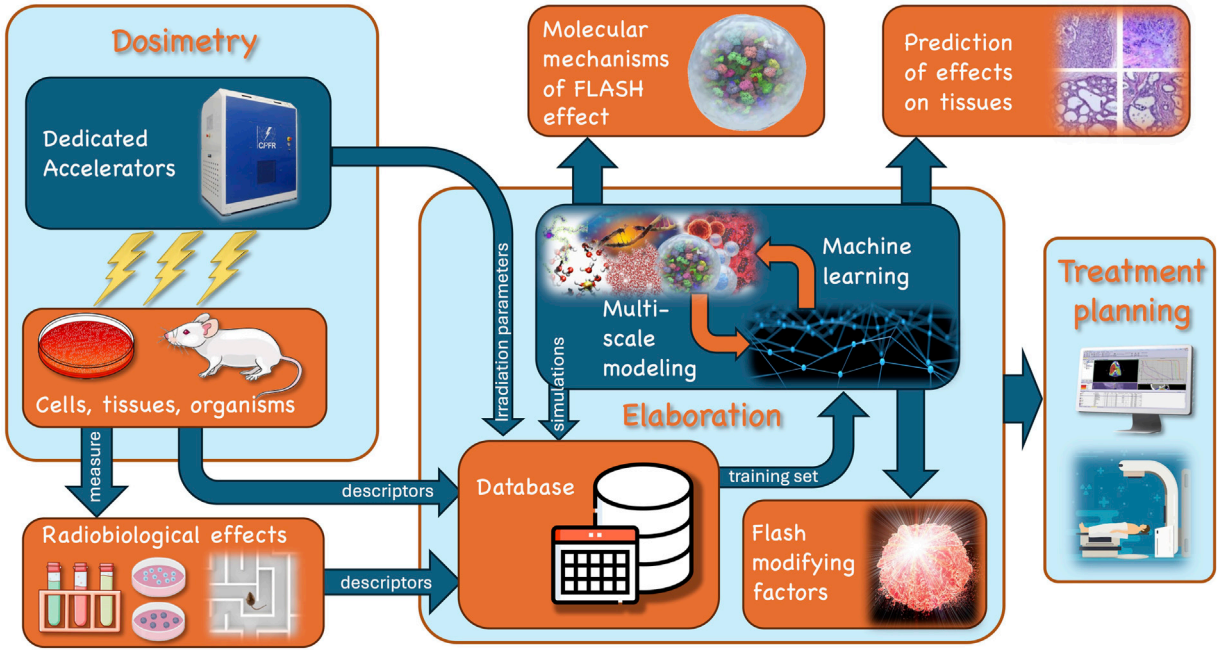


FIGURE 1
Exemplary scheme of the multi-disciplinary efforts involved in the study and exploitation of the FLASH effect. Following the arrow flux from top left of the scheme: 1. dedicated accelerators are needed to generate beams with suitable and tunable parameters (dose rate, dose per pulse, pulse dynamics, linear energy transfer (LET), etc.) to explore the domain of the FLASH irradiation regime; 2. a strong dosimetry effort is needed to characterize the beams and the dose released to the cells in culture and tissues, either *in vitro* or *in vivo;* 3. subsequently, a number of different indicators of the radiobiological effects (e.g., ROS, cell survival, cognitive impairment) can be measured; 4. the descriptors of the radiobiological effects, as well as the descriptors of cell/tissues and the parameters of irradiation may be passed to a database for *in silico* elaboration based on simulations and machine learning algorithms to analyze data and extract the *FLASH modifying factor*; 5. Overall this multi-disciplinary elaboration will clarify the molecular mechanisms, allow a quantitative prediction of the effect on different tissues, and give indication for the treatment planning in a clinical final context.

The full clinical exploitation and optimization of UHDR beams and FLASH-RT requires a multidisciplinary approach. Figure 1 illustrates a possible scheme of such an effort, involving multiple interconnected research areas, from the technology of the beam production and characterization to the final effects on cell and tissues, through the dose distribution and molecular-subcellular dynamics. In this landscape the determinants of the FLASH effect can be identified by providing quantitative relationships between the irradiation parameters, tissue descriptors and radiobiological effects. With these motivations, we selected and collected, in this Frontiers Research Topic 11 contributions covering various aspects of these areas. Among these, Di Martino et al. report the dosimetric characterization of a dedicated UHDP electron linear accelerator (linac Electron Flash (EF) with triode-gun) with the capability of flexibly and independently varying all the beam parameters over a wide range, also allowing the implementation of radiobiological experiments *in vitro* and *in vivo*. This study completes some previous ones from the same authors [6, 7] providing a full description of the EF beams' potential. The real time beam monitoring needs of these new linacs and related issues are addressed by Vojnovic et al. reporting the design of a beam charge integrating transformer achieving a high sensitivity with respect to standard UHDP beam monitoring systems. On the same topic, Medina et al. tested silicon-based sensors on UHDP electron beams and the possibility of using them as beam monitoring systems in FLASH regime by verifying their linear response with dose-per-pulse up to over 10 Gy. A major challenge in the case of protons is the realization of conformal treatments exploiting the spread out of Bragg peak. This topic is detailed in Horst et al., describing a perfect *in vivo* FLASH target station exploiting two different setups for range modulation. Recently, it was also proposed that the spatial fractionation of the beam on the micro-milli scale (amongst which *mini-beam* irradiation) might result in effects similar to FLASH-RT. Pensavalle et al. designed, realized and dosimetrically characterized the first mini-beam and mini-beam/FLASH beams for electrons, by modifying the EF beam optics with tungsten templates. This apparatus can be used for experiments exploring possible synergies between minibeam and FLASH effects in a clinical perspective.

Downstream of the irradiating beam, a vast amount of experimental evidence of the FLASH effect is accumulating. A systematic organization of the literature is difficult, since data are taken in very different conditions and use a multitude of different irradiation conditions and radiobiological "end points". Del Debbio et al. report a systematic review of the *in vitro* experiments on electron-FLASH-RT presenting them in relation to the different hypotheses on the radiobiological mechanisms.

The *in silico* approaches are powerful tools in complement to experiments, to investigate the response of cancer vs normal tissues. Most of the modeling efforts concentrate on the chemical stages of radiation damage, considered as the most sensitive to spatio-temporal features of dose delivery, using e.g., reaction diffusion based models. The simulations by Baikalov et al. see a negligible role of the inter-track interactions in the parameters range where the FLASH effect is

observed with electrons, confirming what was observed with protons [8] and carbon ions [9], indicating that effects might occur on larger time scales. To expand simulation time scales, Abolfath et al. use coarse models of tissues with different connectivity and porosity representing normal and cancer tissues, and show different inter-track effects, arguing this as a possible source of the differential effect of FLASH-RT. With a different approach Battestini et al. explored the connection between the chemical stages and the DNA damage through a multiscale extension of the generalized stochastic microdosimetric model [10] integrated with a chemical network [11], reproducing the experimental trend of the *in vitro* experiments in terms of dose, dose rate and LET dependence of the effect onset. Overall, we envision that combining Monte Carlo with multi-scale molecular dynamics simulations [12] would amplify the predictive power of *in silico* approaches.

The clinical perspectives for FLASH-RT are potentially huge, and their investigation is just at the beginning. Ursino et al. illustrate a clinical scenario of the FLASH effect, supported by pre-clinical *in vivo* studies, and focusing on possible future applications of low and very high energy electron (VHEE) beams. The potential of VHEE is also explored by Muscato et al. in intracranial lesions using a small number of mono-energetic fields and assuming an active-scanning-like beam delivery strategy, compared with conventional x-ray intensity modulated radiation therapy(IMRT) and proton therapy, both considering and not considering a possible FLASH sparing effect.

This Research Topic is a good representation of the state-of-the-art of research towards both the understanding of the mechanisms and the clinical translation of the FLASH effect: much has been done recently both in the field of the production and monitoring/measuring of UHDP beams. These results are the first step to proceed towards a deeper knowledge of the phenomenon and towards its optimal clinical implementation.

## Author contributions

FDM: Conceptualization, Writing–original draft, Writing–review and editing. ES: Conceptualization, Writing–original draft, Writing–review and editing. VP: Writing–review and editing. PM-G: Writing–review and editing. FR: Writing–review and editing. AD: Writing–review and editing. VT: Conceptualization, Visualization, Writing–original draft, Writing–review and editing.

## Funding

The author(s) declare that financial support was received for the research, authorship, and/or publication of this article. The authors acknowledge the support of Next Generation-EU (Piano Nazionale di Ripresa e Resilienza (PNRR), Missione 4, Componente 2, Ecosistemi dell'Innovazione) through the project Tuscany Health Ecosystem (THE-Spoke 1, grant ECS_00000017); European Union - NextGenera-tionEU PNRR - M4C2-I1.3 Project PE 00000019 "HEAL ITALIA", INFN CSN5 through the FRIDA Call and the MIRO project.

## Conflict of interest

The authors declare that the research was conducted in the absence of any commercial or financial relationships that could be construed as a potential conflict of interest.

The author(s) declared that they were an editorial board member of Frontiers, at the time of submission. This had no impact on the peer review process and the final decision.

## Publisher's note



## References

1. Montay-Gruel P, Petersson K, Jaccard M, Boivin T, Germond JF, Petit B, et al. Irradiation in a flash: unique sparing of memory in mice after whole brain irradiation with dose rates above 100 Gy/s. *Radiother Oncol* (2017) 124:365–9. doi:10.1016/j.radonc.2017.05.003

2. Vozenin MC, Bourhis J, Durante M. Towards clinical translation of FLASH radiotherapy. *Nat Rev Clin Oncol* (2022) 19:791–803. doi:10.1038/s41571-022-00697-z

3. Di Martino F, Del Sarto D, Bisogni MG, Capaccioli S, Galante F, Gasperini A, et al. A new solution for UHDP and UHDR (Flash) measurements: theory and conceptual design of ALLS chamber. *Phys Med* (2022) 102:9–18. doi:10.1016/j.ejmp.2022.08.010

4. Gómez F, Gonzalez-Castaño DM, Gómez Fernández N, Pardo-Montero J, Schüller A, Gasparini A, et al. J Paz-Martín Development of an ultra-thin parallel plate ionization chamber for dosimetry in FLASH radiotherapy. *Med Phys* (2022) 49:4705–471. doi:10.1002/mp.15668

5. Romano F, Bailat C, Jorge PG, Lerch MLF, Darafsheh A. Ultra-high dose rate dosimetry: challenges and opportunities for FLASH radiation therapy. *Med Phys* (2022) 49:4912–32. doi:10.1002/mp.15649

6. Felici G, Barca P, Barone S, Bortoli E, Borgheresi R, De Stefano S, et al. Transforming an IORT linac into a FLASH research machine: procedure and dosimetric characterization. *Front Phys* (2020) 8:374. doi:10.3389/fphy.2020.00374

7. Di Martino F, Barca P, Barone S, Bortoli E, Borgheresi R, De Stefano S, et al. FLASH radiotherapy with electrons: issues related to the production, monitoring, and dosimetric characterization of the beam. *Front Phys* (2020) 8:570697. doi:10.3389/fphy.2020.570697

8. Ramos-Méndez J, Domínguez-Kondo N, Schuemann J, McNamara A, Moreno-Barbosa E, Faddegon B. LET-dependent intertrack yields in proton irradiation at ultra-high dose rates relevant for FLASH therapy. *Rad Res* (2020) 194:351–62. doi:10.1667/RADE-20-00084.1

9. Weber UA, Scifoni E, Durante M. FLASH radiotherapy with carbon ion beams. *Med Phys* (2022) 49:1974–92. doi:10.1002/mp.15135

10. Cordoni F, Missiaggia M, Attili A, Welford SM, Scifoni E, La Tessa C. Generalized stochastic microdosimetric model: the main formulation. *Phys Rev E* (2021) 103:012412. doi:10.1103/PhysRevE.103.012412

11. Labarbe R, Hotoiu L, Barbier J, Favaudon V. A physicochemical model of reaction kinetics supports peroxyl radical recombination as the main determinant of the FLASH effect. *Rad Oncol* (2020) 153:303–10. doi:10.1016/j.radonc.2020.06.001

12. Palermo G, Bonvin AMJJ, Dal Peraro M, Amaro RE, Tozzini V. Editorial: multiscale modeling from macromolecules to cell: opportunities and challenges of biomolecular simulations. *Front Mol Biosci* (2020) 7:194. doi:10.3389/fmolb.2020.00194

frontiers | Frontiers in Physics

TYPE Original Research
PUBLISHED 05 May 2023
DOI 10.3389/fphy.2023.1060910



OPEN ACCESS

EDITED BY
Emanuele Scifoni,
Universities and Research, Italy

REVIEWED BY
Francesco Giuseppe Cordoni,
University of Trento, Italy
Valentina Tozzini,
National Research Council (CNR), Italy

*CORRESPONDENCE
Ramin Abolfath,
ramin1.abolfath@gmail.com

RECEIVED 03 October 2022
ACCEPTED 14 April 2023
PUBLISHED 05 May 2023

CITATION
Abolfath R, Baikalov A, Fraile A, Bartzsch S, Schüler E and Mohan R (2023), A stochastic reaction–diffusion modeling investigation of FLASH ultra-high dose rate response in different tissues. *Front. Phys.* 11:1060910. doi: 10.3389/fphy.2023.1060910



# A stochastic reaction–diffusion modeling investigation of FLASH ultra-high dose rate response in different tissues

Ramin Abolfath[1,2]*, Alexander Baikalov[1,3,4], Alberto Fraile[5], Stefan Bartzsch[3,4], Emil Schüler[1] and Radhe Mohan[1]

[1]Department of Radiation Physics, University of Texas MD Anderson Cancer Center, Houston, TX, United States, [2]Physics Department, Sharif University of Technology, Tehran, Iran, [3]Department of Radiation Oncology, School of Medicine and Klinikum Rechts der Isar, Technical University of Munich, Munich, Germany, [4]Helmholtz Zentrum München GmbH, German Research Center for Environmental Health, Institute of Radiation Medicine, Neuherberg, Germany, [5]Nuclear Futures Institute, Bangor University, Bangor, United Kingdom

**Purpose:** The aim of the study was to propose a theory based on topology and geometry of diffusion channels in tissue to contribute to the mechanistic understanding of normal tissue sparing at ultra-high dose rates (UHDRs) and explore an interplay between intra- and inter-track radical recombination through a reaction–diffusion mechanism.

**Methods:** We calculate the time evolution of particle track structures using a system of coupled reaction–diffusion equations on a random network designed for molecular transport in porous and disordered media. The network is representative of the intra- and inter-cellular diffusion channels in tissues. Spatial cellular heterogeneities over the scale of track spacing are constructed by incorporating random fluctuations in the connectivity between network sites, resembling molecular mass and charge heterogeneities at the cellular level.

**Results:** We demonstrate the occurrence of phase separation among the tracks as the complexity in intra- and inter-cellular structure increases. At the strong limit of structural disorder, tracks evolve individually like isolated islands with negligible inter-track as they propagate like localized waves in space, analogous to the Anderson localization in quantum mechanics. In contrast, at the limit of weak disorder in a homogeneous medium, such as water, the neighboring tracks melt into each other and form a percolated network of non-reactive species. Thus, the spatiotemporal correlation among chemically active domains vanishes as the inter-cellular complexity of the tissue increases from normal tissue structure to fractal-type malignancy.

**Conclusion:** Differential FLASH normal tissue sparing may result from the interplay of the proximity of tracks over the intra- and inter-cellular landscape, a transition in the spatial distribution of chemical reactivity, and molecular crowding. In this context, insensitivities in the radiobiological responses of the tumors to FLASH-UHDR are interpreted via a lack of geometrical correlation among isolated tracks. The structural and geometrical complexities of cancerous cells prevent the clustering of tracks over a timescale, in which inter-track chemical reactivities presumably prevail in normal tissues. A series of systematic experiments on radiolysis-induced diffusivity and reactivity in actual normal and cancerous

tissues must be performed to classify the tissues potentially spared by FLASH-UHDRs and verify our theory.

KEYWORDS

**flash, radiotherapy, particle therapy, radiobiology, molecular simulations**

# 1 Introduction

The unique normal tissue sparing of FLASH ultra-high dose rates (UHDRs), which is 40 Gy/s and higher, has recently attracted considerable attention [1–18]. Preclinical studies have shown that FLASH-UHDR delivery reduces the toxic effects of radiation on DNA and cells in normal tissues compared to conventional dose rates (CDRs), whereas tumor tissues seem to be equally responsive to either dose rate modality ([17] and references therein). However, the interpretation of the experimental data and the underlying microscopic mechanism is under intensive investigation and debate among researchers in the field of radiation therapy.

Among the theories proposed for the interpretation of the experimental data [1–6, 8, 9, 11], the authors of the present work hypothesized a transition between intra- and inter-track reactions as the major physical mechanism for differential biological responses of CDR vs. FLASH-UHDR [10, 13, 14]. In these models, the time evolution of radiolysis products is assumed to propagate in homogeneous and uniform media, equivalent to water, regardless of the tissue type. Thus, the presented models lack differentiation with respect to tissue types upon exposure at FLASH-UHDRs.

A series of systematic experiments was recently conducted and published [15] on measurements of chemical yields of 7-hydroxy-coumarin-3-carboxylic acid in solutions irradiated by proton- and carbon-ion beams at UHDRs. These experimental studies have revealed evidence in favor of the inter-track coupling hypothesis, originally predicted by performing molecular dynamics simulations of track–track chemical interactions. The results of these simulations, presented in [10], have led to the interpretation of molecular crowding in populations of reactive oxygen species (ROS) and the formation of agglomerates in the form of non-reactive oxygen species (NROS), consistent with recent observations reported in [15].

In this work, we extend our model calculation on the same physical grounds as in [10, 13, 14] and consider the cellular structure of normal and cancerous tissues at a coarse-grained scale. We develop a mathematical description of tissue structure complexity to examine the interplay between the rates of radical diffusion and recombination as a function of this structural complexity. We predict the occurrence of intra- to inter-track transitions as the structural complexity decreases from, for example, tumor to normal tissue.

## 1.1 Terminology

In a nutshell, the passage of a high-energy particle (electron, proton, or heavier charged particles) through matter leaves a linear dynamical footprint of a cylindrically symmetric (isotropic) exchange of energy with the electrons and nuclei constituting molecular structures. This linear structure and its branches are known as a particle track.

A single track is a random collection of a sharp spatiotemporal distribution of non-ionized and ionized excitations with a varying nanometer-scale diameter, which depends on the particle's kinetic energy that determines the magnitude of energy exchange. Due to the quantum electrodynamic nature of energy exchange, the excitations are created within attoseconds after the passage of the particle.

Immediately after their creation, molecular excitations and ions undergo decay processes. The relaxation time associated with the decay of excitations (including recombination of mobile ions into various types of stable products and chemical species) is much longer than their generation time. Because the excited molecules and ions are mobile in cellular structures, they decay at the same time as they diffuse away from the center of the track.

The presence of high concentrations of localized excitonic energy of molecules surrounding mobilized ions induces an explosive irreversible flow of thermal energy to ion species, which, in turn, theoretically significantly enhances the effective diffusion constant of these ions. The core temperature of a track depends on the particle type and its linear energy loss per unit length (linear energy transfer, LET). It can go up to several thousands of Kelvin for heavy charged particles [13]. Ions move randomly along the radial direction away from the hot core of the tracks with a thermally boosted kinetic energy that generates shock waves [13, 44–46]. They asymptotically lose their kinetic energy and fall into cold diffusion at a thermal equilibrium condition because of collisions and energy exchange with the molecules in the environment. Eventually, ions rest at room temperature with a transformed chemical composition.

It should be noted that such physical and chemical phenomena are not included in standard MC models based on homogenous and uniform water medium. Nonetheless, these phenomena may have significant effects on the measured endpoint of MC simulations, such as radical yields. Throughout this process, biological damage to the host's cellular structure occurs as ions interact chemically with bio-molecules, such as DNA and lipids in membranes.

A typical radiotherapy beam of particles forms a random distribution of expanding and decaying tracks in targeted (tumors) and untargeted (normal tissues) volumes. Initially, as pointed out previously, the tracks expand individually via a time-dependent diffusion mechanism as they decay due to deexcitation and ion-recombination processes. The time evolution of such an ensemble of individually evolving tracks can be reduced to that of a single track if the geometrical overlap among tracks is negligible. We refer to this limit as an "independent track structure". Conversely, the "strongly correlated track structure" can be anticipated at a limit in which the process of inter-track ion exchanges, chemical transformation, and recombination occurs simultaneously due to the destructive interference of sufficiently close tracks, a molecular-

crowding phenomenon. Therefore, we refer to these two distinguishable classes of chemical exchange mechanisms as intra- and inter-track states.

The transition between intra- and inter-track recombination depends on the dose and dose rate. More precisely, the higher the beam flux (the number of particles entering a unit area per unit of time), the higher the compactness of particles in a given time interval hitting the target. In this limit, the probability of overlap among the tracks before their annihilation becomes significant. Thus, under certain conditions, a transition from the intra-track to inter-track reaction can be predicted. In our recent publications [10, 13, 14], the latter has been hypothesized to be a physical mechanism for FLASH-UHDRs.

## 2 Materials and methods

This model aims to describe the effects of intra- and inter-track diffusion and interaction as a function of the structural complexity of the target medium. To this end, we develop a reaction–diffusion model of spatially and temporally separated particle tracks and calculate the interaction of OH radicals from the tracks to form $H_2O_2$. Importantly, the model utilizes a spatially varying diffusion constant, whereby the solutions to the reaction–diffusion system are calculated numerically by stochastic variation of the diffusion constant. Subsequently, this reaction–diffusion system is related to an analogous percolation model of diffusing ions in order to define the target structural heterogeneity with a measure from percolation theory, the site occupation probability $p$, and relate this to the diffusion constant.

### 2.1 Reaction–diffusion model

In this model, the radiation-induced chemicals are concentrated in a core of a cylindrically symmetric body/cloud of track structure. As a track structure is nothing but a cloud of ROS and NROS, the expansion of the track can be interchangeably considered for the description of the time evolution of the system of coupled ROS and NROS (i.e., their diffusion and reaction processes). In particular, we performed the track structure calculation by conventional MC methods in a homogenous water medium where the location of ionization and molecular excitation points were identified. After the construction of a cylindrical cloud of ROS and NROS, we further considered reaction–diffusion solutions in an inhomogeneous and rough cellular medium. This kind of matching between MC and the coarse-grained reaction–diffusion model is inevitable unless atomistic (not volumetric) cellular structures and molecular inhomogeneities are added in the next generations of MC codes.

The mathematical details of our model calculation with analytical solutions for the time evolution of a single track are given in the Supplementary Appendix. We used the analytical formulas given in the Supplementary Appendix to cross-check our numerical solutions obtained from discretizing the space and time in a finite difference approach employed to calculate the solutions of the coupled reaction–diffusion partial differential equations of multi-track structures:

$$\frac{\partial u}{\partial t} = G + \vec{\nabla}\cdot\left(D_f\left(\vec{r}\right)\vec{\nabla}u\right) - k_1 u + k_2 v - 2k_3 u^2 - k_{12}uv, \quad (1)$$

$$\frac{\partial v}{\partial t} = k_1 u - k_2 v + k_3 u^2. \quad (2)$$

Here, $u(\vec{r},t)$ and $v(\vec{r},t)$ represent ROS and NROS densities, respectively, for example, $u = [^{\bullet}OH]$ and $v = [H_2O_2]$ at spatial coordinate, $\vec{r}$, and time, $t$. $G(\vec{r},t)$ and $D_f(\vec{r})$ represent the ROS production yield, proportional to the dose rate, and diffusion constant of the fast-moving species (neglecting the diffusion of slow-moving species), and $k_1$, $k_2$, $k_3$, $k_{12}$ are reaction rate constants. $k_1$ represents the scavenging rate of ROS. The dependence of the diffusion constant on cellular or tissue inhomogeneities has been accounted for in Eq. 1 by $D_f(\vec{r})$.

In the limit of ideal diffusion, where $D_f$ is a constant, independent of the position of ROS in space, and in the absence of all reaction rates, $k_1 = k_2 = k_3 = k_{12} = 0$, the time evolution of a single track, created initially at time $t = 0$, far from the initial nano-scale dimension of the track, represented by radius $w$, asymptotically approaches a Gaussian distribution function modulus, a factor proportional to the initial number of chemical species, $c_0$:

$$u\left(\vec{r},t\right) = \frac{c_0}{4\pi D_f t}\exp\left(-\frac{r^2}{4D_f t}\right), \quad (3)$$

where $c_0 = \pi w^2 u_0$ and $u_0$ is the initial density of ROS, integrated over a unit length along the trajectory of the primary particle. Note that the Gaussian function is the exact solution of the diffusion equation, $\partial u/\partial t = D_f\nabla^2 u$, with a spike-like initial and boundary condition.

As a representative of ROS that causes damage to DNA and/or lipids in membranes, we consider $^{\bullet}OH$-radicals for $u$. $^{\bullet}OH$-radicals are known to diffuse through cellular space and react with biomolecules, including DNA, proteins inside and outside the cells, and lipids in cell membranes. Denoting $k_1$, an average decay (scavenging) rate of a population of $^{\bullet}OH$ in the track (resulting in DNA, proteins, lipids, or, in general, biomolecular (BM) hydrogen abstraction as described in [30] in which $[DNA^{\bullet}]$ and $[BM^{\bullet}]$ partially contribute to $v$, e.g., $v = [H_2O_2] + [DNA^{\bullet}] + [BM^{\bullet}]$) introduces an exponential decay in solutions of $u$, in Eq. 3:

$$u\left(\vec{r},t\right) = \frac{c_0}{4\pi D_f t}\exp\left(-\frac{r^2}{4D_f t} - k_1 t\right). \quad (4)$$

If cells were uniform and homogeneous, like in liquid water, the diffusion of ions induced by radiation must have occurred like in an ordered medium, as described in Eq. 4. However, the current models in radiobiology do not consider intra- and inter-cellular inhomogeneities in the diffusion of radiolysis products due to a lack of experimental data and theoretical models.

To fill the gaps in our understanding of diffusion channels at the microscopic levels, we performed a series of molecular dynamics simulations to investigate the diffusion of $^{\bullet}OH$-radicals [43]. To visualize some of these effects in real time, we uploaded samples of our simulations in the form of videos available on YouTube [26, 27]. The simulations have clearly shown that variability in the molecular mass and charge distribution and, in general, chemical, physical, and mechanical composition of the micro-environment of cells may dramatically alter the diffusion of $^{\bullet}OH$-radicals. Therefore, it is a natural generalization to consider spatial fluctuations in the

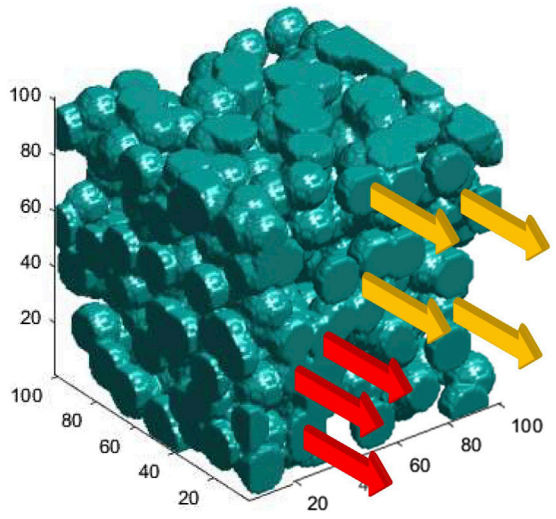


FIGURE 1
Schematic sketch of tracks passing through a porous media, representative of heterogeneities in cells and tissues. Clusters through which diffusion is allowed are shown in blue. In contrast, diffusion is forbidden in the void space among the clusters. Red arrows represent interacting (mediated by diffusion) tracks as they pass through a single cluster; hence, they are connected tracks. Orange arrows passing through isolated islands represent non-interacting tracks.

diffusion constant $D_f(\vec{r})$ because of an abundance of such molecular heterogeneities in cellular tissue. To incorporate the randomness at a coarse-grained level, we performed a Monte Carlo sampling on $D_f$ and solved numerical solutions of the stochastic reaction–diffusion partial differential equations for various realizations of $D_f(\vec{r})$ after discretizing the space and time coordinates.

## 2.2 Random walk percolation model

As a complementary model to the reaction–diffusion model given in Eqs 1, 2, we cross-validated the numerical results against the solutions of random walk or Brownian motion on the same random network throughout the percolation theory [40–42]. More details on the description of the modeling of the diffusion constant can be found in Supplementary Section SE.

In this context, a regular lattice is a lattice with no disorder. It is an ordered lattice with all diffusion links connected to neighboring sites throughout the lattice points. In a classical disorder model, the diffusion from an occupied site to a neighboring occupied site can be simulated through the random walk. In this model, the diffusion can be parameterized in terms of a single site occupation probability $p$ and the random walk probability $q = 1/2d$, where $d$ is the embedding dimension of the square lattice and $2d$ is the geometrical coordination number of any site on the lattice. In other words, on a realization of a random lattice, $p$ and $1 - p$ are the fraction of occupied and unoccupied sites, a parameter that determines the average size of the clusters on the lattice. In this model, the diffusion constant, $D_f$, is an increasing function of $p$. It continuously increases with $p$ above a critical value (a percolation threshold, $p_c$) and reaches a maximum value at $p = 1$, where all lattice sites are occupied, corresponding to a regular lattice with no disorder.

In a random walk, on a regular lattice with $p = 1$, at every trial or simulation time step, the diffusing ion randomly selects one of its nearest neighbor sites with probability $q$ and moves to that selected site. On a random lattice with $p < 1$, we first check if the site is occupied with probability $p$, then the move to that site occurs with probability $q$, and the ion moves one step. Otherwise, the ion stays on the initial site with probability $1 - p$, and the search for another move to another occupied neighboring site continues in the next random walk trial unless no occupied neighboring sites are available.

The diffusion constant of such a Brownian particle can be calculated by the Einstein relation, $\langle r^2 \rangle = 2D_f t$. Here, $\vec{r}$ is the Euclidean distance that measures how far the particle has moved randomly away from the center of the coordinates where it was created. Above the network percolation threshold ($p > p_c$), the Brownian motion can find at least one trajectory to cross the entire system, and $D_f = \langle\langle r^2 \rangle\rangle/2t$ represents the mean diffusion constant of the entire network. Otherwise, if all clusters are found to be isolated, $D_f = 0$ (including at the percolation point, $p = p_c$). In the latter case, although diffusion through the entire network is not possible, a limited diffusion confined within a cluster can still occur. In this case, the diffusion length is limited to the cluster size.

One may expect a finite number of tracks passing through a single cluster to interact and recombine (the red tracks in Figure 1) because diffusion among them is possible. Note that $\langle\langle \vec{r} \rangle\rangle = 0$ because of the unbiased random walk considered in these simulations. For a given $p$, $\langle\langle \cdots \rangle\rangle$ represents double averaging, that is, random walk averaging subjected to a specific network configuration, followed by ensemble averaging over a large number of random network configurations. Thus, $D_f = \langle\langle r^2 \rangle\rangle/2t = \frac{1}{2N_c}\sum_{i=1}^{N_c} \langle r^2 \rangle_i / t_i$, where $i$ is an index going over different realizations of the $N_c$ random configurations subjected to a given $p$. Using the same simulation time for all $N_c$ random configurations, $t_1 = t_2 = \ldots = t_{N_c} = t$ simplifies the expression to $D_f = \frac{1}{2tN_c}\sum_{i=1}^{N_c} \langle r^2 \rangle_i$. An alternative approach on ensemble average over various clusters connecting the opposite boundaries of the lattice is given in Supplementary Section SE.

For a perfect network (a network with no disorder, such as a homogeneous medium in normal cells), where $p = 1$, $D_f$ is at its maximum. It decays continuously to lower diffusion values for $p_c \leq p \leq 1$, vanishes at $p = p_c$, and remains zero within $p \leq p_c$. Note that close to $p = p_c$ (from above), the clusters in the network form a self-similar fractal-type structure in short distances with a Hausdorff dimension that is a measure of the tissue/cell roughness or, more specifically, their fractal dimension [40, 41].

Interested readers may refer to [40–42] for a discussion on the concepts of percolation and fractal dimensionality of a porous network embedded in three-dimensional space. The mathematical techniques introduced in [40–42] are relevant to the present applications, where we consider the porous space of malignant cells in which diffusion of radiolysis products is unlikely to occur in the voids among the clusters.

As a first step in proof-of-principle and to demonstrate the effects of cellular structures and textures on the interpretation of the tissue-sparing of FLASH-UHDR, we consider two types of media to study the transport of chemical species in typical normal and tumor

cells/tissues. Because of substantial differences in intra- and inter-cellular structure and chemical compositions of tumor *versus* normal cells, we solve reaction–diffusion equations in a homogenous and isotropic medium, similar to liquid water, as a representative of normal cells/tissues and in a heterogenous fractal-type porous and disordered medium for tumors [31, 32].

At the limit of strong disorder, the entire cellular structure can be divided into clusters or isolated islands. Consider an object in 3D as sketched in Figure 1, for example, a cell or a tissue segment. A cluster is a set of connected points on that object, disconnected from the rest of the points via diffusion due to structural heterogeneities. Thus, each cluster consists of connected sites, among which the diffusion of radiolysis products occurs normally. Hence, diffusion is forbidden in the space among the clusters. In Figure 1, tracks with different color codes are designated based on their classifications as interacting (red) and non-interacting (orange). The underlying porous media, representing the topology of diffusion channels in tumor cell/tissue, is depicted in blue, where diffusion can be performed. The blobs represent the topography of a spongy structure. The clusters are separated by clear voids, the space where diffusion is forbidden. They represent highly dense chemical heterogeneities at the molecular level that slow down or even block diffusion. Tumor calcification with the density in primary or metastatic lesions, such as metastatic lymph nodes, with a CT value above 60 Hounsfield Unit, represents such voids.

The structure in Figure 1 can be considered at the level of single cells or cell agglomerates in tissues, depending on the scale of the structure at hand. The topology of random diffusion channels, sketched in Figure 1, was constructed mathematically within a single cell and scaled up to the structure of tissues, assuming self-similarity and scale invariance of fractal structures, one of the characteristics of the disorder patterns. At the single-cell level, the rationale behind such a construction is the diffusion of $^{\bullet}$OH radicals through molecular heterogeneities.

The porous structure depicted in Figure 1 was created using a MATLAB code with a random number generator drawn from a uniform distribution to introduce blobs with specific radii at random locations in a 3D cube. The radius was chosen to be slightly larger than half the distance of a pair of nearest neighbor sites to illustrate the overlap between the two nearest neighbor blobs.

At UHDR, where the possibility of finding closely spaced tracks is likely, the ratio of the cellular diffusion correlation length $\xi$ and the mean track spacing determines the domain of intra- and inter-track dominance. $\xi$ is a measure of the size of the isolated islands in a single cell, that is, the mean diameter of the blue blobs in Figure 1.

Note that in our approach, the details of cellular structures, such as the exact locations of various organelles, are averaged out due to the random distribution of cells with respect to the random distribution of tracks, which is equivalent to a compound distribution as considered in the formulation of the theory of dual radiation action (TDRA) [33, 34]. TDRA considers the energy transfer in ionizations and regards the deposited energy proportional to the DNA double-strand breaks and the number of cellular sublethal lesions.

# 3 Results

## 3.1 Track interaction in the reaction–diffusion model

### 3.1.1 Interaction in an ordered medium

Figures 2, 3 present the time evolution of two tracks, simultaneously starting from two cylindrically symmetric clouds of ionization with radius $w$. The real-time motion of these tracks is available online.

In Figures 2A–D, a solution of the aforementioned 2D reaction–diffusion equation as a function of time was calculated in a homogenous and uniform medium, such as water. As shown, two cylindrical tracks evolve initially into two uncorrelated Gaussian probability distribution functions (PDFs) with centers located at $\vec{r}_i$ and $\vec{r}_j$ before they collapse together, where

$$u_i\left(\vec{r},t\right) = c_0 \frac{e^{-\frac{|\vec{r}-\vec{r}_i|^2}{4D_f\,(t-t_i)} - k_1\,(t-t_i)}}{4\pi D_f\,(t-t_i)}, \tag{5}$$

and

$$u_j\left(\vec{r},t\right) = c_0 \frac{e^{-\frac{|\vec{r}-\vec{r}_j|^2}{4D_f\left(t-t_j\right)} - k_1\left(t-t_j\right)}}{4\pi D_f\left(t-t_j\right)}. \tag{6}$$

Here, $D_f$ and $k_1$ are the diffusion constant and reaction rates, respectively. Our approach to numerical calculation of the time-dependent solutions of the diffusion equation subjected to a cylindrically symmetric initial condition and fitting to Gaussian functions at distances away from the cylinder can be found in Supplementary Appendix SD. To clarify the notations, $i$ and $j$ in these equations are the indices of tracks. In a discrete space-time version of reaction–diffusion equations, $\vec{r} = (x, y, z)$ is expressed by $(n_x\Delta_x, n_y\Delta_y, n_z\Delta_z)$, where $n_x, n_y, n_z = \{0, \pm1, \pm2, \ldots\}$ are integer numbers and $(\Delta_x, \Delta_y, \Delta_z)$ are the elements of the space grids along $(x, y, z)$ directions. Similarly, $t = n_t\Delta_t$, where $n_t = 0, 1, 2, \ldots$ and $\Delta_t$ denotes the time intervals.

Without loss of generality, to illustrate the effects of tissue types, we considered the creation time of tracks $t_i = t_j$ in these simulations. This condition approximately fulfills the time sequence of the track inductions at UHDR. Note that, in general, the temporal distribution of the tracks, hence their relative time elapse, depends on the dose rate. However, at UHDR, and only for the sake of simplicity of illustration on the effects of random diffusion on the time evolution of the tracks and the track–track recombination, we have intentionally neglected the time elapse among the tracks in comparison with other time scales involved in the present reaction–diffusion model.

As the simulation time proceeds in Figures 2A–D, two Gaussians merge together and form an elongated single PDF. The geometrical overlap of two Gaussians can be calculated analytically:

$$\begin{aligned}\langle u_i|u_j\rangle\,(t) &= \int d\vec{r}\,u_i\left(\vec{r},t\right)u_j\left(\vec{r},t\right)\\ &= c_0^2\frac{e^{-\frac{|\vec{r}_i-\vec{r}_j|^2}{8D_f t} - 2k_1 t}}{8\pi D_f t}.\end{aligned} \tag{7}$$

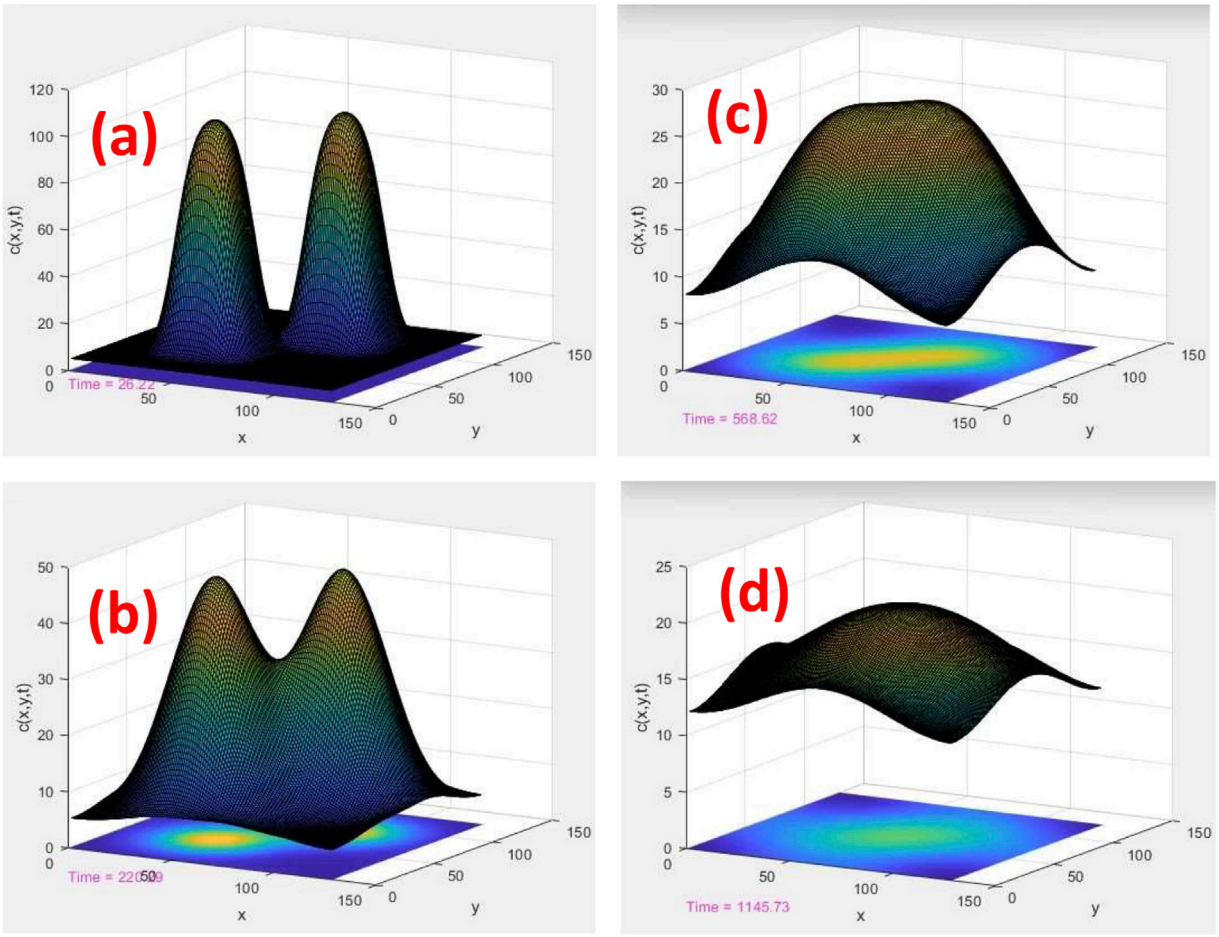


FIGURE 2
Time evolution of two tracks, $u_i$ $(x, y)$ and $u_j$ $(x, y)$, in a homogeneous and uniform medium. $c$ $(x, y) = u_i$ $(x, y) + u_j$ $(x, y)$ is the total density of ROS calculated by the superposition of individual ROSs. $(x, y)$ are the planner coordinates of the plane perpendicular to the axis of cylindrical tracks. The length scales are displayed in nm, and the time scales are 26, 220, 569, and 1,146 ps for **(A–D)**, respectively

As the two Gaussians combine, like melting two droplets into a single droplet, diffusion slows down in the overlap area. Instead, the diffusion is performed with a rate calculated by Eq. 7 from the periphery of combined Gaussians to the outside. In this model, intra-track interaction is parameterized by the rate constants $k_1$, $k_2$, $k_3$, $k_{12}$, and inter-track interaction is the geometrical overlap of the tracks, as given in Eq. 7.

Note that the Gaussian functions in Eqs 5, 6 are the analytical solutions of a single track in a uniform system. These solutions demonstrate the calculation of overlap integral analytically in a uniform system, as given in Eq. 7.

### 3.1.2 Interaction in a disordered medium

In a system of multi-tracks, as in Figure 2, or even a single track in a disordered medium, such as in Figure 3, the analytical solutions are not available, and the overlap integral should be calculated numerically by discretizing space and time. In such situations, we used analytical forms of solutions derived in the Supplementary Appendix to compare with the numerical solutions and check the accuracy of our finite difference method.

As shown in Figures 3A–D, we calculated a solution of a reaction–diffusion equation with an identical initial condition as in Figures 2A–D, except that the calculation was performed on a network with random connectivity between the neighboring sites to mimic the geometrical disorder of tumor cells with strong inhomogeneity and/or fractal-type porosity.

A series of connectivity probabilities $p$ was drawn from a uniform distribution within the interval of zero and one and subsequently convoluted to the diffusion constant $D_f$ for each diffusion site in the network. Although the reaction rate $k_1$ can be considered another random variable, we kept it constant at the same value as in the simulation shown in Figure 2 to isolate the effects of diffusion. Note that a special case of $p = 1$ describes the transport of ions on a homogeneous network with uniform connectivity that links nearest neighbor sites, corresponding to the kinetics of ions among normal cells, with the results depicted in Figure 2.

The time and length scales in Figures 2, 3 were chosen based on the conventional values of the diffusion constants. To simulate the expansion of a track of $^{\bullet}$OH-radicals at thermal equilibrium with the environment at room temperature and by using an empirical value $D_f = 4.3 \times 10^{-9} m^2/s = 0.43 \mathring{A}^2/ps$ [13], we divide the square sides of the

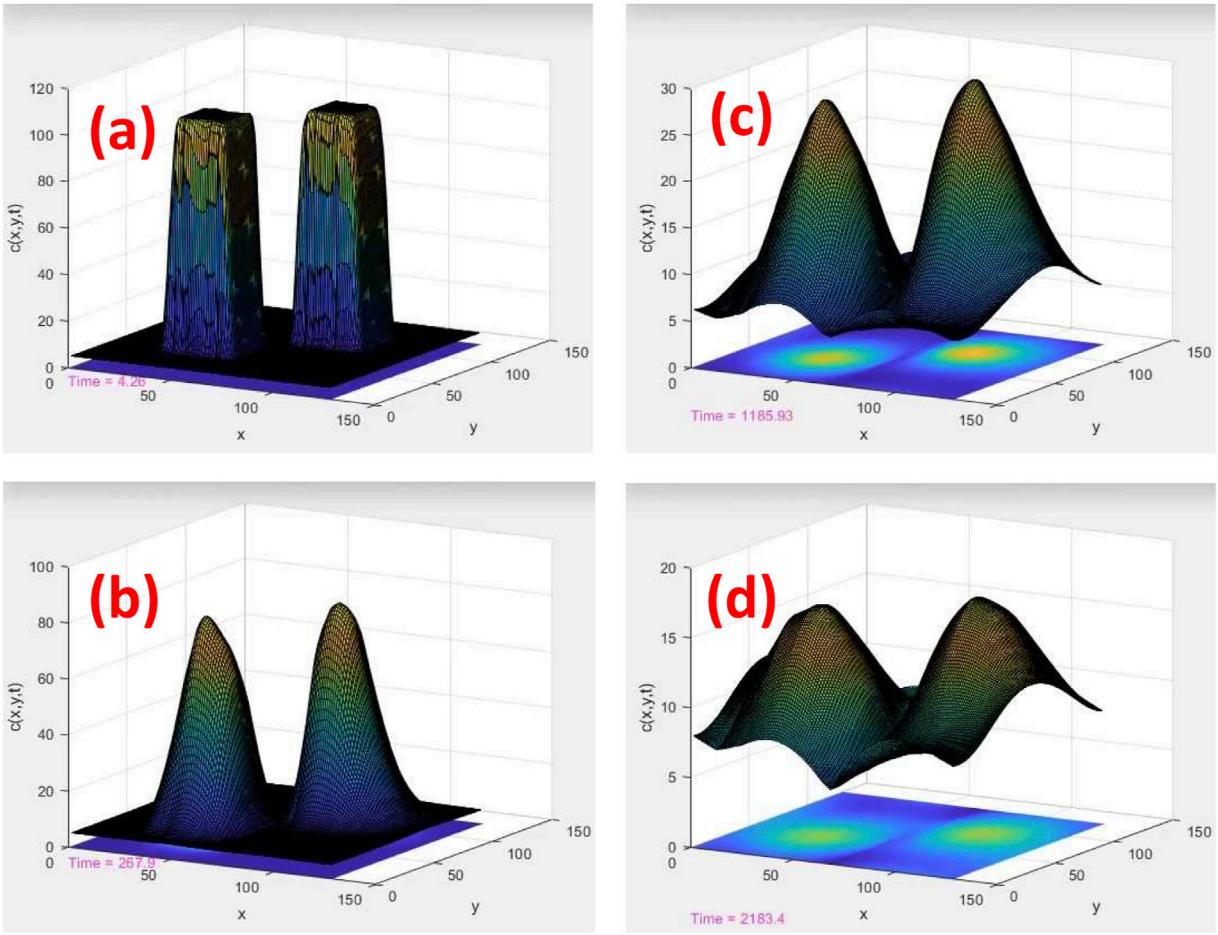


FIGURE 3
Time evolution of two tracks in a porous medium with random connectivity among the diffusion sites. Similar to Figure 2, $c\,(x, y) = u_i\,(x, y) + u_j\,(x, y)$. The length scales are displayed in nm, and the time scales are 4, 268, 1,186, and 2,183 ps for **(A–D)**, respectively

computational boxes into steps with 0.1 nm length. In these calculations, the time advances via 0.1 ps intervals to fulfill the Courant–Friedrichs–Lewy condition or the Nyquist sampling theorem in signal processing, in which the simulation time steps are required to be half or less of the period of the quickest dynamics. Accordingly, such length scales set the lateral sides of the computational boxes in Figures 2, 3 to 13 nm, larger than six folds of the width of a DNA double-stranded helix that is approximately 2 nm. The running times of these simulations were terminated at 0.5 μs with no significant differences from the times corresponding to Figures 2D, 3D. This condition simply allows the simulation to run until the numerical solutions converge to a satisfactory value. By monitoring the overlap integral between two tracks as a function of time, the numerical results do not change significantly beyond a time value, reported as a cutoff time. Once this condition has been fulfilled numerically, we terminate the simulation.

## 3.2 Relation to the percolation model

The overlap between two adjacent tracks is expected to happen at time scale $t = \ell^2/2D_f$ if the relevant length scale for diffusion (i.e., the diffusion length), $\langle\langle r^2\rangle\rangle^{1/2}$, becomes comparable to inter-track spacings $\ell$. Even below the percolation limit, $p < p_c$, where clusters do not connect from one side of the tissue to the other, tracks can overlap through intra-cluster diffusion channels if two or more tracks pass through a single cluster.

Another interesting combination of a system of tracks and isolated clusters can be represented by two neighboring tracks that pass through two separated and disconnected clusters with no diffusion channel between them, corresponding to a non-interacting track configuration as shown in Figure 1, where our construction of the structure and topology of random diffusion channels is illustrated schematically.

A collection of configurations of a system of tracks and tissue clusters under the condition, $p < p_c$, some with finite $D_f$, combined with vanishing $D_f$, leads to a system of tracks with lower effective interaction compared with tissues under the condition $p > p_c$, where all clusters are connected. The former represents tumors, and the latter represents normal tissues. Thus, the problem is interesting from a mathematical point of view as it describes the time evolution of percolating tracks mediated through diffusion channels subjected to percolation of the underlying medium, cellular structures, and tissues (i.e., a compound percolation system).

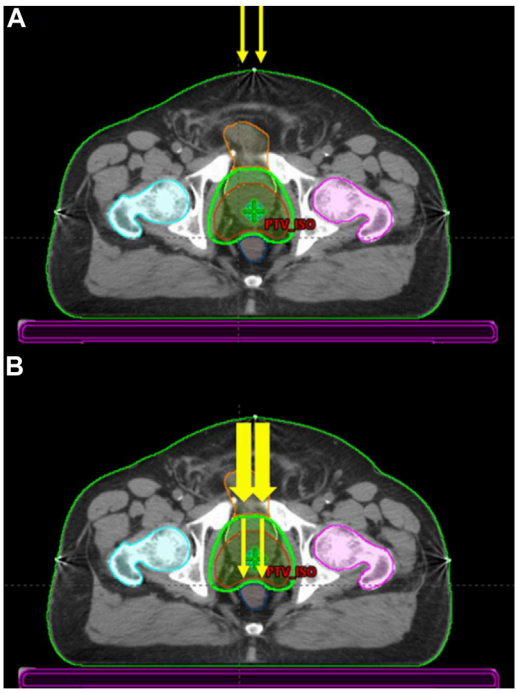


FIGURE 4
Schematic sketch of the diffusion expansion of two-particle tracks in the air before **(A)** and after **(B)** entering the patient body. The width of the arrows in normal tissues (thicker arrows) and the tumor (thinner arrows in the prostate) demonstrates the extent of inter-track overlaps in different tissue types. In normal tissues, the expanded tracks allow inter-track overlaps, whereas, in tumor tissues, the localized tracks yield negligible inter-track overlaps. At a given dose where the number of tracks (shown by arrows) is given, the lack of inter-track overlaps justifies insensitivities of radiobiological responses to dose rates.

At FLASH-UHDR conditions, if the correlation length in the network connectivity, $\xi$, (i.e., a measure of cluster size) is smaller than the mean inter-track distances, diffusion effectively does not occur to the extent of track spacings; thus, the response of the tissue falls into the class of isolated/single track states. This is a scenario the percolation theory predicts for typical tumor cells/tissues irradiated by a source of FLASH-UHDR.

As can be seen clearly from these two simulations, the effect of randomness in connectivity among the diffusion channels is to localize the tracks such that the cell/tissue responses exhibit insensitivity to the time-elapse among the tracks simply because of negligible inter-track overlaps. Hence, the cells and tissues with strong porosities and disorder in their diffusion channels (either normal or cancerous) under radiation must exhibit insensitivity to the dose rate, the same phenomenon observed empirically from the tumors under FLASH-UHDR.

To illustrate the ideas proposed in this work in the clinical setting, Figures 4A, B present schematic sketches of two tracks generated by two beamlets before and after entering the patient's body, respectively. The diffusive expansion of the beamlet tracks in normal tissues, depicted by the thicker arrows, and in tumor (prostate), depicted by thinner arrows, are seen. At a given time after the beamlets enter, they expand more rapidly in normal tissues because of higher diffusivity compared to the two isolated beamlets in tumors. A larger expansion of tracks in normal tissues yields higher overlaps.

We note that the two-track calculation presented in these figures, with the use of a periodic boundary condition, an equivalent of the repetitive configurations, has been presented only to illustrate the effects of disorders. The readers must be aware that this calculation is in no way a substitute for the quantification of the dosimetry aspects of the beams. The latter must be done by a MC toolkit, such as TOPAS [47], with an extension and inclusion of the disorders in the simulation of reaction and diffusion of the chemical species.

## 4 Discussion

Understanding the chemical processes of reaction–diffusion processes of radiation-induced chemical species in cells is crucial to the proper modeling of FLASH UHDRs. Current approaches to this modeling neglect a) the effect of thermal spikes in the cores of particle tracks on the diffusion of the resultant chemical species and b) the influence of spatial heterogeneities within tissue on their diffusion. In recent years, several techniques have been developed to measure molecular diffusion in cellular environments [31, 32, 35–38]. In general, the diffusion constant substantially depends on the size of molecules, the roughness of the inter- and intra-cellular structures, and the chemical composition, such as calcification at the metastatic lesions and texture of the cells. The cellular texture may range from uniform and homogeneous to strongly disordered, exhibiting fractal geometries as in tumor cells [31, 32]. The latter mechanism bounds the range of molecular random walks and blocks the Brownian motion of chemical pathways below the percolation limit of the diffusion at $p = p_c$ associated with the underlying fractal dimensionality and self-similarity of the cellular structure. Despite these reports and observations, there is no study in the radio-biological literature to address the effects of cell types on the diffusion of ion species.

This study aims to qualitatively highlight the tissue heterogeneities in modeling inter-track coupling at FLASH-UHDR, particularly as all models neglect the differences in heterogeneities among tissues and consider all cell types to be equivalent to uniform and homogenous liquid water.

More sophisticated models, such as molecular dynamics simulations, require the incorporation of cellular internal and external structures in the calculation of $D_f$. Our recently performed simulations [43] revealed the sensitivity of $D_f$ on local chemical, physical, and mechanical molecular compositions of the environment of $^{\bullet}$OH-radicals, including the density of water molecules. The details of these simulations are beyond the scope of this work; however, the results clearly support the hypothesis of the present study (e.g., the diffusion processes of ROS and NROS in the following real-time simulations [26, 27]).

Along this line of thoughts, we remark that the reported abnormal growth of the tumor cell membrane [31, 32] and its fractal-type interface may lead us to suggest a correlation with the growth of internal heterogeneities in the physico-chemical and molecular composition in the bulky texture of the cell that influences the Brownian motion and the spatial distribution of small radiolysis molecules including $^{\bullet}$OH radicals. To the best of our knowledge, there is no experimental evidence in favor

or against such correlations; however, we provide plausible justifications below in favor of the existence of the disordered internal molecular structures of cancerous cells.

In our model, diffusion through a disordered system and a porous media, as in a single cell, has been described by random walks through fractal-type structures embedded in three-dimensional space regardless of the roughness of the cellular surface, in which it controls inter-cellular diffusion through the cell membranes. In this model, a combination of these two types of diffusive channels determines the overall intra- and inter-track recombination of chemical species.

Although diffusion and reaction within a single cell and to the cell nucleus are considered a source of DNA damage, there are recent studies related to non-DNA damage through lipids [18] and cell membranes [28] through Ferroptosis pathways [29]. The intra- and inter-cellular diffusion mechanism introduced in this theoretical study correlates the DNA and lipid damage throughout cell nuclei and membranes to the hypothetical intra- and inter-track FLASH mechanisms.

At the level of a single cell, in the absence of any experimental data, one may propose a reasonable assumption that the bulk properties of tumor cells resemble their fractal-type surface morphology unless there was an annealing or relaxation process that allowed repositioning of the atoms and molecules to reside at their equilibrium locations, like in a controlled process of crystal growth of materials. For example, such a process may occur in liquid or more advanced techniques, such as in vapor deposition or epitaxy, where crystal defects and imperfections can be eliminated by controlling environmental and external parameters, such as pressure and temperature.

Under *in vivo* or *in vitro* conditions, the rapid doubling time in the growth process of the wild-type cancerous cells means that such annealing that requires a slower processing timescale is unlikely to occur. Unlike controlled manufacturing conditions in the growth processing of artificial materials, the internal physical structure of tumor cells under uncontrolled growth may face alteration of the stored mechanical energy and tension due to out-of-equilibrium rearrangement of the molecules. Thus, it is expected that the internal structure of tumor cells exhibits roughness in their mechanical properties, heterogeneity in their mass densities, and disorder in their diffusion channels, behaviors observed in growth conditions far from equilibrium.

Snowflakes with internal defects similar to colloidal aggregates in their crystalline structure are another example of natural systems exhibiting bulky heterogeneities with a correlation to their fractal-type surface interface. Similar to our hypothetical malignant cells, they belong to states of matter that exhibit topologically distinct classes of porosity in their mass density. Thus, the systems form under ballistic growth conditions [48]. Metallic glass alloys are yet another example of a glassy or disordered phase of materials that form under a rapid decrease in temperature (i.e., quenching conditions). Closer to our hypothetical heterogeneities in tumor cells, we may enumerate abnormalities, such as grain boundaries, crystalline defects, and dislocations that affect stored mechanical energies and local diffusion channels in normal metallic alloys.

The underlying physical processes of tissue response to radiation dose rate, including differential biological responses of various tissues, either normal or malignant, can be formulated through inter-track overlap. In this model, the tissue's biological responses are categorized based on the geometrical correlation and collective evolution of the tracks. In a single fraction, tracks with negligible overlaps do not lead to a physico-chemical response sensitive to the dose rate. Thus, the typical tumor responses fit into topologically distinct classes of uncorrelated and evolutionary single tracks: dominant intra-track recombination. In contrast, normal tissue responses can fall into another class of collective chemical crowding of the correlated tracks, where inter-track recombination is dominant. The transition between inter- and intra-track reaction–diffusion processes is responsible for these two seemingly distinguished behaviors among tissue types.

As illustrative examples of structural disorders, we presented time evolutions of the solutions of the coupled partial differential equations of two separate tracks, initially created at two locations, in Figures 2, 3. An underlying network among the reaction–diffusion sites is considered to model the diffusion channels in tissues. In this model, a tissue is represented by a network with random connectivity among the sites. In Figure 2, a network with uniform and homogeneous connectivity has been considered to represent normal tissues. In Figure 3, a random network defined by a random represents cancerous cells or tissues identified to behave like self-similar fractals at the percolation threshold, $p = p_c$, the point where the diffusion channels are blocked due to the emergence of isolated islands.

The results shown in Figure 2 illustrate the role of tissue texture in forming overlaps among tracks as a function of time. In Figure 3, randomness in diffusion channels, which is unique to transport through porous and disordered structures, limits the diffusion range. Thus, the tracks evolve individually like isolated islands with negligible overlap. This is consistent with the scaling theory of percolation and localization of thermal waves/Schrödinger equation.

Note that lowering the diffusion constant without incorporating the randomness in the network connectivity does not lead to the localization of Gaussian PDFs, as the absolute value of the diffusion constant does not change the overall effect in inter-track evolution and their overlap. More precisely, the time evolution of the diffusion equation is invariant under the scaling of the diffusion constant. A simultaneous scaling of diffusion length and time gives a similar trend in the tracks' geometrical overlaps. However, with constant intra- and inter-track reaction rates, this scaling rule breaks down unless we scale them simultaneously.

Finally, for the interested readers, we remark that track localization observed in these simulations that is consistent with the percolation theory of diffusion on porous and disordered media was extensively studied in the context of semiconductor physics. The phenomenon known as Anderson localization [49] was extensively studied quantum mechanically to describe the metal-insulator transitions in condensed matter and solid-state physics. Here, we map the normal and tumor tissues problem to a similar transition between metals (where conduction electrons are in the extended states) and insulators (where conduction electrons form pockets of localized states). We suggest that the mechanism modeled in these computer simulations interprets the empirically observed differential tissue-sparing of FLASH-UHDR. The interplay of this hypothesis and that of differential antioxidant or oxygen concentrations is currently under investigation.

The relevance of inter-track interaction has recently been examined in [22] by MC simulation of interacting proton tracks, where no significant changes in $^{\bullet}OH$-radicals or $H_2O_2$ yields were found at clinically relevant doses. This claim is also supported by other simplistic geometric track overlap models. A similar assessment was given for clinical beams of carbon [21].

These theoretical results contrast the experimental evidence of [23], which measured lower $H_2O_2$ yields at UHDR compared to CDR. Furthermore, references [4, 24] observed a similar decrease in $H_2O_2$ yields at UHDR with electrons. This discrepancy and the observation that MC simulations tend to measure an increase in $H_2O_2$ yields as the dose rate increases as opposed to the experimentally measured decrease in $H_2O_2$ yields suggests that the theoretical models and MC simulations do not provide an adequate representation of the interdependent chemical reactions occurring in the irradiation of oxygenated water. This may have to do with limitations of the MC simulations, such as the lack of any simulated dissolved oxygen or the neglect of physical effects, such as thermal spikes. In either case, the chemical impact of inter-track interactions at UHDR continues to demand further studies for a complete understanding but remains outside of the scope of the present manuscript, which instead examines the effect of structural heterogeneity in biological tissue on inter-track interaction.

## 5 Conclusion

This theoretical study aims to present a model calculation based on the reaction–diffusion of reactive species induced by ionizing radiation and points to possible transitions in the molecular crowding of the track structures. This transition is dependent on the structural heterogeneity of the target tissue. As described in the model, higher heterogeneity results in limited diffusion of reactive species, decreasing the probability of inter-track overlap. Tracks with negligible overlaps do not lead to a physico-chemical response sensitive to radiation dose rate. A significant difference in this structural heterogeneity between normal and tumor tissue is hypothesized to result in the observed differential sparing of the FLASH effect. A systematic experimental cell/tissue database must be generated to validate the hypothesis presented in this work.

## Data availability statement

The raw data supporting the conclusion of this article will be made available by the authors without undue reservation.

## Author contributions

RA wrote the main manuscript, prepared figures performed mathematical derivations and computational steps. The rest of the authors (AB, AF, SB, and ES) scientifically exchanged the hypothesis and contributed to writing the manuscript. RM contributed to the scientific proposal and supervised the project.

## Funding

AF is funded through the Sêr Cymru II 80761-BU-103 project by Welsh European Funding Office (WEFO) under the European Development Fund (ERDF).

## Acknowledgments

The authors would like to acknowledge useful discussion and scientific exchanges with Drs. Niayesh Afshordi and Sohrab Rahvar. The first author dedicates this work to Mahsa Amini, who lost her life fighting for women's rights, and would like to acknowledge Drs. Muhammad Sahimi, Nasser Nafari, and Steve Girvin for the percolation theory and the topological aspects of condensed matter physics.

## Conflict of interest

The authors declare that the research was conducted in the absence of any commercial or financial relationships that could be construed as a potential conflict of interest.

## Publisher's note



## Supplementary material

The Supplementary Material for this article can be found online at: https://www.frontiersin.org/articles/10.3389/fphy.2023.1060910/full#supplementary-material

## References

1. Favaudon V, Caplier L, Monceau V, Pouzoulet F, Sayarath M, Fouillade C, et al. Ultrahigh dose-rate FLASH irradiation increases the differential response between normal and tumor tissue in mice. *Sci Transl Med* (2014) 6:245ra93. doi:10.1126/scitranslmed.3008973

2. Montay-Gruel P, Bouchet A, Jaccard M, Patin D, Serduc R, Aim W, et al. X-rays can trigger the FLASH effect: Ultra-high dose-rate synchrotron light source prevents normal brain injury after whole brain irradiation in mice. *Radiother Oncol* (2018) 129(3):582–8. doi:10.1016/j.radonc.2018.08.016

3. Vozenin MC, De Fornel P, Petersson K, Favaudon V, Jaccard M, Germond JF, et al. The advantage of FLASH radiotherapy confirmed in mini-pig and catcancer patients. *Clin Cancer Res* (2019) 25(1):35–42. doi:10.1158/1078-0432.ccr-17-3375

4. Montay-Gruel P, Acharya MM, Petersson K, Alikhani L, Yakkala C, Allen BD, et al. Long-term neurocognitive benefits of FLASH radiotherapy driven by reduced reactive oxygen species. *Proc Natl Acad Sci USA* (2019) 116(22):10943–51. doi:10.1073/pnas.1901777116

5. Buonanno M, Grilj V, Brenner DJ. Biological effects in normal cells exposed to FLASH dose rate protons. *Radiother Oncol* (2019) 139:51–5. doi:10.1016/j.radonc.2019.02.009

6. Vozenin MC, Baumann M, Coppes RP, Bourhis J. FLASH radiotherapy international workshop. *Radiother Oncol* (2019) 139:1–3. doi:10.1016/j.radonc.2019.07.020

7. Darafsheh A, Hao Y, Zwart T, Wagner M, Catanzano D, Williamson JF, et al. Feasibility of proton FLASH irradiation using a synchrocyclotron for preclinical studies. *Med Phys* (2020) 47:4348–55. doi:10.1002/mp.14253

8. Spitz DR, Buettner GR, Petronek MS, St-Aubin JJ, Flynn RT, Waldron TJ, et al. An integrated physico-chemical approach for explaining the differential impact of FLASH versus conventional dose rate irradiation on cancer and normal tissue responses. *Radiother Oncol* (2019) 139:23–7. doi:10.1016/j.radonc.2019.03.028

9. Koch CJ. Re: Differential impact of FLASH versus conventional dose rate irradiation: Spitz et al., *Radiother Oncol* (2019) 139:62–3. doi:10.1016/j.radonc.2019.07.004

10. Abolfath R, Grosshans D, Mohan R. Oxygen depletion in FLASH ultra-high-dose-rate radiotherapy: A molecular dynamics simulation. *Med Phys* (2020) 47:6551–61. doi:10.1002/mp.14548

11. Lai Y, Jia X, Chi Y. Modeling the effect of oxygen on the chemical stage of water radiolysis using GPU-based microscopic Monte Carlo simulations, with an application in FLASH radiotherapy. *Phys Med Biol* (2021) 66:025004. doi:10.1088/1361-6560/abc93b

12. Jansen J, Knoll J, Beyreuther E, Pawelke J, Skuza R, Hanley R, et al. Does FLASH deplete oxygen? Experimental evaluation for photons, protons, and carbon ions. *Med Phys* (2021) 48:3982–90. doi:10.1002/mp.14917

13. Abolfath R, Baikalov A, Bartzsch S, Afshordi N, Mohan R. The effect of non-ionizing excitations on the diffusion of ion species and inter-track correlations in flash ultra-high dose rate radiotherapy. *Phys Med Biol* (2022) 67:105005. doi:10.1088/1361-6560/ac69a6

14. Baikalov A, Abolfath R, Mohan R, Schüler E, Wilkens JJ, Bartzsch1 S. An analytical model of intertrack interaction at ultra-high dose rates and its relevance to the FLASH effect. submitted to Med. Phys (2022).

15. Kusumoto T, Inaniwa T, Mizushima K, Sato S, Hojo S, Kitamura H, et al. Radiation chemical yields of 7-hydroxy-coumarin-3-carboxylic acid for proton- and carbon-ion beams at ultra-high dose rates: Potential roles in FLASH effects. *Radiat Res* (2022) 198:255–262. doi:10.1667/rade-21-00.230.1

16. Van den Heuvel F, Vella A, Fiorini F, Brooke M, Hill M, Ryan A, et al. Using oxygen dose histograms to quantify voxelised ultra-high dose rate (FLASH) effects in multiple radiation modalities. *Phys Med Biol* (2022) 67:125001. doi:10.1088/1361-6560/ac71ef

17. Vozenin M-C, Bourhis J, Durante M. Towards clinical translation of FLASH radiotherapy. *Nat Rev Clin Oncol* (2022) 19:791–803. doi:10.1038/s41571-022-00697-z

18. Froidevaux P, Grilj V, Bailat C, Reiner Geyer W, Bochud F, Vozenin M-C. FLASH irradiation does not induce lipid peroxidation in lipids micelles and liposomes. *Radiat Phys Chem* (2023) 205:110733. doi:10.1016/j.radphyschem.2022.110733

21. Weber UA, Scifoni E, Durante M. FLASH radiotherapy with carbon ion beams. *Med Phys* (2022) 49:1974–92. doi:10.1002/mp.15135

22. Thompson S, Prise K, McMahon S. Investigating the potential contribution of inter-track interactions within ultra-high dose-rate proton therapy. *Phys Med Biol* (2023) 68:055006. doi:10.1088/1361-6560/acb88a

23. Blain G, Vandenborre J, Villoing D, Fiegel V, Fois GR, Haddad F, et al. Proton irradiations at ultra-high dose rate vs. Conventional dose rate: Strong impact on hydrogen peroxide yield. *Radiat Res* (2022) 198:318–324. doi:10.1667/rade-22-00021.1

24. Kacem H, Almeida A, Cherbuin N, Vozenin M-C. Understanding the FLASH effect to unravel the potential of ultra-high dose rate irradiation. *Int J Radiat Biol* (2022) 98:506–16. doi:10.1080/09553002.2021.2004328

26. Abolfath R, Fraile A. Lipid Bilayer destruction by ionizing radiation, thermal spikes and shock waves (2023). Available at: https://www.youtube.com/watch?v=0GYgT8sIpUk (Accessed March 13, 2023).

27. Abolfath R, Fraile A. Nano-bubbles/cavities induced by charged particles simulated by MD-ReaxFF with ≈ 150,000 water molecules. The running time up to 2 ps shows the cavity expands up to 10 nm in diameter (2023). The video is available at: https://www.youtube.com/watch?v=Sh_6s34WzNE (Accessed March 13, 2023).

28. Kale RK, Sitasawad SL. Radiation induced lipid peroxidation in liposomes. *Phys Chem* (1990) 36:361–4. doi:10.1016/1359-0197(90)90019-e

29. Tang Z, Huang Z, Huang Y, Chen Y, Huang M, Liu H, et al. Ferroptosis: The silver lining of cancer therapy. *Front Cel Dev. Biol.* (2021) 9:765859. doi:10.3389/fcell.2021.765859

30. Abolfath RM, van Duin ACT, Brabec T. Reactive molecular dynamics study on the first steps of DNA damage by free hydroxyl radicals. *J Phys Chem A* (2011) 115:11045–9. See the real-time simulations and movies at: http://qmsimulator.wordpress.com/. doi:10.1021/jp204894m

31. Klein K, Maier T, Hirschfeld-Warneken VC, Spatz JP. Marker-free phenotyping of tumor cells by fractal analysis of reflection interference contrast microscopy images. *Nano Lett* (2013) 13:5474–9. doi:10.1021/nl4030402

32. Thiagarajah JR, Kim JK, Magzoub M, Verkman AS. Slowed diffusion in tumors revealed by microfiberoptic epifluorescence photobleaching. *Nat Methods* (2006) 3:275–80. doi:10.1038/nmeth863

33. Kellerer AM, Rossi HH. A generalized formulation of dual radiation action. *Radiat Res* (2012) 178:AV204–13. doi:10.1667/rrav17.1

34. Abolfath R, Helo Y, Bronk L, Carabe A, Grosshans D, Mohan R. Renormalization of radiobiological response functions by energy loss fluctuations and complexities in chromosome aberration induction: Deactivation theory for proton therapy from cells to tumor control. *Eur Phys J D* (2019) 73:64. doi:10.1140/epjd/e2019-90263-5

35. Dix JA, Verkman AS. Crowding effects on diffusion in solutions and cells. *Annu Rev Biophys* (2008) 37:247–63. doi:10.1146/annurev.biophys.37.032807.125824

36. Mourao MA, Hakim JB, Schnell S. Connecting the dots: The effects of macromolecular crowding on cell physiology. *Biophysical J* (2014) 107:2761–6. doi:10.1016/j.bpj.2014.10.051

37. Cross SE, Jin Y-S, Rao J, Gimzewski JK. Nanomechanical analysis of cells from cancer patients. *Nat Nanotechnology* (2007) 2:780–3. doi:10.1038/nnano.2007.388

38. Zink D, Fischer AH, Nickerson JA. Nuclear structure in cancer cells. *Nat Rev Cancer* (2004) 4:677–87. doi:10.1038/nrc1430

40. Stauffer D, Aharony A. *Introduction to percolation theory*. 2nd ed. Oxfordshire: Taylor and Francis (2003).

41. Sahimi M. *Applications of percolation theory*. Boca Raton: CRC Press (2003). Springer-2023 2nd Edition.

42. Li M, Liu R-R, Lü L, Hua M-B, Xu S, Zhang Y-C. Percolation on complex networks: Theory and application. *Phys Rep* (2021) 907:1–68. doi:10.1016/j.physrep.2020.12.003

43. Abolfath RM, Biswas PK, Rajnarayanam R, Brabec T, Kodym R, Papiez L. Multiscale QM/MM molecular dynamics study on the first steps of guanine-damage by free hydroxyl radicals in solution. *J Phys Chem A* (2012) 116:3940–5. doi:10.1021/jp300258n

44. Friis I, Verkhovtsev AV, Solov'yov IA, Solov'yov AV. Lethal DNA damage caused by ion-induced shock waves in cells. *Phys Rev E* (2021) 104:054408. doi:10.1103/physreve.104.054408

45. Friis I, Verkhovtsev A, Solov'yov IA, Solov'yov AV. Modeling the effect of ion-induced shock waves and DNA breakage with the reactive CHARMM force field. *J Comp Chem* (2020) 41:2429–39. doi:10.1002/jcc.26399

46. Fraile A, Smyth M, Kohanoff J, Solov'yov AV. First principles simulation of damage to solvated nucleotides due to shock waves. *J Chem Phys* (2019) 150:015101. doi:10.1063/1.5028451

47. Schuemann J, McNamara AL, Ramos-Mendez J, Perl J, Held KD, Paganetti H, et al. TOPAS-nBio: An extension to the TOPAS simulation toolkit for cellular and sub-cellular radiobiology. *Radiat Res* (2019) 191:125–138. doi:10.1667/rr15226.1

48. Barabasi A-L, Stanley HE. *Fractal concepts in surface growth*. Cambridge: Cambridge University Press (1994).

49. Lee PA, Ramakrishnan TV. Disordered electronic systems. *Rev Mod Phys* (1985) 57:287–337. doi:10.1103/revmodphys.57.287

50. Carslaw HS, Jaeger JC. The Laplace transformation: Problems on the cylinder and sphere. Composite cylindrical regions. In: *Conduction of heat in solids*. New York: Oxford University Press (1959). p. 345–347.

51. Abramowitz M, Stegun IA. *Handbook of mathematical functions*. Mineola: Dover publisher (1964).

52. Arfken GB, Weber HJ. *Mathematical methods for physicists*. 4th ed. Cambridge: Academic Press (1995).

frontiers | Frontiers in Physics

TYPE Mini Review
PUBLISHED 22 May 2023
DOI 10.3389/fphy.2023.1201708



OPEN ACCESS

EDITED BY
Andrzej Stasiak,
Université de Lausanne, Switzerland

REVIEWED BY
Lanchun Lu,
The Ohio State University, United States

*CORRESPONDENCE
Eleonora Da Pozzo,
✉ eleonora.dapozzo@unipi.it

†These authors have contributed equally to this work and share first authorship

‡These authors share last authorship

RECEIVED 07 April 2023
ACCEPTED 09 May 2023
PUBLISHED 22 May 2023

CITATION
Del Debbio F, Bertilacchi MS, Gonnelli A, Da Pozzo E, Tozzini V, Martini C, Capaccioli S and Costa B (2023), An insight into hypothesized biological mechanisms contributing to the Flash effect.
*Front. Phys.* 11:1201708.
doi: 10.3389/fphy.2023.1201708



# An insight into hypothesized biological mechanisms contributing to the Flash effect

Francesca Del Debbio[1†], Maria Sofia Bertilacchi[1†], Alessandra Gonnelli[2,3], Eleonora Da Pozzo[1,3,4*], Valentina Tozzini[3,5], Claudia Martini[1,3,4], Simone Capaccioli[3,4,6‡] and Barbara Costa[1,4‡]

[1]Department of Pharmacy, University of Pisa, Pisa, Italy, [2]Department of Surgical, Medical and Molecular Pathology and Critical Care Medicine, Pisa, Italy, [3]Centro Pisano Multidisciplinare Sulla Ricerca e Implementazione Clinica Della Flash Radiotherapy (CPFR), CPFR@CISUP Facilities—Università di Pisa, Pisa, Italy, [4]Center for Instrument Sharing University of Pisa (CISUP), Pisa, Italy, [5]Istituto Nanoscienze—CNR, NEST-Scuola Normale Superiore, Pisa, Italy, [6]Department of Physics, University of Pisa, Pisa, Italy

In recent years, FLASH radiotherapy (FLASH RT) has gained attention in preclinical studies as a potential advancement in cancer treatment. The great advantage of FLASH RT is the ultra-fast, high doses delivery that have a similar or greater effect on cancer cells while sparing normal, healthy tissue surrounding the tumor site. This is known as the FLASH effect. However, currently, there are not enough *in vitro* and *in vivo* data to transpose FLASH RT to human trials. This mini review summarizes the available *in vitro* data on electron beam FLASH, focusing on possible mechanisms of the FLASH effect. Current studies have focused on various types of cancer, including lung cancer, glioblastoma, uterus adenocarcinoma, cervix carcinoma, prostate carcinoma, melanoma, breast cancer, head and neck squamous cell carcinoma, and colon adenocarcinoma. Several hypotheses have been proposed to explain the biological mechanisms contributing to the to the selective FLASH effect, including differences between healthy and cancer cells in production of reactive oxygen species and free radicals, limitation of Fenton reaction caused by high $Fe^{2+}/^{3+}$ levels in tumor cells, and impaired DNA damage repair mechanisms occurring in cancer.

KEYWORDS

**radiotherapy, multi-scale modeling, Flash effects, cancer, DNA damage repair mechanisms**

## 1 Introduction

Radiation therapy (RT) consists in the administration of the radiations using different types of beams, such as electron, proton, photon, and heavy ions [1]. RT is one of the most effective strategies used in cancer treatment. Recently, the emerging technique called FLASH-RT, an ultra-fast delivery of RT at dose/rate higher than the one used in conventional RT (CONV-RT), has gained attention as advancement with great potentialities. Indeed, the dose needed to kill cancerous cells in CONV-RT can cause early and late damages to healthy tissues [2], and preclinical studies have suggested that FLASH-RT is able to overcome these CONV-RT problems.

The FLASH effect is defined as the sparing of healthy tissues at same terapeutic doses, and it was observed as a reduction of the ionizing radiation's (IR) toxicity on normal tissues when using the ultra-fast delivery at high dose/rate RT [2]. The first evidence of FLASH effect

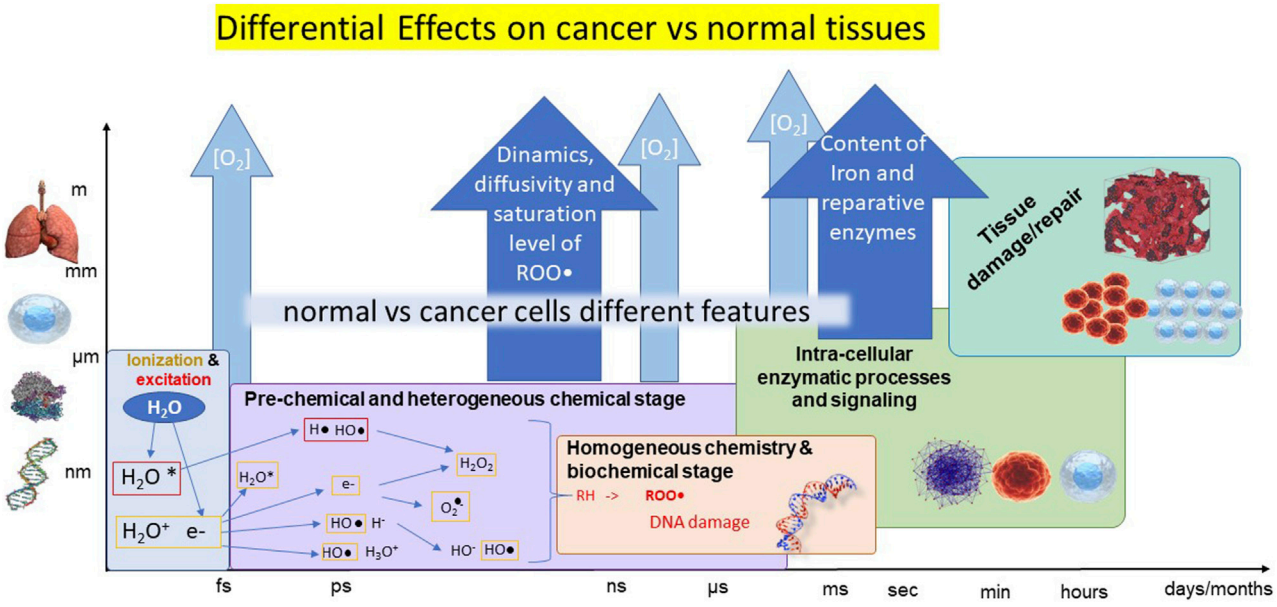


FIGURE 1
Illustrative scheme of the cascade of events occurring after irradiation at the different time scales (horizontal axis) and size scales (vertical axis). The different stages are represented in boxes in different colors, with processes summarily indicated. The possible origins of differential cancer-vs-normal tissues are reported in the blue harrows.

goes back to the seventies in a study on gut and skin toxicity in mouse models [3, 4]. Currently, some additional non-biological factors could be implied in this peculiar effect, like pulsed radiation, and other modality of delivery [5]. Despite the beneficial consequences of FLASH effect in preclinical *in vivo* studies have already been evidenced [6], such as neurocognitive protection [7, 8], reduction of skin toxicity [9], absence of lung fibrosis [10] and reduction of acute intestinal syndrome and intestinal injuries [11, 12], the mechanisms underlying this process are still not well established. The most plausible reason at the root of the FLASH effect is probably the biochemical differences between healthy and cancerous cells. Based on such dissimilarities, the leading hypotheses on the molecular mechanism could be ascribed to biological signatures different between heathy and cancerous cells, such as (i) differences in reactive oxygen species (ROS) and free radical production, (ii) pool levels of $Fe^{2+/3+}$ and (iii) the defective of DNA repair mechanisms.

## 2 Hypothesised radio-mechanism for FLASH effect

Regarding the main hypothesis for the realization of FLASH effect, first, the incoming IR induces the radiolysis of water molecules, generating electrons and hydrogen atoms that in aqueous environment react to form free radicals (see Figure 1).

Then, the formed free radicals perform the abstraction of a hydrogen atom (H•) from aliphatic or unsaturated substrates (RH) resulting in a carbon-centered radical (R•). R• can be trapped by molecular oxygen to form peroxyl radicals (ROO•) [13]. Indeed, kinetic modeling and simulations indicates that the mechanisms of recombination and self-annihilation of radicals are strongly enhanced by the increase of the dose rate, producing a faster reduction of ROO• concentration at very high dose rates, in agreement with the sparing produced by FLASH irradiation modality [13, 14]. At this level, the differential healthy-vs-cancer effect could be ascribed to different concentration/distribution of oxygen, which however do not entirely account for the observations, and/or in other mechanisms finally leading to different saturation levels of ROS.

DNA damages inflicted by RT are a combination of both IR direct effect and the indirect effect of generated ROS [2]. Indirect DNA damages caused by ROS can be exacerbated by $O_2$ through the formation of peroxyl radicals, resulting in a more significant permanent damage [2, 15]. Additionally, DNA damages can result from the reaction of ROO• with nearby nucleobases inducing "tandem lesions", which could result in a strand break [16].

The DNA damage response (DDR) pathway represents a physiological signaling pathway essential for DNA damage repair. However, in cancer cells these mechanisms could be impaired. Indeed, most human cancers present mutations in genes that are implicated in the DDR signaling pathways, like BRCA1 and BRCA2, which are crucial for the double strand break (DSB) repair, RAD51C and RAD51D, involved in the homologous recombination, CHK1 and CHK2, for DNA damage checkpoints, and MSH1 and MSH2, as mismatch repair genes [17]. The absence of a complete working DNA repair system in tumor cells is therefore implicated in the potentially lethal IR damage, while healthy cells remain untouched thanks to their proper functioning.

As mentioned, a second bio-signature differentiating substantially the healthy and cancerous cells is the levels of ROS and free radicals, much higher in the former with respect to the

latter. When cells become tumorigenic, various events take place leading to a higher production of ROS and free radical, including mutations in mitochondrial DNA, which generate mitochondrial dysfunction, mutations in genomic DNA, especially in proto-oncogenes, and the increase of metabolism activity, involving peroxisome activity [18, 19]. Furthermore, levels of antioxidant enzymes are usually lower in cancer cells [20], therefore, the increased production of ROS and free radicals is flanked by an inefficient antioxidant activity, finally resulting in increased oxidative stress. Peroxyl radicals are highly reactive and can undergo three different pathways, two for nucleic acids and one for lipids. In nucleic acids, ROO• can either undergo self-rearrangements or disproportionation via tetroxide intermediates releasing $O_2$ and substrate, like 6-hydroperoxy-5-hydroxy-5,6-dihydrothymine (HHDT) and 5,6-dihydro-5,6-dihydroxythymine (DHDT), leading to chromosome break, mutations, and cell death, or tandem lesions. In lipids, ROO• can free a R• by oxidating an RH and starts a peroxidation chain reaction [13, 16]. Therefore, pre-existing and IR generated ROS and free radicals, combined with a lower level of antioxidant enzymes, might lead to a higher killing effect in tumor cells and a sparing effect in normal healthy cells.

Another crucial biochemical difference between cancer and healthy cells is the labile iron pool availability. Cellular iron is fundamental for the proper functioning of Fe-incorporating enzymes, like mitochondrial cellular respiration enzymes and DNA synthesis enzymes, and it is therefore key to cellular growth and metabolism. On the other hand, iron also takes part in the Fenton reaction, to generate radicals, due to its exchanging electron capacity. Cancerous cells present higher levels of the transferrin receptor ferroportin, an iron efflux pump, and from 2 to 4-folds higher levels of labile iron compared to healthy cells. Labile iron in excess is sequestered inside ferritin to keep it away from entering the Fenton chain reaction and generate free radicals. However, superoxide anion produced by water radiolysis can react with ferritin, and other iron containing proteins, and liberate redox active iron. The latter can therefore enter Fenton chain and react with hydrogen peroxide ($H_2O_2$) generating HO• and RO•, and it can also create complexes with $O_2$ (Fe-$O_2$) enhancing oxidative stress [21, 22]. The higher availability of $Fe^{2+}$ in cancer cells leads to major oxidative damages by the formation of FLASH induced organic hydroperoxide, which is instead promptly removed by healthy cells with lower labile iron levels.

To date, none of the available mechanisms completely and convincingly explains the sparing effect. Already at the early stages of irradiation, the ultra-fast delivery at high dose/rates seems to generate oxygen depletion creating a transient hypoxic environment, which, in turn would reduce oxygen-related radiosensitivity.

It was shown that a mechanism, depending on oxygen depletion, causes a reduction of the produced amount of ROS and free radicals [8]. A lower production of $H_2O_2$ in FLASH-irradiated cells, compared to CONV-RT, less DNA damages, and a limitation in the Fenton reaction were also assessed, in both cancer and healthy cells. Therefore, oxygen appears to be involved in many of the possible pathways generating differential effects, and all the mentioned biochemical differences could play a pivotal role in guaranteeing the toxic effect of the radiation on cancer cells and a sparing effect on normal cells.

## 3 *In vitro* studies on electron FLASH-RT using human cell lines

The majority of FLASH *in vitro* studies use an electron beam sources, but, even if the literature is limited, there are also some works on different type of beams, such as protons, photons and heavy ions.

Regarding electron beams, to elucidate the peculiar CONV and FLASH radiotherapy-induced effects on cell life/death balance, as well as, on molecular mechanisms several *in vitro* studies have been conducted using tumor cell lines or normal cell models. In this mini-review, we decided to focalize the attention only on those studies addressing the investigation of FLASH irradiation on cell lines derived from human specimens, in order to limit the confounding effects that could arise using animal cells.

Most of such *in vitro* studies are comparable one to each other because they report data relating to the clonogenic assay that assess the colony formation capacity of irradiated cells. This *in vitro* assay has been considered the gold standard method to evaluate the cell reproductive capacity after treatment with ionizing radiation; it is based on the ability of a single cell to grow into a colony (at least 50 cells). In brief, before or after irradiation, cells are seeded to form colonies in a few weeks. Colonies are then fixed with glutaraldehyde, stained with crystal violet, and counted [23].

Town et al. [24] irradiated a suspension of human cervix cancer cells (HeLa S-3 cells) with a 15 MeV electron beam, delivered with a single pulse of steady radiation or radiation in pulses on the scale of ms. In the first set of experiments, cells were kept in a static aerobic suspension. In the second set of experiments, air or nitrogen were bubbled in the suspension before and during the irradiation to create gas equilibration and verify if the sparing effect was due to oxygen consumption. Results showed that the survival fraction, up to total delivered dose of 10 Gy, was the same for steady and pulsed radiations, while for higher doses, steady irradiation had a lower effect on cancer cells killing, showing a higher survival fraction. Survival curves from the second set of experiments indicated a higher survival fraction in hypoxic conditions both in single pulse steady and in pulsed irradiation. Though showing an oxygen dependent effect on cell survival, these observations would also indicate an exploitable differential effect of high dose pulsed irradiation on cancer tissues killing.

To further characterize the influence of intracellular oxygen, Epp and colleagues [25] studied the FLASH effect on the same *in vitro* tumoral model (HeLa S-3 cells) by conducting the experiment at different oxygen concentration. HeLa S-3 cells were cultured at 0%, 0.26%, 0.59%, 0.77%, and 0.91% of $O_2$ and then were irradiated with a 350 keV electron beam. The results indicated a much higher surviving fraction in cells kept at percentage lower than 1% compared to those kept at atmospheric $O_2$. Both these studies indicate a higher cell survival in the presence of a hypoxic environment.

The influence of $O_2$ was recently studied also in human prostate cancer. Adrian et al. [26] performed experiments on DU-145 cell line. Irradiation was delivered with a 10 MeV electron beam, with an average dose/rate of 600 Gy/s. Cells response was investigated at different doses, from 0 to 25 Gy, with both FLASH- and CONV-RT, in both normoxic and hypoxic (1.6% $O_2$) conditions. Additionally, cells were tested at different percentages of oxygen (1%, 2%, 4%, 8%,

and 20%) at the same administered dose of 18 Gy. To obtain the desired oxygen concentrations, 1 h prior the irradiation cell cultures were put with specific oxygen percentages. The clonogenic assays were performed, and the survival fraction of cells, treated with different radiation doses, showed no differences in normoxic conditions. On the contrary, under hypoxia, particularly for doses of 15 and 18 Gy, the authors suggested a high sparing effect on cells treated with FLASH-RT. In the case of cells tested at different oxygen percentages, the survival fraction seemed to be higher at lower oxygen concentration. From these results, Adrian and colleagues suggested that the sparing effect was better observed in cells that are already hypoxic, since a dose of few Gy is too low to generate an oxygen depletion in an environment, where the percentage of $O_2$ is similar to the one found in the atmosphere.

Interestingly, Adrian et al. [27] recently studied the sparing effect of FLASH through a comparative study between FLASH and CONV, using six human cancer lines and a healthy cell line: breast cancers (MDA-MB-231, MCF7), colon cancer (WiDr), squamous cell cancer (LU-HNSCC4), an early passage and subclone of HeLa cells, and the healthy human fibroblast cell line (MRC5). Cells were irradiated using a 10 MeV electron beam, for a total dose of 3 Gy, 6 Gy, 9 Gy, and 12 Gy with both FLASH- and CONV-RT. Two weeks following irradiation, the clonogenic assay was performed. HeLa, MDA-MB-231 and MCF7 expressed the higher survival fraction at doses higher than 6 Gy, compared to CONV-RT, while all the other cell lines, did not show significative statistical difference in surviving, compared to CONV RT. Furthermore, DSB-Foci and cell cycle assessment were conducted on MDA-MB-231, LU-HNSCC4 and HeLa, resulting in no differences for double strand DNA break detection. Cell cycle synchronization was observed, but no differences compared to CONV-RT. Such results indicate that the sparing effect could depend on biological factors other than [$O_2$] that vary among different kind of cells. Regarding MRC-5, despite not having a statistically significant data, a higher survival trend is noticeable in those cells treated with FLASH compared to CONV RT, suggesting a sparing effect on the healthy cells.

Khan et al. [6] have studied the FLASH effect using human multicellular spheroids, a 3D cell culture able to recreate the internal hypoxic environment typical of solid tumors. In particular, lung alveolar epithelial adenocarcinoma (A549), colorectal adenocarcinoma (HT-29) and breast cancer (MDA-MB-231) cell lines were employed in this work. Spheroids were irradiated using 16 MeV electrons for a total dose of 5 Gy, 10 Gy, 15 Gy, and 20 Gy with both FLASH- and CONV-RT. Viability and clonogenic assays were conducted on irradiated cells. The researchers expected to observe an increase in the fraction of hypoxic cells proportional to the rising dose, resulting in a more radioresistant tumor. The results showed the 10 Gy showed a higher survival, compared to the same dose delivered with CONV RT, indicating the presence of a sparing on cancer cells.

Finally, the recent study performed by Fouillade et al. [28] have been focused to investigate the molecular mechanisms related to DNA damage potentially involved in sparing effect. This work studied the CONV- vs. FLASH-RT responses of healthy cell models, including two human fibroblast cell line (IMR-90 and MRC5) and the human model of stem cells of pulmonary basal epithelium (PBECs), which were obtained from tissues resected during lobectomies on patients, who underwent surgery for lung cancer. The use of this latest cellular model is justified by the important role that stem cells play following the damage induced by radiotherapy. Indeed, in the presence of damage, stem cells present in the lung epithelium can proliferate and differentiate into ciliated and secretory cells to replace the lost cells. In this study, a human cancer lung epithelial cell line, A549, was also used. Cells were irradiated with a 4.5 MeV electron beam, with total doses of 2 Gy and 4 Gy with both FLASH- and CONV-RT. IMR-90, MRC5 and A549 cells were then examined to investigate the radioinduced damaged on the DNA, 30 min following irradiation, by performing immunofluorescent assays on 53BP1 foci and γH2AX phosphorylation (early DNA damage response). The obtained data indicated that 53BP1 foci formation was significantly lower in IMR-90 and MRC5 exposed to FLASH-RT, compared to those exposed to CONV-RT, and γH2AX phosphorylation was slightly lower, but not statistically significant in FLASH treated cells. No difference was detected for cancer cells during the two irradiation modalities. All together, these results suggested that FLASH minimizes DNA damage in normal cells. Interestingly, the results obtained using PBEC cells showed that the number of stem cells was greater with FLASH- vs. CONV-RT, suggesting the maintenance of stemness in these cells. This phenomenon could ensure the preservation of the cellular reservoir used for the recovery of tissue integrity. All these *in vitro* studies, conducted using various human tumor cell lines or normal cells, are summarized in Table 1.

As reported above, few studies carried out with different sources of beams were reported in literature. About proton beam FLASH, the work of Buonanno and colleagues [29] have focused on the biological effect understanding on human lung fibroblast (IMR90). They observed (i) no significant differences in the clonogenic assay between FLASH- and CONV-RT, but (ii) a reduction of cellular senescence following FLASH, (iii) a decrease of the radiation-induce inflammatory marker expression and (iv) a reduction of foci formation at 20 Gy FLASH.

Auer et al. [30], who have treated the HeLa-RIKENS cancer cell culture with proton FLASH, both in a pulsed and continuous modality, found an increase in the arrest of G2 phase in cells treated with continuous (conventional) compared to pulsed irradiation. Moreover, Bayart and colleagues [31] have studied the proton FLASH impact compared to CONV-RT, on two glioblastoma cell lines (U87-MG and SF763), and on wild type and p53−/− mutated human colon carcinoma (HCT116) cell lines; they found no differences in double strand breaks formation and in the survival fraction for glioblastoma cells, probably due to the high cell radioresistance. Using HCT116 cells, they [31] and Pommarel et al. [32] have suggested an involvement of PARP1 in radioresistance. Regarding heavy ion beams, Tessonnier et al [33] have used two different lung carcinoma cell lines (A549 and H1437) to investigate the presence of a sparing effect by FLASH- and CONV-RT, also considering a possible pivotal role of the oxygen, finding a higher cell survival in the hypoxic state. About photon beams, to the best of our knowledge, the unique article by Berry et al. [34] reported experiments on HeLa cell line to examine the biological effects of a X ray pulsed high dose-rate irradiation and a $^{60}$Co γ ray irradiation. For doses higher than 5 Gy, the X ray pulsed high dose-rates were less effective.

**TABLE 1 Biological parameters induced by Flash radiotherapy in human cancer and healthy cell lines.**

| *In vitro* models | Dose range (Gy) | Biological | Sparing effect | References |
|---|---|---|---|---|
| Hela S3 (cervical carcinoma) | 0–25 | During steady radiation, a higher tumor survival for doses >10 Gy, vs. < 10 Gy | in both normoxia and hypoxia following the steady radiation; in hypoxia only, following pulsed radiation | [24] |
| | 0–35 | A higher tumor cell survival at low oxygen concentration in respect to normoxia | in hypoxia only | [25] |
| Du-145 (central nervous system metastasis of primary prostate adenocarcinoma) | 0–25 | No difference in cancer cell survival following FLASH or conventional irradiations during normoxia. A higher tumor cell survival FLASH irradiation during hypoxia | following FLASH irradiation, in hypoxia only | [26] |
| • MDA-MB-231 (Breast adenocarcinoma)<br>• MCF7 (Breast adenocarcinoma)<br>• WiDr (colon adenocaarcinoma)<br>• LU-HNSCC4 (head and neck squamous cell carcinoma)<br>• HeLa<br>• MRC5 (fibroblasts isolated from the lung tissue derived from an embryo) | 0–12 | A higher cancer cell survival (MDA-MB-231, MCF7 and HeLa) following FLASH irradiation, for does >6 Gy, in respect to Conventional irradiation. A higher survival trend of MRC5 cells irradiated with FLASH modality | following FLASH irradiation | [27] |
| • A549 (lung alveolar basal epithelial adenocarcinoma)<br>• HT-29 (colorectal adenocarcinoma)<br>• MDA-MB-231 (multicellular spheroids) | 0–20 | A higher cancer cell survival following FLASH irradiation with 10 Gy, in respect to Conventional irradiation | following FLASH irradiation | [6] |
| • IMR90 (lung fibroblasts)<br>• MRC5<br>• PBECs (primary bronchial epithelial cells)<br>• A495 | 0–4 | A minor DNA damage and a higher maintenance of stemness in PBECs following FLASH irradiation, in respect to conventional irradiation | following FLASH irradiation | [28] |

# 4 Discussion

The information obtained from the *in vitro* studies reported above pointed to the necessity of further studies to investigate the potential mechanisms for the FLASH effect. The theoretical models and simulations can mechanistically explain the faster saturation and decrease of ROS and radicals as the dose rate increases, and the dependence of this effect on concentration of oxygen, in agreement with the observation of the sparing effect due to high dose rate irradiation and its modulation by oxygen. However, only a very few of them have attempted to include a more realistic and complete representation of the cell environment and processes, e.g., involving the DNA damage and its repair or even a more accurate representation of the radical's production and diffusion. Therefore, quantitative modeling of the healthy-vs-cancer differential effect is still in its infancy and must be complemented with advanced multi-scale approaches to account for the differences due to intra and inter cell architecture, and ultimately for the differential tumor-vs-normal tissue effect [35].

It is anyway worth considering that each organ has a specific normoxia called "physoxia", ranging from 3.4% to 6.8% [36], but most of the cell lines used in the above reported studies are kept at an atmospheric oxygen level (18%). This difference could be decisive in the actual possibility of observing the FLASH effect, since normally used dose of IR (~10 Gy) are not sufficient to create a hypoxic environment. Moreover, the FLASH effect was originally observed *in vivo*, and it referred to the sparing of healthy tissues, maintaining the same effect on cancer ones. While one can measure the sparing of healthy tissues under FLASH irradiation at the same CONV-equivalent released dose, it is more difficult to measure a FLASH effect analyzing only cancer tissues, as done in many of the mentioned papers. In addition, in general, a reduction of the radiobiological effects was observed in cells that were already hypoxic at the time of irradiation, meaning that the effect might depend on the intracellular oxygen concentration [26]. Therefore, further studies should be set to treat cells keeping them at their physiological normoxia. Additionally, when analyzing results, the possibility of different biochemical mechanisms depending on the cell type, which allow them to respond in different ways, should be considered.

Coherently with these considerations, a theory recently gaining ground is worth mentioning, supported by data showing that the

effect occurs in cells that are already hypoxic. Each organ presents niches of stem cells that are naturally hypoxic, and the hypothesis is that FLASH-RT could protects healthy tissue by sparing these hypoxic stem cells niches leaving them untouched and capable of repairing damages inflicted by the radiation [37].

In conclusion, we believe that in the route of the comprehension of the FLASH effect, several issues must be clarified. First an assessment of the phenomenology in rigorously controlled oxygenation conditions should be performed, with FLASH-effect defining parameters capable of accounting both for the sparing in healthy tissues and of the effectiveness in cancer tissues. Second, modeling should introduce in a realistic way the differences between healthy and cancer systems at any level, not only at the molecular one (different concentration of oxygen and biomolecules) but also at cellular level (different cytoplasm composition, different morphology, and mechanics) and at tissue level (different architectural organization and inter-cell communication). Clearly, the clarification the FLASH effect calls into play a strong multidisciplinary effort.

## Author contributions

FDD and MSB contributed primarily to the writing of this work and search of the literature, and share the first authorship; AG and CM contributed to the writing of the manuscript; EDP organized the manuscript scheme, and supervised the final version; VT finalized the modeling part; SC and BC supervised the work and shared the last authorship. All authors contributed to the article and approved the submitted version.

## Funding

We acknowledge CPFR, Fondazione Pisa and the project "Piano Nazionale di Ripresa e Resilienza (PNRR), Missione 4, Componente 2, Ecosistemi dell'Innovazione—Tuscany Health Ecosystem (THE), Spoke 1 "*Advanced Radiotherapies and Diagnostics in Oncology*"—CUP I53C22000780001" for the financial support.

## Acknowledgments

We thank Fabio Di Martino and Emanuele Scifoni for enlightening discussions.

## Conflict of interest

The authors declare that the research was conducted in the absence of any commercial or financial relationships that could be construed as a potential conflict of interest.

## Publisher's note



## References

1. Kaiser A, Eley JG, Onyeuku NE, Rice SR, Wright CC, McGovern NE, et al. Proton therapy delivery and its clinical application in select solid tumor malignancies. *J Vis Exp* (2019) 144. doi:10.3791/58372

2. Hughes JR, Parsons JL FLASH radiotherapy: Current knowledge and future insights using proton-beam therapy. *Int J Mol Sci* (2020) 21(18):6492. doi:10.3390/ijms21186492

3. Hornsey S, Alper T Unexpected dose-rate effect in the killing of mice by radiation. *Nature* (1966) 210:212–3. doi:10.1038/210212a0

4. Field SB, Bewley DK Effects of dose-rate on the radiation response of rat skin. *Int J Radiat Biol Relat Stud Phys Chem Med* (1974) 26(3):259–67. doi:10.1080/09553007414551221

5. Petersson K. FLASH radiotherapy: What, how and why? *Res Outreach* (2020) 2020(117):66–9. doi:10.32907/RO-117-6669

6. Khan S, Bassenne M, Wang J, Manjappa R, Melemenidis S, Breitkreutz DY, et al. Multicellular spheroids as *in vitro* models of oxygen depletion during FLASH irradiation. *Int J Radiat Oncol Biol Phys* (2021) 110(3):833–44. doi:10.1016/j.ijrobp.2021.01.050

7. Montay-Gruel P, Acharya MM, Petersson K, Alikhanic L, Yakkalaa C, Allenc BD, et al. Long-term neurocognitive benefits of FLASH radiotherapy driven by reduced reactive oxygen species. *Proc Natl Acad Sci U S A* (2019) 116(22):10943–51. doi:10.1073/pnas.1901777116

8. Montay-Gruel P, Petersson K, Jaccard M, Boivin G, Germond JF, Petit B, et al. Irradiation in a flash: Unique sparing of memory in mice after whole brain irradiation with dose rates above 100 gy/s. *Radiother Oncol* (2017) 124(3):365–9. doi:10.1016/j.radonc.2017.05.003

9. Vozenin MC, De Fornel P, Petersson K, Favaudon V, Jaccard M, Germond JF, et al. The advantage of FLASH radiotherapy confirmed in mini-pig and cat-cancer patients. *Clin Cancer Res* (2019) 25(1):35–42. doi:10.1158/1078-0432.CCR-17-3375

10. Favaudon V, Caplier L, Monceau V, Pouzoulet F, Sayarath M, Fouillade C, et al. Ultrahigh dose-rate FLASH irradiation increases the differential response between normal and tumor tissue in mice. *Sci Transl Med* (2014) 6(245):245ra93. doi:10.1126/scitranslmed.3008973

11. Hornsey S, Bewley DK Hypoxia in mouse intestine induced by electron irradiation at high dose-rates. *Int J Radiat Biol Relat Stud Phys Chem Med* (1971) 19(5):479–83. doi:10.1080/09553007114550611

12. Levy K, Natarajan S, Wang J, Chow S, Eggold JT, Loo PE, et al. Abdominal FLASH irradiation reduces radiation-induced gastrointestinal toxicity for the treatment of ovarian cancer in mice. *Sci Rep* (2020) 10(1):21600. doi:10.1038/s41598-020-78017-7

13. Labarbe R, Hotoiu L, Barbier J, Favaudon V A physicochemical model of reaction kinetics supports peroxyl radical recombination as the main determinant of the FLASH effect. *Radiother Oncol* (2020) 153:303–10. doi:10.1016/j.radonc.2020.06.001

14. D Boscolo D, Scifoni E, Durante M, Krämer M, Fuss MC May oxygen depletion explain the FLASH effect? A chemical track structure analysis. *Radiother Oncol* (2021) 162:68–75. doi:10.1016/j.radonc.2021.06.031

15. Dewey D, Boag J Modification of the oxygen effect when bacteria are given large pulses of radiation. *Nature* (1959) 183:1450–1. doi:10.1038/1831450a0

16. Favaudon V, Labarbe R, Limoli CL Model studies of the role of oxygen in the FLASH effect. *Med Phys* (2022) 49(3):2068–81. doi:10.1002/mp.15129

17. Hopkins JL, Lan L, Zou L DNA repair defects in cancer and therapeutic opportunities. *Genes Dev* (2022) 36(5-6):278–93. doi:10.1101/gad.349431.122

18. Liou GY, Storz P Reactive oxygen species in cancer. *Free Radic Res* (2010) 44(5):479–96. doi:10.3109/10715761003667554

19. Yang Y, Karakhanova S, Hartwig W, D'Haese JG, Philippov PP, Werner J, et al. Mitochondria and mitochondrial ROS in cancer: Novel targets for anticancer therapy. *J Cel Physiol* (2016) 231(12):2570–81. doi:10.1002/jcp.25349

20. Jelic MD, Mandic AD, Maricic SM, Srdjenovic BU Oxidative stress and its role in cancer. *J Cancer Res Ther* (2021) 17(1):22–8. doi:10.4103/jcrt.JCRT_862_16

21. Torti SV, Torti FM Iron and cancer: More ore to be mined. *Nat Rev Cancer* (2013) 13(5):342–55. doi:10.1038/nrc3495

22. Spitz DR, Buettner GR, Petronek MS, St-Aubin JJ, Flynn RT, Waldron TJ, et al. An integrated physico-chemical approach for explaining the differential impact of FLASH versus conventional dose rate irradiation on cancer and normal tissue responses. *Radiother Oncol* (2019) 139:23–7. doi:10.1016/j.radonc.2019.03.028

23. Franken NA, Rodermond HM, Stap J, Haveman J, van Bree C Clonogenic assay of cells *in vitro*. *Nat Protoc* (2006) 1(5):2315–9. doi:10.1038/nprot.2006.339

24. Town C Effect of high dose rates on survival of mammalian cells. *Nature* (1967) 215:847–8. doi:10.1038/215847a0

25. Epp ER, Weiss H, Djordjevic B, Santomasso A The radiosensitivity of cultured mammalian cells exposed to single high intensity pulses of electrons in various concentrations of oxygen. *Radiat Res* (1972) 52(2):324–32. doi:10.2307/3573572

26. Adrian G, Konradsson E, Lempart M, Bäck S, Ceberg C, Petersson K The FLASH effect depends on oxygen concentration. *Br J Radiol* (2020) 93(1106):20190702. doi:10.1259/bjr.20190702

27. Adrian G, Konradsson E, Beyer S, Wittrup A, Butterworth KT, McMahon SJ, et al. Cancer cells can exhibit a sparing FLASH effect at low doses under normoxic in vitro-conditions. *Front Oncol* (2021) 11:686142. doi:10.3389/fonc.2021.686142

28. Fouillade C, Curras-Alonso S, Giuranno L, Quelennec E, Heinrich S, Bonnet-Boissinot S, et al. FLASH irradiation spares lung progenitor cells and limits the incidence of radio-induced senescence. *Clin Cancer Res* (2020) 26(6):1497–506. doi:10.1158/1078-0432.CCR-19-1440

29. Buonanno M, Grilj V, Brenner DJ Biological effects in normal cells exposed to FLASH dose rate protons. *Radiother Oncol* (2019) 139:51–5. doi:10.1016/j.radonc.2019.02.009

30. Auer S, Hable V, Greubel C, Drexler GA, Schmid TE, Belka C, et al. Survival of tumor cells after proton irradiation with ultra-high dose rates. *Radiat Oncol.* (2011) 18; 139. doi:10.1186/1748-717X-6-139

31. Bayart E, Flacco A, Delmas O, Pommarel L, Levy D, Cavallone M, et al. Fast dose fractionation using ultra-short laser accelerated proton pulses can increase cancer cell mortality, which relies on functional PARP1 protein. *Sci Rep* (2019) 9(1):10132. doi:10.1038/s41598-019-46512-1

32. Pommarel L, Vauzour B, Mégnin-Chanet F, Bayart E, Delmas O, Goudjil F, et al. Spectral and spatial shaping of a laser-produced ion beam for radiation-biology experiments. *Phys Rev Accel Beams* (2017) 20:032801. doi:10.1103/PhysRevAccelBeams.20.032801

33. Tessonnier T, Mein S, Walsh D, Schuhmacher N, Liew H, Cee R, et al. FLASH dose rate helium ion beams: First *in vitro* investigations. *Int J Radiat Oncol Biol Phys* (2021) 111(4):1011–22. doi:10.1016/j.ijrobp.2021.07.1703

34. Berry RJ, Hall EJ, Forster DW, Storr TH, Goodman MJ Survival of mammalian cells exposed to x rays at ultra-high dose-rates. *Br J Radiol* (1969) 42(494):102–7. doi:10.1259/0007-1285-42-494-102

35. Palermo G, Bonvin AMJJ, Dal Peraro M, Amaro RE, Tozzini V Editorial: Multiscale modeling from macromolecules to cell: Opportunities and challenges of biomolecular simulations. *Front Mol Biosci* (2020) 7:194. doi:10.3389/fmolb.2020.00194

36. Wilson JD, Hammond EM, Higgins GS, Petersson K Ultra-high dose rate (FLASH) radiotherapy: Silver bullet or fool's gold? *Front Oncol* (2020) 9:1563. doi:10.3389/fonc.2019.01563

37. Pratx G, Kapp DS Ultra-high-dose-rate FLASH irradiation may spare hypoxic stem cell niches in normal tissues. *Int J Radiat Oncol Biol Phys* (2019) 105(1):190–2. doi:10.1016/j.ijrobp.2019.05.030

frontiers | Frontiers in Physics

TYPE Original Research
PUBLISHED 04 July 2023
DOI 10.3389/fphy.2023.1213779



OPEN ACCESS

EDITED BY
Fabio Di Martino,
Pisana University Hospital, Italy

REVIEWED BY
Vivek Maradia,
Paul Scherrer Institut (PSI), Switzerland
Serena Psoroulas,
Paul Scherrer Institut (PSI), Switzerland
Luigi Raffaele,
Laboratori Nazionali del Sud (INFN), Italy

*CORRESPONDENCE
Felix Horst,
felix.horst@oncoray.de

RECEIVED 28 April 2023
ACCEPTED 26 June 2023
PUBLISHED 04 July 2023

CITATION
Horst F, Beyreuther E, Bodenstein E, Gantz S, Misseroni D, Pugno NM, Schuy C, Tommasino F, Weber U and Pawelke J (2023), Passive SOBP generation from a static proton pencil beam using 3D-printed range modulators for FLASH experiments.
*Front. Phys.* 11:1213779.
doi: 10.3389/fphy.2023.1213779



# Passive SOBP generation from a static proton pencil beam using 3D-printed range modulators for FLASH experiments

Felix Horst[1,2]*, Elke Beyreuther[2,3], Elisabeth Bodenstein[1,2], Sebastian Gantz[2], Diego Misseroni[4], Nicola M. Pugno[4,5], Christoph Schuy[6], Francesco Tommasino[7,8], Uli Weber[6] and Jörg Pawelke[1,2]

[1]Helmholtz-Zentrum Dresden-Rossendorf, Institute of Radiooncology—OncoRay, Dresden, Germany, [2]OncoRay—National Center for Radiation Research in Oncology, Faculty of Medicine and University Hospital Carl Gustav Carus, Technische Universität Dresden and Helmholtz-Zentrum Dresden-Rossendorf, Dresden, Germany, [3]Helmholtz-Zentrum Dresden-Rossendorf, Institute of Radiation Physics, Dresden, Germany, [4]Laboratory for Bioinspired Bionic Nano Meta Materials and Mechanics, Department of Civil Environmental and Mechanical Engineering, University of Trento, Trento, Italy, [5]School of Engineering and Materials Science, Queen Mary University of London, London, United Kingdom, [6]GSI Helmholtzzentrum für Schwerionenforschung GmbH, Darmstadt, Germany, [7]Physics Department, University of Trento, Povo(Tn), Italy, [8]Trento Institute for Fundamental Physics and Applications (TIFPA), Italian National Institute of Nuclear Physics (INFN), Povo(Tn), Italy

The University Proton Therapy facility in Dresden (UPTD), Germany, is equipped with an experimental room with a beamline providing a static pencil beam. High proton beam currents can be achieved at this beamline which makes it suitable for FLASH experiments. However, the established experimental setup uses only the entrance channel of the proton Bragg curve. In this work, a set of 3D-printed range modulators designed to generate spread out Bragg peaks (SOBPs) for radiobiological experiments at ultra-high dose rate at this beamline is described. A new method to optimize range modulators specifically for the case of a static pencil beam based on the central depth dose profile is introduced. Modulators for two different irradiation setups were produced and characterized experimentally by measurements of lateral and depth dose distributions using different detectors. In addition, Monte Carlo simulations were performed to assess profiles of the dose averaged linear energy transfer ($LET_D$) in water. These newly produced range modulators will allow future proton FLASH experiments in the SOBP at UPTD with two different experimental setups.

KEYWORDS

**proton therapy, range modulator, 3D-printing, spread out Bragg peak, FLASH effect, ultra-high dose rate**

## 1 Introduction

The observation of the FLASH effect, the sparing of normal tissue at ultra-high dose rates above ~ 40 Gy/s, while maintaining tumor control has attracted great attention and stimulated research in the radiotherapy community worldwide due to its potential to widen the therapeutic window [1,2]. Though it is suspected that the explanation behind the FLASH effect lies probably in the radiochemical stage of radiation action, its exact mechanism is still barely understood [3]. Therefore, more basic and preclinical research is

necessary towards an understanding of the FLASH effect. The University Proton Therapy facility in Dresden (UPTD), Germany, is equipped with an IBA ProteusPLUS proton therapy system with a 230 MeV isochronous cyclotron that can be operated with beam currents up to 500 nA [4–6]. The proton beam can be delivered to a gantry room for patient treatment and to a research room equipped with two horizontal beamlines. One beamline is equipped with a pencil beam scanning nozzle and the other one provides fixed/static pencil beams. The beam current arriving at the target position depends on the beamline and proton energy used. The highest beam currents can be reached at the fixed beamline where different experiments investigating the FLASH effect have already been performed [7–9].

The irradiation setup previously established at UPTD for ultra-high dose rate experiments [7–9] allowed irradiations at the entrance channel of a 225 MeV proton beam and the maximum dose rate achievable at a usable field size of ~ 8 mm was limited to ~ 300 Gy/s [8, 9]. The irradiation of biological samples in a spread out Bragg peak (SOBP) instead of the entrance channel would be closer to the clinical situation, would provide a higher ionization density and could allow to reach even higher dose rates. For ultra-high dose rate experiments, an SOBP can only be generated passively because for an active energy variation the dead time between the subsequent layers would be too long to maintain the conditions required for the FLASH effect. However, thanks to modern 3D-printing technology [10] almost the same conformality as for active energy switching can be reached with 3D-printed range modulators [11–14], without affecting the radiation quality compared to active dose delivery [15].

In this work, we present a set of 3D-printed range modulators that were specifically designed for the fixed beamline of the experimental area at UPTD with the goal to generate SOBPs at ultra-high dose rate for radiobiological experiments. Two experimental setups providing different field sizes for different biological models are presented. In the first setup, a proton SOBP with 3 cm modulation length and a lateral field size that is large enough to irradiate biological samples with sizes of ~ 8 mm in diameter with a homogeneous dose (comparable to the setup of Karsch et al. [9] for the entrance channel) should be generated. In the second setup, a proton SOBP with 1.5 cm modulation length that is sharply collimated to 5 mm lateral field size and can be used to irradiate partial volumes of small animals while sparing surrounding tissues and organs (comparable to the mouse irradiations at conventional dose rates described by Suckert et al. [16]) should be produced. In both setups, the SOBP is generated using the highest available proton energy of 225 MeV in order to reach maximum dose rates.

Different range modulators were optimized based on measured depth dose distributions of the 225 MeV proton beam and produced by 3D-printing. The modulators for the first setup (3 cm long SOBP without collimation) were printed at GSI Helmholtzzentrum für Schwerionenforschung in Darmstadt, Germany, while those for the second setup (1.5 cm long SOBP with 5 mm collimation) were optimized and printed independently at GSI and in Trento, in a collaboration between the Trento Institute for Fundamental Physics and Applications (TIFPA) and at the Laboratory for Bioinspired, Bionic, Nano Meta Materials and Mechanics of the University of Trento (UniTn) in Italy (optimized at TIFPA, printed at UniTn), and compared in terms of field characteristics and depth dose homogeneity. The optimization of the range modulator geometries followed a novel approach based on the central depth dose profile. The two experimental setups were characterized by measurements with different dosimetric devices as well as by Monte Carlo simulations using the FLUKA and TOPAS/Geant4 Monte Carlo codes.

## 2 Methods and materials

### 2.1 Proton beamline at University Proton Therapy facility in Dresden

As usual for cyclotron-based proton therapy systems, the accelerator at UPTD provides protons with a fixed energy of 230 MeV. The energy variation as required for conformal irradiation of 3D volumes is realized passively in a degrader-based energy selection system. The energy range available at the fixed beamline in the experimental room is 70–225 MeV. The degrader drastically reduces the beam current transported through the beamline due to the widening of the angular and energy distribution by scattering and energy loss straggling. Knowledge of the magnitude of the intensity loss for lower proton energies is important for choosing the optimal energy for FLASH experiments in an SOBP setup. Therefore, the transmission characteristics of the fixed beamline at UPTD were studied experimentally. A PTW Bragg peak chamber (model 34070-2,5 [17]) was placed at the target position directly behind the beamline exit window and read out by a Keithley electrometer (model 6514). The ionization current $I_{ionization}$ measured by the Bragg peak chamber was converted into absolute proton beam current $I_{beam}$ by Eq. 1.

$$I_{beam} = \frac{I_{ionization}}{\left(\frac{dE}{dx}\right)_{air} \cdot \Delta x \cdot \frac{e}{w_{air}}} \cdot e \cdot k_{T,p} \cdot k_S = \frac{I_{ionization} \cdot w_{air}}{\left(\frac{dE}{dx}\right)_{air} \cdot \Delta x} \cdot k_{T,p} \cdot k_S \quad (1)$$

where $(\frac{dE}{dx})_{air}$ is the (energy dependent) stopping power of air for protons [18], $\Delta x$ the air gap between the electrodes (2 mm in the Bragg peak chamber used), $e$ is the elementary charge, $w_{air}$ the mean energy required to create an electron-ion pair in air (34.44 eV for protons [19]), $k_{T,p}$ the correction factor accounting for the temperature and pressure dependent variable density of air and $k_S$ the correction factor accounting for incomplete charge collection due to ion recombination (see Section 2.4). The beam current at the target position divided by the cyclotron current (available from IBA beam control system) gives the transmission.

Figure 1 shows the measured transmission from cyclotron to target position at the fixed beamline. Using the primary 230 MeV proton beam from the cyclotron without any degrader or material in the beam path is not possible with the current beamline settings at UPTD and is not straightforward to implement due to the operation of experiments and clinical treatments in parallel. For 225 MeV, the highest energy that can be transported to the experimental room, the transmission is ~ 45%. This corresponds to a beam current of $1.39 \times 10^{12}$ protons per second arriving in the experimental room. The transmission drops so steeply with decreasing energy that we decided to use the maximum energy of 225 MeV for optimization of the range modulators described in this work.

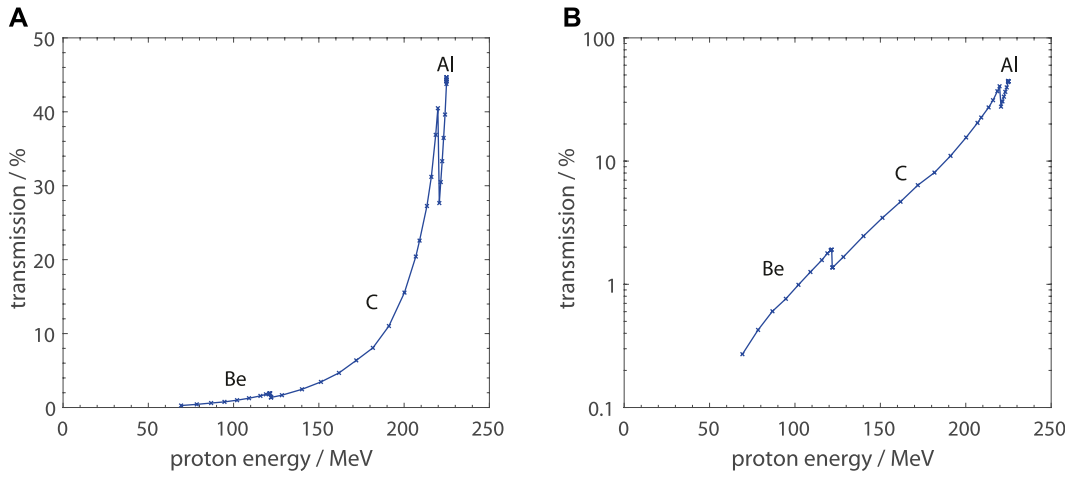


FIGURE 1
Transmission from cyclotron to target position at the fixed beamline in the experimental area of the UPTD as a function of proton energy panel **(A)**: linear scale, panel **(B)**: logarithmic scale). The transmission was determined by measurements of the absolute beam current using a PTW 34070 Bragg peak chamber. The distinct steps are due to the switching of the degrader material (aluminum, carbon, beryllium) depending on the energy range.

Therefore, a thick absorber of ~ 30 cm water-equivalent thickness is required to shift the sample position to the SOBP depth. The use of a lower proton energy would reduce the thickness of absorber material required before the sample, but the strongly decreasing transmission due to the degrader would also greatly reduce the available beam current and therefore is not an option for FLASH experiments at the fixed beamline at UPTD.

## 2.2 Optimization of range modulators to produce SOBPs for a static pencil beam

Several facilities and research groups make use of 3D-printed range modulators to create SOBPs for radiobiological or dosimetric experiments with protons or heavy ions [12,20–23]. These modulators consist of periodically arranged pins or ridges which represent different thicknesses to specific fractions of the beam and therefore modulate the energy and range distribution. The shape of the pins or ridges can be optimized to produce a desired depth dose distribution, e.g., an SOBP. The period should be considerably smaller than the size of the beam spot for an optimal modulation.

Usually the geometry of such modulators is optimized based on a pristine laterally integrated Bragg curve. For modulators optimized in this way, however, in order to obtain a flat central depth dose profile an extended radiation field is required. This is illustrated in Figure 2 where dose distributions in water for 220 MeV protons with and without a range modulator optimized to produce a 5 cm SOBP are shown. The dose distributions were calculated using the FLUKA Monte Carlo code [24,25] and a dedicated sub-routine for implementation of the modulator geometry [26].

The upper panels show 2D dose distributions before and inside the water phantom and the lower panels show 1D depth profiles in water for different cylindrical integration radii (2 mm – 10 cm). Figures 2A,D show the dose distribution of a pristine 220 MeV proton pencil beam (8 mm full width at half maximum) without modulation. It can be observed that the lateral size of the beam widens up strongly during traversal through the water phantom due to lateral scattering. This causes the Bragg peak, which is very pronounced in the laterally integrated depth dose profile, to be attenuated considerably for smaller integration radii. Figure 2B,E show the corresponding dose distribution for the same beam, but with a range modulator in front of the water phantom. As visible in Figure 2B, the edge scattering effects at the range modulator pins cause a ripple in the dose distribution, which again blurs out until the SOBP depth (as studied in detail by Charuchinda et al. [26]). In Figure 2E one can observe that the laterally integrated depth dose profile shows a flat SOBP while the central dose profiles (calculated from smaller integration radii) get a negative slope towards the distal edge due to multiple Coulomb scattering. Figures 2C,F show the corresponding dose distributions for the same modulator but with an extended irradiation field of $4 \times 4$ cm$^2$. For this configuration the SOBP is flat for all integration radii because there is a lateral scattering equilibrium all along the beam path.

Basically all previous experiments applying such range modulators used extended fields, either produced by scattering or scanning of pencil beams. Scanning of the beam is not possible at our fixed beamline and the irradiation fields should be kept small to achieve highest dose rates. Therefore, we tested a different approach using the central depth dose profile (e.g., red curve in Figure 2D) instead of the laterally integrated depth dose profile as input for the optimization of the modulator geometry. Accordingly, also the effect of collimators, which restrict the phase space of the proton beam and modify its depth dose profile, can be taken into account during the optimization of the modulator geometry by including it already during the measurement of the reference depth dose profile. In this work, the reference dose profiles for the different configurations were obtained by measurements with small detectors, a PTW PinPoint 3D ionization chamber (model 31022) and a PTW microdiamond detector (model 60019) scanned along the central axis (see Section 2.4). It should be noted that in the setup used for

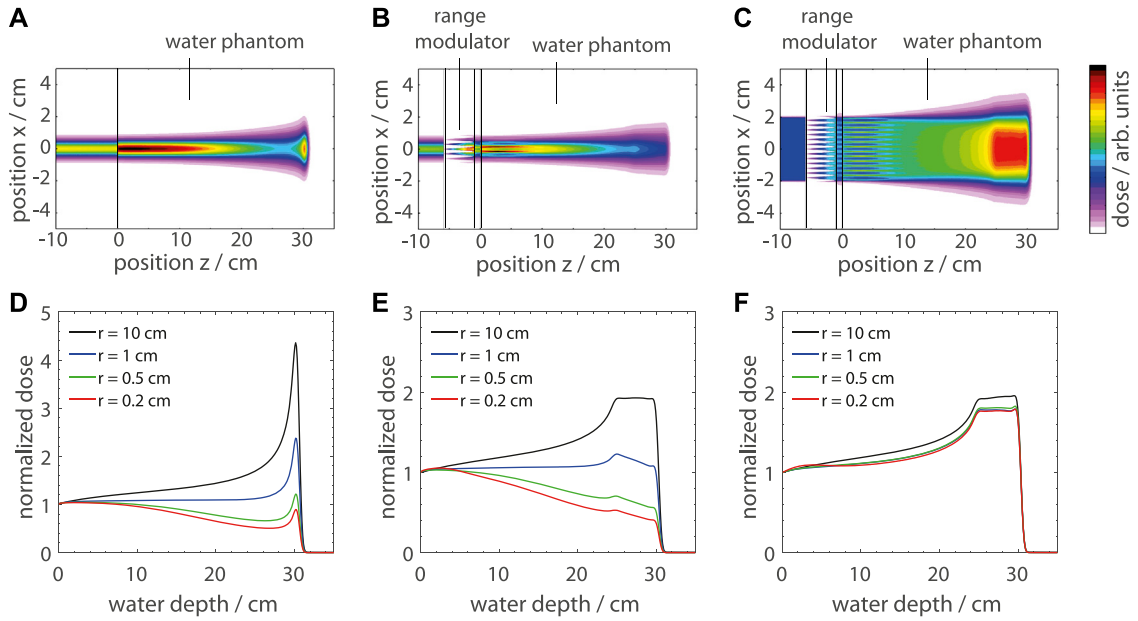


FIGURE 2
Dose distributions for 220 MeV protons impinging on a water phantom with and without a range modulator in front calculated using the FLUKA Monte Carlo code. The upper panels **(A–C)** show 2D dose distributions in air and in the water phantom and the lower panels **(D–F)** show 1D profiles normalized to the entrance dose for different integration radii (0.2 cm – 10 cm). Panel **(A)** and **(D)** show the dose distribution of a pristine pencil beam, **(B)** and **(E)** of a modulated pencil beam and **(C)** and **(F)** of a modulated broad beam.

measurement of the unmodulated central dose profile used as reference, the distances and the configuration (especially collimator position) should be as close as possible to those in the final setup that is used for SOBP irradiations.

## 2.3 Experimental setups

The two experimental setups intended for FLASH irradiation within proton SOBPs that were realized within this work are shown schematically in Figure 3. They were designed to be set up quickly and in a robust way, using PMMA absorbers instead of water.

Figure 3A shows SETUP A which is intended for irradiation of small biological samples with dimensions $< 1$ cm (e.g., 0.5 mL Eppendorf tubes containing zebrafish embryos) in the center of a 3 cm long SOBP with homogeneous dose (inhomogeneity $\leq \pm 5\%$) at ultra-high dose rate ($> 100$ Gy/s). A PTW Bragg peak chamber positioned right after the exit window of the beamline serves as beam monitor because of its good performance (lower recombination losses than the transmission ionization chamber built in the beamline, see Section 2.4) at high dose rates. The Bragg peak chamber has an additional water equivalent thickness of ~ 1 cm which slightly increases the beam spot size and whose range shift needs to be taken into account. The 3D-printed range modulator is placed right behind the Bragg peak chamber. After the modulator, a 23.5 cm PMMA absorber is placed which on one hand broadens the beam due to lateral scattering and on the other hand shifts the sample position into the SOBP depth. The samples (e.g., Eppendorf tubes) can be placed inside a plastic phantom with a bore hole. Alternatively, a PTW PinPoint 3D chamber can be inserted inside the sample holder for dose measurements.

Figure 3B shows SETUP B which can be used for irradiation of partial volumes (e.g., partial brain irradiation) of small animals with a 1.5 cm long SOBP at ultra-high dose rate while surrounding tissues and organs are spared. However, for 225 MeV protons the distal edge has an extension of ~ 1.5 cm in water which is broader than the entire mouse brain. Therefore, in order to reach ultra-high dose rates the setup has to be arranged as a shoot-through SOBP setup. In contrast to SETUP A, a 3.3 cm thick Brass collimator with a hole of 5 mm diameter is added. The collimator is not placed behind the entire absorber, but 2.5 cm before the end. The additional 2.5 cm PMMA after the collimator helps to absorb the dose overshoots which typically occur right behind collimators due to edge scattering effects. If a very sharp lateral dose falloff at the sample position is required, a second collimator can be added after the second absorber right in front of the animal. Typically mice are in a container during irradiation which has to be taken into account for the choice of the exact thicknesses of the absorber plates.

## 2.4 Dosimetric characterization

Dose profiles for pristine and for modulated proton beams for both setups were obtained. Different detectors were used to characterize the dose distributions.

The IBA Giraffe multi-layer ionization chamber [27] was used for measuring laterally integrated depth dose profiles of SETUP A.

For measurements of central dose profiles of SETUP A, a PTW water phantom (model 41023) together with a PTW PinPoint 3D ionizaton chamber (model 31022) read out by a PTW UNIDOS Tango electrometer was used. For large water depths, a PMMA range

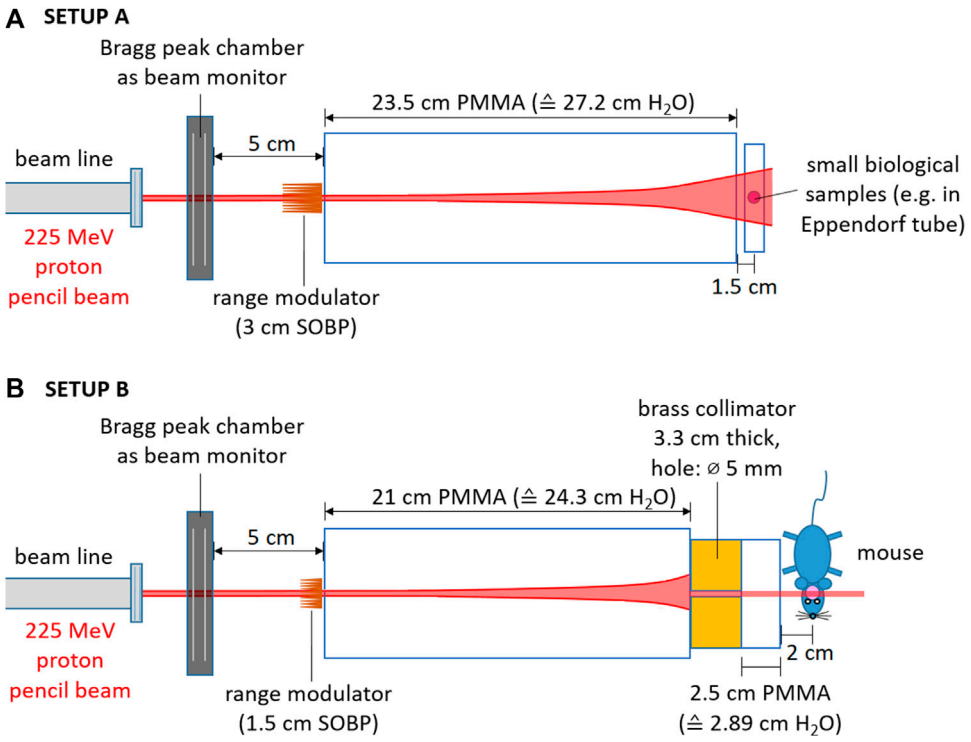


FIGURE 3
Experimental setups for proton SOBP irradiations at ultra-high dose rate using 3D-printed range modulators. Panel **(A)**: SETUP (A) irradiation of small samples with a homogeneous dose in the center of a 3 cm SOBP. Panel **(B)**: SETUP (B) irradiation of partial volumes of small animals with a sharply collimated 1.5 cm SOBP.

shifter with 7.6 cm water equivalent thickness was placed in front of the water phantom. A transmission ionization chamber built-in the beamline (model 34058 by PTW) served as reference detector [5].

For the collimated fields of SETUP B, a PTW microdiamond detector (model 60019) was used (as, e.g., also by Togno et al. [28]) which allows dose profile measurements with micrometer resolution. Instead of scanning it in beam direction through a water phantom, the microdiamond was placed in a PMMA plate at 5 mm geometrical depth and scanned along the lateral direction (using a linear stage by OWIS) to detect the central dose maximum for each measurement depth. The different measurement depths were realized by placing PMMA plates of varying thickness in between the collimator and the microdiamond detector and simultaneously increasing the distance between both. The ionization current signal of the diamond detector was read out by a PTW UNIDOS electrometer (model 10001) and logged together with the lateral position.

The different detectors, their characteristics and their field of application are summarized in Table 1.

The characterization of the dose profiles was done at moderate proton beam currents (~ 1 nA at the target position for PinPoint measurements and ~ 0.1 nA for the lateral profile scans using the microdiamond) to avoid recombination effects [29,30] or other issues related to high dose rate [31]. By scaling the dose rates measured at low intensities up to 500 nA cyclotron current, the maximum reachable dose rates can be estimated with good accuracy. In addition, also separate measurements at the maximum beam current were carried out at selected depth points, taking into account recombination correction factors for the air-filled ionization chambers used (PTW Bragg peak chamber as monitor and PTW

**TABLE 1 Detectors used for experimental characterization of the proton beam at UPTD and the dose distributions produced by 3D-printed range modulators.**

| Detector | Characteristics | Application |
|---|---|---|
| PTW 34058 transmission chamber | lateral integration of beam<br>built-in at beam line exit | beam monitor |
| PTW 34070-2,5 Bragg Peak chamber | lateral integration of beam, low recombination effects | beam monitor, transmission measurements |
| PTW 31022 PinPoint 3D chamber | small active volume (0.016 $cm^3$), low recombination effects | depth dose profile and dose rate measurements |
| PTW 60019 microdiamond | very small active volume (0.004 $mm^3$) | lateral and depth dose profile measurements |
| IBA Giraffe multi-layer ionization chamber | lateral integration of beam | depth dose profile measurements |

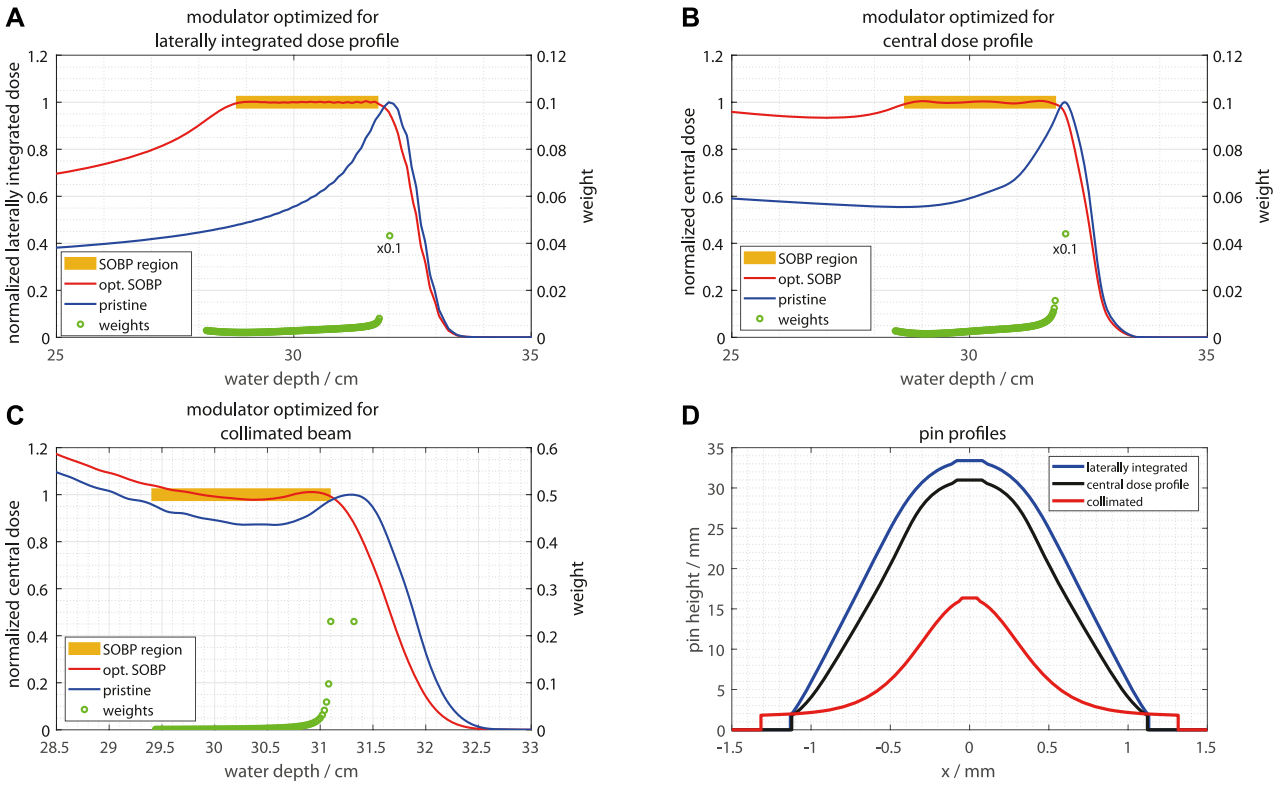


FIGURE 4
Depth dose profiles for the different range modulators optimized and produced at GSI within this work panel **(A–C)** and their pin geometries (panel **(D)**). The blue curves in panel **(A–C)** show the pristine Bragg curves used as input for the optimization, the red curves show the optimized SOBPs for the yellow marked region and the green symbols show the weights of the shifted Bragg curves. In panel **(A)** and **(B)**, the first (deepest) weight was scaled down by a factor of 0.1 for better visibility of the other weights.

PinPoint 3D as field detector). The recombination correction factors $k_S$ determined for the maximum beam current by means of Jaffé diagrams were 1.045 for the Bragg peak chamber and 1.02 for the PinPoint 3D chamber.

## 2.5 Design and 3D-printing of range modulators

The range modulators designed for the present study have pins with a pyramid shape and a square base as the basic geometry which are periodically repeated. Protons passing through different thicknesses of the pins lose a different amount of energy and therefore result in Bragg peaks with different ranges. The pin shape and thereby the weighted superposition of these shifted Bragg curves can be optimized to result in a homogeneous SOBP.

The optimization principle behind the modulators optimized and produced at GSI is described in detail by Simeonov et al. [12] and Holm et al. [21]. The optimization of the modulators for the present work is illustrated in Figure 4. Each of Figures 4A–C shows one of the different modulators that was produced and tested within this work. The blue curves are the measured pristine depth dose profiles which are the basic input for the optimization. One modulator was optimized on the measured laterally integrated depth dose profile (Figure 4A) for SETUP A, another one on the measured central depth dose profile (Figure 4B) for SETUP A and a third one on the measured central dose profile of a collimated beam (Figure 4C) for SETUP B. The yellow areas mark the depth range in which the optimizer (chi-square minimization) should create a homogeneous dose. The red curves show the optimized SOBPs and the green symbols indicate the optimized weights for the shifted Bragg peaks, which are basically shifted copies of the blue curves (pristine Bragg peaks). Figure 4D compares for the three modulators the profiles of the pins whose shape is based on these optimized weights. The weights have gap after a first high weight in order to sharpen the distal fall-off of the SOBP and are normalized to have a sum of 1. The square pyramids were then exported as .stl files and printed on a 3DSystems ProJet MJP 2500 Plus 3D-printer using VisiJet M2S-HT250 as printing material and VisiJet M2 SUP as support material. The printing material has a water equivalent density of 1.162 g/cm$^3$ (determined by previous measurements with proton beams). The modulator structures were embedded in a frame for better stability and have a 2 mm thick base plate on which the pins are standing. The pins were arranged as a 16 × 16 matrix with a 3 mm period (Figure 4D).

At TIFPA/UniTn, a range modulator for SETUP B was optimized combining previously calculated look-up tables of depth dose profiles with the solution of a linear system using a dedicated script. The look-up tables were generated with TOPAS Monte Carlo simulations [32],

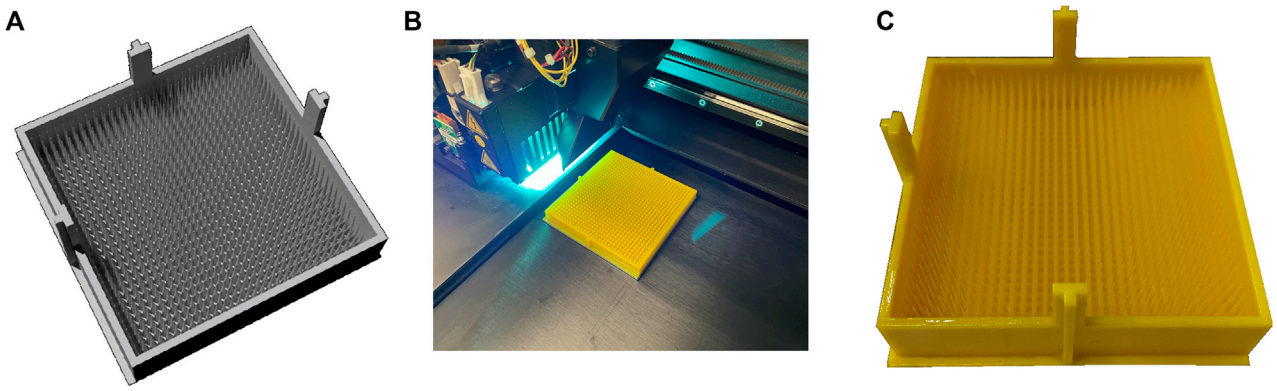


FIGURE 5
Schematic showing the manufacturing process of the range modulator at UniTn. Panel **(A)**: range modulator CAD file, panel **(B)**: manufacturing of the range modulator, panel **(C)**: 3D-printed range modulator.

by reproducing the beam properties and the geometry of the experimental setup and scoring the resulting depth dose distribution in a voxelized water phantom (voxel size comparable to the microdiamond detector volume of 0.004 $mm^3$) and checking that it matches with the previously measured depth dose profile. Separate simulations were then performed for the beam traversing layers of increasing thicknesses of water, resembling the different layers of the range modulator pin. A total of 21 layers in 0.5 mm steps was simulated. The weights of the different shifted Bragg curves were optimized to produce a flat SOBP. The resulting weights were then converted into a pin geometry and scaled by the water-equivalent thickness of the printer material. The pins were arranged in a matrix of adjacent pins with 3 mm edge length at the base. After verification with another TOPAS simulation, the modulator geometry was converted into a .stl file and 3D-printed at UniTn using the PolyJet technique, a type of additive manufacturing, using a Stratasys J750 3D printer, which is known for its exceptional printing capabilities (see Figure 5). This approach has been extensively developed and tested at UniTn for printing samples with very complicated geometry [10].

To achieve the required level of precision, the printer was set to high-quality mode, resulting in a layer height resolution of 14 $\mu$m, meaning that each successive layer of photopolymer was only 14 $\mu$m thick. This level of resolution is critical for creating small, intricate structures like the pins of the range modulator. In addition, the dimensional accuracy of the printer was set to 100 $\mu$m to ensure that the final product was very close to the intended dimensions. The range modulator was printed with pins aligned vertically (in the $z$-direction) with respect to the printer head. This alignment was critical for ensuring that the pins were properly formed and that the final product would function as intended. The Vero Yellow RGD836 printing material was chosen due to its excellent mechanical properties and chemical resistance. To ensure that the very thin pins were not damaged during printing, a glossy surface finishing mode was used, which reduced the need for supporting materials that could have caused the pins to break during removal. Like the GSI modulators, also the TIFPA/UniTn modulator has a 2 mm thick base plate on which the pins were printed.

The most notable difference in the two optimization methods is how to obtain the shifted Bragg curves used as input for optimization of the modulator geometry. In contrast to the fast numerical approach with (reasonable) simplifications used by GSI, TIFPA/UniTn follows a full Monte Carlo approach to have maximum accuracy already at the stage of optimization but at the cost of increased calculation time. The Monte Carlo approach could be of special interest for complex setups, e.g., with multiple collimators and air gaps, where a simple 1D approximation might not be accurate enough.

### 2.6 Monte Carlo simulations to obtain $LET_D$ profiles

The most common descriptor of radiation quality is the dose averaged *LET* ($LET_D$) in water [33]. Since this quantity is not straightforward to measure, a common method is to calculate it via radiation transport calculations, typically using a Monte Carlo code. Monte Carlo simulations to calculate profiles of $LET_D$ in water for the different setups were carried out using the FLUKA Monte Carlo code (version 2021 2.9) [24,25] and the TOPAS toolkit which is based on Geant4 [32].

In FLUKA, the modulator geometries were implemented in the simulations with a dedicated sub-routine [26]. *LET* spectra in water taking into account all primary and secondary charged particles were scored with the USRYIELD card. From these spectra, the dose averaged *LET* was calculated offline by averaging.

In TOPAS, the modulator geometry was implemented in the simulation by means of a custom TOPAS extension. The dose-average *LET* taking into account primary and secondary protons was retrieved with the standard TOPAS *LET* scorer, by setting the *LET* computation to look up the electronic stopping power of water for the pre-step proton energy.

## 3 Results and discussion

### 3.1 Dosimetric characterization

The different modulators designed and produced within this work were characterized in detail experimentally and by means of Monte Carlo simulations.

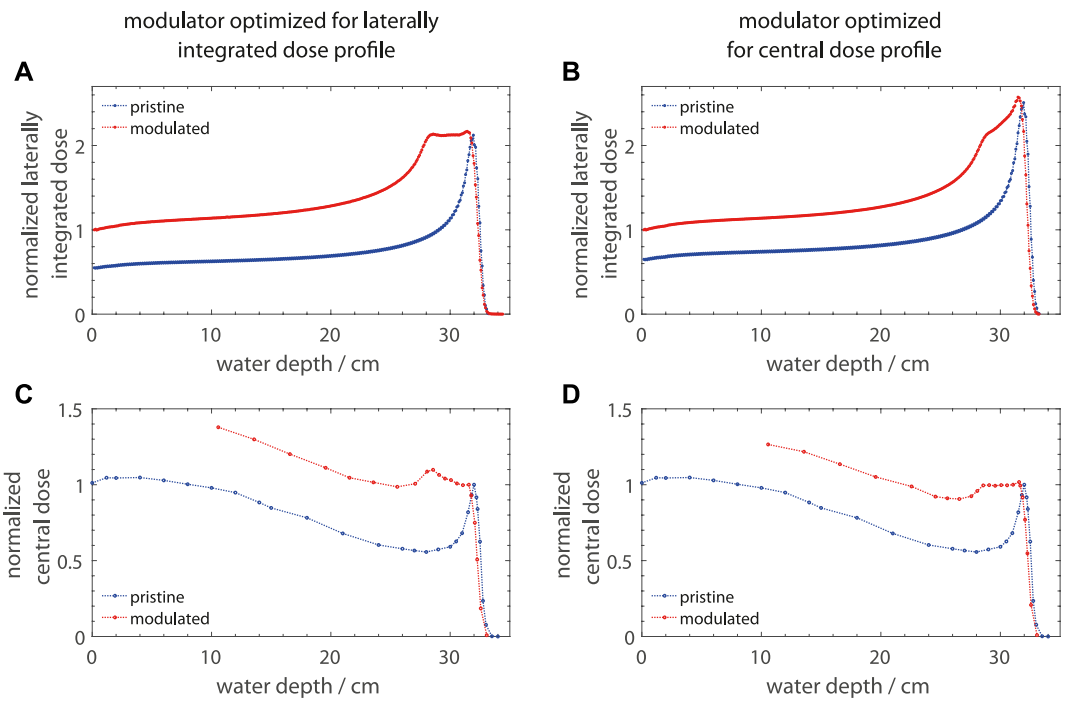


FIGURE 6
Measured laterally integrated panel **(A)** and **(B)** and central depth dose profiles panel **(C)** and **(D)** for 225 MeV protons for two range modulators optimized for SETUP A (one for laterally integrated and the other one for the central dose profile). Panel **(A)** and **(C)** show data for a modulator that was optimized for the laterally integrated depth dose profile of the pristine beam while the modulator for panel **(B)** and **(D)** was optimized using the central depth dose profile.

### 3.1.1 Depth dose profiles

Figure 6 shows measured laterally integrated depth dose profiles (Figures 6A,B) measured with the IBA Giraffe detector as well as central depth dose profiles measured with a PTW PinPoint 3D ionization chamber (radius of sensitive volume: 1.45 mm) in a water phantom (Figures 6C,D) for SETUP A. The measurements were performed for the pristine 225 MeV proton beam and two types of range modulators optimized to produce an SOBP with 3 cm modulation width (SETUP A). One modulator was optimized in the conventional way using the laterally integrated dose profile of the pristine beam (blue curve in Figures 6A,B) as input for the optimization of the modulator geometry, while the other one was optimized using the central depth dose profile (blue curve in Figures 6C,D), see Figure 4. The conventionally optimized modulator was added to the present study in order to verify the expectation that the SOBP is not flat when irradiated with a static pencil beam (shown in Figure 2) while the modulator optimized on the central dose profile is the one intended for the actual experimental setup.

The obtained depth dose profiles are in line with the general picture shown in Figure 2 which was obtained by FLUKA simulations. As visible in Figures 6A,C, the optimization on the laterally integrated depth dose profile of the pristine beam creates a flat SOBP in the laterally integrated profile but introduces a tilted SOBP in the central depth dose profile which would be relevant for

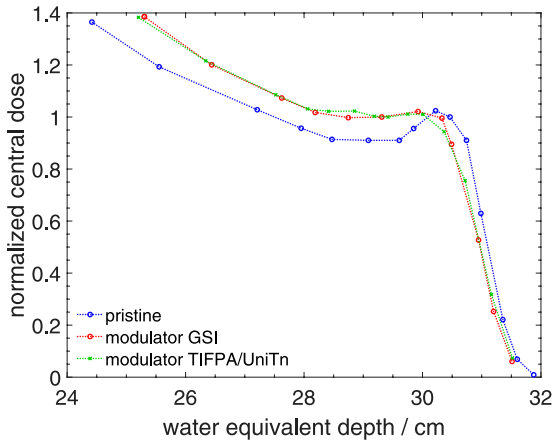


FIGURE 7
Measured central depth dose profiles for 225 MeV protons for two range modulators optimized for SETUP (B). The pristine Bragg peak (blue curve) was used for optimization of the modulators. One modulator (red curve) was optimized and produced at GSI in Darmstadt, Germany and the other one (green curve) at TIFPA/UniTn in Trento, Italy. A brass collimator with 5 mm hole was placed at 24 cm water equivalent depth. Behind the collimator, the depth dose profiles were measured with a PTW microdiamond detector in PMMA plates. The PMMA depths were re-scaled to water equivalent depths.

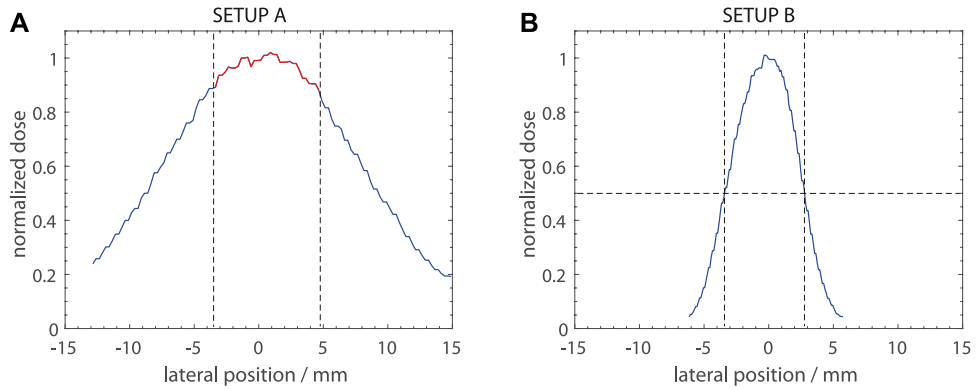


FIGURE 8
Measured lateral dose profiles at the SOBP center for the SETUP A panel **(A)** and SETUP B (panel **(B)**). The dose profiles were measured with a PTW microdiamond detector in a PMMA plate scanned along the lateral direction with a linear axis drive. The water equivalent depth was 29.5 cm for both measurements. The dashed lines in panel **(A)** indicate the useable field size (dose inhomogeneity $\leq \pm$ 5%) and in panel **(B)** the 50% dose level.

the irradiation of samples with a static pencil beam. By using the central depth dose profile of the pristine beam for optimization (Figures 6B,D), the central depth dose profile gets a flat SOBP which is sufficient to irradiate samples while the laterally integrated profile gets a positive slope towards the distal end. Therefore, such a range modulator can be considered as a specialized solution for SOBP irradiations with static pencil beams.

Figure 7 shows central depth dose profiles for SETUP B measured behind the collimator (see Figure 3B). A PTW microdiamond detector was used to measure lateral profiles at different PMMA depths and the dose maxima in these lateral profiles give the central depth dose profile. These measurements were performed for the pristine 225 MeV proton beam and for two range modulators optimized and produced independently at two different institutes (GSI and TIFPA/UniTn).

In the central depth dose profile for the pristine beam (Figure 7, blue curve) one can observe that the Bragg peak almost disappears due to the presence of the collimator at 24 cm water equivalent depth. However, a flat depth dose distribution right before the end of the range that is comparable with a classical SOBP can be produced even for this sharply collimated configuration (red and green curves in Figure 7) while the two modulators that were optimized and produced independently at GSI and TIFPA/UniTn produce comparable depth dose profiles.

### 3.1.2 Lateral dose profiles

A general difference between SETUP A and SETUP B are the produced lateral dose profiles. While SETUP A is designed to deliver a homogeneous dose to a small sample, SETUP B is supposed to produce a sharply confined radiation field to irradiate partial volumes in small animals and spare surrounding organs and tissues. Comparable experiments to SETUP B with conventional dose rates have been established at UPTD [16,34] where a 90 MeV proton beam is degraded in plastic absorbers, collimated to a size of a few millimeters and stopped in the center of a mouse brain.

Figure 8 compares the lateral dose distributions of the two setups (SETUP A and SETUP B) at the SOBP center depth (29.5 cm water equivalent depth). The lateral dose profiles were measured with the PTW microdiamond detector behind PMMA slabs as described above. The noise on the profiles is due to the low beam currents used for the lateral scans.

The lateral dose profile for SETUP A (Figure 8A) shows that samples with sizes of 8–9 mm can be irradiated with a relatively homogeneous dose (±5%), as marked by the red line. This is a sufficient field size for, e.g., 0.5 mL Eppendorf tubes (inner tube diameter of 6.5 mm). If a larger field size is required the sample can be positioned at a larger distance, however, at the cost of a lower dose rate. In contrast to this broad field, the lateral dose profile of SETUP B (Figure 8B) is sharply collimated. The dose drops down to 50% of the maximum value at a lateral distance from the center of ~ 3 mm. At distances larger than 5 mm, the dose contributions fall below 10%. Such a small irradiation field can be used for precise irradiation of partial volumes in small animals. For an even sharper lateral dose fall-off, a second collimator that further trims the penumbra can be added right before the animal.

## 3.2 $LET_D$ profiles

Monte Carlo simulations using the FLUKA and TOPAS Monte Carlo codes were performed to study $LET_D$ profiles. Figure 9 shows calculated $LET_D$ profiles together with the measured central depth dose profiles for the two irradiation setups (SETUP A and SETUP B).

The $LET_D$ profiles have a shape that is typical for proton SOBPs. At the entrance channel moderate $LET_D$ values below 1 keV/$\mu$m can be observed while it gets elevated to ~ 2.5 keV/$\mu$m in the SOBP region for both setups. Towards the end of the SOBP, the $LET_D$ rises even further and reaches values up to 9 keV/$\mu$m at the distal edge. For proton beams the region with maximum *LET* always lies at the distal fall-off behind the Bragg peak. The $LET_D$ profiles calculated for the different modulators optimized for

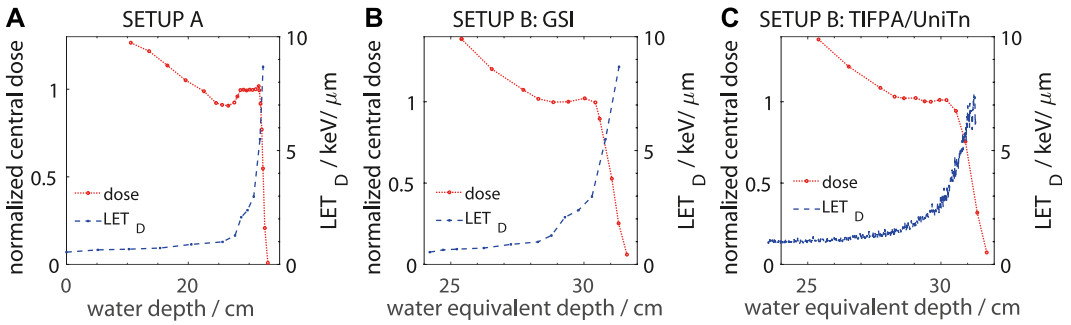


FIGURE 9
Measured central depth dose profiles for 225 MeV protons for range modulators optimized for SETUP A (panel **(A)**) and SETUP B (panel **(B)** and **(C)**) together with Monte Carlo calculated $LET_D$ profiles in water. Panel **(B)** shows the results for the modulator for SETUP B optimized and manufactured at GSI, Darmstadt and panel **(C)** shows the modulator optimized and manufactured at TIFPA/UniTn, Trento. The $LET_D$ profiles in panel **(A)** and **(B)** were calculated using the FLUKA Monte Carlo code while for the $LET_D$ profile in panel **(C)** was obtained from TOPAS/Geant4 simulations. For SETUP A, the depth dose profile was measured in water while for SETUP B they were measured in PMMA plates and converted to water equivalent depth.

SETUP B (Figures 9B,C) show the same trend but the absolute $LET_D$ values differ slightly in some regions. It is well known that $LET_D$ profiles predicted by different Monte Carlo codes (FLUKA in Figure 9B, TOPAS/Geant4 in Figure 9C can show such variations due to differences in the scoring methods [35,36]. Taking this into account, one can state that the two experimental setups imitate the radiation quality in the SOBP as it would occur in proton therapy treatments in a realistic way, both qualitatively and quantitatively [36,37].

## 3.3 Maximum dose rates

Since the experimental setups described in this work are intended for FLASH irradiations, the maximum dose rates that can be reached in the SOBP region are also important to consider. From the transmission data in Figure 1, the maximum available beam current at the fixed beamline in the experimental room of UPTD for 225 MeV protons can be calculated as 223 nA (44.6% of 500 nA cyclotron current), corresponding to $1.39 \times 10^{12}$ protons per second.

The maximum dose rates that were reached in dosimetric tests, where the dose was measured in an irradiation pulse of 100 m using a PinPoint 3D ionization chamber positioned on the central axis at the central depth of the SOBP (where the relative dose profiles in Figures 6, 7, 8, and 9 are normalized to), were 610 Gy/s for SETUP A and 405 Gy/s for SETUP B. The about 30% lower dose rate in SETUP B compared to SETUP A is due to the additional collimation which cuts out protons coming at large angles. These dose rates are clearly high enough for FLASH experiments and with both setups even large doses up to 100 Gy can be applied with irradiation times far below 500 m, allowing studies of the FLASH effect at highest doses (as investigated previously with electrons [38]). The applied dose can be adjusted by the pulse length which at the fixed beamline at UPTD can be set with millisecond accuracy.Low dose rates in the order of 10 Gy/min could be reached as well by simply reducing the beam current. When changing the beam current, no change of the beam properties (e.g., position or spot size) was detected. Therefore, reference irradiations are possible without any changes to the setups.

# 4 Summary and conclusion

Range modulators for SOBP irradiations at the static proton beamline in the experimental room of UPTD using a 225 MeV proton beam were designed, produced and tested experimentally. A new concept for the optimization of range modulators for static pencil beams and in presence of collimators, based on the central depth dose profiles as input into the optimization process, was introduced and shown to work well. The depth and lateral dose profiles were characterized in detail by measurements using a PinPoint chamber and a microdiamond detector. Two modulators, independently optimized and produced at two different institutes (GSI, Darmstadt, Germany and TIFPA/UniTn, Trento, Italy) were compared and found equivalent in terms of SOBP flatness and field characteristics.

Dose rates in the center of the SOBPs up to 610 Gy/s and 405 Gy/s were reached for the two new experimental setups, which is higher than what was possible with the previously used irradiation setup at the entrance channel of a pristine 225 MeV proton beam.

In addition to the dosimetric characterization, $LET_D$ profiles were obtained by means of Monte Carlo simulations and found to compare well with typical clinical proton SOBPs.

The newly produced range modulators will allow future proton FLASH experiments in the SOBP at UPTD with two different experimental setups.

# Data availability statement

The raw data supporting the conclusion of this article will be made available by the authors, without undue reservation.

## Author contributions

FH, EBe, and JP designed the present study. CS, DM, NP, FT, and UW designed and produced the range modulators. FH, EBe, EBo, SG, and JP designed and built the experimental setups and performed the dosimetric characterization. FH and FT performed the Monte Carlo simulations. FH compiled the initial draft of the manuscript. All authors contributed to the article and approved the submitted version.

## Funding

The range modulator studies performed in Trento were partially supported by the FRIDA project, funded by INFN CSN5.

## Acknowledgments

The authors would like to thank Mabroor Ahmed from Helmholtz Center Munich for providing the software controlling the linear axis and electrometer readout used for measuring the lateral dose profiles. Warisara Charuchinda from GSI is acknowledged for providing the FLUKA routines for loading the modulator geometries. Remo Cristoforetti, now at DKFZ in Heidelberg, is acknowledged for the preliminary work performed on range modulator optimization in the Trento group. Jozef Bokor from IBA is acknowledged for providing helpful information concerning the transmission of the proton therapy system at UPTD.

## Conflict of interest

The authors declare that the research was conducted in the absence of any commercial or financial relationships that could be construed as a potential conflict of interest.

## Publisher's note



## References

1. Favaudon V, Caplier L, Monceau V, Pouzoulet F, Sayarath M, Fouillade C, et al. Ultrahigh dose-rate flash irradiation increases the differential response between normal and tumor tissue in mice. *Sci Transl Med* (2014) 6:245ra93. doi:10.1126/scitranslmed.3008973

2. Vozenin M-C, Hendry J, Limoli C. Biological benefits of ultra-high dose rate flash radiotherapy: Sleeping beauty awoken. *Clin Oncol* (2019) 31:407–15. doi:10.1016/j.clon.2019.04.001

3. Limoli CL, Vozenin M-C. Reinventing radiobiology in the light of flash radiotherapy. *Annu Rev Cancer Biol* (2023) 7:1–21. doi:10.1146/annurev-cancerbio-061421-022217

4. Helmbrecht S, Baumann M, Enghardt W, Fiedler F, Krause M, Lühr A. Design and implementation of a robust and cost-effective double-scattering system at a horizontal proton beamline. *J Instrument* (2016) 11:T11001. doi:10.1088/1748-0221/11/11/T11001

5. Beyreuther E, Baumann M, Enghardt W, Helmbrecht S, Karsch L, Krause M, et al. Research facility for radiobiological studies at the university proton therapy dresden. *Int J Part Ther* (2018) 5:172–82. doi:10.14338/IJPT-18-00008.1

6. Henthorn NT, Sokol O, Durante M, De Marzi L, Pouzoulet F, Miszczyk J, et al. Mapping the future of particle radiobiology in Europe: The inspire project. *Front Phys* (2020) 8. doi:10.3389/fphy.2020.565055

7. Beyreuther E, Brand M, Hans S, Hideghéty K, Karsch L, Leßmann E, et al. (2019). Feasibility of proton flash effect tested by zebrafish embryo irradiation. *Radiother Oncol* 139, 46–50. doi:10.1016/j.radonc.2019.06.024

8. Jansen J, Knoll J, Beyreuther E, Pawelke J, Skuza R, Hanley R, et al. Does flash deplete oxygen? Experimental evaluation for photons, protons, and carbon ions. *Med Phys* (2021) 48:3982–90. doi:10.1002/mp.14917

9. Karsch L, Pawelke J, Brand M, Hans S, Hideghéty K, Jansen J, et al. Beam pulse structure and dose rate as determinants for the flash effect observed in zebrafish embryo. *Radiother Oncol* (2022) 173:49–54. doi:10.1016/j.radonc.2022.05.025

10. Mora S, Pugno NM, Misseroni D. 3d printed architected lattice structures by material jetting. *Mater Today* (2022) 59:107–32. doi:10.1016/j.mattod.2022.05.008

11. Simeonov Y, Weber U, Penchev P, Ringbæk TP, Schuy C, Brons S, et al. 3d range-modulator for scanned particle therapy: Development, Monte Carlo simulations and experimental evaluation. *Phys Med Biol* (2017) 62:7075–96. doi:10.1088/1361-6560/aa81f4

12. Simeonov Y, Weber U, Schuy C, Engenhart-Cabillic R, Penchev P, Durante M, et al. Monte Carlo simulations and dose measurements of 2d range-modulators for scanned particle therapy. *Z für Medizinische Physik* (2021) 31:203–14. doi:10.1016/j.zemedi.2020.06.008

13. Simeonov Y, Weber U, Schuy C, Engenhart-Cabillic R, Penchev P, Flatten V, et al. Development, Monte Carlo simulations and experimental evaluation of a 3d range-modulator for a complex target in scanned proton therapy. *Biomed Phys Eng Express* (2022) 8:035006. doi:10.1088/2057-1976/ac5937

14. Liu R, Charyyev S, Wahl N, Liu W, Kang M, Zhou J, et al. An integrated physical optimization framework for proton stereotactic body radiation therapy flash treatment planning allows dose, dose rate, and linear energy transfer optimization using patient-specific ridge filters. *Int J Radiat Oncol Biol Phys* (2023) 116:949–59. doi:10.1016/j.ijrobp.2023.01.048

15. Barna S, Meouchi C, Resch AF, Magrin G, Georg D, Palmans H. 3d printed 2d range modulators preserve radiation quality on a microdosimetric scale in proton and carbon ion beams. *Radiother Oncol* (2023) 182:109525. doi:10.1016/j.radonc.2023.109525

16. Suckert T, Müller J, Beyreuther E, Azadegan B, Brüggemann A, Bütof R, et al. High-precision image-guided proton irradiation of mouse brain sub-volumes. *Radiother Oncol* (2020) 146:205–12. doi:10.1016/j.radonc.2020.02.023

17. Kupfer T, Lehmann J, Butler DJ, Ramanathan G, Bailey TE, Franich RD. Commissioning of a ptw 34070 large-area plane-parallel ionization chamber for small field megavoltage photon dosimetry. *J Appl Clin Med Phys* (2017) 18:206–17. doi:10.1002/acm2.12185

18. Berger M, Coursey J, Zucker M. *Estar, pstar, and astar: Computer programs for calculating stopping-power and range tables for electrons, protons, and helium ions (version 1.21)*. [Dataset] (1999).

19. Seltzer SM, Fernández-Varea JM, Andreo P, Bergstrom PM, Burns DT, Bronić IK, et al. *Key data for ionizing-radiation dosimetry: Measurement standards and applications, icru report 90* (2016).

20. Tommasino F, Rovituso M, Bortoli E, La Tessa C, Petringa G, Lorentini S, et al. A new facility for proton radiobiology at the trento proton therapy centre: Design and implementation. *Physica Med* (2019) 58:99–106. doi:10.1016/j.ejmp.2019.02.001

21. Holm KM, Weber U, Simeonov Y, Krauss A, Jäkel O, Greilich S. 2d range modulator for high-precision water calorimetry in scanned carbon-ion beams. *Phys Med Biol* (2020) 65:215003. doi:10.1088/1361-6560/aba6d5

22. Titt U, Yang M, Wang X, Iga K, Fredette N, Schueler E, et al. Design and validation of a synchrotron proton beam line for flash radiotherapy preclinical research experiments. *Med Phys* (2022) 49:497–509. doi:10.1002/mp.15370

23. Kourkafas G, Bundesmann J, Denker A, Fanselow T, Heufelder J, Röhrich J, et al. Epd007 - a 3d range modulator for ultra-short proton flash irradiation. *Physica Med* (2022) 94:S64–S65. doi:10.1016/S1120-1797(22)01578-2

24. Ferrari A, Sala PR, Fassò A, Ranft J. *FLUKA: A multi-particle transport code* (2005). *CERN-2005-10*.

25. Böhlen T, Cerutti F, Chin M, Fassò A, Ferrari A, Ortega P, et al. The FLUKA code: Developments and challenges for high energy and medical applications. *Nucl Data Sheets* (2014) 120:211–4. doi:10.1016/j.nds.2014.07.049

26. Charuchinda W, Horst F, Simeonov Y, Schuy C, Penchev P, Poulsen P, et al. 3d range-modulators for proton therapy: Near field simulations with fluka and comparison with film measurements. *J Phys Conf Ser* (2023) 2431:012081. doi:10.1088/1742-6596/2431/1/012081

27. Bäumer C, Koska B, Lambert J, Timmermann B, Mertens T, Talla PT. Evaluation of detectors for acquisition of pristine depth-dose curves in pencil beam scanning. *J Appl Clin Med Phys* (2015) 16:151–63. doi:10.1120/jacmp.v16i6.5577

28. Togno M, Nesteruk K, Schäfer R, Psoroulas S, Meer D, Grossmann M, et al. Ultra-high dose rate dosimetry for pre-clinical experiments with mm-small proton fields. *Physica Med* (2022) 104:101–11. doi:10.1016/j.ejmp.2022.10.019

29. Gotz M, Karsch L, Pawelke J. A new model for volume recombination in plane-parallel chambers in pulsed fields of high dose-per-pulse. *Phys Med Biol* (2017) 62: 8634–54. doi:10.1088/1361-6560/aa8985

30. Baack L, Schuy C, Brons S, Horst F, Voss B, Zink K, et al. Reduction of recombination effects in large plane parallel beam monitors for flash radiotherapy with scanned ion beams. *Physica Med* (2022) 104:136–44. doi:10.1016/j.ejmp.2022.10.029

31. Kranzer R, Schüller A, Bourgouin A, Hackel T, Poppinga D, Lapp M, et al. Response of diamond detectors in ultra-high dose-per-pulse electron beams for dosimetry at flash radiotherapy. *Phys Med Biol* (2022) 67:075002. doi:10.1088/1361-6560/ac594e

32. Perl J, Shin J, Schümann J, Faddegon B, Paganetti H. Topas: An innovative proton Monte Carlo platform for research and clinical applications. *Med Phys* (2012) 39: 6818–37. doi:10.1118/1.4758060

33. Grün R, Friedrich T, Traneus E, Scholz M. Is the dose-averaged let a reliable predictor for the relative biological effectiveness? *Med Phys* (2019) 46:1064–74. doi:10.1002/mp.13347

34. Schneider M, Bodenstein E, Bock J, Dietrich A, Gantz S, Heuchel L, et al. Combined proton radiography and irradiation for high-precision preclinical studies in small animals. *Front Oncol* (2022) 12:982417. doi:10.3389/fonc.2022.982417

35. Kalholm F, Grzanka L, Traneus E, Bassler N. A systematic review on the usage of averaged let in radiation biology for particle therapy. *Radiother Oncol* (2021) 161: 211–21. doi:10.1016/j.radonc.2021.04.007

36. Hahn C, Ödén J, Dasu A, Vestergaard A, Fuglsang Jensen M, Sokol O, et al. Towards harmonizing clinical linear energy transfer (let) reporting in proton radiotherapy: A European multi-centric study. *Acta Oncologica* (2022) 61:206–14. doi:10.1080/0284186X.2021.1992007,

37. Grün R, Friedrich T, Krämer M, Scholz M. Systematics of relative biological effectiveness measurements for proton radiation along the spread out Bragg peak: Experimental validation of the local effect model. *Phys Med Biol* (2017) 62:890–908. doi:10.1088/1361-6560/62/3/890

38. Horst F, Brand M, Hans S, Karsch L, Lessmann E, Löck S, et al. In regard to böhlen et al. *Int J Radiat Oncology*Biology*Physics* (2023) 115:1006–7. doi:10.1016/j.ijrobp.2022.11.015

frontiers | Frontiers in Physics

TYPE Original Research
PUBLISHED 06 July 2023
DOI 10.3389/fphy.2023.1185598



OPEN ACCESS

EDITED BY
Eliana Maria Vasquez Osorio,
The University of Manchester,
United Kingdom

REVIEWED BY
Olga Sokol,
Helmholtz Association of German Research Centres (HZ), Germany
Daniele Panetta,
National Research Council (CNR), Italy
Abdeslem Rrhioua,
Mohamed Premier University, Morocco

*CORRESPONDENCE
A. De Gregorio,
Angelica.Degregorio@uniroma1.it

RECEIVED 13 March 2023
ACCEPTED 22 June 2023
PUBLISHED 06 July 2023

CITATION
Muscato A, Arsini L, Battistoni G, Campana L, Carlotti D, De Felice F, De Gregorio A, De Simoni M, Di Felice C, Dong Y, Franciosini G, Marafini M, Mattei I, Mirabelli R, Muraro S, Pacilio M, Palumbo L, Patera V, Schiavi A, Sciubba A, Schwarz M, Sorbino S, Tombolini V, Toppi M, Traini G, Trigilio A and Sarti A (2023), Treatment planning of intracranial lesions with VHEE: comparing conventional and FLASH irradiation potential with state-of-the-art photon and proton radiotherapy.
*Front. Phys.* 11:1185598.
doi: 10.3389/fphy.2023.1185598



# Treatment planning of intracranial lesions with VHEE: comparing conventional and FLASH irradiation potential with state-of-the-art photon and proton radiotherapy

A. Muscato[1,2,3], L. Arsini[2,4], G. Battistoni[5], L. Campana[1], D. Carlotti[4,6], F. De Felice[7], A. De Gregorio[4,2]*, M. De Simoni[2,8], C. Di Felice[9], Y. Dong[5], G. Franciosini[1,2], M. Marafini[2,3], I. Mattei[5], R. Mirabelli[1,2], S. Muraro[5], M. Pacilio[9], L. Palumbo[1,2], V. Patera[1,2], A. Schiavi[1,2], A. Sciubba[1,10], M. Schwarz[11], S. Sorbino[1], V. Tombolini[7], M. Toppi[1,2], G. Traini[2], A. Trigilio[4,10] and A. Sarti[1,2]

[1]Dipartimento di Scienze di Base e Applicate per l'Ingegneria, Sapienza Università di Roma, Roma, Italy, [2]INFN Sezione di Roma I, Roma, Italy, [3]Museo Storico della Fisica e Centro Studi e Ricerche Enrico Fermi (CREF), Roma, Italy, [4]Dipartimento di Fisica, Sapienza Università di Roma, Roma, Italy, [5]INFN Sezione di Milano, Milano, Italy, [6]Radiation Oncology, Fondazione Policlinico Universitario Campus Bio-medico, Rome, Italy, [7]Dipartimento di Scienze Radiologiche, Oncologiche e Anatomo Patologiche, Sapienza Università di Roma, Roma, Italy, [8]Departement of Medical Physics Ludwig Maximilians Universität München (LMU) Munich, Munich, Germany, [9]Unità di Fisica Sanitaria, Azienda Ospedaliero-Universitaria Policlinico Umberto I, Roma, Italy, [10]Istituto Nazionale di Fisica Nucleare (INFN) Sezione dei Laboratori di Frascati, Roma, Italy, [11]Radiation Oncology Department, University of Washington & Fred Hutchinson Cancer Center, Seattle, CA, United States

The treatment of deep-seated tumours with electrons of very high energies (VHEE, 70–150 MeV) has already been explored in the past, suggesting that a dosimetric coverage comparable with state-of-the-art proton (PT) or photon radiotherapy (RT) could be achieved with a large ( > 10) number of fields and high electron energy. The technical and economical challenges posed by the deployment of such beams in treatment centres, together with the expected small therapeutic gain, prevented the development of such technique. This scenario could radically change in the light of recent developments that occurred in the compact, high-gradient, electron acceleration technology and, additionally, of the experimental evidence of the sparing of organs at risk achieved in ultra-high dose rate irradiation, also referred to as FLASH. Electrons with the energy required to treat intracranial lesions could be provided, at dose rates compatible with what is needed to trigger the FLASH effect, by accelerators that are a few metres long, and the organ sparing could be exploited to significantly simplify the irradiation geometry, decreasing the number of fields needed to treat a patient. In this paper, the case of two patients affected by a chordoma and a meningioma, respectively, treated with protons in Trento (IT) is presented. The proton plans have been compared with VHEE plans and X-ray intensity-modulated radiotherapy (IMRT) plans. The VHEE plans were first evaluated in terms of physical dose distribution and then assuming that the FLASH regimen can be achieved. VHEE beams demonstrated their potential in obtaining plans that

have comparable tumour coverage and organs at risk sparing when benchmarked against current state-of-the-art IMRT and PT. These results were obtained with a number of explored fields that was in the range between 3 and 7, consistent with what is routinely performed in IMRT and PT conventional irradiations. The FLASH regimen, in all cases, showed its potential in reducing damage to the organs placed nearby the target volume, allowing, particularly in the chordoma case where the irradiation geometry is more challenging, a better tumour coverage with respect to the conventional treatments.

KEYWORDS

external beam radiotherapy, intracranial lesions, FLASH effect, very high-energy electrons, deep-seated tumours

## 1 Introduction

In the framework of constant research and effort to improve the therapeutic efficacy of deep-seated tumour treatments with external beam radiotherapy (EBRT), different radiation types have been explored in the past. However, the vast majority of treatments are delivered using X-ray radiotherapy, and a smaller fraction of patients is treated with particle therapy (PT) delivered with either protons or heavier ions.

The experience gained so far allowed both IMRT and PT to obtain remarkable results, providing a high level of dose conformity to the target volume. As the therapeutic window of IMRT also depends on normal tissue complication probability, a continuous effort is devoted to improve the sparing of the organs at risk (OARs). In this respect, IMRT and PT treatments have different characteristics and have to be carefully optimised in different ways, providing optimal solutions to different disease sites on the specific position and accessibility of the target volume. As electrons are light-charged particles, their unique features of interaction with matter could be additionally exploited to provide treatments capable of overcoming limitations of IMRT and PT in specific districts or irradiation modalities.

Electrons with energies in the range of 60–120 MeV (VHEE) can be used to treat deep-seated tumours, as they are capable of reaching the needed depth and exhibiting a wide dose peak, whose position changes according to the beam energy. Their use have already been explored in the past [1–3], and a performance comparable with volumetric modulated arc therapy (VMAT) and proton irradiations was demonstrated, at the cost of using a complex irradiation system with many fields (13 or more) or high beam energy (at least 100 MeV) [4, 5]. At the same time, the production of high-energy beams required long accelerating sections that were not easily compatible with existing clinical centres. These conditions contributed, in the past, to make the VHEE solution less cost-effective for a clinical centre with respect to IMRT or other photon-based modalities.

Nowadays, the creation of an accelerating, compact, lower-cost structure for producing high-energy electron fields is possible with the advent of C-band accelerating structures, which is capable of accelerating electrons with the required high charge and fields of up to 50 MeV/m in the hospital setting [6].

In addition, there is increasing evidence from preclinical studies showing that if the dose rate is radically increased (~40 Gy/s, at least) with respect to conventional treatments (~0.01 Gy/s), induced radiotoxicity in healthy tissues can be significantly reduced, while maintaining the same cytotoxic effects on cancer cells. Such effects will be further referred to as the FLASH effect [4, 7–9]. The implementation of FLASH beams in clinical centres [10] still has to overcome significant technical challenges. Although FLASH intensities have already been achieved for proton and electron beams (e.g., the low-energy electron beams used for intra-operative radiation therapy), mostly in pre-clinical settings, the implementation of FLASH IMRT with photons is still in its early development stage [8, 11].

The recent advancements in electron accelerating technology, together with the experimental exploration of the FLASH effect, have re-fuelled the interest in the planning and delivery of VHEE for therapeutic applications [12].

In this manuscript, following the approach previously described in [13], the potential of VHEE, with a low number of fields and maximal energy of 130 MeV to treat intracranial lesions, has been studied. The results of conventional irradiation have been compared with state-of-the-art IMRT and PT treatments, and, in addition, the FLASH effect potential for the treatment of such pathologies has been explored.

The first study to explore the feasibility of VHEE to treat deep-seated tumours with a limited number of irradiation fields ([13]) was made on a prostate cancer case, performing comparisons with high-quality results that can be attainable with IMRT and PT at conventional dose rates. In this work, a meningioma and a chordoma case were chosen to investigate how VHEE could be exploited to handle challenging treatments, where the planning target volume (PTV) is closely surrounded by several OARs whose sparing is made difficult by the patient's anatomy and the corresponding dosimetric prescriptions and constraints. In addition, the reason for choosing this region and, in particular, intracranial lesions to assess the FLASH potential is that they are an excellent ground to test the potential of conventional and FLASH irradiation in providing additional sparing to the OARs that are currently limiting the dose prescription to PTV.

The selected cases, dose prescriptions, dosimetric constraints for the OARs, and the treatment plans optimised at the Trento PT Centre (Azienda Provinciale per i Servizi Sanitari, APSS—Trento[1]) are documented. Details are also provided based on the plans

1 https://www.apss.tn.it/

**TABLE 1** Planning prescriptions for patient M1. $D_{max}$ and $D_{mean}$ are the maximum and average dose absorbed in the volume of interest, respectively. $V_{XX}$ is the fractional volume of a given OAR (or PTV) receiving a minimum dose of (*XX* Gy). $V_{95\%} > 95\%$ requirement means that 95% of the volume should receive more than 95% of the prescribed dose. $D_1 \leq$ YY Gy requirement means that the minimum dose in the hottest 1% of the volume should not exceed YY Gy. Total volume (in cc) of the PTV and OARs is listed in the last column.

| Patient M1 | Dosimetric constraint | Volume (cc) |
|---|---|---|
| PTV | $V_{95\%} > 95\%$, $D_{max} \leq 105\%$ | 20.71 |
| Optic nerves | $D_1 \leq 54$ Gy (RBE) | 0.95 |
| Chiasm | $D_1 \leq 54$ Gy (RBE) | 0.03 |
| Posterior optical path | $D_1 \leq 54$ Gy (RBE) | 0.45 |
| Eyeballs | $D_1 \leq 40$ Gy (RBE) | 8.14 |
| Brainstem | $D_1 \leq 54$ Gy (RBE) | 28.19 |
| Carotid arteries | $D_{max} \leq 105\%$ | 1.15 |

**TABLE 2** Planning prescriptions for patient C1. $D_{max}$, $D_{mean}$, $V_{XX}$, and $D_1$ definitions and uses are same as those explained in the caption of Table 1.

| Patient C1 | Dosimetric constraint | Volume (cc) |
|---|---|---|
| PTV | $V_{95\%} > 95\%$, $D_{max} \leq 107\%$ | 99.15 |
| PTV boost | $V_{95\%} > 95\%$, $D_{max} \leq 107\%$ | 71.94 |
| Brainstem | $D_1 \leq 55$ Gy (RBE) | 27.09 |
| Spinal cord | $D_1 \leq 54$ Gy (RBE) | 8.25 |
| Parotid glands | $D_{mean} \leq 26$ Gy(RBE) | 26.26 |
| Middle ears | $D_{mean} \leq 30$ Gy(RBE) | 3.80 |
| Cochlea | $D_{mean} \leq 35$ Gy(RBE) | 0.35 |

optimised in conventional irradiation modality for both IMRT and VHEE. The field's characteristic definition and the process of VHEE pencil beam fluence optimisation have also been detailed. The comparison of actual delivered plans (protons) and IMRT and VHEE plans with and without including the FLASH effect is presented in the Results section followed by a discussion on the implications of the findings in the landscape of VHEE treatments delivered in both conventional and FLASH modalities.

# 2 Methods

Two patients who underwent PT in Trento (at the APSS centre) to treat a chordoma (hereinafter, patient C1) and a meningioma (M1) were chosen for this study. The patients were treated with protons using a conventional dose rate (~Gy/min), and the prescriptions are currently in use at the Trento therapy centre. The target volumes were identified, and the constraints on PTV coverage, OAR sparing, and details on the irradiation approach were defined. More information about the two PT plans, containing the prescriptions expressed in terms of the biological dose and hence in Gy (RBE) or absorbed dose multiplied by the relative biological effectiveness (RBE), is reported as follows:

- Patient M1: Three fields were used, with a prescription to the PTV of 54 Gy(RBE) in 27 fractions. The dosimetric constraints are listed in Table 1.
- Patient C1: Four fields were used. The treatment was delivered with a simultaneously integrated boost (SIB) technique for a total dose of 60 Gy(RBE) to the boost PTV and 54 Gy(RBE) to the PTV in 30 fractions. A sequential boost of 6 Gy (RBE) in three fractions was then delivered to the boost PTV increasing its final dose to 66 Gy(RBE). The dosimetric constraints are listed in Table 2.

Both treatment plans had to fulfil the planning goals reported in the corresponding table (1 or 2 for M1 and C1, respectively) for the most relevant OARs identified for each treatment.

The clinical proton plans delivered to the patients were sent to the Medical Physics Unit of Policlinico Umberto I in Rome to carry out the IMRT treatment planning, together with the dose prescriptions, the details about the OARs constraints, and the computed tomography (CT) imaging data. The same information was also used to plan VHEE treatments.

The IMRT plans were optimised assuming a static field delivered on a 6 MV-Elekta Versa HD linear accelerator (Elekta [14]). Plans were optimised using the Pinnacle [15] software suite (RTP system version 16, https://pinnacle-software.com/), according to the prescribed dose and constraints provided by the Trento APSS particle therapy centre. Both plans comprised seven fields and matched the requirements set in Table 1 and Table 2.

## 2.1 VHEE plans

While the IMRT and PT plans can be optimised by means of commercial software used in clinical practice, no medically certified software suite is currently available for the planning of VHEE. In addition, VHEE planning lacks a therapeutic protocol that would be helpful in choosing irradiation geometry. For this reason, plan optimisation software based on the inverse planning approach that uses the absorbed dose relative to pencil beams as an input had to be developed from scratch. The details about the implemented software and the optimisation strategy are discussed in a previous study [13].

When producing the absorbed dose maps needed for the planning procedure, the details of the beam characteristics and the beam acceleration and delivery technology play a crucial role. The specific details (e.g., percentage depth dose distributions and penumbra) of the electron beams considered for the treatment of deep-seated tumours can be found in [16]. There are currently several attempts made at providing the technology needed to provide VHEE, with the required intensity in the treatment room of a therapy centre. First of all, there are radio frequency (RF)-based approaches, like the ones pursued in the Phaser collaboration [5] or the ones exploiting the C-band acceleration technology [6]. A different approach foresees the use of the laser-driven acceleration principle, and it is currently investigated both at the CLEAR facility at CERN [17] and at the Intense Laser Irradiation Laboratory at CNR-INO [18] in Pisa, Italy. In this study, the compact C-band solution detailed in [6], which is suitable to be implemented with a low number of fields and capable of being

**TABLE 3** Field electron energies used to perform treatment simulation for the M1 and C1 patients under study. Energies up to 130 MeV were necessary in order to match the electron absorbed dose peak centre with the PTV region.

| M1—energy [MeV] | | | | | | | |
|---|---|---|---|---|---|---|---|
| | Field 1 | Field 2 | Field 3 | Field 4 | Field 5 | Field 6 | Field 7 |
| Three fields | 110 | 110 | 100 | - | - | - | - |
| Seven fields | 90 | 100 | 100 | 110 | 100 | 100 | 90 |
| M1—gantry angle [degrees] | | | | | | | |
| Three fields | 250° | 110° | 270° | - | - | - | - |
| Seven fields | 80° | 110° | 140° | 180° | 220° | 250° | 280° |
| C1—energy [MeV] | | | | | | | |
| Four fields | 120 | 90 | 90 | 120 | - | - | - |
| Seven fields | 120 | 80 | 60 | 60 | 60 | 60 | 80 |
| C1—gantry angle [degrees] | | | | | | | |
| Four fields | 165° | 195° | 55° | 305° | - | - | - |
| Seven fields | 0° | 40° | 80° | 120° | 240° | 280° | 320° |

delivered with an "active scanning"-like approach, was considered and implemented due to its advanced technological readiness level when compared with the laser-plasma-based solutions.

Using the information from the patient planning CT, the entry points, size, and aperture of the electron pencil beams used to irradiate the PTV were defined following an approach similar to active scanning implemented in proton beam delivery. A plane perpendicular to the line joining the electron beam emission point with the PTV centre was used to project the PTV and define the area that has to be covered by the single pencil beam in each field. The overall field geometrical information was inherited from the RT and PT plans used for comparison. For the definition of the number and irradiation geometry of each VHEE pencil beam inside a given field, the only additional input needed was the beam angular divergence. A compact C-band technology was assumed, as in [13], capable of delivering such beams, and hence, an angular aperture of ~ (O mrad) with a negligible energy spread [6] was used when setting up the beam model for MC simulations.

The FWHM of each pencil beam was set to 1 cm, a reasonable value for electrons of such energy whose target is a deep-seated tumour and hence experience a significant broadening due to multiple scattering interactions. All these parameters are specific of the beam acceleration technique that has been assumed for the delivery of VHEE beams [6] and will have to be updated when exploring other solutions (e.g., VHEE from laser-plasma acceleration).

Once the size and spacing of each pencil beam were defined, their number was computed. Then, using a single pencil beam aiming at the centre of the PTV, the energy needed to place the absorbed dose peak at the centre of the PTV was computed. Two beam configurations were defined for each patient: three or seven fields for M1 and four or seven fields for C1, using the beam directions chosen for IMRT and PT plans. The energies needed to irradiate the two targets are shown in Table 3. In all cases, the energy was less than 150 MeV.

Such evaluations were conducted by means of an accurate FLUKA [19, 20] Monte Carlo (MC) simulation that used, as input, the patient's CT scan. The simulation that allowed us to evaluate the field energy was also used to build the absorbed dose map for each pencil beam of each field and eventually compute the dose maps used as inputs for the pencil beam fluence optimization algorithm.

To reduce the impact of statistical fluctuations on the absorbed dose distribution, each pencil beam simulation was performed using $10^6$ events. The robustness of the results was verified by changing the random seeds used for the simulation and obtaining absorbed dose maps that showed negligible discrepancies on the whole CT volume.

The absorbed dose maps, normalised to the number of primaries used in the simulation, for the plans with three and seven fields for patient M1 are shown in Figure 1. No treatment optimisation was performed in this case, i.e., the figures show the absorbed dose for pencil beams that contain $10^6$ electrons each which are the inputs for the optimisation step.

## 2.2 Treatment optimisation

Once the absorbed dose maps have been obtained performing MC simulations for each PB in the treatment plan, the fluence of each PB was optimised to ensure the required PTV coverage and OAR sparing. The implemented algorithms are similar to the previous prostate cancer study ([13]) and are similar to those used in the active scanning TPS used for PT [21]. A cost function with two terms was used: the first term constrains the absorbed dose in the PTV to the target value, while the other term is activated whenever a threshold in the OAR voxels is surpassed. Considering the different priorities when minimising the cost function, a weighing strategy was adopted when including the PTV, OARs, and normal tissue voxels, consistent with what has been carried out in standard software tools used for TPS planning (e.g., Pinnacle). The output of the optimisation process is the absorbed dose map used to

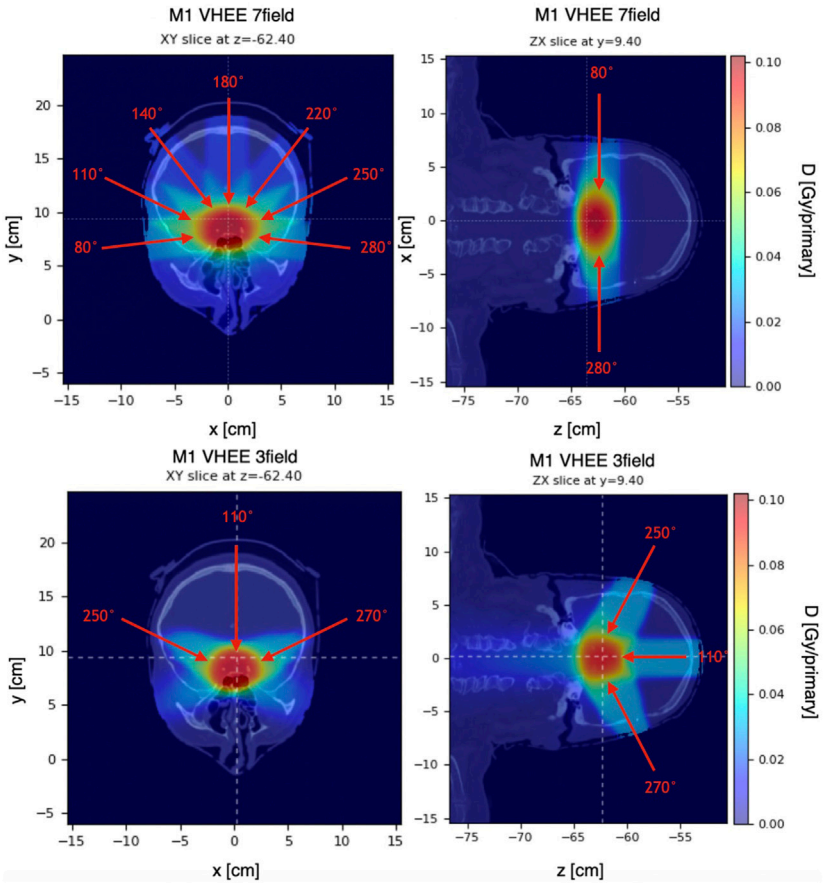


FIGURE 1
Absorbed dose distribution of M1, normalised to the number of primaries, used as an input for the optimisation process. Figures on the left show the configuration using three fields (proton-like), while the figures on the right show the configurations with seven fields (IMRT-like). All pencil beams have $10^6$ electrons.

compute dose volume histograms (DVHs) and compare with the standard RT and PT treatments.

The same fractionation scheme (with 2 Gy fractions) implemented in the delivered PT plans was adopted when optimising the IMRT and VHEE plans delivered in the conventional mode.

## 2.3 FLASH effect modelling

The first aim of our study is to compare absorbed dose distributions from IMRT and PT treatments with VHEE optimised plans, showing the potential of high-energy electrons for treatment planning without any potential gain from the ultra-high dose rate irradiation. Then, the possible impact of the FLASH effect in increasing the treatment efficacy [22, 23] was also studied. Particularly, the study focused on how the reduced damage in the OARs can be exploited to increase the prescription dose of the PTV, allowing for better tumour control. Therefore, the treatment delivery was assumed to satisfy the requirements of the dose rate (DR) that were needed to trigger the FLASH effect in OAR sparing (DR larger than 40 Gy/s).

To quantify the decrease in radiation-induced toxicity in normal tissues due to the FLASH approach, when comparing to conventional radiotherapy, the FLASH modifying factor (FMF) dependent on the absorbed dose in each voxel was implemented according to [24]. The FMF has been defined as proposed in [24]:

$$FMF = \frac{D_{CONV}}{D_{UHDR}}\Big|_{Isoeffect,}$$

and the dependence on the absorbed dose (D) was implemented, according to [24], as follows:

$$\mathrm{FMF}(D)_{\mathrm{FMF}^m,D_T} = 1 - \mathrm{FMF}^m \quad \frac{D_T}{D} + \mathrm{FMF}^m \quad \text{for} \quad \mathrm{D} > \mathrm{D_T}, \qquad (1)$$

while it was taken to be equal to 1 for $D \leq D_T$.

The parameters $D_T$ and $FMF^m$ that quantify the aforementioned threshold must be carefully selected to determine which significant contributions from the FLASH effect are expected and what is the asymptotic or maximal gain for the sparing of the OARs under study. In this manuscript, the absorbed dose to be used in FMF modelling was assumed to be the total absorbed dose associated with the treatment, whereas the $D_T$ value was fixed to 20 Gy. Such value amounts to nearly one-third of the whole treatment and has been chosen to signify that under real clinical conditions to trigger the FLASH effect, a sizeable dose needs to be absorbed by normal tissues in order to result in an appreciable sparing.

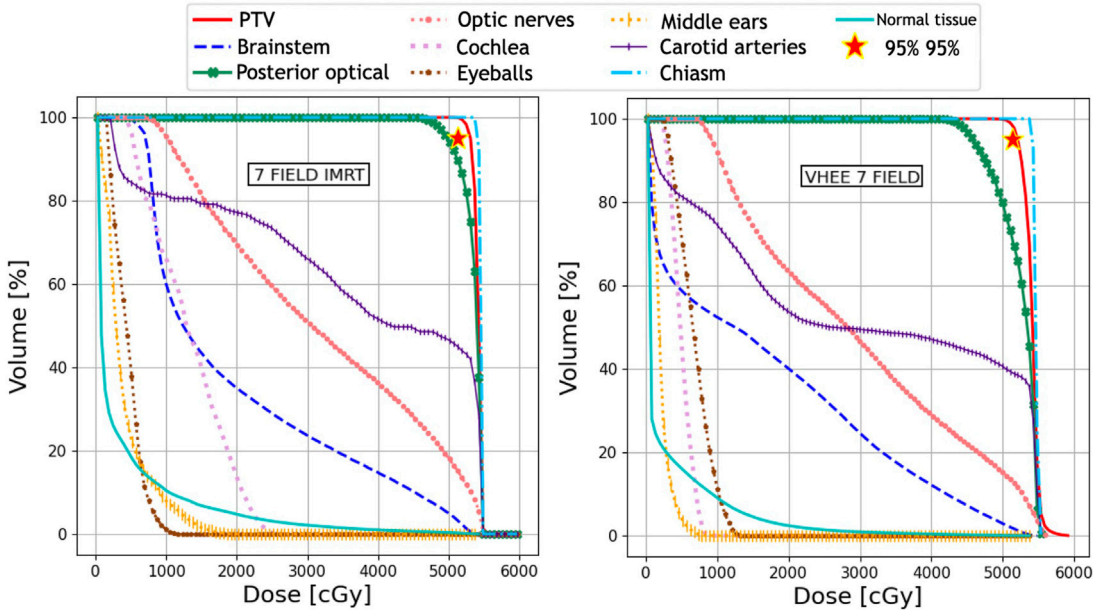


FIGURE 2
Plan comparison between IMRT and VHEE for patient M1. DVHs for the PTV and OARs from the IMRT plan are reported on the left, whereas the VHEE results obtained assuming an irradiation with seven fields are shown on the right. The absorbed dose relative to the unspecified normal tissue (NoT in the legend) is also shown.

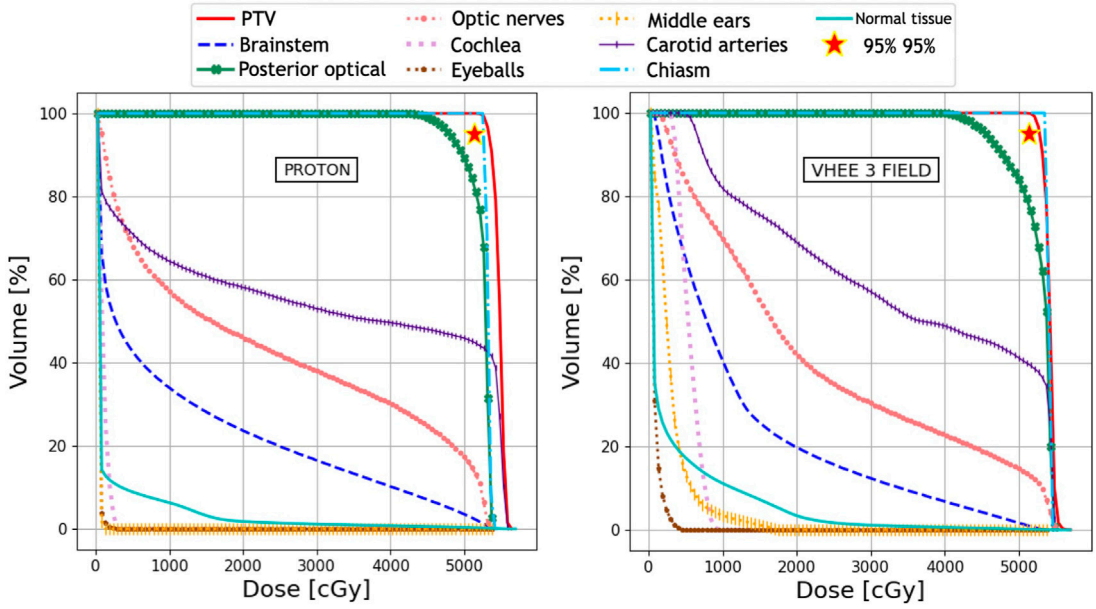


FIGURE 3
Plan comparison between PT and VHEE for patient M1. DVHs for the PTV and OARs from the PT plan are reported on the left, whereas the VHEE results obtained assuming an irradiation with three fields are shown on the right. The absorbed dose relative to the unspecified normal tissue (NoT in the legend) is also shown.

The actual values of $D_T$ and $\mathrm{FMF}^m$ that are used in a real case scenario are strongly dependent on the outcome of the ongoing experimental campaign that aims at defining the FLASH conditions in terms of the absorbed dose, dose rate, and fractionation schemes [10]. Therefore, $\mathrm{FMF}^m$ equal to 0.8 was chosen, a value that can be optimistically used at this moment to describe what can be expected as OAR sparing for internal organs during FLASH irradiations. Tissue-dependent values were not

**TABLE 4** Values of $V_{XX}$ and $D_1$ for the PTV and different OARs relevant to the planning of patient M1. Different columns show the values obtained from the proton, IMRT, VHEE with three fields, and VHEE with seven field . The result obtained for the carotid arteries is given in terms of $V_{105}$. All the obtained values satisfy the requirements shown in Table 1.

| M1 | Parameter | Proton | Photon | VHEE with three fields | VHEE with seven fields |
|---|---|---|---|---|---|
| PTV | $V_{95\%}$ | 100% | 99.30% | 98.97% | 97.00% |
| | $V_{105\%}$ | 0.01% | 0.009% | 0.05% | 1.27% |
| Optic nerves | $D_1$ | 52.98 Gy | 53.76 Gy | 54 Gy | 54 Gy |
| Chiasm | $D_1$ | 53.52 Gy | 54 Gy | 53.68 Gy | 53.71 Gy |
| Posterior optical path | $D_1$ | 53.58 Gy | 53.82 Gy | 53.94 Gy | 53.67 Gy |
| Eyeballs | $D_1$ | 1.25 Gy | 10.52 Gy | 3.30 Gy | 11.82 Gy |
| Brainstem | $D_1$ | 52.59 Gy | 51.99 Gy | 50.40 Gy | 51.02 Gy |
| Carotid arteries | $V_{105\%}$ | 0.03% | 9.11% | 2.54% | 1.16% |

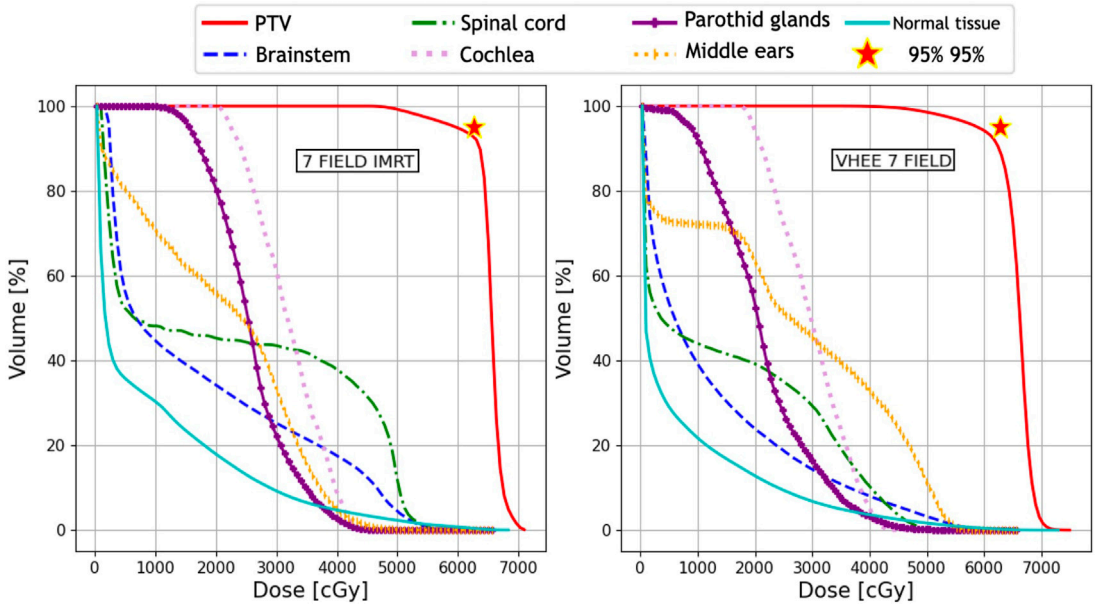


FIGURE 4
Plan comparison between IMRT and VHEE for patient C1. DVHs for the PTV and OARs from the IMRT plan are reported on the left, whereas the VHEE results obtained assuming an irradiation with seven fields are shown on the right. The absorbed dose relative to the unspecified normal tissue (NoT in the legend) is also shown.

implemented, and the same FMF value (computed accordingly to Eq. 1) was used for all the voxels that did not belong to the PTV and are either described as OARs or normal tissue (NoT).

The evaluation of the FLASH effect potential was performed after treatment optimisation. Once the final dose maps were available, the dose in each voxel was rescaled by the FMF from Eq. 1, and then the DVH calculation and evaluation of plan adequacy were re-assessed.

## 3 Results

The absorbed dose maps for the three techniques (IMRT, PT, and VHEE) were used to compute the DVHs and quantitatively compare the treatment plans. The DVH comparisons are shown in Figure 2 (IMRT vs. VHEE) and Figure 3 (PT vs. VHEE) for M1 and in Figure 4 (IMRT vs. VHEE) and Figure 5 (PT vs. VHEE) for C1.

For plan comparisons, VHEE plan optimisation was performed assuming the same field number and geometry (same gantry angle) as those adopted with the other radiotherapeutic techniques (see also Section 2.1).

The optimised dose maps for all the patients and radiation types are shown in Supplementary Appendix Figures S8, S9 which show the results, respectively, for M1 and C1 using IMRT, PT, and the different VHEE field geometries. The isodose curves are shown in Supplementary Appendix Figures S11, S12.

Figure 2 demonstrates that IMRT and VHEE plans have a comparable quality: while IMRT provides a better PTV coverage,

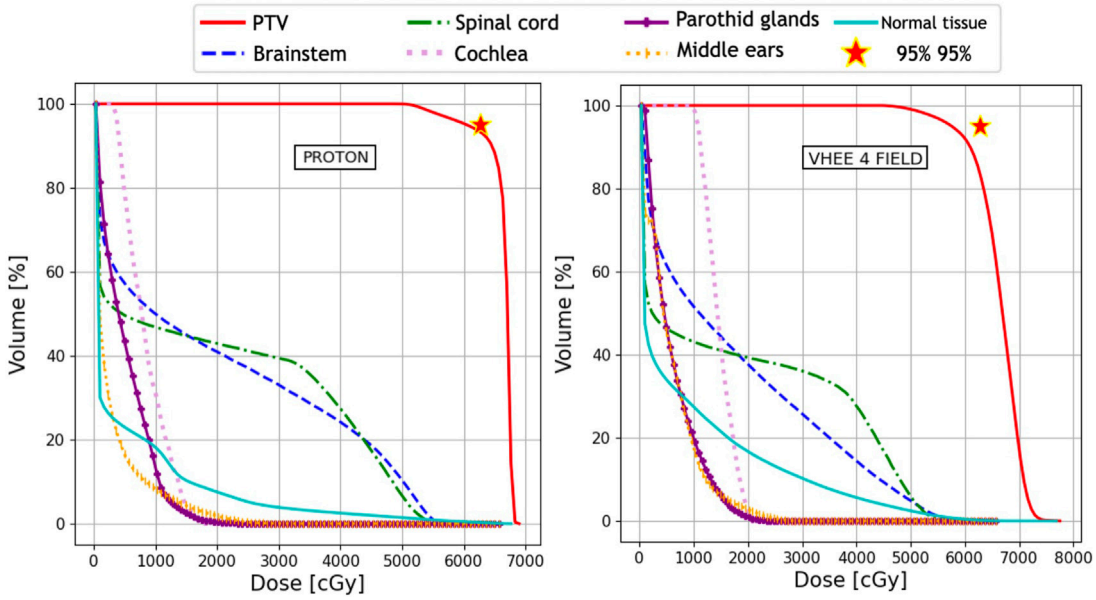


FIGURE 5
Plan comparison between PT and VHEE for patient C1. DVHs for the PTV and OARs from the PT plan are reported on the left, whereas the VHEE results obtained assuming an irradiation with four fields are shown on the right. The absorbed dose relative to the unspecified normal tissue (NoT in the legend) is also shown.

**TABLE 5 Values of $V_{XX}$, $D_{mean}$, and $D_1$ for the PTV and different OARs relevant for the planning of patient C1. Different columns show the values obtained from the proton, IMRT, VHEE with four fields, and VHEE with seven fields plans. All the obtained values satisfy the requirements shown in Table 2.**

| C1 | Constraint | Proton | Photon | VHEE with four fields | VHEE with seven fields |
|---|---|---|---|---|---|
| PTV boost | $V_{95\%}$ | 93.57% | 92.96% | 85.52% | 90.61% |
| | $V_{105\%}$ | 0% | 3.05% | 28.32% | 6.12% |
| Brainstem | $D_1$ | 54.64 Gy | 53.79 Gy | 55.04 Gy | 55.15 Gy |
| Spinal cord | $D_1$ | 53.39 Gy | 54.04 Gy | 53.54 Gy | 47.77 Gy |
| Parotid glands | $D_{mean}$ | 4.74 Gy | 25.29 Gy | 5.73 Gy | 20.82 Gy |
| Middle ears | $D_{mean}$ | 2.63 Gy | 20.63 Gy | 5.40 Gy | 25.94 Gy |
| Cochlea | $D_{mean}$ | 7.98 Gy | 31.54 Gy | 14.32 Gy | 29.39 Gy |

the VHEE irradiation is better at sparing the cochlea. In addition, Figure 3 shows that the VHEE configuration with three fields provides a better PTV coverage than the configurations with seven fields, matching the performance of the PT plan. A quantitative analysis supporting these statements is shown in Table 4, where the values of interest for evaluating the plan goodness are shown for all the M1 treatment plans.

C1 is a more complex case where OAR sparing limits the PTV coverage for all plans. For this reason, priority was given to limit the absorbed dose to the brainstem and spinal cord even if this meant not reaching the desired PTV coverage. For this patient, the DVH analysis of the VHEE configurations with four and seven fields, as shown in Figure 4 and Figure 5, indicates that increasing the number of fields can help in improving the target coverage: the PTV boost coverage shown in the first row in terms of $V_{95\%}$ increases from 85.5% to 90.6%.

The values of $V_{XX}$, $D_{mean}$, and $D_1$ that are used to evaluate the C1 plan are shown in Table 5. Although VHEEs achieve a lower coverage of the PTV, they also result in a better sparing of the spinal cord. The comparison between the irradiation with four and seven fields clearly shows that different geometries can be explored to provide a better sparing of given OARs, and as an example, it is possible to observe that the ear canals, the cochlea, and the parotid glands receive a significantly different mean dose in the two cases.In summary it is possible to conclude that all plans obtained with PT, IMRT, and VHEE, both for M1 and C1, satisfy the constraints and are compatible with the clinical prescriptions.

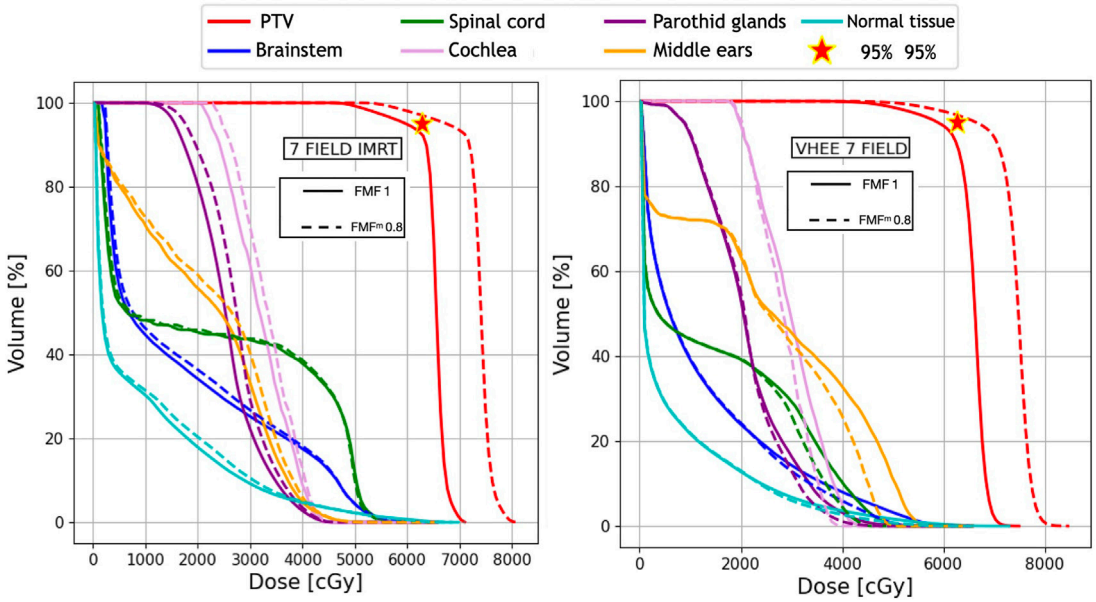


FIGURE 6
Plan comparison between IMRT and VHEE for patient C1. The biological dose relative to an $FMF^m$ of 0.8 is shown in dashed lines. DVHs for the PTV, OARs, and NoT from the IMRT plan are reported on the left, whereas the VHEE results obtained assuming an irradiation with seven fields (see Table 3) are shown on the right.

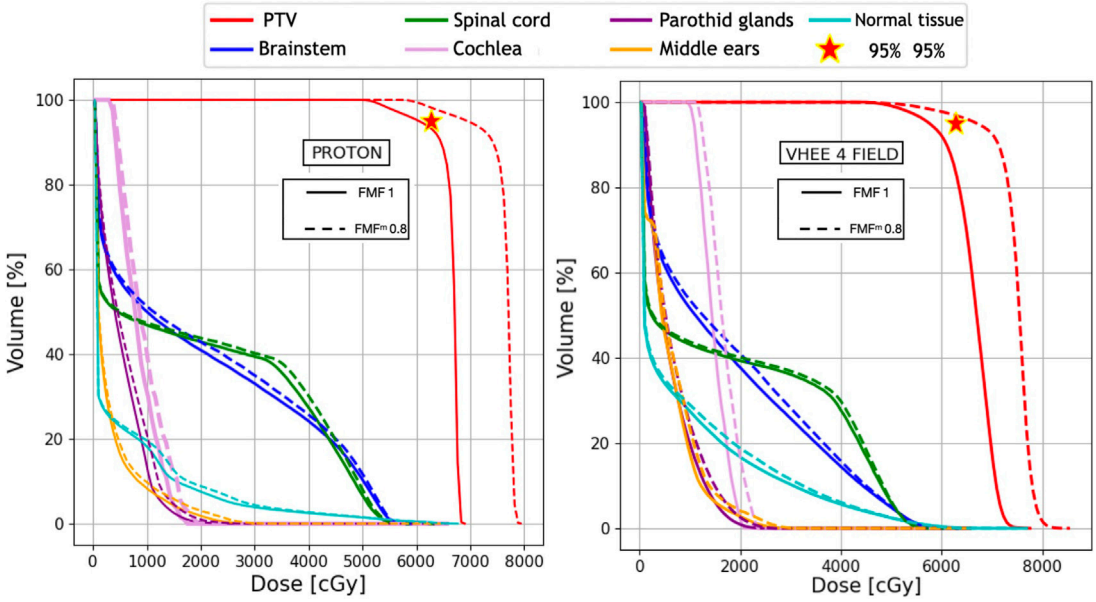


FIGURE 7
Plan comparison between PT and VHEE for patient C1. The biological dose relative to an $FMF^m$ of 0.8 is shown in dashed lines. DVHs for the PTV, OARs, and NoT from the PT plan are reported on the left, whereas the VHEE results obtained assuming an irradiation with four fields (see Table 3) are shown on the right.

## 3.1 FLASH effect impact

The optimised plans have also been used to evaluate the potential of FLASH irradiation. Thus, the absorbed dose maps for each plan have been processed, and the absorbed dose in each voxel not belonging to the PTV has been multiplied by the FMF(D) value computed according to Eq. 1. In this way, the sparing of the OARs due to the FLASH effect was accounted for and DVHs

**TABLE 6** Values of $V_{XX}$, $D_{mean}$, and $D_1$ obtained after considering the reduced biological dose due to FMF(D) sparing of patient M1. $V_{105\%}$ relative to the carotid arteries becomes negligible and it is not shown.

| M1 | Constraint | Proton | IMRT | VHEE with three fields | VHEE with seven field |
|---|---|---|---|---|---|
| PTV | $V_{95\%}$ | 100% | 99.30% | 98.97% | 97.00% |
| | $V_{105\%}$ | 0.01% | 0.009% | 0.05% | 1.27% |
| Optic nerves | $D_1$ Gy(FMF) | 46.39 | 47.51 | 47.64 | 47.29 |
| Chiasm | $D_1$ Gy(FMF) | 47.47 | 46.81 | 47.38 | 47.36 |
| Posterior optical path | $D_1$ Gy(FMF) | 46.86 | 47.47 | 47.59 | 47.26 |
| Eyeballs | $D_1$ Gy(FMF) | 1.25 | 9.73 | 3.34 | 11.98 |
| Brainstem | $D_1$ Gy(FMF) | 46.07 | 45.94 | 44.74 | 43.77 |

**TABLE 7** Values of $V_{XX}$, $D_{mean}$, and $D_1$ obtained after considering the reduced biological dose due to FMF(D) sparing of patient C1, and an overall absorbed dose scaling is applied to increase the PTV coverage while maintaining the dose inside the OARs under an affordable limit.

| C1 | Constraint | PROTON | IMRT | VHEE with four fields | VHEE with seven fields |
|---|---|---|---|---|---|
| PTV boost | $V_{95\%}$ | 97.71% | 96.65% | 96.58% | 96.43% |
| | $V_{105\%}$ | 95.27% | 92.84% | 91.04% | 93.08% |
| Brainstem | $D_1$ Gy(FMF) | 54.85 | 54.79 | 54.76 | 54.37 |
| Spinal cord | $D_1$ Gy(FMF) | 53.69 | 53.41 | 53.39 | 47.70 |
| Parotid glands | $D_{mean}$ Gy(FMF) | 5.44 | 27.23 | 6.53 | 22.67 |
| Middle ears | $D_{mean}$ Gy(FMF) | 3.02 | 21.86 | 6.14 | 26.69 |
| Cochlea | $D_{mean}$ Gy(FMF) | 9.06 | 33.02 | 16.33 | 31.07 |

were re-evaluated. The impact of the FLASH effect on sparing the OARs, according to the assumptions made here previoulsy, can be observed in DVHs shown in Figure 6 and Figure 7.

Table 6 shows the results obtained for patient M1. In this case, as the PTV coverage is already satisfactory without invoking the FLASH effect, the latter would produce an additional reduction of the dose absorbed by OARs and therefore resulting in additional OAR sparing. When compared to Table 4, it is possible to observe the significant reduction in $D_1$, from 55 to 47 Gy(RBE), for the OARs that are located close to the PTV. DVHs are computed by taking into account FLASH sparing, as shown in the Appendix, in Supplementary Appendix Figure S10.

For C1, where the PTV coverage is limited by the dose constraints on the OARs, a different approach was followed: the $D_1$ values were computed once the FLASH effect was applied, and then the overall dose was rescaled until the limit on OAR sparing (54 Gy) was reached. Under that condition, the PTV coverage was assessed to determine the net increase that could be achieved by exploiting the FLASH effect. The results are shown in Figure 6 and Figure 7, respectively, for IMRT compared with VHEE using seven irradiation fields and PT compared with VHEE using four irradiation fields.

The results obtained for patient C1 are shown in Table 7, demonstrating that the additional OAR sparing provided by the FLASH effect could be exploited to increase the PTV coverage when treating such lesions. Profiting from the reduced absorbed dose, it was possible to reach a PTV coverage with $V_{95\%}$ larger than 95% while satisfying the dose limits on the brainstem. The irradiation using seven fields, in this case, provides a PTV coverage comparable with the irradiation achievable with four fields but, in addition, allows for better sparing of the spinal cord.

## 4 Discussion

The potential of VHEE irradiations of intracranial lesions using a small number (between three and seven) of mono-energetic fields and assuming an active-scanning-like beam delivery strategy has been explored.

VHEE with maximum energy of 130 MeV were found to be suitable for the treatment of deep-seated tumours in disease sites with difficult irradiation geometries, allowing a limited number of fields to achieve performances comparable with PT and IMRT. This result, obtained under the assumption of a conventional dose rate, is promising in itself, as it suggests that compact electron accelerators could provide appropriate treatment quality at an affordable cost and with minimal impact on the infrastructures [25], thus providing a valid alternative to PT and IMRT treatments.

The VHEE plans obtained with different irradiation geometries demonstrated that there is a significant room for improvement when

trying to optimise not only the beam fluence to cover the target volume but also the field geometry and its energy. The lack of experience in planning treatments with electrons makes it hard to assess if the best possible configurations are the configurations already tested in this manuscript, without an automated tool that can systematically explore the different number of fields, irradiation directions, and beam energies like what is currently performed for photons and protons. The full potential of VHEE will be reassessed once such tool will finally be available.

The beam scanning method used for VHEE treatments allowed us to reach the desired absorbed dose conformity to the PTV while maintaining each field mono-energetic. This condition plays a crucial role when discussing the suitability of VHEE to be used for FLASH therapy irradiations; since there is no need to change the energy within a field, each field can be delivered in a very short time (no more than a few hundred ms), making it easier to achieve an Ultra-High Dose Rate (UHDR) regime. The technological challenge of delivering more than one field in a very short period of time required to ensure FLASH sparing of the OARs is to be addressed yet, but one thing that VHEE plans have in common with proton plans is especially the number of fields that have to be delivered is, in some cases, identical (e.g., the case of M1).

The potential impact of FLASH in terms of OAR sparing has been explored as well, under reasonable assumptions that a maximum sparing effect between 20% and 35% could be achieved, whenever the total absorbed dose in each voxel exceeded the 20 Gy threshold. Meanwhile, although the values of $FMF^n$ and $D_T$ still need an extensive experimental characterisation and have been assumed to be constant against different types of tissues and independent of the dose rate, the results show that the additional sparing obtained from UHDR would be helpful in improving OAR sparing (e.g., in the case of M1) or allowing for dose escalation that could be used to improve the PTV coverage (as in the case of C1). In both cases, the FLASH effect could be exploited to improve the treatment efficacy, broadening the therapeutic window of the treatment. Both pancreatic cancer and lung cancer seem to be particularly interesting in this respect: hypo-fractionation regimes have already been explored for such treatments, thus representing good candidates to account for the dose and dose rate dependencies of the FMF in a realistic clinical scenario.

The rather basic handling of FLASH effect modelling implemented in this study follows the limited experimental knowledge of the conditions needed to trigger OAR sparing. In this work, no dependence of the FMF on the tissue type or the dose rate was considered. The comparison of the results obtained with FMF equal to 1 (no FLASH effect) and implementing an FMF that has a dose-dependence based on real data with an asymptotic value of 0.8 allow for evaluating the FLASH potential under a robust, well-defined condition that reflects the current best experimental description of the effect. As no fractionation scheme compatible with UHDR irradiations is currently available, for the irradiation of intracranial lesions, we have also decided to maintain the plan constraints coming from the conventional fractionation scheme (2 Gy per fraction). The results presented are not aiming at evaluating which plan, among RT, PT, and VHEE, is the best for the treatment of the specific intracranial lesions used for the simulation study. Instead the main purpose of the presented study is to allow a robust and fair evaluation of the VHEE potential both in conventional and UHDR irradiation modalities.

A refined experimental input, and a better modelling of the FMF, when available, will be used to improve the evaluations presented in this contribution, allowing for a better estimate of the FLASH therapy advantages achievable in a clinical scenario.

## 5 Conclusion

The treatment of intracranial lesions with VHEE has been explored. VHEEs were compared against IMRT and PT plans for two patients previously treated with protons, and the results demonstrated that VHEE can achieve performances that are comparable with the state-of-the-art irradiation techniques even in the absence of additional sparing provided by the FLASH effect.

Considering that the VHEE mono-energetic beam interaction with the patient's tissue results in an absorbed dose distribution that exhibits a very broad peak, and that FLASH rates have already been demonstrated to be deliverable for low-energy electron applications (IOeRT [26, 27]), it was also possible to explore the additional increase that could be achieved when switching to a UHDR configuration. The results demonstrate that under reasonable assumptions on the conditions needed to trigger the FLASH effect, and on its actual value, the FLASH effect could effectively be used to reduce the impact on the OARs surrounding the PTV or to improve the PTV coverage, depending on the actual characteristics of the target volume and the constraints on the OARs crossed by the beam. In all cases and for all particle types, the FLASH effect showed a clear potential in significantly improving the therapeutic window of EBRT treatments.

## Data availability statement

The raw data supporting the conclusions of this article will be made available by the authors, without undue reservation.

## Ethics statement

Ethical review and approval was not required for the study on human participants, and written informed consent for participation was obtained.

## Author contributions

ASar, AM, AdG, MS, GF, MP, ASch, and VP wrote the main manuscript text. ASar, MS, GF, MM, and ASch prepared the figures. LC, DC, FdF, CdF, MP, MS, SS, and VT provided information about the dosimetric constraints that plans have to satisfy and the treatment plans with photons and protons. GB, YD, IM, RM, LP, SM, and MT defined the dose-modifying factor modelling inside the optimisation algorithms. LP, ASch, ASci, and ASar provided information about the beam model to be used in the Monte Carlo simulations. LA, MdS, IM, RM, SM, VP, LR, DR, ASar, ASch, GT, MT, and AT implemented the simulation, optimization algorithms, and performed the data analysis. All

authors contributed to the article and approved the submitted version.

## Funding

The work presented here was partially funded by the FRIDA INFN CSN5 project and by the regional funding of POR FESR Lazio 2014–2020—ROT. A0375-2020-36748—Avviso Pubblico "Gruppi di ricerca 2020."

## Conflict of interest

ASa and VPa participated in research projects funded by the company Sordina IORT Technologies (SIT). The research was also funded by the royalties of the TPS system developed for the SIT IOeRT machine.

The remaining authors declare that the research was conducted in the absence of any commercial or financial relationships that could be construed as a potential conflict of interest.

The reviewer OS declared a past co-authorship with the authors MDS to the handling Editor.

## Publisher's note



## Supplementary material

The Supplementary Material for this article can be found online at: https://www.frontiersin.org/articles/10.3389/fphy.2023.1185598/full#supplementary-material

## References

1. Bazalova-Carter M, Qu B, Palma B, Hårdemark B, Hynning E, Jensen C, et al. Treatment planning for radiotherapy with very high-energy electron beams and comparison of vhee and vmat plans. *Med Phys* (2015) 42:2615–25. doi:10.1118/1.4918923

2. Schüler E, Eriksson K, Hynning E, Hancock SL, Hiniker SM, Bazalova-Carter M, et al. Very high-energy electron (vhee) beams in radiation therapy; treatment plan comparison between vhee, vmat, and ppbs. *Med Phys* (2017) 44:2544–55. doi:10.1002/mp.12233

3. Krim D, Rrhioua A, Zerfaoui M, Bakari D. Monte Carlo modeling of focused very high energy electron beams as an innovative modality for radiotherapy application. *Nucl Instr Methods Phys Res Section A: Acc Spectrometers, Detectors Associated Equipment* (2023) 1047:167785. doi:10.1016/j.nima.2022.167785

4. Ronga MG, Cavallone M, Patriarca A, Leite AM, Loap P, Favaudon V, et al. Back to the future: Very high-energy electrons (vhees) and their potential application in radiation therapy. *Cancers* (2021) 13. doi:10.3390/cancers13194942

5. Maxim PG, Tantawi SG, Loo BW. Phaser: A platform for clinical translation of flash cancer radiotherapy. *Radiother Oncol* (2019) 139, 28–33. FLASH radiotherapy International Workshop. doi:10.1016/j.radonc.2019.05.005

6. Giuliano L, Bosco F, Carillo M, Arcangelis D, Ficcadenti L, Migliorati M, et al. *Preliminary studies of a compact vhee linear accelerator system for flash radiotherapy* (2021). doi:10.18429/JACoW-IPAC2021-MOPAB410

7. Venkatesulu BP, Sharma A, Pollard-Larkin JM, Sadagopan R, Symons J, Neri S, et al. Author correction: Ultra high dose rate (35 gy/sec) radiation does not spare the normal tissue in cardiac and splenic models of lymphopenia and gastrointestinal syndrome. *Scientific Rep* (2020) 10:1. doi:10.1038/s41598-020-67913-7

8. Bourhis J, Montay-Gruel P, Gonçalves Jorge P, Bailat C, Petit B, Ollivier J, et al. Clinical translation of flash radiotherapy: Why and how? *Radiother Oncol* (2019) 139, 11–7. FLASH radiotherapy International Workshop. doi:10.1016/j.radonc.2019.04.008

9. Bourhis J, Sozzi WJ, Jorge PG, Gaide O, Bailat C, Duclos F, et al. Treatment of a first patient with flash-radiotherapy. *Radiother Oncol* (2019) 139, 18–22. FLASH radiotherapy International Workshop. doi:10.1016/j.radonc.2019.06.019

10. Vozenin MC, Bourhis J, Durante M. Towards clinical translation of flash radiotherapy. *Nat Rev Clin Oncol* (2022) 19:791–803. Cited By 2. doi:10.1038/s41571-022-00697-z

11. Montay-Gruel P, Corde S, Laissue JA, Bazalova-Carter M. Flash radiotherapy with photon beams. *Med Phys* (2022) 49:2055–67. doi:10.1002/mp.15222

12. Zhang G, Zhang Z, Gao W, Quan H. Treatment planning consideration for very high-energy electron flash radiotherapy. *Physica Med* (2023) 107:102539. doi:10.1016/j.ejmp.2023.102539

13. Sarti A, De Maria P, Battistoni G, De Simoni M, Di Felice C, Dong Y, et al. Deep seated tumour treatments with electrons of high energy delivered at flash rates: The example of prostate cancer. *Front Oncol* (2021) 11. doi:10.3389/fonc.2021.777852

14. Narayanasamy G, Saenz D, Cruz W, Ha CS, Papanikolaou N, Stathakis S. Commissioning an elekta versa hd linear accelerator. *J Appl Clin Med Phys* (2016) 17:179–91. doi:10.1120/jacmp.v17i1.5799

15. Xia P, Murray E. 3d treatment planning system—Pinnacle system. *Med Dosimetry* (2018) 43:118–28. Special Issue: 3D Treatment Planning Systems. doi:10.1016/j.meddos.2018.02.004

16. Rahman M, Trigilio A, Franciosini G, Moeckli R, Zhang R, Böhlen TT. Flash radiotherapy treatment planning and models for electron beams. *Radiother Oncol* (2022) 175:210–21. doi:10.1016/j.radonc.2022.08.009

17. Poppinga D, Kranzer R, Farabolini W, Gilardi A, Corsini R, Wyrwoll V, et al. Vhee beam dosimetry at cern linear electron accelerator for research under ultra-high dose rate conditions. *Biomed Phys Eng Express* (2020) 7:015012. doi:10.1088/2057-1976/abcae5

18. Labate L, Palla D, Panetta D, Avella F, Baffigi F, Brandi F, et al. Toward an effective use of laser-driven very high energy electrons for radiotherapy: Feasibility assessment of multi-field and intensity modulation irradiation schemes. *Scientific Rep* (2020) 10. doi:10.1038/s41598-020-74256-w

19. Ferrari A, Sala PR, Fasso A, Ranft J. *Fluka: A multi-particle transport code (program version 2005)* (2005). *CERN-2005-010, SLAC-R-773, INFN-TC-05-11*.

20. Battistoni G, Bauer J, Boehlen TT, Cerutti F, Chin MPW, Dos Santos Augusto R, et al. The fluka code: An accurate simulation tool for particle therapy. *Front Oncol* (2016) 6:116. doi:10.3389/fonc.2016.00116

21. Schaffner B, Pedroni E, Lomax A. Dose calculation models for proton treatment planning using a dynamic beam delivery system: An attempt to include density heterogeneity effects in the analytical dose calculation. *Phys Med Biol* (1999) 44:27–41. doi:10.1088/0031-9155/44/1/004

22. Wilson JD, Hammond EM, Higgins GS, Petersson K. Ultra-high dose rate (flash) radiotherapy: Silver bullet or fool's gold? *Front Oncol* (2020) 9:1563. doi:10.3389/fonc.2019.01563

23. Wilson JD, Hammond EM, Higgins GS, Corrigendum PK. Ultra-high dose rate (flash) radiotherapy: Silver bullet or fool's gold? *Front Oncol* (2020) 10:210. doi:10.3389/fonc.2020.00210

24. Bohlen TT, Germond JF, Bourhis J, Vozenin MC, Ozsahin EM, Bochud F, et al. Normal tissue sparing by flash as a function of single-fraction dose: A quantitative analysis. *Int J Radiat Oncol Biol Phys* (2022) 114:1032–44. A Red Journal Special IssueOligometastasis, Part 2. doi:10.1016/j.ijrobp.2022.05.038

25. Faillace L, Alesini D, Bisogni G, Bosco F, Carillo M, Cirrone P, et al. Perspectives in linear accelerator for flash vhee: Study of a compact c-band system. *Physica Med* (2022) 104:149–59. doi:10.1016/j.ejmp.2022.10.018

26. Felici G, Barca P, Barone S, Bortoli E, Borgheresi R, De Stefano S, et al. Transforming an iort linac into a flash research machine: Procedure and dosimetric characterization. *Front Phys* (2020) 8. doi:10.3389/fphy.2020.00374

27. Calvo FA, Serrano J, Cambeiro M, Aristu J, Asencio JM, Rubio I, et al. Intraoperative electron radiation therapy: An update of the evidence collected in 40 years to search for models for electron-flash studies. *Cancers* (2022) 14. doi:10.3390/cancers14153693

frontiers | Frontiers in Physics

TYPE Original Research
PUBLISHED 08 August 2023
DOI 10.3389/fphy.2023.1215422



OPEN ACCESS

EDITED BY
Emanuele Scifoni,
Universities and Research, Italy

REVIEWED BY
Andrea Attili,
National Institute of Nuclear Physics of Rome, Italy
Mark A. Hill,
University of Oxford, United Kingdom

*CORRESPONDENCE
Alexander Baikalov,
a.baikalov@tum.de

RECEIVED 01 May 2023
ACCEPTED 20 July 2023
PUBLISHED 08 August 2023

CITATION
Baikalov A, Abolfath R, Schüler E, Mohan R, Wilkens JJ and Bartzsch S (2023), Intertrack interaction at ultra-high dose rates and its role in the FLASH effect. *Front. Phys.* 11:1215422. doi: 10.3389/fphy.2023.1215422



# Intertrack interaction at ultra-high dose rates and its role in the FLASH effect

Alexander Baikalov[1,2,3]*, Ramin Abolfath[3], Emil Schüler[3,4], Radhe Mohan[3], Jan J. Wilkens[1] and Stefan Bartzsch[1,2]

[1]Department of Radiation Oncology, School of Medicine and Klinikum rechts der Isar, Technical University of Munich, Munich, Germany, [2]Institute of Radiation Medicine, Helmholtz Zentrum München GmbH, German Research Center for Environmental Health, Neuherberg, Germany, [3]Department of Radiation Physics, The University of Texas MD Anderson Cancer Center, Houston, TX, United States, [4]Graduate School of Biomedical Sciences, University of Texas, Houston, TX, United States

**Background:** The mechanism responsible for the FLASH effect remains undetermined yet critical to the clinical translation of FLASH radiotherapy. The potential role of intertrack interactions in the FLASH effect, arising from the high spatio-temporal concentrations of particle tracks at UHDRs, has been widely discussed but its influence is unknown.

**Methods:** We construct an analytical model of the distribution, diffusive evolution, and chemical interaction of particle tracks in an irradiated target. We fit parameters of the model to Monte Carlo (MC) simulations of electron tracks, and include the effects of scavenging capacities of different target media. We compare the model's predictions to MC simulations of many interacting electron tracks, and use the comparison to predict the prevalence of intertrack interactions in the parameter space where the FLASH effect is observed *in vivo*, and where differential reactive species (RS) yields have been observed *in aqua*.

**Results:** MC simulations of interacting electron tracks demonstrate negligible changes in RS yields at 12 Gy both in oxygenated water and in cellular scavenging conditions, but significant changes at 58 Gy in oxygenated water. The model fits well to the simulation data, and predicts that pulse doses $>90$ Gy delivered in 0.5 $\mu$s would be necessary for intertrack interactions to affect RS yields in cellular scavenging conditions, and $>13$ Gy in 0.5 $\mu$s for water at 4% $O_2$. The model defines optimal beam parameters (e.g., dose, pulse width, LET) to maximize intertrack interactions, and indicates that decreasing the pulse width of electron pulses further below $\approx$0.5 $\mu$s has no effect on intertrack interactions.

**Conclusion:** The results of the MC simulations indicate that intertrack interactions do not play a role in the parameters space where the FLASH effect is observed. However, potentially critical limitations in the simulations performed provide the possibility that intertrack interactions occur much more readily than predicted. More accurate simulations, as well as experimental characterization of RS yields across the pulse parameter space, are necessary to more confidently confirm or deny the role of intertrack interactions in the FLASH effect.

KEYWORDS

**FLASH radiotherapy, ultra-high dose rate, intertrack interaction, normal tissue sparing, oxygen, mechanism, simulation, model**

# 1 Introduction

The past decade has witnessed a surge in investigations into the effects of high dose rate irradiation on tissue toxicity. Many *in vitro* and *in vivo* studies have reported a "FLASH effect", that is, normal tissue sparing by irradiation at ultra-high dose rates (UHDRs, $>40$ Gy/s) relative to conventional dose rates (CDRs, ≈0.01 Gy/s) while maintaining equivalent tumor control probability [1–4]. UHDR FLASH radiation therapy holds the potential for substantial improvements to clinical radiotherapy. Understanding the mechanisms underlying the FLASH effect is paramount for establishing the beam parameters needed to reproducibly and optimally elicit the FLASH effect while avoiding potential side effects.

The time scale of FLASH irradiations hints at the source of the FLASH effect. Induction of the FLASH effect has been linked to a decrease in the overall irradiation time to less than 0.5 s. Examining the spatial and temporal separation of particle tracks for a typical electron FLASH delivery[1], direct physical interactions of individual tracks, which take place in ps after irradiation and in a few nm around each track, are probably unaffected. Biological responses, although certainly subsequently affected by FLASH irradiation, are also unlikely to be the direct source of the FLASH effect, as they occur at much larger time scales (e.g., after ms for DNA repair [6]). Chemical interactions though, which take place on the ns − ms and $\mu$m scales, could be sensitive to this change in beam parameters. This hypothesis is supported by a long history of experiments demonstrating a dose rate dependence of chemical radiolysis yields in water in this parameter space [7]. However, the effect of the cellular chemical environment on these reactions as opposed to a pure water environment must not be neglected [7].

Many potential chemical mechanisms of normal tissue sparing at UHDR have since been proposed, mostly pertaining to the modified reaction kinetics of radiolytic reactive species between CDRs and UHDRs [8–18]. Theoretical models and experimental data have been presented to both support and refute these mechanisms, although no proposed mechanism has been proven valid to date [19, 20].

From a chemical perspective, irradiation of a biological target comprises the spatially and temporally separated arrival of multiple particle tracks, each consisting of a trail of radiolytic reactive species (RS) (Figure 1). The RS of a track diffuse and interact with each other and their immediate environment (e.g., water, dissolved oxygen, cellular antioxidants, cellular macromolecules), resulting in the simultaneous spatial expansion and concentration decay of the track (Figure 2). Traditionally, at CDRs, each track is assumed to evolve independently of other tracks; i.e., the chemical influence of the track on its immediate environment does not affect that of any other tracks as their arrivals are greatly separated by time. However, at UHDRs, the temporal separation of tracks is substantially reduced, and the assumption that individual tracks evolve independently of each other breaks down [12, 22]. In this case, the effect of one track on its immediate environment may indirectly affect the dynamics of a following or neighboring track by, for example, transient local oxygen depletion. Alternatively, the RS of one track may directly interact with the RS of another track (intertrack interaction). In either case, the resulting chemical yields no longer depend solely on the deposited dose, but now also depend on the dose rate.

Discussion of intertrack effects on high dose rate radiation chemistry [23–25] began long before its more recent discussions in the context of a FLASH mechanism [12, 22, 26–31]. The effect is commonly investigated by Monte Carlo (MC) simulation of varying spatio-temporal distributions of particle tracks and their resulting RS yields [22, 29, 31]. MC simulations suffer from high computational load, often limiting the extent of the analyses to short time scales ($\leq 1$ $\mu$s), which may neglect relevant interactions of longer-lived RS, and to small spatial scales of only a few adjacent tracks, neglecting the full 3D distribution of tracks and their overlaps. MC simulations are also typically done in a pure water medium, neglecting the chemical scavenging effects of the full cellular environment.

Here, we seek to answer the question of to what extent intertrack interactions occur in the parameter space where the FLASH effect is observed. Our model addresses the shortcomings of the aforementioned approaches by 1) taking an analytical approach, thereby avoiding the computational burden of MC simulations and 2) incorporating the effects of the cellular chemical environment. The spatio-temporal distribution, evolution, and interaction of tracks are presented as a function of beam parameters, and the implications of intertrack interactions on the radiation chemistry of the irradiated target are discussed.

# 2 Methods

We began by developing a model that geometrically describes the initial distributions of RS around tracks in an irradiated target, their evolution, and their chemical interactions. We used MC simulations of electron tracks for fitting certain parameters of this model, and we used the completed model to predict the influence of intertrack interactions in an irradiated target as a function of beam parameters (e.g., dose, dose rate, linear energy transfer [LET]) and the scavenging capacity of the target medium. Finally, we compared the model's predictions to MC simulations of interacting tracks and to experimental data in *aqua* and *in vivo* conditions.

## 2.1 Development of a model of track interaction

### 2.1.1 Track definition

In this model, particle tracks are assumed to be perfectly straight and homogeneous along the beam axis, and can thus be described in the 2-dimensional plane orthogonal to the beam axis with the

1 For comparison, we examine an *in vivo* study by Montay-Gruel et al. in which mice were exposed to a total of 10 Gy from a 100 Hz, 1.8 $\mu$s pulse-width pulsed electron beam [5]. Induction of the FLASH effect was observed when the beam parameters changed from roughly 50 0.2 Gy pulses to 17 0.6 Gy pulses. From the dimensions of the target we can estimate an average deposition of 1.28 nGy per primary electron. Within each pulse, this corresponds to an increase of 6–19 electrons per $\mu m^{-2}$ and 87 to 260 electrons per ps. The temporal spacing between pulses remained constant at 10 ms.

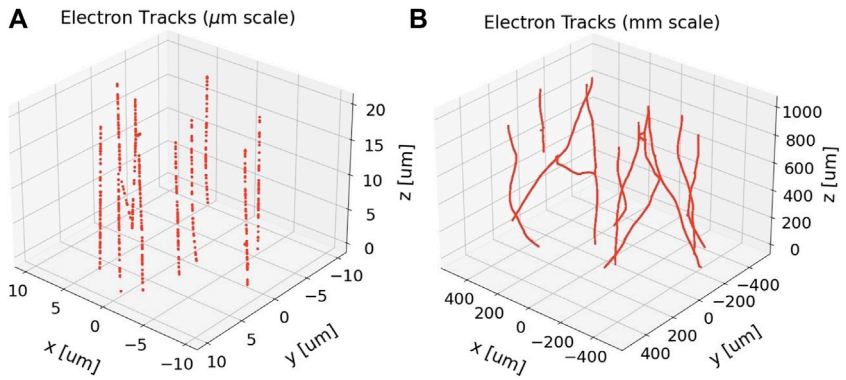


FIGURE 1
Reactive species (red points) produced by 10 uniformly-randomly distributed 1 MeV electron tracks at 1 ps after passage of the primary electrons, before any species diffusion processes are simulated. The electrons were set to impinge on a cylindrical simulation volume with length and diameter both at **(A)** 20 $\mu$m and **(B)** 1 mm. The beam axis is the $z$-axis. This energy was chosen owing to the high-energy limit of 1 MeV of the electron physics processes in the simulation toolkit used, TOPAS n-Bio [21], but is nonetheless clinically relevant as higher energy electrons would have even straighter tracks. The differences in straightness along each track at these different spatial scales is evident. For reference, the particle fluence depicted in **(A)** is approximately 2.5 × $10^5$ times lower than the expected particle fluence from 10 Gy in the whole brain irradiation study by Montay-Gruel et al. [5].

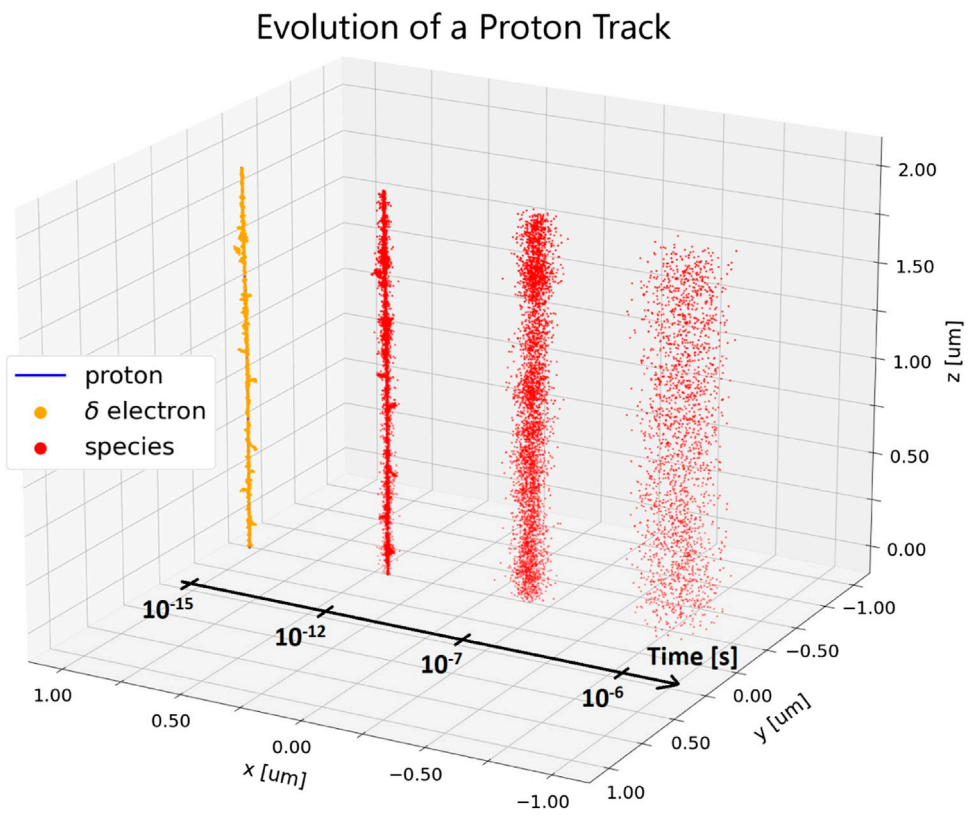


FIGURE 2
A small section of a simulated proton track in a 2 $\mu$s side length pure water cube. The energy and LET of the proton within this volume are 1 MeV and 26 keV/$\mu$m, respectively. At $10^{-15}$s, the individual ionization events of the primary proton (blue, hidden) and its secondary electrons (yellow) are shown. Reactive species (red) created by these ionization events are shown undergoing thermal diffusion at different time points ($10^{-12}$s - $10^{-6}$s). The track is shifted spatially along the $x$-axis for each time point for better visualization. The beam axis is the $z$-axis. Simulations were performed with TOPAS n-Bio [21].

position vector $\vec{r} = (x, y)$. We consider a system of $N$ particle tracks distributed across a target. The spatio-temporal distribution of the RS of an arbitrary track at position $\vec{r_i}$ and arrival time $t_i$ is defined by a probability density function (PDF) $c_i(\vec{r}, t)$. We do not differentiate between different RS and instead describe the net dynamics of all RS of the track together. The track diffuses, interacts with its

environment, and potentially interacts with other tracks. Thus, the evolution of a track is governed by a reaction-diffusion equation comprising a radially symmetric diffusion term with diffusion coefficient $\alpha$, an environmental scavenging term with rate constant $k_e$, and a track-track interaction term with rate constant $k_r$:

$$\frac{\partial}{\partial t}c_i(\vec{r},t) = \alpha\nabla^2 c_i(\vec{r},t) - k_e c_i(\vec{r},t) - k_r \sum_{i,j}^{N} c_i(\vec{r},t)c_j(\vec{r},t). \quad (1)$$

Track-track interactions are assumed to have a net reductive effect on the total number of RS, since they mostly comprise primary radical combination into secondary molecules. The track-track interaction term can be decomposed into an intratrack interaction term (where $i = j$) and an intertrack interaction term (where $i \neq j$). Since the model follows track dynamics up till the point at which intertrack interactions become significant, it is assumed that intertrack interactions negligibly affect the evolution dynamics of individual tracks up until that point. Thus, the intertrack interaction term is neglected, and intertrack interaction is quantified separately in Section 2.1.3.

The intratrack interaction term and the environmental scavenging term, both of which contribute to a decline in the number of RS in the track, are combined into one decay term with effective decay constant $k_s$. This is done in order to keep Eq. 1 linear and thus allow for an analytical solution. Thus, the simplified diffusion-decay reaction defining individual tracks in this model is

$$\frac{\partial}{\partial t}c_i(\vec{r},t) = \alpha\nabla^2 c_i(\vec{r},t) - k_s c_i(\vec{r},t). \quad (2)$$

Setting $c_0$ to be the initial total number of RS in the track, the solution to this partial differential equation (see Supplementary Appendix SA1) yields the PDF of an arbitrary track centered at $\vec{r_i}$ for $t > t_i$, a normal distribution about the arrival point of the track that broadens and decays with time:

$$c_i(\vec{r},t) = c_0 \cdot \frac{e^{-\frac{|\vec{r}-\vec{r}_i|^2}{4\alpha(t-t_i+\tau_0)} - k_s(t-t_i)}}{4\pi\alpha(t-t_i+\tau_0)}. \quad (3)$$

Here, we applied a temporal shift parameter $\tau_0$, such that the track has a finite width upon its arrival $t = t_i$, which represents the spatial variance along the primary particle's path.

## 2.1.2 Track distribution

The beam is assumed to have a constant dose rate over the exposure time $T$, and thus the PDF of the arrival time $t_i$ of the $i$th track at time $t$ is

$$P_t(t_i) = \begin{cases} \dfrac{1}{\min(t,T)} & \text{for} \quad 0 \le t_i \le \min(t,T) \\ 0 & \text{elsewhere.} \end{cases} \quad (4)$$

The expected total number of tracks on the target over time $N(t)$ can be expressed with the total energy deposited in the target $E$ and the average energy deposited per track $E_t$ for a target of density $\rho$, depth $z$ (measured along the beam axis), and cross-sectional area $A$.

$$N(t) = \frac{E}{E_t} \cdot \frac{\min(t,T)}{T} \quad (5)$$

$$= \frac{D \cdot A \cdot \rho \cdot z}{E_t} \cdot \frac{\min(t,T)}{T} \quad (6)$$

$$= \frac{D \cdot A \cdot \rho}{L} \cdot \frac{\min(t,T)}{T}. \quad (7)$$

The LET ($L = E_t/z$) is introduced in the last step and will depend on the radiation quality.

Assuming a spatially homogeneous beam across the target area $A$, the expected number of tracks within any circular area of radius $R$ can be expressed as a fraction of the total number of tracks on the target:

$$N_R(t) = N(t) \cdot \frac{\pi R^2}{A} \quad (8)$$

The PDF of the displacement $s$ between one arbitrary track and any other track within a radius $R$ is given by the ratio between the area element $2\pi s$ and the total area $\pi R^2$:

$$P_s(s) = \frac{2s}{R^2}, \quad s \le R. \quad (9)$$

## 2.1.3 Track-track interaction

The quantification of track-track interaction is a critical component of this model. A measure is needed that accounts for the spatial variations of different tracks, and reflects a physical quantity relevant to the radiation chemistry at hand. To this end, first the interaction rate $\omega$ is first defined, which yields the rate of change of the quantity of species at time $t$ due to the interaction of two tracks assuming second order reactions with reaction rate $k_r$.

$$\omega_{1,2}(t) = \int k_r \cdot c_1(\vec{r},t) \cdot c_2(\vec{r},t)\, dV \quad (10)$$

$$= k_r \cdot c_0^2 \cdot \frac{e^{-\frac{|\vec{r}_1-\vec{r}_2|^2}{8\alpha(2t-t_1-t_2+2\tau_0)} - k_s(2t-t_1-t_2)}}{8\pi\alpha(2t-t_1-t_2+2\tau_0)}. \quad (11)$$

Different reaction rates will be specified for intertrack interactions $k_{r,inter}$ and intratrack interaction $k_{r,intra}$.

Integrating the interaction rate in Eq. 11 over time yields the total track-track conversion $I$, which represents the net change in the quantity of species due to the interaction over the relevant time period:

$$I_{1,2}(t) = \int_0^t \omega_{1,2}(t')\, dt'. \quad (12)$$

$I$ is the measure of interest in this model, as it represents an empirically measurable quantity.

## 2.1.4 Intertrack interaction

The expected interaction rate of an arbitrary track $a$ with all neighboring tracks within an interaction volume of radius $R$ can be found by multiplying the number of tracks inside that interaction volume $N_R$ by the expected interaction rate between one arbitrary track and another within that volume:

$$\sum_i \omega_{a,i}(t) = N_R(t) \cdot \langle \omega_{1,2}(t) \rangle, \quad (13)$$

The total intertrack conversion of all tracks in the target volume is then

$$I_{\text{inter}}(t) = \frac{N(t)}{2} \cdot \int_0^t \lim_{R\to\infty} N_R(t') \cdot \langle \omega_{1,2}(t') \rangle \, dt', \tag{14}$$

where $R$ approaches infinity under the assumption that each track is effectively within an infinite isotropic volume. The factor $\frac{1}{2}$ ensures that each intertrack interaction is not double-counted.

Evaluating this expression (see Supplementary Appendix SA2) yields

$$I_{\text{inter}}(t) = \begin{cases} \lim_{\epsilon\to 0} \frac{B}{2} \cdot t \cdot \left[ \ln\left(\frac{t}{\epsilon}\right) - \Gamma(0, 2k_s t) + 2\Gamma(0, k_s t) + \Gamma(0, 2k_s\epsilon) - 2\Gamma(0, k_s\epsilon) \right] & \text{for} \quad t \le T \\ I_{\text{inter}}(T) + \frac{B}{2} \cdot \frac{\left(e^{k_s T} - 1\right)^2}{2k_s} \cdot \left(e^{-2k_s T} - e^{-2k_s t}\right) & \text{for} \quad t > T, \end{cases} \tag{15}$$

where

$$B = \frac{N(t)^2}{A} \cdot \frac{k_{r,\text{inter}}}{k_s^2} \cdot c_0^2 \cdot \left( \frac{1}{\min(t, T)} \right)^2, \tag{16}$$

and $\Gamma(s, x)$ is the incomplete upper gamma function given by

$$\Gamma(s, x) = \int_x^\infty t^{s-1} e^{-t} \, dt. \tag{17}$$

### 2.1.5 Intratrack interaction

The total intratrack conversion across the entire target volume is simply a sum of each track's self-interaction

$$I_{\text{intra}}(t) = \sum_i^{N(t)} \int_0^t \omega_{i,i}(t') \, dt'. \tag{18}$$

This expression can be simplified with a suitable approximation, removing the need for tedious summation over all tracks. A track's outward diffusion means that the amount of intratrack conversion of a single track asymptotically converges over time to a maximum value. If the time it takes for the amount of conversion to almost fully converge is negligible relative to the total exposure time, the total intratrack conversion can be approximated as a linear increase over the exposure time towards the total maximum amount of intratrack conversion of all tracks on the target.

$$I_{\text{intra}}(t) \approx N(t) \cdot \int_0^\infty \omega_{i,i}(t) \, dt \tag{19}$$

$$= N(t) \cdot \int_0^\infty k_{r,\text{intra}} \cdot c_0^2 \cdot \frac{e^{-2k_s t}}{8\pi\alpha(t + \tau_0)} \, dt \tag{20}$$

$$= N(t) \cdot k_{r,\text{intra}} \cdot c_0^2 \cdot \frac{e^{2k_s\tau_0}}{8\pi\alpha} \cdot \Gamma(0,\ 2k_s\tau_0). \tag{21}$$

If the convergence time is long relative to the total exposure time, this approximation will underestimate the amount of intratrack interaction at short time scales, but will converge on the correct value at longer time scales.

### 2.1.6 Quantifying the influence of intertrack interaction

Although $I_{\text{inter}}$ gives the absolute effect of intertrack interaction, we were interested in quantifying its relative effect on the total ongoing radiation chemistry, which normally consists of only intratrack interactions. We therefore calculated the relative change that intertrack interactions cause to the total radiation chemistry.

**TABLE 1** Variables described in this model.

| Variable | Description |
|---|---|
| $K$ | Reaction rate ratio |
| $\alpha$ | Track diffusion coefficient |
| $\tau_0$ | Track minimum age |
| $k_s$ | Track decay constant |
| $\rho$ | Target density |
| $L$ | LET |
| $D$ | Dose |
| $T$ | Exposure time |
| $F$ | Primary particle fluence |

$$\Phi(t) = \frac{I_{\text{inter}}(t) + I_{\text{intra}}(t)}{I_{\text{intra}}(t)} - 1 \tag{22}$$

$$= \frac{I_{\text{inter}}(t)}{I_{\text{intra}}(t)}. \tag{23}$$

$\Phi(t)$ thus remains 0 until intertrack interactions begin to affect the radiation chemistry; once $\Phi(t)$ has surpassed some critical value $\Phi_c$, we may consider intertrack interactions to be significant. $\Phi(t)$ is the main measure of interest in this model.

Evaluating this measure with Eqs 7, 14, 18 yields

$$\Phi(t) = K \cdot 2\pi\alpha \cdot \frac{D \cdot \rho}{L} \cdot \frac{e^{-2k_s\tau_0}}{k_s^2 \cdot \Gamma(0, 2k_s\tau_0)} \cdot \frac{1}{T} \cdot \begin{cases} f_1(t, k_s) & \text{for} \quad t \le T \\ f_1(T, k_s) + \frac{\left(e^{k_s T} - 1\right)^2}{k_s T} \left(e^{-2k_s T} - e^{-2k_s t}\right) & \text{for} \quad t > T \end{cases} \tag{24}$$

where

$$f_1(t', k_s) = 2 \cdot \lim_{\epsilon\to 0} \left[ \ln\left(\frac{t'}{\epsilon}\right) - \Gamma(0, 2k_s t') + 2\Gamma(0, k_s t') + \Gamma(0, 2k_s\epsilon) - 2\Gamma(0, k_s\epsilon) \right], \tag{25}$$

$K = k_{r,\text{inter}}/k_{r,\text{intra}}$ is the ratio of reaction rates between intertrack and intratrack interactions, and $\Gamma(s, x)$ is defined as in Eq. 17. Table 1 summarizes all variables and their definitions.

The primary particle fluence can be expressed using Eq. 7 as.

$$F = \frac{N}{A} \tag{26}$$

$$= \frac{D \cdot \rho}{L}. \tag{27}$$

The value of $\Phi(t)$ for $t \gg T$ is of interest for analyzing the final ratio of intertrack-to-intratrack interactions after all tracks have decayed and no more interactions can occur. This value, using Eqs 24, 27, is given by.

$$\Phi_{t\gg T} = \lim_{t\to\infty} \Phi(t) \tag{28}$$

$$= K \cdot \alpha \cdot F \cdot f_2(T, k_s, \tau_0), \tag{29}$$

where

$$f_2(T, k_s, \tau_0) = \frac{e^{-2k_s\tau_0}}{k_s^2 \cdot \Gamma(0, 2k_s\tau_0)} \cdot \frac{2\pi}{T} \cdot \left[ f_1(T, k_s) + \frac{\left(e^{-k_sT} - 1\right)^2}{k_sT} \right]. \tag{30}$$

## 2.2 Consideration of pulsed beams

UHDR beamlines are often pulsed, which contrasts with the constant dose rate assumption of the model detailed in Section 2.1.2. For example, linear accelerators typically deliver electrons in microsecond-long pulses with pulse repetition frequencies, $f$, on the order of 10–100 Hz. Intertrack interaction may occur within each pulse, but may also occur between pulses if the time between pulses is shorter than the decay of tracks, i.e., if $1/f$ is of the same order of magnitude or smaller than the effective track decay constant $k_s$. However, as shown in Section 3.2, typically $k_s \gg 1/f$ and it is safe to assume that no intertrack interaction occurs between pulses. In that case, each pulse can be considered independently of the other pulses, and the dose per pulse $D_p$ and pulse width $w$ become the only relevant parameters with regards to intertrack interaction. This concept is considered in the model by viewing each pulse as an effectively constant-dose-rate exposure with a duration $T = w$ and a dose $D = D_p$.

## 2.3 Monte Carlo simulation

MC simulations were performed with the MC radiolysis toolkit TOPAS n-Bio [21] to estimate values of the model parameters $\alpha$, $\tau_0$, and $k_s$, which modulate the radial diffusion and the decay rate of each track. A 1 MeV electron beam was set to impinge on the face of a cylindrical target volume made of anoxic water. The depth and diameter of the target volume differed for different simulations depending on the type of analysis needed and the amount of computational load. The beam's average energy loss through the water volume in all cases was negligible. The physics modules *g4em-dna* was used to simulate the physical interactions of the beam with the target, and the step-by-step chemistry module *TsEmDNAChemistryExtended* was used to simulate the production, diffusion, and interaction of resulting RS through the end of the chemical stage (1 $\mu$s). The simulation time steps were set as follows: 1 ps for the first 1 ns, then 10 ps until 10 ns, 100 ps until 100 ns, and 1 ns until the end of the simulation at 1 $\mu$s. Replicate simulations were performed with different random seeds; the mean and its standard error across these replicates is reported in the subsequent analysis for any computed values.

Although the simulation medium was pure water, the effects of scavenging in different target media were simulated by removing select RS at a specified rate throughout the simulation; the resulting reaction product was not simulated and thus did not undergo subsequent reactions. Table 2 details these different scavenging modes. The complete spectrum of RS and their reactions included in the TOPAS n-Bio chemistry module were simulated; however, only a select few RS were considered in the subsequent analysis in order to focus the analysis on the RS deemed most important for biological damage. These selected RS are: $^{\bullet}OH$, $e_{aq}^{-}$, $H^{\bullet}$, and $H_2O_2$.

**TABLE 2** Simulated half-lives of reactive species (RS) for different scavenging modes. The physoxic and normoxic scavenging modes represent pure water at 4% and 21% $O_2$, respectively. The half-life $\tau_{1/2}$ is related to the first-order scavenging rate $k$ by: $k \cdot \tau_{1/2} = \ln(2)$. Empty values indicate no scavenging reaction was defined for that species.

| Species | Half-life [$s$] | | |
|---|---|---|---|
| | Physoxic [32] | Normoxic [32] | Cellular [33, 34] |
| $^{\bullet}OH$ | | | $4 \times 10^{-9}$ |
| $e_{aq}^{-}$ | $7.30 \times 10^{-7}$ | $1.82 \times 10^{-7}$ | $2 \times 10^{-7}$ |
| $H^{\bullet}$ | $6.93 \times 10^{-7}$ | $1.73 \times 10^{-7}$ | $2 \times 10^{-7}$ |
| $H_2O_2$ | | | $10^{-3}$ |

**TABLE 3** The number of replicate simulations and the average CPU time per replicate for different simulation modes. 'Inter' and Non-inter' refer to the interacting and non-interacting simulations respectively.

| Dose | CPU time per Rep, # Reps | | | |
|---|---|---|---|---|
| | Physoxic Inter | Physoxic Non-inter | Cellular Inter | Cellular Non-inter |
| 12 Gy | 7357 s, 60 | 151 s, 60 | 2402 s, 36 | 97 s, 50 |
| 58 Gy | 274,667 s, 4 | 737 s, 10 | 85,182 s, 5 | 459 s, 10 |

### 2.3.1 Simulation of a single particle track

To analyze the spatio-temporal evolution of a single track, modulated by the model parameters $\alpha$ and $\tau_0$, the radial variance of the first 1 $\mu$m of a simulated track in a 10 $\mu m$ diameter water volume is compared with its variance over time as predicted by the model: $2\alpha(t + \tau_0)$. Only the first 1 $\mu$m of the simulated track is analyzed to avoid the effects of beam straggling deeper in the target, which would erroneously affect the analysis of the track's variance due to RS diffusion.

To analyze the decay in number of RS caused by the combination of intratrack interactions and scavenging, modulated by the model parameter $k_s$, the number of RS of the first 20 $\mu$s of the simulated track in a 10 $\mu m$ diameter water volume is compared with the model's simplified decay term, $e^{-k_s t}$, where $k_s$ is the effective track decay constant.

### 2.3.2 Simulation of interacting particle tracks

MC simulations of multiple particles and their interacting tracks were performed to compare with the model's estimation of intertrack interaction. The impinging particles were distributed uniformly randomly across the face of the 1 $\mu$s diameter, 1 $\mu$s deep cylindrical target volume. Other than the stated differences, all other simulation parameters remained equal to those in the aforementioned simulations (Section 2.3.1). Two different doses, 12 Gy and 58 Gy, were simulated by adjusting the number of primary electrons to 393 and 1963, respectively. The CPU times for these simulations are reported

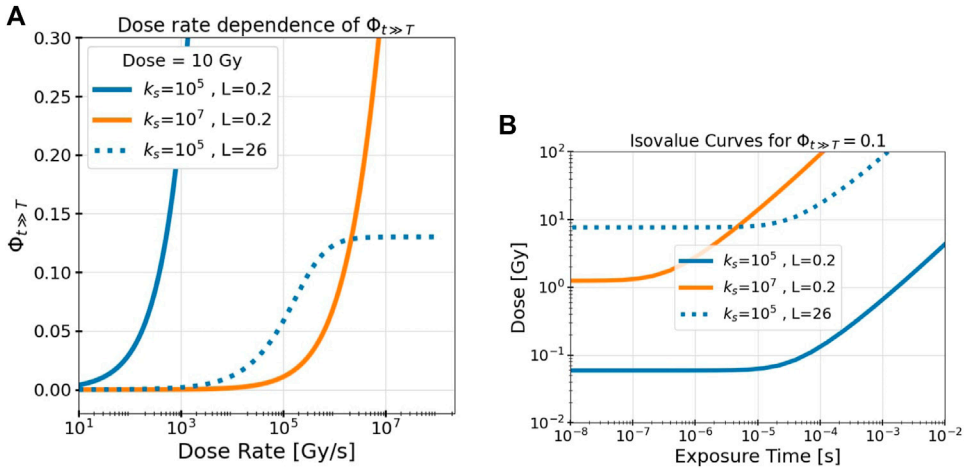


FIGURE 3
The model's measure of intertrack interaction, $\Phi_{t\gg T}$, depends on the dose, the dose rate, the LET $L$, and the effective track decay constant $k_s$. **(A)** Dose rate dependence of $\Phi_{t\gg T}$ and **(B)** isovalue curves at $\Phi_{t\gg T}$ = 0.1 for different values of $k_s$ and $L$ illustrate these dependencies. Results are shown for different track decay constants $k_s$ (indicated by color, given in $s^{-1}$) and beam LET (indicated by line style, given in keV/$\mu$m).

in Table 3. The exposure time did not vary because within TOPAS n-Bio, all tracks arrive in the target simultaneously, yielding an effectively infinite dose rate. These simulations were repeated for all three scavenging modes.

Two otherwise identical simulations were performed: one in which tracks were simulated independently of one another and thus unable to interact, and one in which all tracks were simulated together, such that tracks were able to chemically interact. These simulation modes are referred to as 'non-interacting' and 'interacting', respectively. The 'non-interacting' simulations represent the radiation chemistry at the low-dose-rate limit, where interactions consist only of intratrack and scavenging interactions. The 'interacting' simulations add on the effects of intertrack interactions. The number of RS in each simulation type was recorded over time and compared.

# 3 Results

An analytical model was developed that describes the spatio-temporal distribution of RS in a particle track, the spatio-temporal distribution of multiple particle tracks in a target as a function of beam parameters, and the expected values of intertrack and intratrack interaction as a function of time during and after irradiation. The model measures the influence of intertrack interactions with the variable $\Phi$, which gives the ratio between the amount of intertrack and intratrack interaction during and after an irradiation. $\Phi$ is initially 0, but grows as intertrack interaction begins to increase.

## 3.1 Model parameter dependencies

Eq. 29 demonstrates that the final value $\Phi$ approaches after an irradiation of exposure time $T$, $\Phi_{t\gg T}$, depends on only two physical beam parameters: the fluence $F$ and the exposure time $T$, which respectively yield the spatial and the temporal separation of tracks. The fluence then depends on the dose and the LET as expressed in Eq. 27. All other dependencies pertain to parameters specific to the track or target: the reaction rate ratio between intertrack and intratrack reactions $K$, the track diffusion constant $\alpha$, the minimum track age $\tau_0$, and the effective track decay constant $k_s$ (which may depend on the target medium).

$\Phi_{t\gg T}$ is linearly dependent on $K$ and $\alpha$, and increases with increasing $\tau_0$ or decreasing $k_s$. Numerical values of $\alpha$ and $\tau_0$ can be easily estimated by fitting the radial variance of the model's track to that of MC simulations (Section 3.2). $k_s$ can be fit in a similar fashion (Section 3.2), although it could vary widely depending on which RS are being considered and on the scavenging capacity of the target. Thus, results are shown for different values of $k_s$ to better understand its effect on $\Phi_{t\gg T}$. A numerical value of $K$ is difficult to determine, as it effectively represents all differences in reaction dynamics between intertrack and intratrack interactions for which the model does not otherwise account, which likely depends on the RS considered, the scavenging capacity of the target, and even the amount of intertrack interaction that occurs. We thus left $K$ as a free model parameter to be fit to experimental data.

Focusing on the beam parameter dependencies, $\Phi_{t\gg T}$ is essentially controlled by the spatial and the temporal concentration of tracks; an increase in either increases $\Phi_{t\gg T}$. The spatial concentration is modulated by the fluence $F$, which is linearly dependent on the dose $D$ and inversely dependent on the LET $L$. A higher LET beam requires fewer particles, and thus fewer tracks, to achieve the same dose, resulting in less intertrack interaction. The temporal concentration is determined solely by $T$; $\Phi_{t\gg T}$ strictly decreases with increasing $T$.

Figure 3A depicts the dependence of $\Phi_{t\gg T}$ on $T$ for a constant dose (the dose rate is given by $D/T$). $\Phi_{t\gg T}$ increases from 0 as the dose rate increases but eventually reaches an asymptotic plateau at very high dose rates. This occurs once all tracks arrive almost instantaneously relative to their decay lifetimes. Here, the amount of intertrack interaction is limited solely by their spatial separation

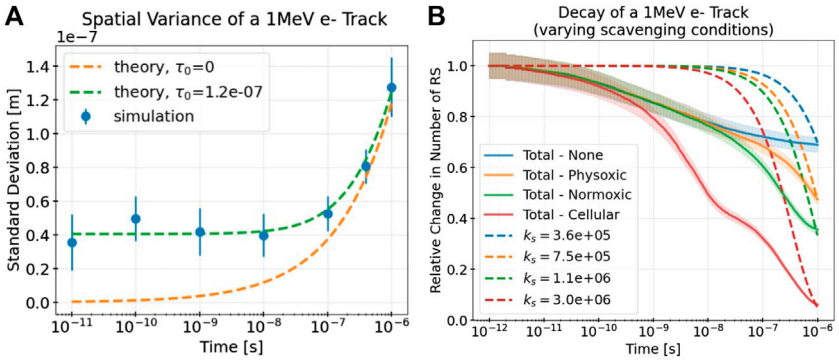


FIGURE 4
**(A)** Standard deviations of the radial displacements (a measure of radial track width) of select RS ($^{\bullet}OH$, $e_{aq}^-$, $H^{\bullet}$, $H_3O^+$, $H_2O_2$, and $O_2^{-\bullet}$) of a simulated electron track (points with standard error) under cellular scavenging conditions alongside theoretical standard deviations (dashed lines) assuming a normal distribution ($\sigma = \sqrt{2\alpha(t+\tau_0)}$). Including the minimum track age correction $\tau_0$ (given in s) results in a better fit of the simulated track, owing to its initial non-zero spatial variance. **(B)** Simulated (solid lines with shaded standard error) relative decays of these RS of an electron track caused by intratrack and scavenging reactions for different scavenging modes (denoted by color) alongside exponential (dashed) decays with different effective decay constants $k_s$ given in $s^{-1}$. The "None" scavenging mode displays the track decay without any scavenging reactions defined, and thus is due solely to intratrack interactions.

and is unaffected by any further increase in dose rate. An increasing $k_s$ delays the onset of intertrack interaction and diminishes its final asymptotic value as tracks decay more quickly before interacting. This plateau occurs in all cases, but is only visible in this figure for the higher LET.

To visualize the space and time dependencies of $\Phi_{t\gg T}$ simultaneously, Figure 3B depicts the isovalue curve where $\Phi_{t\gg T}$ = 0.1 over the dose/exposure time parameter space for different values of $k_s$ and $L$. The isovalue of 0.1 represents where 10% of the interactions of RS are between tracks, but notably these results are shown only to demonstrate the beam parameter dependencies; the precise location of the isovalue curve also depends on the values of other model parameters ($K$, $\alpha$, $\tau_0$, and $k_s$) which are determined in the following section. Evidently, for any set of irradiation parameters, there is a minimum dose (fluence) and a maximum exposure time necessary to achieve a given value of intertrack interaction. Again, as in Figure 3A, once the temporal separation is low enough, there is no more dependency on the temporal domain and only a dose dependency remains.

## 3.2 Model parameter fitting to simulations

MC simulations of a 1 MeV electron track were obtained to determine numerical values for the model parameters describing the spatio-temporal evolution of a track, $\alpha$ and $\tau_0$, and the rate of decay of the track, $k_s$. Figure 4A depicts the radial variance of a simulated track over time compared with the model's prediction with the fitted model parameters $\alpha$ and $\tau_0$. These results differ slightly for different scavenging modes (see Table 4) but remain good fits to the simulation data in all cases. The minimum track age parameter $\tau_0$ clearly improves the model's description of the track, especially at short time scales.

Figure 4B depicts the decay in number of RS of the simulated track due to intratrack interactions and scavenging and compares this decay with the decay as predicted by the exponential decay term of the model, with different effective decay constants $k_s$. Even with no simulated scavenging reactions (see the line labeled "None"), the track still decays owing to intratrack recombination. As expected, the higher the simulated levels of scavenging, the larger the decay and thus the larger the corresponding value of $k_s$. Notably, even in the cellular scavenging mode, the track does not completely decay within nanoseconds because several different RS are being tracked, some of which are long-lived.

The values of $k_s$ were chosen to best match the simulated decay at the longest simulated time of $10^{-6}$s. As the plot is depicted with a logarithmic time scale, this long time scale value is close to what the simulated decay converges to, despite the seemingly rapid declines seen in the plot. Clearly, the exponential decay term underestimates the simulated decay at short time scales, because of rapid initial intratrack recombination, and overestimates it at longer time scales. This is preferable, however, because the relative error of this initial underestimation does not exceed 50% at any time point, even for the highest scavenging levels (cellular). On the other hand, a better fit at short time scales would result in a severe, orders of magnitude larger overestimation of the decay at longer time scales owing to the nature of exponential decay.

**TABLE 4 Best fit values for different model parameters for different scavenging modes (see Table 2) based on MC simulations of a single track (for $\alpha$ and $\tau_0$ and $k_s$) and of multiple interacting tracks (for $K$).**

| Parameter | Fitted value for scavenging mode | | |
|---|---|---|---|
| | Physoxic | Normoxic | Cellular |
| $\alpha$ [$m^2/s$] | 4.3 $\times^{-9}$ | 4.2 $\times^{-9}$ | 6.9 $\times^{-9}$ |
| $\tau_0$ [s] | 2.6 $\times^{-7}$ | 2.4 $\times^{-7}$ | 1.2 $\times^{-7}$ |
| $k_s$ [$s^{-1}$] | 7.5 $\times^{5}$ | 1.1 $\times^{6}$ | 3.0 $\times^{6}$ |
| $K$ | 0.003 | 0.002 | 0.001 |

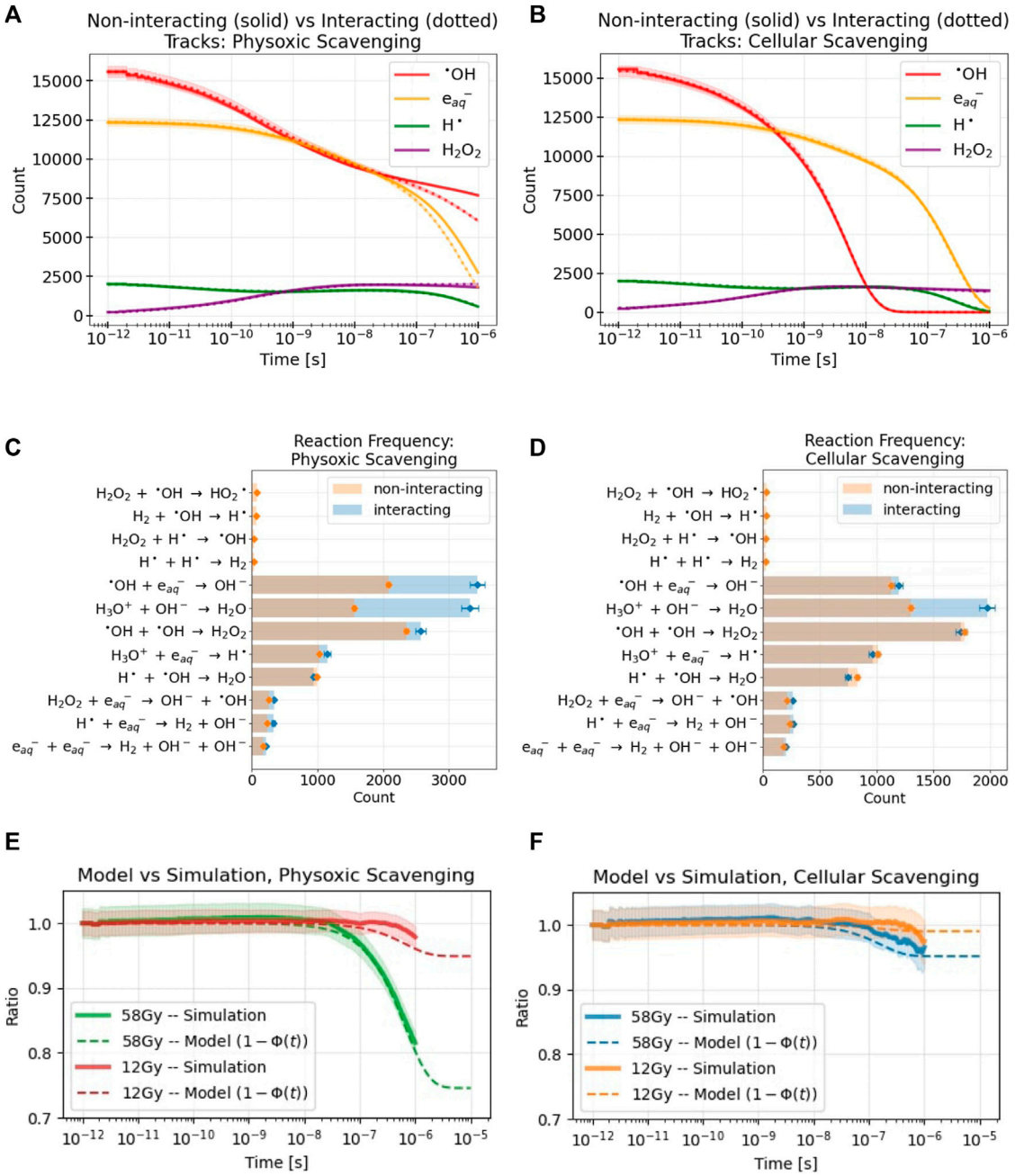


FIGURE 5
Results are shown from MC simulations of multiple tracks delivering 58 Gy to a water volume under physoxic **(A,C,E)** and cellular **(B,D,F)** scavenging conditions. For all simulation results, the standard error across replicate simulations is denoted with either shaded regions **(A,B,E,F)** or error bars **(C,D)**. **(A,B)** the difference in yields of select RS over time between non-interacting tracks (solid lines) and interacting tracks (dotted lines) simulations **(C,D)** The frequencies of different reactions between the two simulation types. The background scavenging that removes select RS at a specified rate (see Table 2) is not included in this plot. Also, any reaction occurring less than 20 times during the simulation was omitted **(E,F)** Comparison of the simulation results, the ratio of sums of the counts of the RS between the interacting and non-interacting tracks simulations shown in **(A,B)**, for both simulated doses to the model's analogous measure. The model parameter $K$ was used to fit the model's results to the simulation's with values of 0.003 and 0.001, respectively. Although the simulations were stopped at $10^{-6}$s, the model results are shown to $10^{-5}$s to examine the value that 1– Φ finally approaches. Values for the model parameters used in these results are listed in Table 4.

## 3.3 Model comparison to simulations of interacting tracks

### 3.3.1 Simulation results

MC simulations of many interacting tracks were used for comparison with the model's estimation of influence of intertrack interaction. This was repeated for two doses, 12 Gy and 58 Gy, and all three scavenging modes. Figures 5A, B show the numbers of the different RS of interest during a simulation where tracks were not allowed to interact (solid lines) or allowed to interact (dotted lines). Results are shown here only for the 58 Gy simulations and the physoxic and cellular scavenging modes. The normoxic scavenging

mode results tended to lie between the physoxic and cellular results (Supplementary Appendix SA3, Supplementary Figures S7A, B), whereas the 12 Gy simulation showed far smaller differences between the interacting and non-interacting simulations for all scavenging modes.

For the physoxic scavenging mode, intertrack interactions resulted in a decrease in the yields of $^{\bullet}OH$ and $e_{aq}^{-}$, and a slight increase in the yield of $H_2O_2$, beginning at $\approx 10^{-7}$s (Figure 5A). Figure 5C reveals the individual reactions most responsible for these differential yields. Intertrack depletion of $^{\bullet}OH$, and $e_{aq}^{-}$ is almost solely caused by their reaction with each other, whereas the self-recombination of $^{\bullet}OH$, and the consumption of $e_{aq}^{-}$ by $H_3O^+$, contribute only slightly. For the cellular scavenging mode, the quick depletion of $^{\bullet}OH$ and $e_{aq}^{-}$ due to high background scavenging is evident in Figure 5B. Here, intertrack interactions consist mostly of the reaction of $H_3O^+$ with $OH^-$ (Figure 5D) and are negligible with respect to the yields of the RS of interest.

### 3.3.2 Comparison to model

To compare the simulation results with those of the model, the ratio of the sums of the RS of the two simulation types shown in Figures 5A, B are taken and depicted by the solid lines with shaded in errors in Figures 5E, F. This ratio is a measure of the influence of intertrack interactions; it yields the relative difference of the RS counts caused solely by intertrack interactions. At very short time scales, this ratio remains 1 as there is no difference between the simulation types. At longer time scales, once intertrack interactions begin to affect RS yields, this ratio deviates from 1. Unsurprisingly, the higher the dose and the lower the amount of scavenging, the larger the effect of intertrack interactions. Notably, the slight deviation from 1 in the cellular scavenging results is almost entirely due to the change in $H_3O^+$ yields, as shown in Figure 5D. Results for the normoxic scavenging mode are not shown for brevity; as expected, they tended to fall between the results of the cellular and physoxic scavenging modes, remaining closer to the physoxic results (Supplementary Appendix SA3, Supplementary Figure S7C).

This ratio is directly compared with an analogous measure from the model, that is, $1 - \Phi(t)$. The ratio aligns quite well with what $1 - \Phi$ of the model actually represents based on Eq. 23. $\Phi$ is subtracted from 1 because intertrack interactions resulted in a net decrease in the number of the selected RS. The final free parameter of the model, the reaction rate ratio $K$, was adjusted to fit $1 - \Phi$ to the simulation results. The variables used to calculate $\Phi(t)$ (see Eq. 24) were: $T = 10^{-15}$s, $L = 0.14$ keV/$\mu$m, $\rho = 997$ kg/m$^3$, $D$ was adjusted to match the simulation dose, and $K$, $\alpha$, $\tau_0$, and $k_s$ were adjusted depending on the scavenging mode to the values in Table 4. The value of $T$ was chosen to simulate an effectively infinite dose rate since all particles arrived simultaneously in the simulation; decreasing $T$ to even lower values had negligible effects on the resulting values of $\Phi(t)$.

## 3.4 Model extrapolation to experimental results

### 3.4.1 In aqua conditions

The model output was shown to align well with MC simulation data when fitted with the variable $K = 0.001$. We also performed a similar comparison, now with experimental results of $H_2O_2$ yields after electron irradiation of physoxic water. Kacem et al irradiated 4% $O_2$ water with a pulsed electron beam in 3 different setups, which we labeled A-C, and observed a decrease in the resultant G-value of $H_2O_2$ ($G_{H_2O_2}$) with increasing dose rate, as shown in Table 5 [35]. By following the argument in Section 2.2, we assume that there are no interactions between the pulses, which were delivered at 100 Hz. Thus, the mean dose rate and number of pulses are irrelevant, and the only parameters that matter are the dose and dose rate within the pulse.

**TABLE 5** Pulse parameters and the absolute value of the relative change in the G-values of $H_2O_2$ relative to Setup A for different setups of electron irradiation of physoxic water by [35]. Below these are the value of $\Phi$ for each setup calculated with the model parameters in Table 4 for physoxic conditions. Below that is the value for $\Phi$ for each setup when one model parameter is changed (indicated by the parentheses) in order to match the value of $\Phi$ at Setup B to the observed relative change in $G_{H_2O_2}$ of 17%.

| Setup | A | B | C |
|---|---|---|---|
| Pulse Dose [Gy] | 0.01 | 1 | 10 |
| Pulse Dose Rate [Gy/s] | $10^4$ | $5.6 \times 10^5$ | $5.6 \times 10^6$ |
| Relative Change in $G_{H_2O_2}$ | – | 0.17 | 0.34 |
| $\Phi$ | $4.3 \times 10^{-5}$ | $4.1 \times 10^{-3}$ | 0.041 |
| $\Phi$ ($K = 0.13$) | $1.9 \times 10^{-3}$ | 0.17 | 1.70 |
| $\Phi$ ($k_s = 3.6 \times 10^3$ s$^{-1}$) | $1.7 \times 10^{-3}$ | 0.17 | 1.71 |
| $\Phi$ ($\tau_0 = 2.6 \times 10^{-5}$ s) | $1.8 \times 10^{-3}$ | 0.17 | 1.72 |

$\Phi$ was calculated for these pulse parameters by using the values for model parameters $\alpha$, $\tau_0$, $k_s$, and $K$ derived in the above sections for physoxic scavenging conditions, and its value is compared with the measured change in $G_{H_2O_2}$ relative to Setup A. A 17% decrease in $G_{H_2O_2}$ was observed in Setup B relative to Setup A, although the model predicts negligibly low intertrack interaction ($\Phi = 4.1 \times 10^{-3} \ll 0.17$) at Setup B.

In the case the derived values for the model parameters are off, we examined what changes to these parameters could result in a fit to this experimental data; i.e., $\Phi = 0.17$. We saw that either increasing $K$, increasing $\tau_0$, or decreasing $k_s$ could yield agreement between the value of $\Phi$ and the experimentally observed changes. We are not as interested in matching the values at Setup C because we expect $\Phi$ to be overestimated as intertrack interaction increases, due to the weakly-interacting tracks assumption made in Section 2.1.1.

The pulse parameters of this study can also be visualized on the heatmap (Figure 6) introduced in the following section, which displays $\Phi$ over the pulse parameter space for cellular scavenging conditions. The heatmap of $\Phi$ for physoxic scavenging conditions looks similar, but the isovalue curve is shifted slightly down towards lower doses and to the right towards higher exposure times. The 'corner' of the white isovalue curve occurs in this case at 13 Gy and 2 $\mu$s for $K = 0.003$, and 0.3 Gy and 2 $\mu$s for $K = 0.13$.

### 3.4.2 *In vivo* conditions

To compare the predictions of the model with experimental *in vivo* data from the literature, we used a heatmap of the value of $\Phi$ over the dose and exposure time parameter space (Figure 6). Again, by following the argument in Section 2.2, we can consider this to be

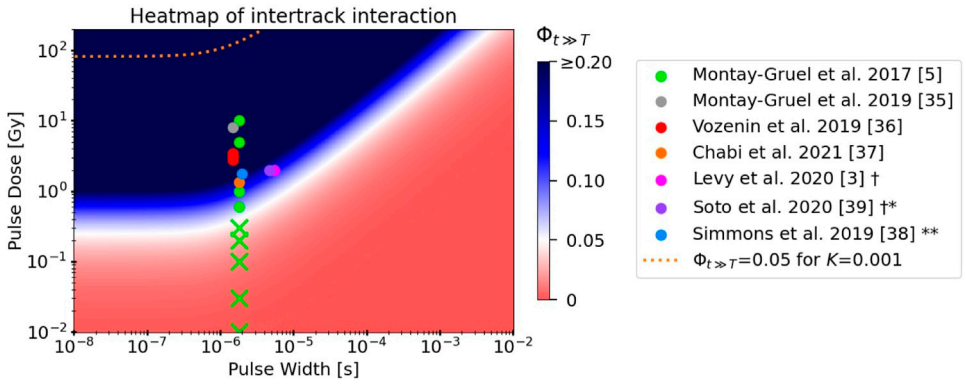


FIGURE 6
Heatmap depicting the value of $\Phi_{t\gg T}$, the model's measure of intertrack interaction, as a function of dose per pulse and pulse width. All model parameters used reflect those of a 1 MeV electron beam in cellular scavenging conditions, except for the parameter $K$ = 0.33 which was fitted to the experimental electron FLASH data displayed. The isovalue curve at $\Phi_{t\gg T}$ = 0.05 for $K$ = 0.001 (from fits to MC simulations) is indicated by the orange dashed line. The pulse parameters of electron FLASH studies from the literature that observed the FLASH effect (solid circles) or did not observe the FLASH effect ("Xs") are superimposed on the heatmap [3, 5, 36–40]. The conventional dose rates in most studies involved doses per pulse that were too low to be depicted on this plot. † Both studies used the same parameters; their respective points on the plot were slightly horizontally shifted for better visualization. * FLASH normal tissue sparing was observed only for total doses ≥30 Gy ** FLASH normal tissue sparing was observed only when the pulse repetition frequency was above a certain value.

the pulse dose and pulse width of each pulse in a pulsed electron delivery. Results are shown using the values for model parameters $\alpha$, $\tau_0$, and $k_s$ derived in the above sections for cellular scavenging conditions, with the notable exception of $K = 0.33$, which was chosen as it best fits these experimental data. The white and blue regions of the heatmap indicate where the model predicts intertrack interaction to have a $\geq 5\%$ effect on the yields of reactive species. The pulse parameters from *in vivo* electron FLASH data are superimposed on this heatmap.

# 4 Discussion

The model fit well to the results of the MC simulations of interacting tracks (Figures 5E, F), yielding values for the model's fitting parameter $K$ that were between 0.001–0.003, depending on the scavenging mode. These findings gives credence to the model's ability to replicate the results of MC simulations, although the simulations themselves suffer from limitations (discussed in detail in Section 4.2 below). In addition, because the simulations were limited to 1 $\mu$s, it is not clear if the model fits would remain accurate beyond 1 $\mu$s to the final value of the ratio, $\Phi_{t\gg T}$. Further work on this topic should prioritize extending the simulation times to provide more accurate fits at longer time scales. Regardless, assuming that the complete model with all fitted parameters is accurate, the model predicts that intertrack interactions are completely negligible in the parameter space where 1) decreased $H_2O_2$ yields are observed (first row of values of $\Phi$ in Table 5) and 2) where the FLASH effect is observed (dashed orange line in Figure 6). In fact, the model predicts that doses per pulse in excess of 90 Gy at pulse widths ≤1 $\mu$s would be necessary for intertrack interactions to induce a consequential change in the radiation chemistry. In that case, clearly some other mechanism must be responsible for the observed UHDR effects.

Alternatively, one or a combination of the fitted model parameters could be incorrect, thus yielding erroneously low predictions of intertrack interaction. The bottom three rows of Table 5 show how an increased reaction rate ratio $K$, an increased minimum track age $\tau_0$, or a decreased track decay constant $k_s$ could cause the model predictions to align with the experimental data. A similar approach was taken to create the heatmap in Figure 6, where a value of $K$ = 0.33 was chosen as it fits well to the experimental data. How these inaccurate fits could have come about is explored below (Section 4.2).

## 4.1 Application to FLASH RT

Before discussing the limitations of the model and simulations, we investigated the implications of the model for FLASH RT if indeed one or more of the model's parameters were found to be inaccurate, and the updated parameter resulted in the model's predictions aligning with what is shown in the heatmap in Figure 6. Here, the model demonstrates that induction of the FLASH effect coincides with the regions of the parameter space where intertrack interactions significantly affect the radiation chemistry, the extent of which decreases with increasing scavenging capacity. It is clear that, although the doses per pulse vary over a large range throughout the data, the range of pulse widths is very narrow because all presented data used linear accelerators. Interestingly, it appears that lowering the pulse width below ≈0.5 $\mu$s would have no benefit to increasing intertrack interactions, as they depend solely on the dose per pulse in this parameter space range.

The argument presented in Section 2.2 states that if the RS created by a pulse have all been scavenged in the ≈0.01 s that typically separate linac electron pulses, each pulse can be considered independently of the others. Although that almost certainly holds for the primary RS like $^{\bullet}OH$ and $e_{aq}^{-}$, lingering effects of secondary or beyond molecules could cause interpulse

effects, *in aqua* and *in vivo*. For example, the relatively stable molecule $H_2O_2$ can interact with primary radicals of subsequent pulses, and is certainly relevant to biological damage [41]. In that case, the number of pulses, the time between them, and thus the mean dose rate, would also play a role. This hypothesis is supported by experimental data: Simmons et al. reported an induction of the FLASH effect simply by decreasing the time between adjacent pulses [39]. A similar idea of a two-step mechanism has also been proposed by Blain et al. [42].

In fact, even within a single electron pulse, which has thus far been assumed to have a constant dose rate across the ≈2 $\mu$s pulse, there is a micro-pulse structure [26]. This structure is on the order of 30 ps pulses at 3 GHz, and may have serious implications for the fast reactions of species like $^{\bullet}$OH. However, one must bear in mind that the model suggests that further temporal bunching below ≈0.5 $\mu$s (the specific value will depend on the model parameters) is negligible; thus, the micro-pulse structure may be irrelevant.

Proton FLASH RT also raises similar concerns. Depending on the proton source, the pulse structure of proton delivery varies widely [26], and the potential for interpulse effects remains significant. In addition, the commonly used scanning pencil beam method of proton delivery presents a challenge to modeling intertrack interaction because of the beam's spatial inhomogeneity [43]. Regardless, even at the infinite dose rate limit, where all protons are delivered simultaneously, the model predicts (with the simulation-derived fit parameter $K$ = 0.001) that again doses upwards of 90 Gy would be necessary for low-LET protons, which is much higher than the doses for which the FLASH effect has been observed [44]. For higher LET protons, proportionately higher doses would be necessary. In agreement with these simulation-derived predictions, Thompson et al. observed negligible changes in radical yields in Monte Carlo simulations of interacting low-LET proton tracks at 8 Gy in pure water [31]. Again, however, the MC simulations on which these predictions are made harbor potentially critical limitations which are addressed in Section 4.2.

Lastly, even if intertrack interactions were significant in the parameter space where the FLASH effect is observed, the mechanism by which such interactions could cause differential sparing of normal and tumor tissue is not obvious. One hypothesis for this mechanism is that of reduced indirect damage due to reduced primary radical yields, like those of $^{\bullet}$OH. Alternatively, many higher order processes have been proposed [12, 16–18]. As for the differential effect, the higher scavenging capacity of tumor tissue could reduce intertrack interaction [45]. None of these proposed mechanisms indicate an effect of intertrack interactions on direct damage, responsible for ≈ 1/3 of DNA damage for low-LET radiation [15, 46]. Direct damage must be taken into consideration in the context of a sparing mechanism, but a complete mechanistic description of how intertrack interactions could cause the FLASH effect remains out of the scope of this work.

## 4.2 Simulation limitations

The MC simulations done for comparison with the model results also have limitations. For instance, the simulated medium is pure anoxic water. To simulate the effects of different scavenger concentrations, affected species were removed from the simulation at a given rate. However, this approach ignores the products of these reactions while also ignoring spatio-temporal inhomogeneities in the scavenger concentration, which would surely occur owing to local scavenger depletion in and near the track. Research into the FLASH mechanism continues to underscore the importance of detailed modeling of varying oxygen concentrations and other chemical differences between normal and tumor tissue, as well as morphological/structural differences between the tissue types [20, 47]. Another limitation of the MC simulations due to their inherently large computational load is the total time scale, which was limited in this case to 1 $\mu$s. Figures 5E, F indicate that intertrack interactions were perhaps only beginning to become significant at 1 $\mu$s, and carrying the simulations out to longer time scales would be quite informative. Also, because all particles arrive simultaneously, the effects of varying the dose rate could not be studied and compared with the model's predictions.

These MC simulations also ignore some potentially critical microscopic effects of water radiolysis. Abolfath et al. demonstrated that, for example, local temperature increases in the core of particle tracks due to non-ionizing excitations of water molecules may temporarily elevate diffusion constants and reaction rates, boosting the initial radial diffusion of track RS [48]. This could be represented in the model by a significant increase in the parameter $\tau_0$, which modulates the initial width of each track. Also, interactions between RS like electrostatic shielding, which are ignored by the MC simulation, may significantly affect the ability of RS to diffuse and damage biomolecules [12].

In fact, the MC simulations quite clearly do not perfectly reflect all the chemical dynamics of water radiolysis. Kacem et al. demonstrated that increasing dose rates resulted in lower $G_{H_2O_2}$, and these findings have been replicated elsewhere [36], also with protons [42]. This is in stark contrast to the increase in $G_{H_2O_2}$ observed in MC simulations of increased intertrack interaction (Figure 5A). Figure 5C demonstrates that this simulated increase is due to an increase in the reaction $2^{\bullet}OH \rightarrow H_2O_2$. In a recent study measuring $G_{H_2O_2}$ after UHDR proton irradiation, in which the same trend of decreased $G_{H_2O_2}$ was observed as in Kacem et al., Blain et al proposed that increases in intertrack interaction caused by UHDRs preferentially increase the reaction $^{\bullet}OH + e_{aq}^{-} \rightarrow OH -$, leaving less $^{\bullet}$OH available for recombination to $H_2O_2$, and thus lower $G_{H_2O_2}$. Indeed, this predicted increase in $^{\bullet}OH + e_{aq}^{-}$ is strongly supported by the MC results (Figure 5C), but seems to not occur to the extent necessary to reduce $^{\bullet}$OH recombination. Moreover, the reaction $H_2O_2 + e_{aq} \rightarrow OH^{-} + ^{\bullet}OH$ may be relevant, especially in interpulse interaction considerations, as it occurred in consequential amounts in the MC simulations and increased due to intertrack interactions. Discrepancies between the MC simulations and experimental results could be partly explained by the MC simulations' ignoring the products of oxygen-related reactions, such as the hydroperoxyl radical formed in part by $H^{\bullet} + O_2 \rightarrow HO_2^{\bullet}$, which reacts readily with $H^{\bullet}$ again to form $H_2O_2$, or can react with $^{\bullet}OH$ or $e_{aq}^{-}$. Clearly, the interdependent nature of these reactions may cause unexpected results when one part of the system is ignored or misrepresented.

## 4.3 Model outlook

In order to address the concerns of interpulse interactions, the pulse structure of proton beamlines, and the micro-pulse structure of electron linacs, the model could be adjusted relatively easily to describe pulsed beams by adjustment of Eq. 4. The model could also be edited to describe spatially inhomogeneous beams, such as in scanning pencil beams or even spatially fractionated radiation therapy. However, this would require significant reworking of the

model's foundations as the assumption of a homogeneous and isotropic radiation field significantly simplifies the model.

Currently, the model does not differentiate between different RS in a track, and instead applies effective reaction and decay constants for all different RS. This was done as a first order approximation of track interaction, without considering the different types of possible reactions and their respective rates. In order to better describe the reactions of the different RS that make up a track, the model could be bifurcated into a two-compartment model, one which describes the initial fast reaction of primary RS, and one which tracks the accumulation and interpulse interaction of longer lived RS. Alternatively, the model could track each RS individually, each with its own diffusion and reaction constants, and sum over the total amount of measured interaction.

Such an approach could also be used to model downstream reaction products, such as organic peroxides formed by primary radical reactions with cellular macromolecules. These longer lived RS, in combination with other important environmental reagents like oxygen, may play a vital role in the dose rate dependent chemical dynamics that are neglected by the current model.

## 5 Conclusion

An analytical model was developed that describes the spatio-temporal distribution, diffusive evolution, and chemical interaction of RS in particle tracks in an irradiated target with different scavenging capacities. The model measures the expected relative change in the radiation chemistry due to intertrack interactions with the parameter Φ. Φ increases with increasing spatial concentration of tracks, either by increasing the dose or decreasing the LET. Φ also increases with increasing temporal concentrations of tracks, but below a certain exposure time (which depends on the decay rate of the tracks), further decreases in the exposure time have no effect.

The model parameters describing the diffusive broadening of each track, as well as those describing the track's decay due to intratrack and scavenging reactions, were fit to MC simulations of electron tracks. Significant reductions in $^{\bullet}OH$ and $e_{aq}^{-}$ yields due to the simulated intertrack interactions were observed by 1 $\mu$s at 58 Gy in physoxic and normoxic water, but not in cellular scavenging conditions or at 12 Gy for any scavenging conditions. The model fit well to this simulation data with values of the model's fitting parameter $K$ between 0.001 and 0.003, depending on the scavenging conditions. With these values of the fitting parameter, the model predicts that doses upwards of 90 Gy delivered within 0.5 $\mu$s for cellular scavenging conditions, or 13 Gy delivered within 2 $\mu$s for physoxic water, are necessary for consequential intertrack interaction.

Multiple limitations of the simulations were presented which, if rectified, could potentially lead to much higher model predictions of intertrack interactions. In this case, intertrack interaction could coincide with the observed FLASH effect in the dose and exposure time parameter space. However, extensive follow up analysis would be necessary to verify such claims. Additionally, a complete mechanism for how intertrack interactions could result in a differential sparing effect between normal and tumor tissue remains to be elucidated.

The analysis in this work assumes pulses in a typical pulsed electron delivery from a linac can be considered independently, and thus the only important beam parameters are the pulse dose and pulse width, as all relevant RS decay in the typical times between pulses (≈10 ms). However, evidence in support of a two-step mechanism is discussed in which the initial fast reaction dynamics of primary radicals and the following, slower reaction dynamics of secondary molecules are considered separately. This consideration indicates the possibility of interpulse interactions in pulsed electron beam deliveries, whereby more beam parameters such as the pulse repetition frequency and the number of pulses would become important.

## Data availability statement

The raw data supporting the conclusion of this article will be made available by the authors, without undue reservation.

## Author contributions

AB wrote the manuscript, performed the mathematical derivations and computational simulations, and prepared all figures. The rest of the authors contributed to the development of the model and the discussion of the results. All authors contributed to the article and approved the submitted version.

## Funding

The authors acknowledge funding from the German Research Foundation (Deutsche Forschungsgemeinschaft, DFG) through the Emmy Noether Programme (grant number 416790481 and the research grant 389238549), from the DFG Research Training Group 2274 (grant number 299102935), and from the Klinikum rechts der Isar of the Technical University of Munich.

## Acknowledgments

We thank Christine F. Wogan, MS, ELS, of MD Anderson's Division of Radiation Oncology, for editorial contributions to this article.

## Conflicts of interest

The authors declare that the research was conducted in the absence of any commercial or financial relationships that could be construed as a potential conflict of interest.

## Publisher's note

All claims expressed in this article are solely those of the authors and do not necessarily represent those of their

affiliated organizations, or those of the publisher, the editors and the reviewers. Any product that may be evaluated in this article, or claim that may be made by its manufacturer, is not guaranteed or endorsed by the publisher.

## Supplementary material

The Supplementary Material for this article can be found online at: https://www.frontiersin.org/articles/10.3389/fphy.2023.1215422/full#supplementary-material

## References


1. Favaudon V, Caplier L, Monceau V, Pouzoulet F, Sayarath M, Fouillade C, et al. Ultrahigh dose-rate FLASH irradiation increases the differential response between normal and tumor tissue in mice. *Sci translational Med* (2014) 6(245):245ra93. doi:10.1126/scitranslmed.3008973

2. Bourhis J, Montay-Gruel P, Jorge PG, Bailat C, Petit B, Ollivier J, et al. Clinical translation of FLASH radiotherapy: Why and how? *Radiother Oncol* (2019) 139:11–7. doi:10.1016/j.radonc.2019.04.008

3. Levy K, Natarajan S, Wang J, Chow S, Eggold JT, Loo PE, et al. Abdominal FLASH irradiation reduces radiation-induced gastrointestinal toxicity for the treatment of ovarian cancer in mice. *Scientific Rep* (2020) 10(1):21600–14. doi:10.1038/s41598-020-78017-7

4. Montay-Gruel P, Acharya MM, Gonçalves Jorge P, Petit B, Petridis IG, Fuchs P, et al. Hypofractionated FLASH-RT as an effective treatment against glioblastoma that reduces neurocognitive side effects in mice. *Clin Cancer Res* (2021) 27:775–84. doi:10.1158/1078-0432.ccr-20-0894

5. Montay-Gruel P, Petersson K, Jaccard M, Boivin G, Germond JF, Petit B, et al. Irradiation in a flash: Unique sparing of memory in mice after whole brain irradiation with dose rates above 100 Gy/s. *Radiother Oncol* (2017) 124(3):365–9. doi:10.1016/j.radonc.2017.05.003

6. Joubert A, Foray N. Repair of radiation-induced DNA double-strand breaks in human cells: History, progress and controversies. *New Res DNA Repair* (2006) 2006. Published online. doi:10.1016/j.dnarep.2007.11.008

7. Wardman P. Radiotherapy using high-intensity pulsed radiation beams (FLASH): A radiation-chemical perspective. *Radiat Res* (2020) 194(2020):607–17. doi:10.1667/RADE-19-00016

8. Adrian G, Konradsson E, Lempart M, Bäck S, Ceberg C, Petersson K. The FLASH effect depends on oxygen concentration. *Br J Radiol* (2020) 92(1106):20190702. doi:10.1259/bjr.20190702

9. Petersson K, Adrian G, Butterworth K, McMahon SJ. A quantitative analysis of the role of oxygen tension in FLASH radiation therapy. *Int J Radiat Oncology* Biology* Phys* (2020) 107(3):539–47. doi:10.1016/j.ijrobp.2020.02.634

10. Pratx G, Kapp DS. A computational model of radiolytic oxygen depletion during FLASH irradiation and its effect on the oxygen enhancement ratio. *Phys Med Biol* (2019) 64(18):185005. doi:10.1088/1361-6560/ab3769

11. Durante M, Bräuer-Krisch E, Hill M. Faster and safer? FLASH ultra-high dose rate in radiotherapy. *Br J Radiol* (2018) 91(1082):20170628. doi:10.1259/bjr.20170628

12. Abolfath R, Grosshans D, Mohan R. Oxygen depletion in FLASH ultra-high-dose-rate radiotherapy: A molecular dynamics simulation. *Med Phys* (2020) 47(12):6551–61. doi:10.1002/mp.14548

13. Ling CC. Time scale of radiation-induced oxygen depletion and decay kinetics of oxygen-dependent damage in cells irradiated at ultrahigh dose rates. *Radiat Res* (1975) 63(3):455–67. doi:10.2307/3574097

14. Zakaria AM, Colangelo NW, Meesungnoen J, Azzam EI, Plourde MÉ, Jay-Gerin JP. Ultra-high dose-rate, pulsed (FLASH) radiotherapy with carbon ions: Generation of early, transient, highly oxygenated conditions in the tumor environment. *Radiat Res* (2020) 194(6):587–93. doi:10.1667/rade-19-00015.1

15. Spitz DR, Buettner GR, Petronek MS, St-Aubin JJ, Flynn RT, Waldron TJ, et al. An integrated physico-chemical approach for explaining the differential impact of FLASH versus conventional dose rate irradiation on cancer and normal tissue responses. *Radiother Oncol* (2019) 139:23–7. doi:10.1016/j.radonc.2019.03.028

16. Jansen J, Knoll J, Beyreuther E, Pawelke J, Skuza R, Hanley R, et al. Does FLASH deplete oxygen? Experimental evaluation for photons, protons, and carbon ions. *Med Phys* (2021) 48:3982–90. doi:10.1002/mp.14917

17. Koch CJ. Re: Differential impact of FLASH versus conventional dose rate irradiation: Spitz et al. *Radiother Oncol* (2019) 139:62–3. doi:10.1016/j.radonc.2019.07.004

18. Labarbe R, Hotoiu L, Barbier J, Favaudon V. A physicochemical model of reaction kinetics supports peroxyl radical recombination as the main determinant of the FLASH effect. *Radiother Oncol* (2020) 153:303–10. doi:10.1016/j.radonc.2020.06.001

19. Limoli CL, Vozenin M-C. Reinventing radiobiology in the light of FLASH radiotherapy. *Annu Rev Cancer Biol* (2023) 7:1–21. doi:10.1146/annurev-cancerbio-061421-022217

20. Del Debbio F, Maria Sofia B, Gonnelli A, Da Pazzo E, Tozzini V, Martini C, et al. An insight into hypothesized biological mechanisms contributing to the Flash effect. *Front Phys* (2023) 11:396. doi:10.3389/fphy.2023.1201708

21. Schuemann J, McNamara AL, Ramos-Méndez J, Perl J, Held KD, Paganetti H, et al. TOPAS-nBio: An extension to the TOPAS simulation toolkit for cellular and subcellular radiobiology. *Radiat Res* (2019) 191(2):125–38. doi:10.1667/rr15226.1

22. Ramos-Méndez J, Domínguez-Kondo N, Schuemann J, McNamara A, Moreno-Barbosa E, Faddegon B. LET-dependent intertrack yields in proton irradiation at ultra-high dose rates relevant for FLASH therapy. *Radiat Res* (2020) 194(4):351–62. doi:10.1667/rade-20-00084.1

23. Anderson AR, Hart EJ. Radiation chemistry of water with pulsed high intensity electron Beams1. *J Phys Chem* (1962) 66:70–5. doi:10.1021/j100807a014

24. Shiraishi H, Katsumura Y, Hiroishi D, Ishigure K, Washio M. Pulse-radiolysis study on the yield of hydrated electron at elevated temperatures. *J Phys Chem* (1988) 92:3011–7. doi:10.1021/j100321a061

25. Kreipl MS, Friedland W, Paretzke HG. Interaction of ion tracks in spatial and temporal proximity. *Radiat Environ Biophys* (2009) 48(4):349–59. doi:10.1007/s00411-009-0234-z

26. Kim MM, Darafsheh A, Schuemann J, Dokic I, Lundh O, Zhao T, et al. Development of ultra-high dose-rate (FLASH) particle therapy. *IEEE Trans Radiat Plasma Med Sci* (2021) 6(3):252–62. doi:10.1109/trpms.2021.3091406

27. Boscolo D, Scifoni E, Durante M, Krämer M, Fuss MC. May oxygen depletion explain the FLASH effect? A chemical track structure analysis. *Radiother Oncol* (2021) 162:68–75. doi:10.1016/j.radonc.2021.06.031

28. Lai Y, Jia X, Chi Y. Modeling the effect of oxygen on the chemical stage of water radiolysis using GPU-based microscopic Monte Carlo simulations, with an application in FLASH radiotherapy. *Phys Med Biol* (2021) 66(2):025004. doi:10.1088/1361-6560/abc93b

29. Alanazi A, Meesungnoen J, Jay-Gerin JP. A computer modeling study of water radiolysis at high dose rates. Relevance to FLASH radiotherapy. *Radiat Res* (2021) 195(2):149–62. doi:10.1667/rade-20-00168.1

30. Zhu H, Li J, Deng X, Qiu R, Wu Z, Zhang H. Modeling of cellular response after FLASH irradiation: A quantitative analysis based on the radiolytic oxygen depletion hypothesis. *Phys Med Biol* (2021) 66(18):185009. doi:10.1088/1361-6560/ac226d

31. Thompson SJ, Prise KM, McMahon SJ. Investigating the potential contribution of inter-track interactions within ultra-high dose-rate proton therapy. *Phys Med Biol* (2023) 68:055006. doi:10.1088/1361-6560/acb88a

32. Buxton GV, Greenstock CL, Helman WP, Ross AB. Critical Review of rate constants for reactions of hydrated electrons, hydrogen atoms and hydroxyl radicals (OH/O- in Aqueous Solution. *J Phys Chem reference Data* (1988) 17(2):513–886. doi:10.1063/1.555805

33. Roots R, Okada S. Estimation of life times and diffusion distances of radicals involved in X-ray-induced DNA strand breaks or killing of mammalian cells. *Radiat Res* (1975) 64(2):306–20. doi:10.2307/3574267

34. Andrés C, Curieses M, Juan CA, Plou FJ, Pérez-Lebeña E. Chemistry of hydrogen peroxide formation and elimination in mammalian cells, and its role in various pathologies. *Stresses* (2022) 2:256–74. doi:10.3390/stresses2030019

35. Kacem H, Psoroulas S, Boivin G, Folkerts M, Grilj V, Lomax T, et al. Comparing radiolytic production of H2O2 and development of Zebrafish embryos after ultra high dose rate exposure with electron and transmission proton beams. *Radiother Oncol* (2022) 175(2022):197–202. doi:10.1016/j.radonc.2022.07.011

36. Montay-Gruel P, Acharya MM, Petersson K, Alikhani L, Yakkala C, Allen BD, et al. Long-term neurocognitive benefits of FLASH radiotherapy driven by reduced reactive oxygen species. *Proc Natl Acad Sci* (2019) 116(22):10943–51. doi:10.1073/pnas.1901777116

37. Vozenin MC, De Fornel P, Petersson K, Favaudon V, Jaccard M, Germond JF, et al. The advantage of FLASH radiotherapy confirmed in mini-pig and cat-cancer patients. *Clin Cancer Res* (2019) 25(1):35–42. doi:10.1158/1078-0432.ccr-17-3375

38. Chabi S, Van To TH, Leavitt R, Poglio S, Jorge PG, Jaccard M, et al. Ultra-high-dose-rate FLASH and conventional-dose-rate irradiation differentially affect human acute lymphoblastic leukemia and normal hematopoiesis. *Int J Radiat Oncol Biol Phys* (2021) 109(3):819–29. doi:10.1016/j.ijrobp.2020.10.012

39. Simmons DA, Lartey FM, Schüler E, Rafat M, King G, Kim A, et al. Reduced cognitive deficits after FLASH irradiation of whole mouse brain are associated with less hippocampal dendritic spine loss and neuroinflammation. *Radiother Oncol* (2019) 139: 4–10. doi:10.1016/j.radonc.2019.06.006

40. Soto LA, Casey KM, Wang J, Blaney A, Manjappa R, Breitkreutz D, et al. FLASH irradiation results in reduced severe skin toxicity compared to conventional-dose-rate irradiation. *Radiat Res* (2020) 194(6):618–24. doi:10.1667/rade-20-00090

41. Dal Bello R, Becher T, Fuss MC, Kramer M, Seco J. Proposal of a chemical mechanism for mini-beam and micro-beam efficacy. *Front Phys* (2020) 8:564836. doi:10.3389/fphy.2020.564836

42. Blain G, Vandenborre J, Villoing D, Fiegel V, Fois GR, Haddad F, et al. Proton irradiations at ultra-high dose rate vs. conventional dose rate: Strong impact on hydrogen peroxide yield. *Radiat Res* (2022) 198(2022):318–24. doi:10.1667/RADE-22-00021.1

43. Folkerts MM, Abel E, Busold S, Perez JR, Krishnamurthi V, Ling CC. A framework for defining FLASH dose rate for pencil beam scanning. *Med Phys* (2020) 47:6396–404. doi:10.1002/mp.14456

44. Diffenderfer ES, Sørensen BS, Mazal A, Carlson DJ. The current status of preclinical proton FLASH radiation and future directions. *Med Phys* (2022) 49(3): 2039–54. doi:10.1002/mp.15276

45. Hu A, Qiu R, Li WB, Zhou W, Wu Z, Zhang H, et al. Radical recombination and antioxidants: A hypothesis on the FLASH effect mechanism. *Int J Radiat Biol* (2023) 99: 620–8. doi:10.1080/09553002.2022.2110307

46. Santivasi WL, Xia F. Ionizing radiation-induced DNA damage, response, and repair. *Antioxid Redox signaling* (2014) 21:251–9. doi:10.1089/ars.2013.5668

47. Abolfath R, Baikalov A, Fraile A, Bartzsch S, Schüler E, Mohan R. A stochastic reaction–diffusion modeling investigation of FLASH ultra-high dose rate response in different tissues. *Front Phys* (2023) 11:1060910. doi:10.3389/fphy.2023.1060910

48. Abolfath R, Baikalov A, Bartzsch S, Afshordi N, Mohan R. The effect of non-ionizing excitations on the diffusion of ion species and inter-track correlations in FLASH ultra-high dose rate radiotherapy. *Phys Med Biol* (2022) 67:105005. doi:10.1088/1361-6560/ac69a6

frontiers | Frontiers in Physics

TYPE Original Research
PUBLISHED 11 September 2023
DOI 10.3389/fphy.2023.1185237



OPEN ACCESS

EDITED BY
Fabio Di Martino,
Pisana University Hospital, Italy

REVIEWED BY
Giuseppe Felici,
Sordina IORT Technologies S.p.A., Italy
Anna Vignati,
University of Turin, Italy

*CORRESPONDENCE
Kristoffer Petersson,
✉ kristoffer.petersson@oncology.ox.ac.uk

RECEIVED 13 March 2023
ACCEPTED 21 August 2023
PUBLISHED 11 September 2023

CITATION
Vojnovic B, Tullis IDC, Newman RG and Petersson K (2023), Monitoring beam charge during FLASH irradiations. *Front. Phys.* 11:1185237. doi: 10.3389/fphy.2023.1185237



# Monitoring beam charge during FLASH irradiations

Borivoj Vojnovic[1], Iain D. C. Tullis[1], Robert G. Newman[1] and Kristoffer Petersson[1,2]*

[1]Department of Oncology, Oxford Institute for Radiation Oncology, University of Oxford, Oxford, United Kingdom, [2]Department of Haematology, Oncology, and Radiation Physics, Skåne University Hospital, Lund University, Lund, Sweden

In recent years, FLASH irradiation has attracted significant interest in radiation research. Studies have shown that irradiation at ultra-high dose rates (FLASH) reduces the severity of toxicities in normal tissues compared to irradiation at conventional dose rates (CONV), as currently used in clinical practice. Most pre-clinical work is currently carried out using charged particle beams and the beam charge monitor described here is relevant to such beams. Any biological effect comparisons between FLASH and CONV irradiations rely on measurement of tissue dose. While well-established approaches can be used to monitor, in real time, the dose delivered during CONV irradiations, monitoring FLASH doses is not so straightforward. Recently the use of non-intercepting beam current transformers (BCTs) has been proposed for FLASH work. Such BCTs have been used for decades in numerous accelerator installations to monitor temporal and intensity beam profiles. In order to serve as monitoring dosimeters, the BCT output current must be integrated, using electronic circuitry or using software integration following signal digitisation. While sensitive enough for FLASH irradiation, where few intense pulses deliver the requisite dose, the inherent insensitivity of BCTs and the need for a wide detection bandwidth makes them less suitable for use during CONV "reference" irradiations. The purpose of this article is to remind the FLASH community of a different mode of BCT operation: direct monitoring of charge, rather than current, achieved by loading the BCT capacitively rather than resistively. The resulting resonant operation achieves very high sensitivities, enabling straightforward monitoring of output during both CONV and FLASH regimes. Historically, such inductive charge monitors have been used for single pulse work; however, a straightforward circuit modification allows selective resonance damping when repetitive pulsing is used, as during FLASH and CONV irradiations. Practical means of achieving this are presented, as are construction and signal processing details. Finally, results are presented showing the beneficial behaviour of the BCT versus an (Advanced Markus) ionisation chamber for measurements over a dose rate range, from <0.1 $Gys^{-1}$ to >3 $kGys^{-1}$.

KEYWORDS

**FLASH, LINAC, radiobiology, electron beam charge, dosimetry, pre-clinical irradiation, pre-clinical radiotherapy**

## 1 Introduction

The study of ultra-high dose rate (FLASH) irradiation using charged particle beams has attracted significant recent interest. A number of studies have demonstrated that FLASH irradiation reduces the severity of toxicities in normal tissues compared to irradiation at conventional dose rates (CONV), as currently used in clinical practice [1–8]. The mechanism responsible for reduced tissue toxicity following FLASH radiotherapy has not yet been

elucidated and it is likely that both basic and pre-clinical work will proceed for some time to come. Understanding the FLASH effect in multiple tissue sites and species will be essential before widely applying the technique in clinical studies [9–15].

One of the major factors limiting the preclinical use of FLASH RT is the difficulty in obtaining accurate dosimetry and in measuring FLASH irradiation parameters (such as dose, mean and instantaneous dose rate, dose per pulse, etc.) using well-established, conventional radiation detectors [16, 17]. The ability to monitor and control the output of radiation source during both FLASH and reference CONV scenarios is particularly desirable. Commonly, radiation must be monitored in real time. For CONV irradiations, transmission ionisation chambers in the head of an electron linear accelerator or within the output beam lines of a charged ion installation can be used. The transmission chambers can be used to monitor dose, dose rate, beam flatness, beam symmetry, and so on, in real time as the beam traverses the chamber. In the case of FLASH irradiations, the accuracy of transmission ionisation chambers suffers because of saturation effects caused by the high dose per pulse conditions present during FLASH18. Several publications have noted the difficulties associated with accurate dosimetry [18, 19] when dose rates in the range of 30 Gy $s^{-1}$ to several MGy $s^{-1}$, delivered in multiple or single pulses are to be monitored. Ion recombination and other effects in ionisation chambers will preclude their use at these high dose rates [20–24] unless they are operated at very high bias voltages and appropriate corrections are applied. Hence, off-line dosimeters like alanine and radio-chromic film are the preferred dosimeters [25–27]; other approaches are reviewed by [28]. To date, most preclinical work has been performed using electron beams generated by linear accelerators (linacs) of energies 4–20 MeV [29–31]. The use of protons for FLASH irradiation, or other hadron beams [32, 33] has also been investigated and it may be possible to adapt the approach described here to such studies.

Maximising the output beam current is usually required for FLASH work, and the extent to which this can be achieved in a given linac design, assuming that beam current is available from the gun, is determined by the available radio frequency (RF) power and other accelerator design parameters, such as the shunt resistance and quality factor of the accelerating waveguide. Typical peak beam currents of 10 mA to 1 A, over pulse widths ranging from 1–4 μs are used for FLASH work, at repetition rates of several hundred macro-pulses per second. CONV irradiations are often performed at similar or lower repetitions rates (10–200 Hz) and lower peak beam currents, or performed with shorter-lasting macro-pulses. In addition to the need to perform dosimetry, it is often useful to be able to return to specific previously used beam characteristics and to have the ability to check performance: an on-line beam charge monitor is thus essential, providing the ability to monitor each output macro-pulse during the irradiation sequence. Indeed, for clinical applications, such monitors are mandatory [34].

# 2 Materials and methods

## 2.1 Non-intercepting beam charge monitoring

Beam current transformers (BCTs) are non-intercepting, inductive current monitors that have shown promise for real-time monitoring of electron FLASH beams [35, 36]. These devices are toroidal inductive sensors where the moving electron charge forms a primary turn that induces a voltage in the secondary toroidal winding. BCTs are based on well-established current transformer design approaches [37] that can be used even at picosecond times [38]. They offer unique advantages whenever time-varying electrical currents (in conductors or in beams) are to be measured. No direct connection to the measured circuit is necessary, ensuring isolation and relative freedom from spurious ground currents.

For a given irradiation geometry and with a given beam energy, measurement of beam charge has been found by others to correlate well with delivered dose [35, 36], as would be expected. We have successfully used, for many years, inductive non-intercepting charge monitoring as a surrogate indicator of dose. It is noted that such monitors are only able to measure the charge pulses leaving the accelerator and not charge pulses impinging on the tissue or target of interest. Such devices must thus be independently calibrated in order to provide a (surrogate) dose readout, and re-calibrated when the working distance is changed [39, 40], or beam scattering [41–43] introduced.

Wide bandwidths (typically 5–20 MHz) are required to monitor microsecond wide pulses that are usually associated with rise/fall times of tens to hundreds of nanoseconds. Means of constructing and analysing such devices have been described [44, 45], where resonances in the secondary winding due to capacitance between the core winding and electrical shields are appropriately damped.

The electron beam can be assumed to be a current filament moving through the axis of a toroidally wound coil of $N$ turns, it can be considered to act as a single-turn primary, generating a current, $i_s$, in the secondary:

$$i_s = N^{-1} d\varphi/dt \tag{1}$$

where $d\varphi/dt$ is the rate of change of magnetic flux due to the moving charge. The output current thus approximates to the first time differential of the beam current. A voltage output is obtained by sampling $i_s$ through a small enough value of output resistance, typically a few tens of ohms. It is noted that little magnetic flux crosses the surface of the secondary winding, none in the ideal case, and the magnetic core thus receives little magnetization. Furthermore, it can be shown that the secondary current is equal in magnitude and phase throughout the secondary, provided that the time of propagation of the magnetic field is considered to be negligible. The secondary current flows at all points simultaneously, particularly when the load resistance is very small. It is thus not necessary for current induced at various points along the secondary to propagate to the output to be monitored. Travelling waves around the secondary thus play relatively little part in such a transformer, although common-mode resonances can be induced in some circumstances [44].

For a pulsed electron linear accelerator in the mega-electron voltage (MeV) range, the voltage induced at the output of a BCT can be readily approximated as a function of the electron density of the pulse and the cross-sectional area of the BCT [46]. Using BCTs to measure the output of FLASH beams is useful because the beam(s) can be monitored in real time with negligible perturbation and, just as importantly, without saturation effects [35]. However, because of the necessary load resistance must have a low value in order to

achieve a suitably low minimum frequency, their sensitivity, for CONV beams in particular, can be limiting. This does not imply that BCTs cannot be used to monitor CONV irradiations, but the signal levels are low and electrical interference from the accelerator and from other sources make their design and implementation challenging.

However, such transformers can be made to operate in a distinctly different manner that permits direct integration of the current pulse; these devices will be termed Beam Current Integrating Transformers (BCITs). A readout of the integrated pulse current is preferred when a readout proportional to beam charge is required. The charge per pulse is proportional to dose delivered by the beam and dose monitoring is of interest during FLASH and CONV irradiations. This integrating mode is achieved by simply loading the secondary coil capacitively and by using a high load resistance: assuming negligible core and loading losses, a resonant circuit is formed, resulting in an oscillating output voltage, $V_s$, across the coil of peak value given by:

$$V_s = Q_p / N \times C \tag{2}$$

Where $Q_p$ = charge flowing through primary = beam charge per pulse; $N$ = number of turns wound on core and $C$ = load capacitance (assuming an infinite load resistance).

It is highlighted that this resonant mode of operation is not particularly novel; such devices were extensively used with low repetition rate accelerators (or single-shot machines) [47–50]. Nevertheless, it has become clear to the authors that BCITs have been largely "forgotten" by the FLASH community and our intention is to stimulate renewed interest in these simple, effective and useful dose monitoring devices. What is novel here is the use of a differential arrangement that allows effective damping of the oscillation initiated by a given charge pulse, in readiness for the "next" pulse charge to be observed. This arrangement can handle very high repetition rates, such as occur during FLASH, while also providing the requisite sensitivity for CONV irradiations.

This resonant operation mode has significant advantages. The voltage across $C$ is proportional to the beam pulse *charge*, rather than to the peak pulse current. For dosimetry purposes, if beam energy and irradiation geometry are invariant, charge measurement is what is needed. If observation of the temporal pulse profile is needed, a current monitoring device is required. This resonant mode offers technical advantages as compared to the (low) resistive load operation: the electronic system for the signal detection is significantly simpler since only low-frequency components are needed. Furthermore, measurement of the resonant peak voltage can be performed at some time after the radiation has ended. Any electromagnetic interference resulting from the accelerator's modulator and radiofrequency system thus does not contribute to the measurement. Finally, the output voltage is significantly higher than that of resistively-loaded BCTs since the resonant circuit operates into a high load resistance. This could be considered as a disadvantage as the circuit loading must be minimised, potentially increasing the likelihood of unwanted electrostatic coupling into the device. However, electrostatic shielding is straightforward to implement.

Any oscillating tuned circuit involves the transfer of energy between inductor and capacitor. This exchange will persist as long as the circuit losses allow; in the devices discussed here, oscillations can last for many hundreds of microseconds or longer. This feature appears unattractive when high pulse repetition rates need to be monitored. After the measurement of the pulse charge, this energy transfer must be damped in readiness for the "next" charge pulse. The simple solution is to introduce, post-pulse-measurement, a significantly lower load resistance that will damp down tuned circuit oscillation: a switched load resistance is suggested. Such switching inevitably introduces additional unwanted charge into the circuit through switch charge transfer processes; this in turn limits the highest output sensitivity that can be reached.

A very simple modification to the basic BCIT is to operate it in a balanced or differential mode by introducing a centre-tap into the inductor, and sensing the output voltage with a differential or instrumentation amplifier. Damping resistors are then switched in at both ends of the centre-tapped inductor at the time the resonance is to be damped. Since these introduce equal and opposite charges, they no longer contribute to spurious signals and sensitivity is maintained. The ultimate sensitivity has been shown [51] to be limited by the band-limited noise introduced by the tuned circuit shunt resistance. With careful design, the sensitivity can reach $10^{-11}$ coulombs for short-lasting pulses. For microsecond long pulses from typical electron linacs, there is little point in aiming for sensitivities much better than $10^{-10}$ coulombs per pulse (e.g., peak current of 25 μA for 4 μs): the radiofrequency-induced dark current associated most linacs used for radiobiological studies is well above this peak current. BCITs even with sensitivity near to $10^{-9}$ coulombs per pulse can thus be considered to be near-perfect charge monitoring devices for use with electron linacs.

Differences between BCT, BCIT and differential BCIT operating modes are illustrated in Figure 1. A conventional BCT is shown in the top left panel. The temporal pulse shape of the electron pulse is reproduced by the wideband amplifier and this must be integrated in subsequent circuitry or software to provide an output proportional to beam pulse charge. A BCIT is outlined in Figure 1, lower left panel: the secondary inductance resonates with the load capacitance $C$ resulting in a ringing waveform that decays slowly, at a rate defined by circuit losses and by $R_p$; this arrangement is not appropriate for sensing repetitive pulses, unless $R_p$ is made low. When the value of $R_p$ is high and circuit losses are low, the pulse charge can be measured many hundreds of microseconds after the passage of the electron pulse, essentially eliminating all interference from the accelerator power systems.

A switched damping resistor, $R_d$, is introduced in the top panel on the right of Figure 1. While this can quickly damp the resonance, after a few cycles when $R_p$ is high, charge feedthrough from the switch introduces spurious signals in the output. At low charge levels, these unwanted signals can all too easily interfere with any subsequent charge signal processing. Nevertheless, for measuring charges of the order of a $>10^{-8}$ coulombs, this arrangement is perfectly acceptable for FLASH work. A much more sensitive arrangement can be constructed along the lines shown in Figure 1 bottom right. Here a symmetrical arrangement, using a centre-tapped core winding and a pair of reset switches and damping resistors, along with a low bandwidth differential amplifier allows substantial increases in sensitivity to be achieved, allowing sub-nanocoulomb charges per pulse to be measured.

In practice, even though the inductor responds to magnetic fields only, some electric field coupling takes place since the cores

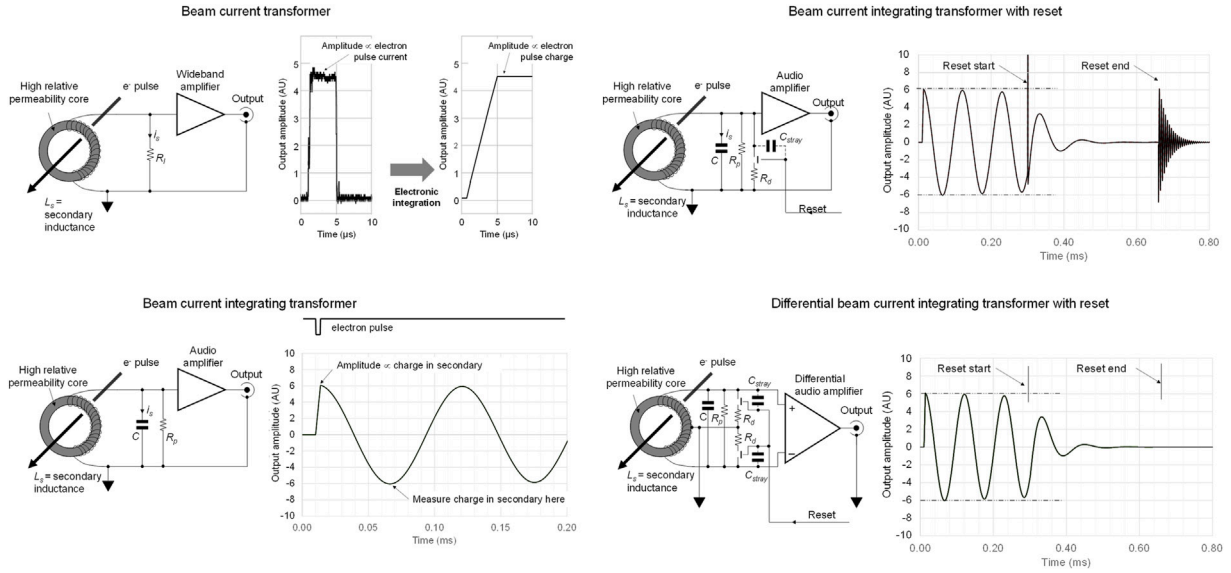


FIGURE 1
Top left: conventional beam current transformer with secondary current $i_s$ flows through load resistor $R_l$; the electron pulse waveform is reproduced and may be integrated in subsequent electronic processing. Bottom left: conventional beam current integrating transformer where $i_s$ initiates a resonance. Top right: beam current integrating transformer with damping, where artefacts from reset switch charge feedthrough through $C_{stray}$ result in spurious signal that may interfere with subsequent processing of signals. Bottom right: differential beam current integrating transformer, where all reset artefacts are suppressed, leaving the system ready for the 'next' electron pulse.

tend to be physically large in order to allow beam traversal. A differential arrangement is much less prone to such interferences. An electrostatic shield can be placed around the inductor to further eliminate any such unwanted signals.

It is noted that the switched damping resistor could also be replaced by using a soft, slow release that allows the shunting impedance to rise slowly. This approach has been exploited [48] using a field-effect transistor operated as a voltage-controlled resistance, driven by an exponentially decaying shorting waveform. Such an approach would still require time to complete the reset process. When used with high repetition rate machines, the differential approach presented here offers a fast-acting and easy-to-implement solution.

## 2.2 BCT and BCIT output comparison

It is constructive to compare the performance of BCTs, BCITs and differential BCITs and examine practical requirements. While the BCT signal is clearly simpler to 'understand', describing the pulse amplitude, shape and width, the BCIT signal carries information only about pulse-integrated charge. Attempts to derive other pulse characteristics as provided by the BCT from a BCIT signal, through differentiation of the leading edge, would result in comparable or worse signal-to noise ratios than what BCTs provide.

Both high and low frequency specification of BCTs needs to be considered. For typical 1–4 μs wide linac macro-pulses, a decay time constant of at least $\times 10^2$ to $\times 10^3$ higher is required if the pulse is to be faithfully reproduced. While BCTs with responses down to DC have been developed [52, 53], the decay time constant in simple single-winding BCTs is determined by the secondary inductance $L_s$ and the load resistance, $R_l$:

$$\text{BCT decay time constant} = L_s/R_l \tag{3}$$

Typical inductances of 100 mH are necessary when $R_l$ is 50 Ω. The inductance can be calculated using details presented in Supplementary Information S1. Core permeabilities range from $\mu_r \approx 10^3$ to $>10^4$ for typical MnZn ferrites, while for high-nickel magnetic alloy tape wound cores [54] these values can reach $5 \times 10^4$ or higher; the highest permeability materials are amorphous or nanocrystalline soft magnetic materials [55] or "supermalloys" [56] that reach relative permeabilities of $>10^5$ or higher. A high permeability allows $N$ to be reduced for a given sensitivity, and improved performance can be obtained with nanocrystalline materials compared to high permeability ferrites. With ferrites, typically 50-100 turns are required to reach the required inductance.

In the case of BCITs, the resonance frequency, $f$, is given by the usual tuned circuit relation ($L$ = inductance, $C$ = capacitance), when $R_p$ is made large and winding losses can be neglected:

$$f = 1/2\pi\sqrt{LC} \tag{4}$$

Similar limitations to those associated with BCT inductance apply to BCITs in order to ensure that charge pulses are integrated with minimal error. It can be shown [48, 49] that the percentage error Δ in integrating a radiation pulse width, $\tau$, using a BCIT resonant frequency $f$ can be approximated by:

$$\Delta(\%) \approx f^2\tau^2 \times 1000/6 \tag{5}$$

For a <1% integration error, a resonant frequency of <~22.2 kHz should be attained. Using the same inductance as in the BCT (100 mH), this suggests a ~500 pF integrating capacitor.

In the above example (100 turns) a typical FLASH electron pulse current of 50 mA peak (200 nC in 4 μs) will thus result in a secondary current of 0.5 mA peak. A peak output voltage of 25 mV across a 50 Ω load will be obtained using a BCT.

The output voltage of a BCIT, for the same charge and number of turns can be calculated using equation (2) and found to be 4 V, a factor of 160x higher, clearly demonstrating the superior output afforded by the use of a BCIT. Furthermore, a BCT output would need to be boosted by a high bandwidth amplifier, of bandwidth >5 MHz for typical slow rise/fall times present in a linac output pulse. In the case of a BCIT, subsequent processing bandwidths need not exceed a few tens of kHz.

The minimum charge detectable by a BCT depends on the noise voltage generated by a load resistor and by current noise performance of any subsequent amplifier. When the load is, e.g., 50 Ω, the resulting thermal noise is ≈ 2 μV over a 5 MHz bandwidth and at room temperature, as derived from the usual thermal noise relation:

$$\text{RMS noise} = 4k_B T R_l B \tag{6}$$

Where $R_l$ = load resistance; $k_B$ = Boltzmann's constant; $T$ = absolute temperature; and $B$ = detection bandwidth.

In order to perform a comparison, it will be assumed that the gain of the subsequent amplifier is 160x, and that a well-designed voltage amplifier would have a noise voltage density of ~1–2 nV $Hz^{-1/2}$, resulting in a total input-referred noise voltage of ~500 μV. The rms signal-to-noise ratio (SNR), for a 200 nC charge, in this example is 50:1. Of course once the BCT output is integrated in a subsequent signal processing system, the Signal to Noise Ratio (SNR) improves as the measurement bandwidth is reduced.

In the case of the BCIT the noise performance is determined by (a) the thermal noise of the real part of the effective source impedance, (b) the noise generated by the amplifier input current flowing across $R_p$ and, (c) the noise introduced by the preamplifier. This last component can be considered to be negligible. The magnitude of the first two components has already been analysed in a detailed manner [51] and will not be repeated here. It has been shown to be:

$$\text{rms noise of components (a) and (b)} = \sqrt{k_B T + \frac{1}{2} q i_{in} \frac{R_p}{C}} \tag{7}$$

where $i_{in}$ is the amplifier input current and $q$ is the charge of an electron.

The value of $R_p$ is dominated by core and winding losses and typical values will be a few mega-ohms. Furthermore, the noise bandwidth is centred on the narrow, tuned circuit resonance and values of the coil inductance, the core losses, etc. must be included to derive the expected noise. Typically, noise voltages of the order 20–100 μV, significantly more that the contribution due to (c). It is noted that any subsequent filtering of the BCIT signal will not yield an improvement in the SNR, since the noise spectral density is associated with a clearly pronounced peak at the BCIT resonance frequency. This also indicates that only the peak output value, or the peaks of the first few cycles, yield information with a high SNR.

The rms SNR in a BCIT, for a 200 nC charge, is thus >> $10^4$:1 and this is achieved without any signal processing. In the case of the differential BCIT, it would not be expected that this SNR would reduce significantly, since the amplifier noise contribution would remain small.

If we were to integrate the BCT output for, say ~100 μs, (a typical time similar to when a BCIT reading would be obtained) its SNR would improve to ~2000:1; this is still worse that what can be achieved with a BCIT.

However, the noise performance of the BCT can be improved substantially by increasing the core permeability and achieving the required inductance using fewer turns and hence providing a higher $i_s$. Furthermore, as the pulse width is reduced, the BCT's SNR for a constant charge pulse improves. A significantly better approach is to increase the BCT $L_s/R_l$ ratio by following it with a transimpedance (virtual earth) amplifier, as recently highlighted [57]. The low number of turns (<10 typ.) needed to reach the required sensitivity (high $i_s$), may, however, introduce some variations in the output signal when the beam position is varied, depending on the leakage inductance. In fact, BCTs can be used to determine the spatial characteristics of electron beams [58]. Very high permeability cores would then be required (~$10^5$) to support the pulse width and the requirement for high detection bandwidths would remain. Moreover, the permeability of such cores drops drastically with frequency. In addition, when short rise/fall time are used, connection to the virtual earth can result in reflections and ringing that spoil the edge response. In addition, the need for subsequent signal processing remains. For comparison, a BCIT fashioned in this way can handle very long, low amplitude charged pulses [59, 60].

Whichever approach is used, a BCT always operates as an alternating current transformer and cannot transmit a direct current component: the transformer output voltage must have positive and negative portions of equal area [47]. This implies that there is a need for some form of baseline restoration to be applied. In addition, the winding resistance places a limit on the highest $L_s/R_l$ ratio achievable. This winding resistance can be compensated for by following the BCT with a stage with a negative input resistance [61] or other topologies can be used [52, 53].

The use of BCIT is generally advantageous as large signals can be readily obtained for typical linac macro-pulses used during both FLASH and CONV irradiations, using cores of even moderate relative permeability. More importantly, when CONV irradiations are performed, the SNR of BCTs can all too easily become limiting. One of the specific advantages of the BCIT is that the same charge monitoring system can be used for CONV and FLASH irradiations and that measurements are acquired long after most accelerator-induced interference has elapsed.

The BCIT described here was used with an in-house developed, FLASH-optimised [13] 6 MeV nominal electron energy horizontal-firing electron linac. This is constructed around a travelling wave accelerating waveguide (type SL75TW, Elekta, Crawley, United Kingdom), an S-band (2.89 GHz) magnetron radiofrequency source (type MG5125, Teledyne e2v—United Kingdom, Chelmsford, United Kingdom) conventionally modulated by a thyratron (type CX1140, Teledyne e2v—United Kingdom, Chelmsford, United Kingdom) and a 4 μs pulse forming network. Radiofrequency, and hence electron, pulse triggering is performed by a phase-locked-loop with a 25 Hz reference (derived from 50 Hz ac mains) capable of providing pulse repetition rates in the range 25–300 Hz. Electrons are generated by a diode type of gun that is pulsed synchronously with the radiofrequency source and that can deliver any required number of pulses. The electron beam current is varied by changing the thermionic emission temperature of the gun.

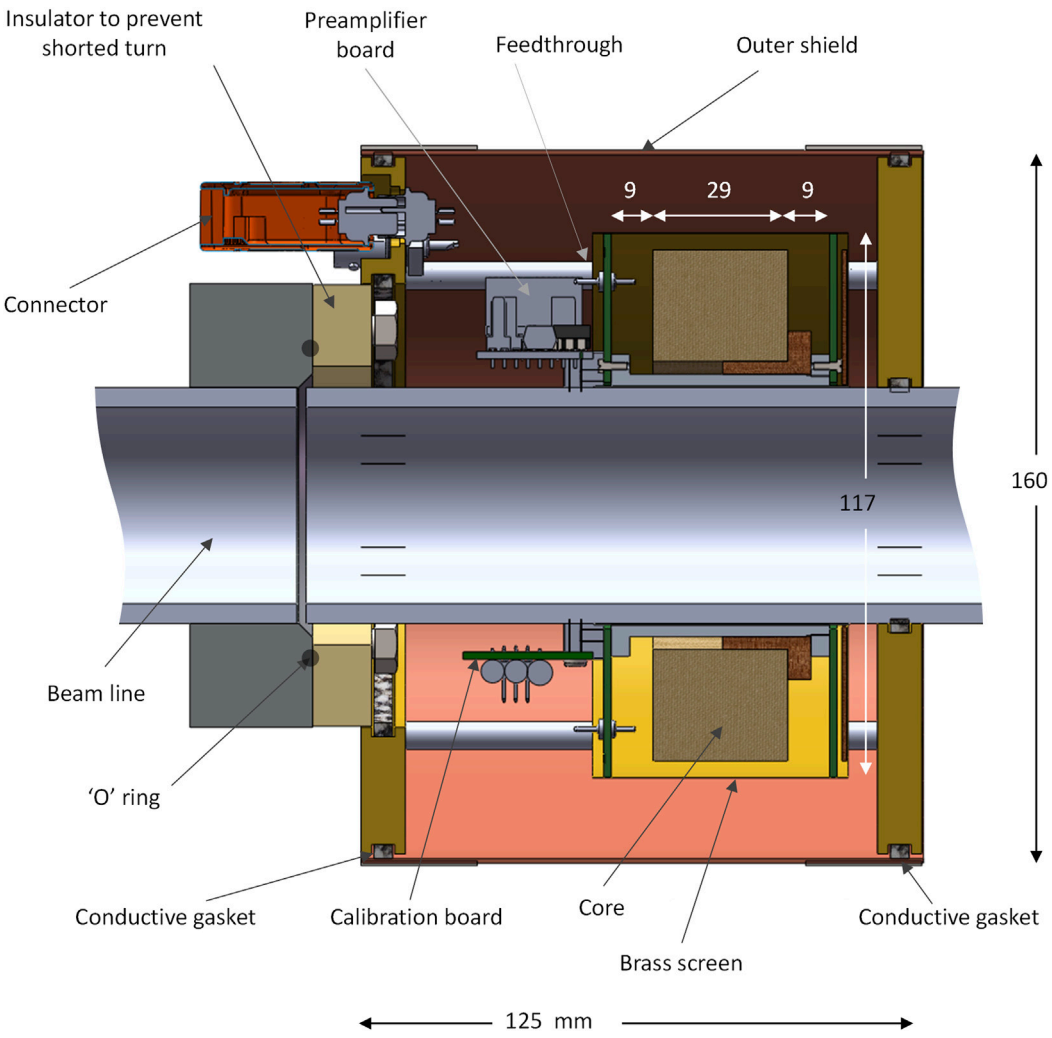


FIGURE 2
Construction of BCIT around a 50.8 mm diameter beam line. The wound core is enclosed in an electrostatic shield fashioned from copper-clad FR4 printed circuit board end cheeks a brass screen cover; a break in the board copper ensures that a shorted turn is not formed. The electron beam return path is ensured by using an outer shield made from brass end-plates and a copper outer cover, using conductive gaskets to ensure good electrical continuity. An insulating portion on the beam line prevents the formation of a shorted turn in this outer metalwork. A differential preamplifier board and a calibration board are fitted on either side of the beam line is fitted next to the wound core as is a calibration board.

The BCIT is placed after the accelerating waveguide and before a thin output window (10 μm thick beryllium-copper foil); electron pulses are fired into a temperature controlled experimental area. Additional beam scattering is usually employed, provided by a titanium foil, 30 μm thick, positioned 8.5 mm downstream from the output window.

Since a travelling wave type of electron linac is used, the beam output energy can be readily varied by slight detuning of the magnetron matching network. The beam energy is monitored [62] and is maintained at a constant value irrespective of electron pulse amplitude.

## 2.3 A practical differential BCIT

A differential BCIT was developed around a ferrite core of 26 ± 0.8 mm thickness, 107 ± 2 mm outer diameter and 65 ± 1.3 mm internal diameter (3F3 material from Ferroxcube, Netherlands, T107 format, available at the time of writing from Farnell Ltd, Canal Rd, Armley, Leeds United Kingdom as part #2103396). The relative permeability of the 3F3 ferrite is ~2000 at 25°C, though this value rises with temperature to ~2,500 at 50°C. We note that this particular ferrite is far from optimal but was readily available at low cost. If required, significantly better performance can be achieved by using other core types, as listed in Supplementary Information S2.

The core was first protected with transformer tape and was wound with 2 × 70 turns using 0.55 mm diameter enamelled copper wire, spaced ~1 mm between turns on the core inner diameter. The wound core was dipped in polyurethane varnish, dried, overwound with insulating transformer tape and again dipped in varnish. The core inductance factor is specified as 5.184 μH, suggesting that an inductance of 101.6 mH would be obtained.

The completed core is then fitted onto the accelerator output beam line, as shown in Figure 2. An earthed electrostatic screen surrounds the core, coil connections are brought out of the inner

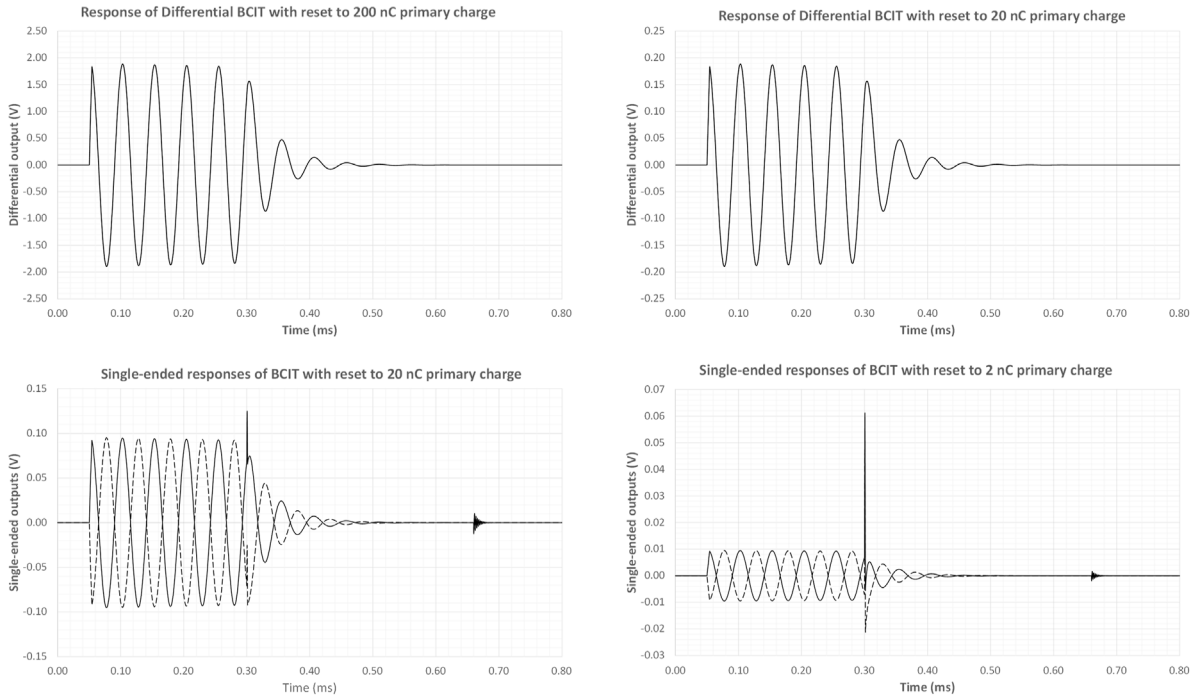


FIGURE 3
LT Spice Simulations of BCIT responses for different charge inputs. Additional charge is introduced by the leading edge of the reset pulse while the trailing edge excites a series resonance from the feedthrough capacitance and the transformer inductance. These additional charges become increasingly prominent as the primary charge is reduced, but are eliminated through differential sensing.

end-cheeks through low loss PTFE feedthroughs and these connect directly to a differential amplifier placed within the outer shield. This inner shield makes it easy to perform electrical calibrations without risk of interference injection. The outer shield is only connected to the beam line and serves to provide a return path for the electron pulse back to the accelerator.

Other construction methods can also be used without significant changes in performance; the approach described here was appropriate for our installation. It is, of course, essential that no shorted turns are accidentally formed; it is also important that the whole system is made mechanically rigid so as to prevent induction of signals from external magnetic fields. Furthermore, since stray capacitance is always present, a rigid mechanical construction ensures stable sensitivity.

The differential BCIT was simulated using LTspice XVII® [63] and the circuit was excited with pulses of different charge. The simulation was performed using measured inductance, capacitance and core parameter values; the resonance damping resistors, $R_d$, were 2 × 15 kΩ and 3 pF switch feedthrough capacitance was assumed. Following resonance excitation and a few cycles of oscillation, a reset pulse (~360 μs wide) was simulated. The differential outputs, shown in the top panels of Figure 3, show the expected response and clean damping of the resonance. The lower panels of Figure 3 show the single-ended responses at either end of the transformer. It is clear that as the input charge is reduced, artefacts resulting from reset switch feedthrough become more prominent at the differential approach eliminates these unwanted signals.

## 2.4 BCIT signal processing

The differential damping pre-amplifier is presented in Figure 4. This is based around an INA111 instrumentation amplifier, U1 in Figure 4, (Texas Instruments Inc, Dallas, Texas) that features low input bias currents and that provides negligible loading of the tuned circuit. The resonance damping was achieved by using U2 and U3 in Figure 4, a pair of field-effect opto-couplers, (type H11F1, Onsemi, Phoenix, Arizona, United States). The gain of the instrumentation amplifier is made switchable, using x1, ×10 and ×100 relative amplification factors, permitting a very wide dynamic range to be covered. Gain switching is performed with a pair of reed-relays (type 9007-12-01, Coto Technology, Tokyo, Japan) energised with a bipolar control signal through diodes D1-D4. The gain-setting resistor values shown provide the correct gain within ±0.02% and were made up using selected resistors, measured with a component bridge (model LCR400, Thurlby-Thandar Instruments Ltd. Huntingdon, Cambs., United Kingdom). The full-scale output, at a ×1 gain, corresponds to 1 μC. Should a less sensitive system be required, the value of tuned circuit capacitance (C in Figure 4) can be increased and the resonant frequency lowered. For convenience, we used a value for C such that a sensitivity of 100 nC/V was obtained: for 140 turns, 714.3 pF is required, made up from the parallel combination of a physical tuning capacitor and system stray capacitance; see Supplementary Information S3 for details.

No physical $R_p$ resistor is fitted across the tuned circuit. Core losses are responsible for an equivalent shunt resistance, the value of which can be estimated from measurement of tuned circuit

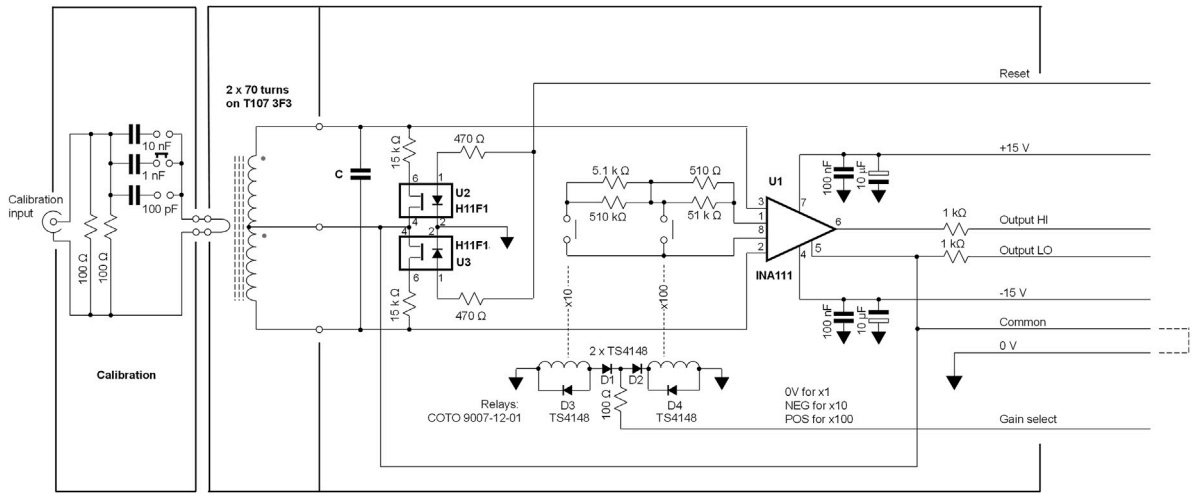


FIGURE 4
Circuit diagram of the BCIT differential preamplifier. The circuit is constructed on a double-sided printed circuit board, 85 × 25 mm.

bandwidth *BW* or its quality factor (*QF*). This can be determined using the usual tuned circuit relationships:

$$BW = 1/R_pC \tag{8}$$

$$QF = R_p\sqrt{L_s/C} = R_p/2\pi L_s = 2\pi f R_p C \tag{9}$$

We did not perform a detailed analysis on core losses, since the complex permeability of many commercially available soft ferrites (such as the 3F3 material used in this work) varies with frequency; nevertheless, straightforward modelling approaches are available [64] for readers who may be interested in using alternative ferrites. In this application, core losses are quite acceptable and cause a repeatable decay of <<0.5% of the integrated charge signal in the first quarter cycle of the resonance.

Photographs of the internal components of the charge monitor are presented in Figure 5. A "break" in the printed circuit board end-cheek prevents the formation of a shorted turn. No special precautions were used during construction other than ensuring that the differential amplifier input circuitry is arranged in a symmetrical manner.

Absolute charge calibration is achieved by using a single turn winding and a series capacitor across a voltage step generator. A precision polystyrene capacitor, in the range 0.1–10 nF and a known voltage step thus generate a known charge input. In our set-up we are able to choose between three capacitor values, as shown on the left of Figure 4 and on the right of Figure 5.

Although output data can be captured and analysed directly on a modern digital oscilloscopes with a deep memory, it is convenient to use a peak detector to sample the first negative peak of the differential amplifier output. This circuitry is shown in Figure 6 and is installed remotely from the charge sensor. A simple difference amplifier, U4, (type INA133, Texas Instruments Inc, Dallas, Texas, United States) takes care of any common mode voltages that may be introduced between the two locations. A conventional peak detector, formed by U5-7 and D5-6, provides the required output signal that can be subsequently sampled. The high slew rate of U5 (type ADA4637-1) copes with reverse recovery while U7 (type AD825) prevents droop on the peak-hold capacitor, 10 nF polystyrene, while the analogue switch, U6, type ADG1201 features a <1 pC charge injection. These devices are manufactured by Analog Devices Inc (Wilmington, MA, United States).

Any small DC offsets can be corrected using a trimmer potentiometer. There is a 4% loss resulting from the use of two 1 kΩ line isolating resistors at the output of the differential amplifier. This is readily compensated for in software. Finally, a generic operational amplifier is used to drive the gain control line from logic gain-control inputs.

A transient digitiser, (PicoScope 6403, 200 MHz Bandwidth, 1 GS/s, 512 MS memory; Pico Technology, St Neots, Cambs., United Kingdom) is used to acquire charge data from the beam pulses. Alternatively, a custom-designed digitiser (Supplementary Information S4) can be used to provide statistical data of beam performance, pulse counting, etc. and to stop accelerator pulsing when the required charge or dose is delivered.

## 2.5 Timing

There is nothing particularly critical about timing signals required by the BCIT. While the device could be operated in a mode where a reset pulse is generated a few milliseconds after an output above, e.g., 10 mV were detected, in practice it is much simpler to use a pre-trigger pulse derived from the accelerator timing system. This pre-trigger pulse is delayed and acts as a reset pulse, e.g., <2 ms after the linac pulse. Any jitter in this pulse is not critical, provided enough time is allowed for the reset action (>0.5 ms) and for any data acquisition systems to acquire and transfer charge data. Since most linacs operate at repetition rates of <500 Hz, this requirement is easily satisfied.

## 2.6 Beam measurements

Dose deposition measurements were performed using solid water (15 × 15 $cm^2$ rectangular slabs to a total of 10 cm of RW3,

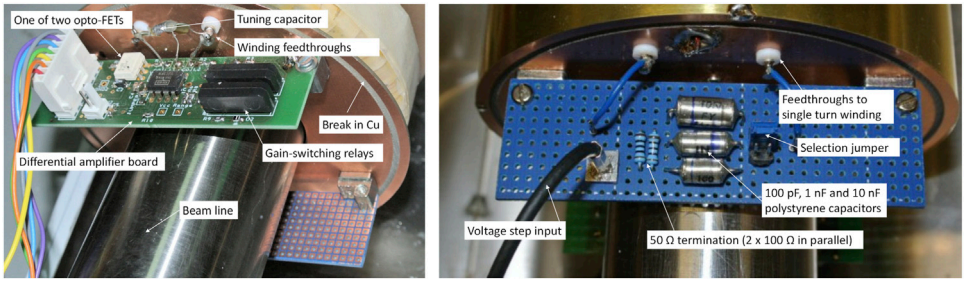


FIGURE 5
Practical details of BCIT front-end electronics. Left: the BCIT differential preamplifier board. Right: the BCIT calibration board.

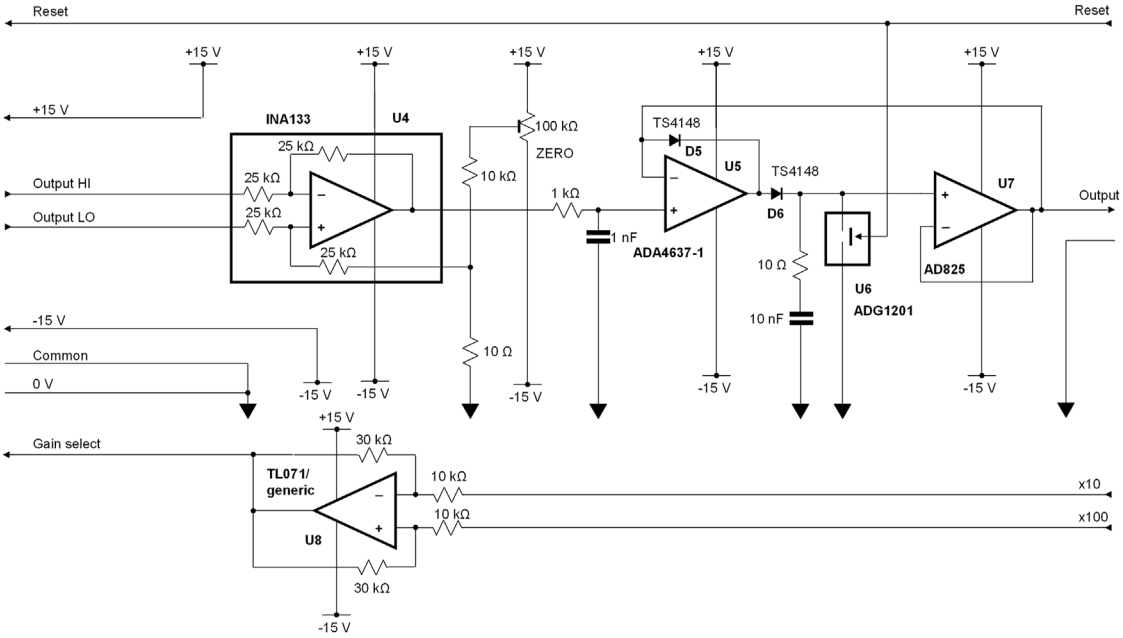


FIGURE 6
Peak detector interface between the differential amplifier and subsequent signal digitisation. For clarity, power supply decoupling components are not included in this circuit diagram.

PTW Freiburg GmbH, Freiburg, Germany) and with radiochromic film (EBT-XD, Ashland Inc., Covington, KY, United States). The films were read out with a film scanner (Epson Perfection v850 Pro, Seiko Epson Corporation, Nagano, Japan) and analysed with ImageJ (version 1.52a, Wayne Rasband, NIH, United States). The films were previously calibrated in a 6 MeV clinical electron beam from a Varian Truebeam (Varian Medical Systems Inc., Palo Alto, CA, United States) linac at the Churchill Hospital site in Oxford, United Kingdom.

An Advanced Markus® ionisation chamber (AMC) (model 34045, PTW-Freiburg, Freiburg, Germany) was used for dose measurement in conjunction with an electrometer (UNIDOS webline, PTW-Freiburg, Freiburg, Germany). The chamber was operated at a bias voltage of −300 V.

# 3 Results

## 3.1 Charge response

The response of the calibrated differential BCIT to electrical charge pulses introduced through the single-turn calibration winding are presented in Figure 7. These data indicate a good dynamic range and acceptable readout errors in the range of 20 pC to 1 μC.

The plots also indicate an acceptable overlap across ranges. On the most sensitive range, differential amplifier and peak detector DC offsets were removed. It was not readily possible to estimate the absolute error as we did not have access to a step generator of adequate precision, but there is no reason to expect that this could

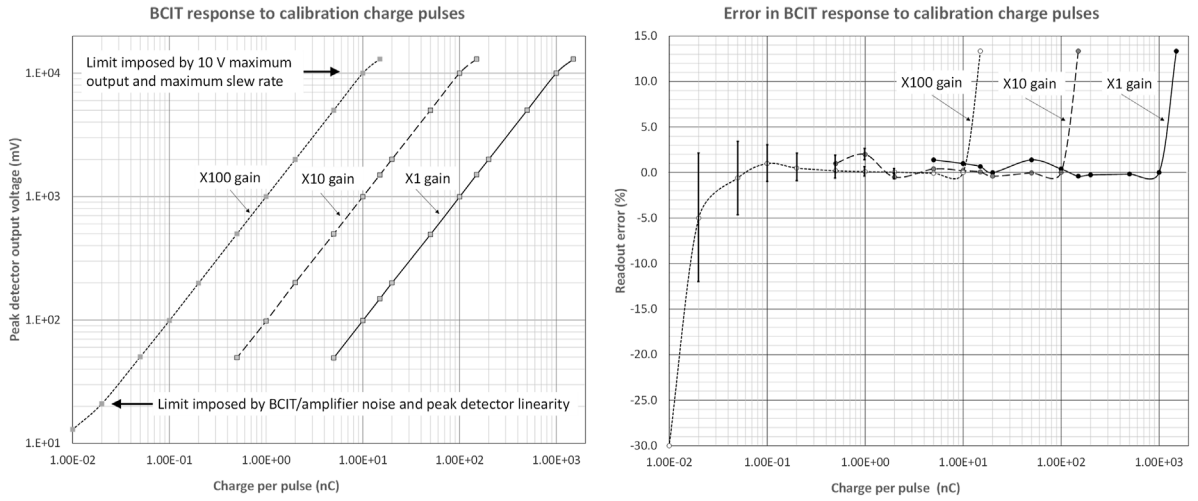


FIGURE 7
Left: Differential BCIT monitor response to electrical charge pulses introduced through the calibration single-turn winding for different gains, covering the range 20 pC/pulse to 1 μC/pulse: the charge is defined by the amplitude of a voltage step from a pulse generator and by the single-turn coupling capacitor. Right: Percentage readout errors across the same gains and the same input charge/pulse range. For clarity, error bars (±1 SEM) are only included for charges below 2 nC. Readings for 25 pulses were used to calculate SEM limits.

not be calibrated out. In use, it is always preferred to use the highest gain possible, commensurate with the ~10 V maximum output.

BCIT responses to our linac output pulses (nominally 3.8 μs wide) are summarised in Figure 8. In the top panel, the differential amplifier gain is set to unity. At the 50 μs/division timebase, not enough time has elapsed to show the start of the reset signal. The charge integration at the start of electron pulse is obvious. However, it is clear that some charge is lost, resulting from core losses, at each half-cycle subsequent to the start of the resonance. This is commensurate with the expected decay resulting from resonance curve bandwidth (Supplementary Information S3).

In Figure 8 middle panel, the differential amplifier gain is set to x10 and the timebase of the recording instrument/display is increased to 0.5 ms/div. The linac pulse repetition frequency is 300 Hz. A clean damping of the resonance is observed starting some 2 ms after the electron pulse. Finally, in the lower panel of Figure 8, the amplifier gain is increased to x100. In this last trace, output band-limited baseline noise is observed ~5.6 mV rms or ~8 mV peak-peak, (equivalent to ~8 pC peak-peak). This narrowband noise waveform is just what would be expected in a resonant system such as that used here. Inevitable mechanical vibrations of our beam line contribute to this noise, as do varying magnetic fields not related to the beam pulse. Charges per pulse of <~20 pC on a pulse-pulse basis should be avoided, corresponding to 20 mV output (×100 gain) and ~5 μA peak pulse current. However, since FLASH is usually performed over <200 ms, charge from ten or more pulses is summed and the noise induced errors can be considered negligible, even when lower peak currents are employed during longer-lasting CONV irradiations. The charge monitor can be used to good effect to optimise the accelerator tuning during FLASH irradiations, as shown in the Supplementary Information, Supplementary Figure S4.

## 3.2 Application of the differential BCIT as dose monitor

As mentioned earlier, charge and dose are distinctly different physical quantities. Nevertheless, dose can be *monitored* with a charge monitor when beam energy, beam position and beam scattering are kept constant. In our case, since the core was wound evenly and since the beam diameter within the monitor is small we would not expect to, and we do not, observe significant changes in response to a given charge resulting from beam movement. On the other hand, any angular beam movement is likely to affect the dose distribution at the sample.

In Figure 9, measurements of dose with radiochromic film (mean across a 5 × 5 $mm^2$ areas in the centre of films, 23 × 34 mm) are compared with measurements of charge from the AMC and with beam charge as determined by the BCIT. Both film and the AMC were positioned in the centre of the horizontal beam, at 10 mm depth in solid water, and at a source-to-surface distance (SSD) of 50.0 cm, (see Supplementary Information S7) and measurements of charge from the BCIT, during CONV irradiations at 25 Hz pulse repetition rate and low pulse currents (left panel) and during FLASH irradiations at 300 Hz repetition rate and high pulse currents (right panel). The charge per pulse was varied by adjusting the beam injection at the accelerator's gun and all data at a given charge per pulse were acquired simultaneously. Our installation includes an energy monitor [62] and the data presented in Figure 9 have been acquired under conditions where the energy has been maintained constant (at 6 MeV).

While the BCIT can readily monitor dose per pulse ranging from <<2 cGy/pulse to over >>5 Gy/pulse, many older linacs, such as ours, are subject to beam loading effects [65, 66] that inevitably result in changes of beam energy at very high charges per pulse. More modern linac designs are less prone to such effects, and BCITs

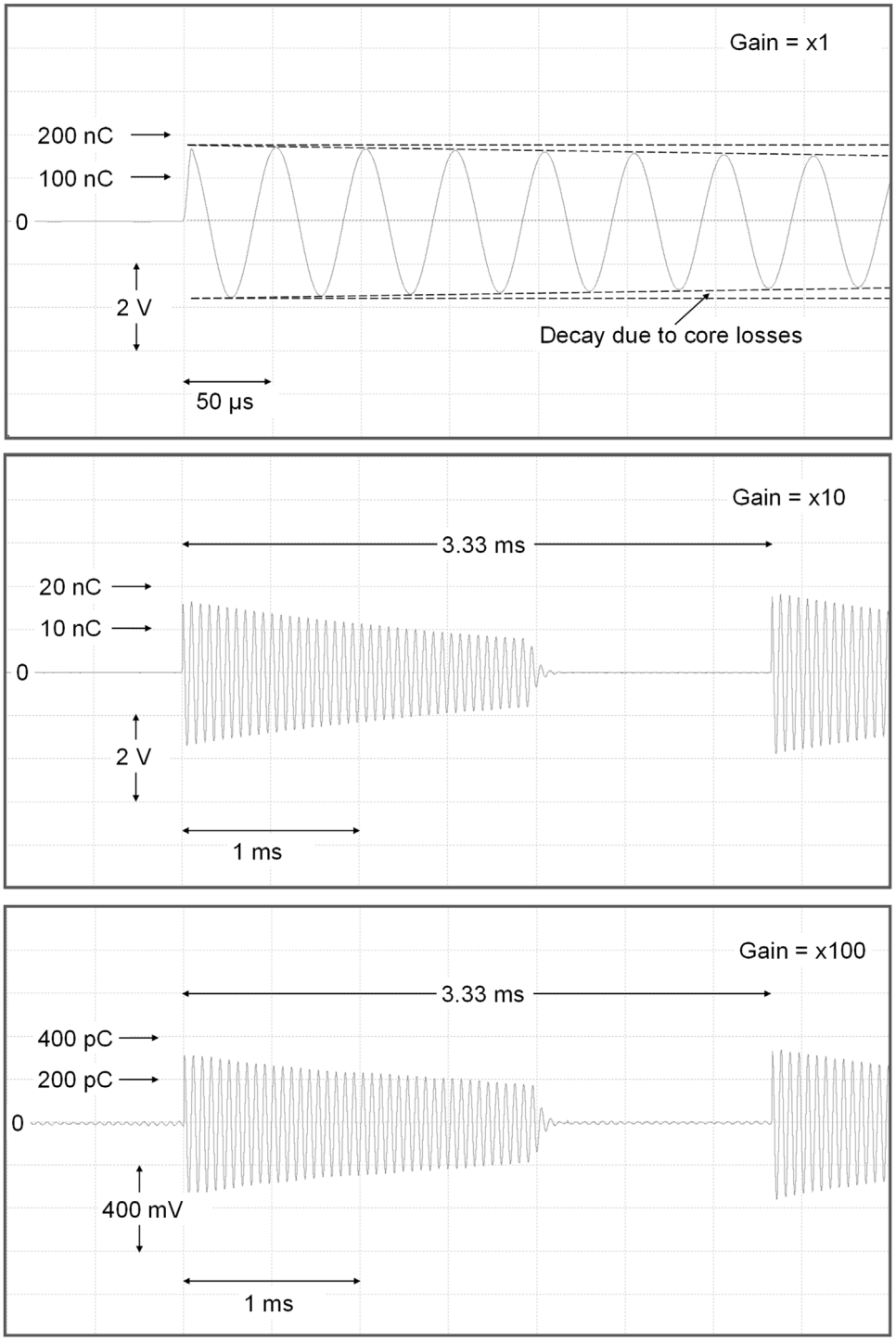


FIGURE 8
Responses of the differential BCIT to individual 3.8 µs linac electron pulses, ranging from 330 pC to 170 nC, using sensitivities of 100 nC/V (top). 10 nC/V (middle) and 1 nC/V (bottom).

can then operate as excellent dose monitors well above several tens of Gy/pulse.

At low charges per pulse, the readout from the AMC is linear and dose monitoring can be performed successfully, as would be expected, as shown on the left panel of Figure 9.

However, at high charges per pulse, and doses per pulse above 0.2–0.5 Gy, the AMC output is no longer proportional to dose per pulse or charge per pulse: the AMC's ion collection efficiency decreases as the dose per pulse increases [18, 67, 68], in accordance with Boag theory, extended to include a free

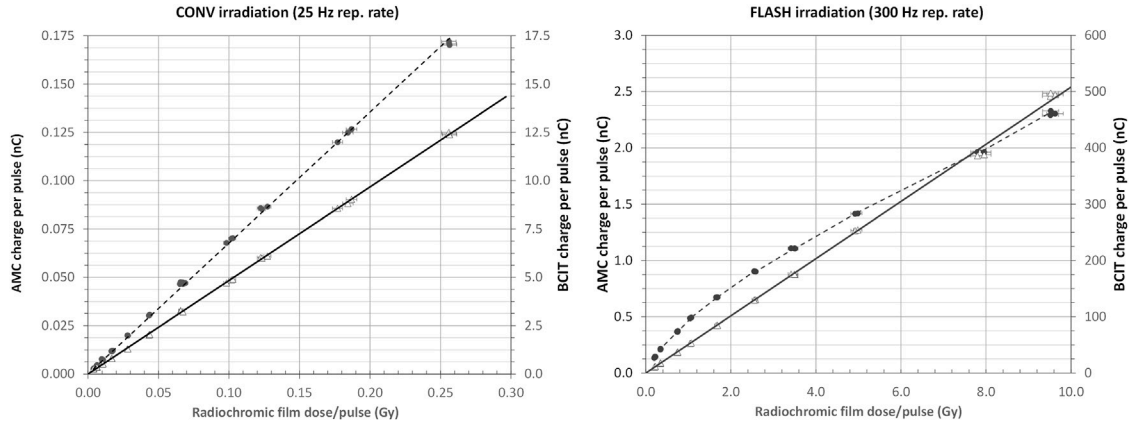


FIGURE 9
Left panel: Response of AMC (dotted line and filled circles) and BCIT (solid line and open triangles) dose monitors during CONV irradiation performed with low peak current, (~25 μA - 1 mA) low repetition rate (25 Hz) electron pulses. Right panel: Response of AMC (dotted line and filled circles) and BCIT (solid line and open triangles) dose monitors during FLASH irradiation performed with high peak current, (~1–>100 mA) high repetition rate (300 Hz) electron pulses. In both panels, the error bars correspond to a 2% uncertainty in dose measurement with radiochromic films.

electron component [69, 70] as well as other experimentally derived corrections [24, 71]. Linearity is, however, preserved in the BCIT's response, as shown in the right panel of Figure 9, up to at least ~10 Gy per pulse. The relationship between beam charge and dose is, of course dependent on the irradiation geometry.

In its current state, our accelerator provides only nominal 3.8 μs wide pulses as the short-pulsing driver has been de-commissioned. Many other installations reduce the pulse width for CONV irradiations. We reduce the pulsing repetition rate, down to 25 Hz, from 300 Hz used during FLASH irradiations. The expected variation when shorter pulses are used are presented in Supplementary Information S8. It is clear that the charge monitor, when used for monitoring dose, can provide similar information to "Monitor units (MUs)" conventionally employed [72] for dose delivery monitoring. The long-term (6 months) absolute stability of the calibration of the device has been found to be ±5% (SD) for doses of the order of a few Gy/pulse and ±2.6% (SD) for doses of the order of a few mGy/pulse. These errors include errors resulting from potential beam misalignment. The device can thus provide an indication of dose delivered to a particular sample geometry in real time. Long-term electrical calibrations (i.e., determined by introducing known voltage steps through the calibration winding and capacitor) have been found to be <±0.5% (SD).

## 4 Discussion

A non-intercepting beam charge monitor that can be used for dose monitoring has been presented. It is noted that even though this device is far from optimal, its simplicity and performance make it particularly suitable for use during both FLASH and CONV irradiations. The device is based on a resonant toroidal transformer, arranged in a balanced configuration in order to permit fast damping of the resonance in between electron pulses, a requirement for use with high pulse repetition rates. In principle, with appropriate changes in reset timing, pulse repetition rates in excess of several thousand pulses per second could be handled.

The magnetic performance of the core can be improved substantially by using more stable, higher permeability materials, as described in Supplementary Information S2. The particular core used is, however, readily available at low cost. This charge monitor was installed in 2015 and has operated without problems since that time. We have not observed any radiation-induced damage to the electronics. One potential disadvantage of the approach presented here is that the differential amplifier has to be mounted physically close to the toroidal winding and is thus not readily radiation shielded. Nevertheless, no obvious radiation damage has been observed after several years' operation. The simplicity, immunity from accelerator induced noise and low cost of signal processing are all considered be advantageous.

We have presented results here using nominal 3.8 μs electron pulse width. However, the same device has been used without problems with much shorter electron pulses, down to ~15 ns and below, using a now de-commissioned short pulse driver. Our intention was to highlight operation for commonly used 4 μs linac macro-pulses, where the BCITs offer significant advantages over BCTs that have attracted recent attention when used for FLASH. Although we used a peak detector to provide a charge-pulse readout, software peak detection could also be exploited.

The device described here is appropriate for pulsed electron beams. In principle a lower sensitivity version of the same could be used for emerging photon FLASH sources [73, 74], although the sensitivity of BCTs is likely to be adequate for such work, when intense electron pulses are used on a photon-generating target. Many specialised electron linacs that are used for electron irradiation also generate pulses in the 1–4 μs region and charges in the range 4 nC to ~2.50 μC [75, 76]. Similar beams are generated by FLASH and intraoperative radiotherapy (IORT) machines. For FLASH, typical maximum charges/pulse of 400 nC are used, delivered at 100 mA peak and 4 μs pulse width

(corresponding to ~2.5 × $10^{12}$ electrons). Our monitor readily monitors charge per pulse in this range, with an upper limit of ~1 μC/pulse for a 10 V output signal. For other pulsed charge monitoring applications, charges/pulse ~20 pC can be measured with repetitive sources when much of the BCIT/amplifier noise is subtracted out, corresponding to peak currents of ~5 μA. Though unnecessary for work with linacs, this lower limit can be readily extended by using higher permeability, lower loss cores, as outlined in the Supplementary Information S2, down to a few picocoulombs.

Our results clearly show the benefit of using BCIT to monitor dose delivery during FLASH studies, as the BCIT response is linear with dose (as measured with film) over the dose rate range tested (0.1 $Gys^{-1}$–3 $kGys^{-1}$). Measurements with an ionisation chamber (AMC) in the same dose rate range shows a loss of linearity above 0.2–0.5 Gy per pulse, due to decrease in ion collection efficiency with increasing dose per pulse (Figure 9).

Neither BCTs or BCITs are able to provide beam cross-section and spatial distribution information since they are only sensitive to the beam charge passing through them. Other approaches must be used for determination of beam dimensions, flatness, symmetry energy and other parameters [77, 78].

The BCIT described here is mainly aimed at work with electron macro-pulses generated by electron linacs; dose monitoring must be provided in such machines used clinically, where the IEC 60601-2-1 Medical electrical equipment standard applies [34], in conjunction with IEC 60976 [76]. While a BCT can be used to monitor temporal variations of instantaneous beam current, it requires a large signal processing bandwidth and its output must be digitised, baseline-restored, and integrated in software in order to derive a value for beam pulse charge. Integration is inherent in a BCIT and it does not require a large measurement bandwidth. The sensitivity possible with a BCIT is therefore excellent. While there are few fundamental reasons why a BCT system of comparable sensitivity cannot be developed, practical realisations with BCTs tend to be complex. BCTs demand the use of a few turns in order to provide good sensitivity, and the core must therefore have a very high permeability in order to provide enough inductance to support the pulse width. BCTs can also be constructed in a balanced arrangement in order to provide adequate rejection of accelerator-induced electrical noise [79]. Charge calibration is also much simplified in BCITs compared to BCTs.

BCTs provide information on temporal pulse profiles. In most machines, instantaneous dose rate changes within the pulse are minimised. Nevertheless, the output pulses are rarely associated with a flat 'top' and are often associated with overshoots and undershoots/oscillations during the pulse. Although the FLASH phenomenon is dose-rate dependent, it is unlikely that such dose rate variations within the pulse are responsible for the biological findings and in all published work to date with BCTs, the current pulse is integrated in software.

Other similar machines developed for FLASH work [80–82] and linear induction accelerators [73] provide beams appropriate for monitoring with the device described here. The optimum resonant frequency, for lowest narrowband noise, is ~50–60 kHz and macro-pulses would then be limited to ~1–2 μs. The use of lower number of turns, e.g., 2 × 5–10 turns on very high permeability cores will always be beneficial, provided the resonant frequency is appropriate for the pulse width utilised.

For protons or hadron FLASH irradiations, where charges per pulse are lower and pulse structures are varied [83, 84], the challenges are distinctly different [85]. More complex inductive monitoring such as parametric beam monitors [52, 86] that can operate down to DC or synchronous beam monitors [87] would perhaps be better suited, while other types of monitoring can also be used [88].

## 5 Conclusion

Key information for the design of a beam charge integrating transformer that exploits resonance to achieve a high sensitivity has been presented. Simple additions to permit use of such resonant transformer with high repetition rate pulsed electron beams have been described. Such non-intercepting beam charge monitors can be used to monitor dose delivery during both CONV and FLASH irradiations, or indeed when single, individual, pulses are used. A wide dynamic range can be readily handled. They are not susceptible to saturation effects and can thus be used for high charge/pulse FLASH beams. However, the charge in CONV beams can be also monitored with the same device, as a result of their good sensitivity.

Although resistively-loaded beam current transformers have gained recent popularity for use during electron FLASH measurement, their sensitivity, particularly for long pulses, is often not optimal. Furthermore, such transformers require wide bandwidths, hardware- or software-based integration along with baseline correction. One of our aims in presenting this work was to bring to the foreground resonant inductive beam sensors that inherently integrate the beam charge per pulse and offer far greater versatility during radiobiology experiments using electron pulses. Physicists are interested in temporal pulse profiles, and rightly so. Dose per pulse, however, is of greater immediate interest to radiobiologists. The low electrical bandwidths of BCITs and almost perfect immunity from accelerator-generated noise provides a significant advantage in work involving charge pulses acquired over a wide dynamic range, including when low doses/pulse need to be monitored. The charge measurement is performed several hundred microseconds after the electron pulse and is thus free of any interference generated by the linac modulator and radiofrequency system. It is hoped that these versatile devices will gain wider acceptance by the electron FLASH community.

## Data availability statement

The original contributions presented in the study are included in the article/Supplementary Material, further inquiries can be directed to the corresponding author.

## Author contributions

All the authors substantial contributions to conception and use of the device, designed by BV and IT, who also performed electrical data acquisition while RN performed all electronic construction. KP

and IT acquired all dosimetry data. All authors contributed to the article and approved the submitted version.

## Funding

Past financial support of Cancer Research UK and current financial support Cancer Research UK—RadNet (C6078/A28736) is gratefully acknowledged. We thank the Medical Research council for providing funds towards the linac shielding and for current financial support through a programme grant (MR/X006611/1). We also thank the National Cancer Institute/NIH/DHHS for their support towards this work (1P01CA257904).

## Acknowledgments

The contribution of the Department of Oncology Mechanical Workshop has been essential for the completion of this work: thanks go to John Prentice, Kyle Hallett, and Gerald Shortland for their patience in machining disparate materials that fitted together just as our mechanical models predicted they would!

## Conflict of interest

The authors declare that the research was conducted in the absence of any commercial or financial relationships that could be construed as a potential conflict of interest.

## Publisher's note



## Supplementary material

The Supplementary Material for this article can be found online at: https://www.frontiersin.org/articles/10.3389/fphy.2023.1185237/full#supplementary-material

## References

1. Favaudon V, Caplier L, Monceau V, Pouzoulet F, Sayarath M, Fouillade C, et al. Ultrahigh dose-rate FLASH irradiation increases the differential response between normal and tumor tissue in mice. *Sci Transl Med* (2014) 6(245):245ra93. doi:10.1126/scitranslmed.3008973

2. Loo BW, Schuler E, Lartey FM, Rafat M, King JG, Trovati S, et al. P003) Delivery of ultra-rapid flash radiation therapy and demonstration of normal tissue sparing after abdominal irradiation of mice. *Int J Radiat Oncol Biol Phys* (2017) 98:E16. doi:10.1016/j.ijrobp.2017.02.101

3. Montay-Gruel P, Petersson K, Jaccard M, Boivin G, Germond J-F, Petit B, et al. Irradiation in a flash: Unique sparing of memory in mice after whole brain irradiation with dose rates above 100 Gy/s. *Radiother Oncol* (2017) 124:365–9. doi:10.1016/j.radonc.2017.05.003

4. Bourhis J, Montay-Gruel P, Gonçalves Jorge P, Bailat C, Petit B, Ollivier J, et al. Clinical translation of FLASH radiotherapy: Why and how? *Radiother Oncol* (2019) 139:11–7. doi:10.1016/j.radonc.2019.04.008

5. Bourhis J, Jeanneret Sozzi W, Gonçalves Jorge P, Gaide O, Bailat C, Duclos F, et al. Treatment of a first patient with FLASH-radiotherapy. *Radiother Oncol* (2019) 139:18–22. doi:10.1016/j.radonc.2019.06.019

6. Montay-Gruel P, Meziani L, Yakkala C, Vozenin M. Expanding the therapeutic index of radiation therapy by normal tissue protection. *Br J Radiol* (2019) 92:20180008. doi:10.1259/bjr.20180008

7. Vozenin M-C, De Fornel P, Petersson K, Favaudon V, Jaccard M, Germond J-F, et al. The advantage of FLASH radiotherapy confirmed in mini-pig and cat-cancer patients. *Clin Cancer Res* (2019) 25:35–42. doi:10.1158/1078-0432.CCR-17-3375

8. Wardman P. Radiotherapy using high-intensity pulsed radiation beams (FLASH): a radiation-chemical perspective. *Radiat Res* (2020) 194:607–17. doi:10.1667/RADE-19-00016

9. Adrian G, Konradsson E, Lempart M, Bäck S, Ceberg C, Petersson K. The FLASH effect depends on oxygen concentration. *Br J Radiol* (2020) 93:20190702. doi:10.1259/bjr.20190702

10. Wilson JD, Hammond EM, Higgins GS, Petersson K. Ultra-high dose rate (FLASH) radiotherapy: silver bullet or fool's gold? *Front Oncol* (2020) 9:1563. doi:10.3389/fonc.2019.01563

11. Maxim PG, Keall P, Cai J. FLASH radiotherapy: Newsflash or flash in the pan? *Med Phys* (2019) 46(10):4287–90. [published online ahead of print 2019/06/28]. doi:10.1002/mp.13685

12. Friedl AA, Prise KM, Butterworth KT, Montay-Gruel P, Favaudon V. Radiobiology of the FLASH effect. *Med Phys* (2022) 49:1993–2013. doi:10.1002/mp.15184

13. Ruan J-L, Lee C, Wouters S, Tullis IDC, Verslegers M, Mysara M, et al. Irradiation at ultra-high (FLASH) dose rates reduces acute normal tissue toxicity in the mouse gastrointestinal system. *Int J Radiat Oncol Biol Phys* (2021) 111(5):1250–61. doi:10.1016/j.ijrobp.2021.08.004

14. Okoro CM, Schüler M, Taniguchi CM. The therapeutic potential of FLASH-RT for pancreatic cancer. *Cancers (Basel)* (2022) 14(5):1167. [published online ahead of print 2022/03/11]. doi:10.3390/cancers14051167

15. Wu Y, No HJ, Breitkreutz DY, Mascia AE, Moeckli R, Bourhis J, et al. Technological basis for clinical trials in FLASH radiation therapy: A review. *Appl Rad Oncol* (2021) 2:6–14. doi:10.37549/aro1280

16. Schuler E, Acharya M, Montay-Gruel P, Loo BW, Vozenin M-C, Maxim PG. Ultra high dose rate electron beams and the FLASH effect: From preclinical evidence to a new radiotherapy paradigm. *Med Phys* (2022) 49:2082–95. doi:10.1002/mp.15442

17. Ashraf MR, Rahman M, Zhang R, Williams BB, Gladstone DJ, Pogue BW, et al. Dosimetry for FLASH radiotherapy: A review of tools and the role of radioluminescence and cherenkov emission. *Front Phys-lausanne* (2020) 8:328. doi:10.3389/fphy.2020.00328

18. Petersson K, Jaccard M, Germond J-F, Buchillier T, Bochud F, Bourhis J, et al. High dose-per-pulse electron beam dosimetry - a model to correct for the ion recombination in the advanced Markus ionization chamber. *Med Phys* (2017) 44:1157–67. doi:10.1002/mp.12111

19. Gonçalves Jorge P, Jaccard M, Petersson K, Gondré M, Durána MT, Desorgher L, et al. Dosimetric and preparation procedures for irradiating biological models with pulsed electron beam at ultra-high dose rate. *Radiother Oncol* (2019) 139:34–9. doi:10.1016/j.radonc.2019.05.004

20. Konradsson E, Ceberg C, Lempart M, Blad B, Bäck S, Knöös T, et al. Correction for ion recombination in a built-in monitor chamber of a clinical linear accelerator at ultra-high dose rates. *Radiat Res* (2020) 194:580–6. doi:10.1667/RADE-19-00012

21. Boag JW. Ionization measurements at very high intensities: I. Pulsed radiation beams. *Br J Radiol* (1950) 23:601–11. doi:10.1259/0007-1285-23-274-601

22. Boag JW, Currant J. Current collection and ionic recombination in small cylindrical ionization chambers exposed to pulsed radiation. *Br J Radiol* (1980) 53:471–8. doi:10.1259/0007-1285-53-629-471

23. Gotz M, Karsch L, Pawelke J. A new model for volume recombination in plane-parallel chambers in pulsed fields of high dose-per pulse. *Phys Med Biol* (2017) 62:8634–54. doi:10.1088/1361-6560/aa8985

24. Di Martino F, Giannelli M, Traino AC, Lazzeri M. Ion recombination correction for very high dose-per-pulse high-energy electron beams. *Med Phys* (2005) 32:2204–10. doi:10.1118/1.1940167

25. Fainstein C, Winkler E, Saravi M. ESR/Alanine gamma-dosimetry in the 10–30 Gy range. *Appl Radiat Isot* (2000) 52:1195–6. doi:10.1016/s0969-8043(00)00070-1

26. Hayes RB, Haskell EH, Wieser A, Romanyukha AA, Hardy BL, Barrus JK. Assessment of an alanine EPR dosimetry technique with enhanced precision and

accuracy. *Nucl Instrum Methods Phys Res A* (2000) 440:453–61. doi:10.1016/S0168-9002(99)00957-2

27. Arjomandy B, Tailor R, Zhao L, Devic S. EBT2 film as a depth-dose measurement tool for radiotherapy beams over a wide range of energies and modalities. *Med Phys* (2012) 39:912–21. doi:10.1118/1.3678989

28. Karsch L, Beyreuther E, Burris-Mog T, Kraft S, Richter C, Zeil K, et al. Dose rate dependence for different dosimeters and detectors: TLD, OSL, EBT films, and diamond detectors. *Med Phys* (2012) 39:2447–55. doi:10.1118/1.3700400

29. Schüler E, Trovati S, King G, Lartey F, Rafat M, Villegas M, et al. Experimental platform for ultra-high dose rate FLASH irradiation of small animals using a clinical linear accelerator. *Radiat Oncol Biol Phys* (2017) 97:195–203. doi:10.1016/j.ijrobp.2016.09.018

30. Jaccard M, Durán MT, Petersson K, Germond J-F, Liger P, Vozenin M-C, et al. High dose-per-pulse electron beam dosimetry: Commissioning of the Oriatron eRT6 prototype linear accelerator for preclinical use. *Med Phys* (2018) 45:863–74. doi:10.1002/mp.12713

31. Lempart M, Blad B, Adrian G, Bäck S, Knöös T, Ceberg C, et al. Modifying a clinical linear accelerator for delivery of ultrahigh dose rate irradiation. *Radiother Oncol* (2019) 139:40–5. doi:10.1016/j.radonc.2019.01.031

32. Patriarca A, Fouillade C, Auger M, Martin F, Pouzoulet F, Nauraye C, et al. Experimental set-up for FLASH proton irradiation of small animals using a clinical system. *Int J Radiat Oncol Biol Phys* (2018) 102:619–26. doi:10.1016/j.ijrobp.2018.06.403

33. Diffenderfer ES, Verginadis II, Kim MM, Shoniyozov K, Velalopoulou A, Goia D, et al. Design, implementation, and *in vivo* validation of a novel proton FLASH radiation therapy system. *Int J Radiat Oncol Biol Phys* (2019) 106:440–8. doi:10.1016/j.ijrobp.2019.10.049

34. International Electrotechnical Commission. *As defined by IEC 60601-2-1: Medical electrical equipment - Part 2-1: Particular requirements for the basic safety and essential performance of electron accelerators in the range 1 MeV to 50 MeV* (2020).

35. Oesterle R, Gonçalves Jorge P, Grilj V, Bourhis J, Vozenin M-C, Germond J-F, et al. Implementation and validation of a beam current transformer on a medical pulsed electron beam LINAC for FLASH-RT beam monitoring. *J Appl Clin Med Phys* (2021) 22:165–71. doi:10.1002/acm2.13433

36. Gonçalves Jorge P, Grilj V, Bourhis J, Vozenin C-M, Germond JF, Bochud F, et al. Technical note: Validation of an ultrahigh dose rate pulsed electron beam monitoring system using a current transformer for FLASH preclinical studies. *Med Phys* (2022) 49:1831–8. doi:10.1002/mp.15474

37. Webber RC. Tutorial on beam current monitoring. *AIP Conf Proc* (2000) 546:83. doi:10.1063/1.1342580

38. Simmons RH, Ng JST. A toroidal charge monitor for high-energy picosecond electron beams. *Nucl Instr Meth Phys Res A* (2007) 575:334–42. doi:10.1016/j.nima.2007.03.002

39. ICRU. Radiation dosimetry: Electron beams with energy between 1 and 50 MeV). ICRU report no. 35 (1985). Med. Phys. 12, 813.

40. Klevenhagen SC. *Physics of electron beam therapy medical Physics handbook*. Boston: Adam Hilger Ltd (1985). p. 13.

41. Berger MJ, Seltzer SM. The Influence of scattering foils on absorbed dose distributions from electron beams NBSIR 78-1552 (1978). Available at: https://doi.org./10.6028/nbs.ir.78-1552.

42. Patil BJ, Bhoraskar V, Dhole SV. Optimization of dual scattering foil for 6-20 MeV electron beam radiotherapy. In: PAC-2011-THP010 Proc. 2011 Particle Accelerator Conf 110328; March 28-April 1, 2011; New York, NY, USA (2011). p. 2157–9.

43. Jeong DH, Lee M, Lim H, Kang SK, Lee J, Kim HC, et al. Electron beam scattering device for FLASH preclinical studies with 6-MeV LINAC. *Nucl Eng Technol* (2021) 53:1289–96. doi:10.1016/j.net.2020.09.019

44. Anderson JM. Wide frequency range current transformers. *Rev Scientific Instr* (1971) 42:915–26. doi:10.1063/1.1685307

45. Kondrath N, Kazimierczuk MK. Bandwidth of current transformers. *IEEE Trans Instrum Meas* (2009) 58:2008–16. doi:10.1109/TIM.2008.2006134

46. Leggieri A, Passi D, di Paolo F, Ciccotelli A, De Stefano S, Marangoni F, et al. Real-time beam monitor for charged particle medical accelerators. *IEEE Trans Nucl Sci* (2016) 63(2):869–77. doi:10.1109/TNS.2015.2504403

47. Pruitt JS. Electron beam current monitoring system. *Nucl Instr Meth* (1971) 92:285–97. doi:10.1016/0029-554X(71)90206-0

48. Steiner R, Merle K, Andresen HG. A high-precision ferrite-induction beam-current monitoring system. *Nucl Instr Meth* (1975) 127:11–5. doi:10.1016/0029-554X(75)90295-5

49. Zimek Z. A single-pulse toroidal coil beam-charge monitor. *Radiat Phys Chem* (1978) 11:179–81. doi:10.1016/0146-5724(78)90080-8

50. Vojnovic B. A sensitive single-pulse beam charge monitor for use with charged particle accelerators. *Radiat Phys Chem* (1984) 24:517–22. doi:10.1016/0146-5724(84)90187-0

51. Dolbilkin BS, Kondratev RL, Lisin VP, Polonsky AL. The choice of optimum parameters of a toroidal charge monitor for precision measurements. *Nucl Instrum Meth.Physics Res* (1984) 226:271–80. doi:10.1016/0168-9002(84)90041-X

52. Unser K. Beam current transformer with DC to 200 MHz range. *IEEE Trans Nucl Sci* (1969) 16:934–8. doi:10.1109/TNS.1969.4325406

53. Sharp JB. The induction type beam monitor for the PS: Hereward transformer MPS-Int-CO-62-15. CERN-MPS-Int-CO-62-15 (1962).

54. Telcon Ltd. Toroidal cores (2013). Lowfield Heath, Crawley, West Sussex, United Kingdom, RH11 0PR; Available at: http://www.telcon.co.uk/Toroidal%20Cores.html (Accessed July 23, 2022).

55. AguileraOdier SP, Ruffieux R. Magnetic materials for current transformers. In: Proceedings of the 2nd International Beam Instrumentation Conference; 16 - 19 Sep 2013; Oxford, UK (2013). ISBN 978-3-95450-127-4 pp263-266.

56. Mag-Inc. Magnetics, 110 delta drive, Pittsburgh, PA 15238-0428 (2018). Available at: https://www.mag-inc.com/Products/Tape-Wound-Cores/Supermalloy (Accessed July 23, 2022).

57. Lahaye C, Fontbonne J-M, Salvador S. Low noise optimization of an electron beam current transformer for conventional radiotherapy up to ultra high dose rate irradiations. *J Instrumentation* (2022) 17:P08018. doi:10.1088/1748-0221/17/08/P08018

58. Boriskin VN, Gurin VA, Dovbnya AN, Popenko VA, Reprintsev LV, Savchenko AN, et al. Magnetic induction monitor measurements of beam spatial characteristics in technological electron linear accelerators. *Proc 2001 Part. Accelerator Conf* (2001) 2:1336–8. doi:10.1109/PAC.2001.986672

59. Vojnovic B. Sensitive long pulse beam charge monitor for use with charged particle accelerators. *Int J Radiat App Instrum C Radiat Phys.Chem* (1987) 29:409–13. doi:10.1016/1359-0197(87)90015-4

60. Dewa H, Iwashita Y, Fujita H, Ikegami M, Inoue M, Kakigi S, et al. Pulsed Beam Current monitor with a toroidal core. In: Proceedings of the 1994 International Linac Conference; 21 - 26 August 1994; Tsukuba, Japan (1994).

61. Larky A. Negative-impedance converters. *IRE Trans Circuit Theor* (1957) 4:124–31. doi:10.1109/TCT.1957.1086360

62. Berne A, Petersson K, Tullis IDC, Newman RG, Vojnovic B. Monitoring electron energies during FLASH irradiations. *Phys Med Biol* (2021) 66:045015. doi:10.1088/1361-6560/abd672

63. Analog. LTspice version XVII downloaded from (2023). Available at: https://www.analog.com/en/design-center/design-tools-and-calculators/ltspice-simulator.html Win10 64 bit version (Accessed July 23, 2022).

64. WilsonRoss PRJN, Brown AD. Modeling frequency-dependent losses in ferrite cores. *IEEE Trans Mag* (2004) 40:1537–41. doi:10.1109/TMAG.2004.826910

65. Arai S, Katayama T, Tojyo E, Yoshida K. Beam loading effects in a standing wave accelerator structure. *Part Accel* (1980) 11:103–11.

66. Arai S, Kobayashi K, Toio E, Yoshida K. Detuning effect in a travelling-wave accelerator structure due to beam loading. *Part Accel* (1984) 15:99–114.

67. Gotz M, Karsch L, Pawelke J. A new model for volume recombination in plane-parallel chambers in pulsed fields of high dose-per-pulse. *Phys Med Biol* (2017) 62(22):8634–54. doi:10.1088/1361-6560/aa8985

68. Kranzer R, Poppinga D, Weidner J, Schuller A, Hackel T, Looe HK, et al. Ion collection efficiency of ionization chambers in ultra-high dose-per-pulse electron beams. *Med Phys* (2021) 48(2):819–30. doi:10.1002/mp.14620

69. Boag JW, Hochhauser E, Balk OA. The effect of free-electron collection on the recombination correction to ionization measurements of pulsed radiation. *Phys Med Biol* (1996) 41:885–97. doi:10.1088/0031-9155/41/5/005

70. Di Martino F, Del Sarto D, Barone S, Giuseppina Bisogni M, Capaccioli S, Galante F, et al. A new calculation method for the free electron fraction of an ionization chamber in the ultra-high-dose-per-pulse regimen. *Phys Med* (2022) 103:175–80. doi:10.1016/j.ejmp.2022.11.001

71. Laitano RF, Guerra AS, Pimpinella M, Caporali C, Petrucci A. Charge collection efficiency in ionization chambers exposed to electron beams with high dose per pulse. *Phys Med Biol* (2006) 51:6419–36. doi:10.1088/0031-9155/51/24/009

72. Gibbons JP, Antolak JA, Followill DS, Huq MS, Klein EE, Lam KL, et al. Monitor unit calculations for external photon and electron beams: Report of the AAPM therapy Physics committee task group No. 71. *Med Phys* (2014) 41:031501. doi:10.1118/1.4864244

73. Sampayan SE, Sampayan KC, Caporaso GJ, Chen Y-J, Falabella S, Hawkins SA, et al. Megavolt bremsstrahlung measurements from linear induction accelerators demonstrate possible use as a FLASH radiotherapy source to reduce acute toxicity. *Sci Rep* (2021) 11:17104. doi:10.1038/s41598-021-95807-9

74. Esplen N, Egoriti L, Paley B, Planche T, Hoehr C, Gottberg A, et al. Design optimization of an electron-to-photon conversion target for ultra-high dose rate x-ray (FLASH) experiments at TRIUMF. *Phys Med Biol* (2022) 67:105003. doi:10.1088/1361-6560/ac5ed6

75. Ticoș D, Scurtu A, Oane M, Diplașu C, GiubegaI G, Călina I, et al. Complementary dosimetry for a 6 MeV electron beam. *Results Phys* (2019) 14:102377. doi:10.1016/j.rinp.2019.102377

76. Schüller A, Illemann J, Renner F, Makowski C, Kapsch R-P. Traceable charge measurement of the pulses of a 27 MeV electron beam from a linear accelerator. *J Instrum* (2017) 12:P03003. doi:10.1088/1748-0221/12/03/P03003

77. Podgorsak EB. *Radiation oncology Physics: a handbook for teachers and students*. Vienna: International Atomic Energy Agency (2005). Sponsored by IAEA 2005. STI/PUB/1196. ISBN 92–0–107304–6.

78. International Electrotechnical Commission. *IEC 60976 Medical electrical equipment – Medical electron accelerators – functional performance characteristics, 2007 describes the tests to be performed* (2007).

79. Williams AJ, Mcewen MR, Burns DT. A new beam current monitor for the NPL linear accelerator facility. NPL Technical Report number: CIRM(EXT)12, National Physical Laboratory Teddington, Middlesex, UK, TWII OLW, ISSN1369-6793 (1998).

80. Faillace L, Barone S, Battistoni G, Di Francesco M, Felici G, Ficcadenti L, et al. Compact S-band linear accelerator system for ultrafast, ultrahigh dose-rate radiotherapy. *Phys Rev Accel Beams* (2021) 24:050102. doi:10.1103/PhysRevAccelBeams.24.050102

81. Jaccard M, Duran MT, Petersson K, Germond JF, Liger P, Vozenin MC, et al. High dose-per-pulse electron beam dosimetry: Commissioning of the Oriatron eRT6 prototype linear accelerator for preclinical use. *Med Phys* (2018) 45(2):863–74. doi:10.1002/mp.12713

82. Moeckli R, Gonçalves Jorge P, Grilj V, Oesterle R, Cherbuin N, Bourhis J, et al. Commissioning of an ultra-high dose rate pulsed electron beam medical LINAC for FLASH RT preclinical animal experiments and future clinical human protocols. *Med Phys* (2021) 48(6):3134–42. doi:10.1002/mp.14885

83. Darafsheh A, Hao Y, Zwart T, Wagner M, Catanzano D, Williamson JF, et al. Feasibility of proton FLASH irradiation using a synchrocyclotron for preclinical studies. *Med Phys* (2020) 47:4348–55. doi:10.1002/mp.14253

84. Nesteruk KP, Psoroulas S. FLASH irradiation with proton beams: Beam characteristics and their implications for beam diagnostics. *Appl Sci* (2021) 11:2170. doi:10.3390/app11052170

85. Vignati A, GiordanengoFausti SF, Villarreal OAM, Mas Milian F, Mazza G, Shakarami Z, et al. Beam monitors for tomorrow: The challenges of electron and photon FLASH RT. *Front Phys* (2020) 8:375. doi:10.3389/fphy.2020.00375

86. Unser KB. The parametric current transformer, a beam current monitor developed for LEP. *AIP Conf.Proc.* (1992) 252:266. Published Online: 02 June 2008. doi:10.1063/1.42124

87. Covo MK. Nondestructive synchronous beam current monitor. *Rev Sci Instr* (2014) 85:125106. doi:10.1063/1.4902903

88. Cardelli F, Ampollini A, Bazzano G, Nenzi P, Piersanti L, Ronsivalle C, et al. Design and test of a compact beam current monitor based on a passive RF cavity for a proton therapy linear accelerator. *Rev Sci Instrum* (2021) 92:113304. doi:10.1063/5.0062509

frontiers | Frontiers in Oncology

TYPE Perspective
PUBLISHED 23 October 2023
DOI 10.3389/fonc.2023.1254601



OPEN ACCESS

EDITED BY
Andrea Lancia,
San Matteo Hospital Foundation (IRCCS), Italy

REVIEWED BY
Angelica Facoetti,
National Center of Oncological Hadrontherapy, Italy

*CORRESPONDENCE
Stefano Ursino
stefano.ursino@med.unipi.it

RECEIVED 14 July 2023
ACCEPTED 25 September 2023
PUBLISHED 23 October 2023

CITATION
Ursino S, Gadducci G, Giannini N, Gonnelli A, Fuentes T, Di Martino F and Paiar F (2023) New insights on clinical perspectives of FLASH radiotherapy: from low- to very high electron energy. *Front. Oncol.* 13:1254601. doi: 10.3389/fonc.2023.1254601



# New insights on clinical perspectives of FLASH radiotherapy: from low- to very high electron energy

Stefano Ursino[1,2,3*], Giovanni Gadducci[1,2], Noemi Giannini[1,2], Alessandra Gonnelli[1,2], Taiushia Fuentes[1,2], Fabio Di Martino[2,4] and Fabiola Paiar[1,2,3]

[1]Department of Translational Research and New Technologies in Medicine and Surgery, University of Pisa, Pisa, Italy, [2]Centro Pisano Multidisciplinare sulla Ricerca e implementazione clinica della Flash Radiotherapy (CPFR), University of Pisa, Pisa, Italy, [3]Center for Instrument Sharing University of Pisa (CISUP), University of Pisa, Pisa, Italy, [4]Unit of Medical Physics, S. Chiara University Hospital, Pisa, Italy

Radiotherapy (RT) is performed in approximately 75% of patients with cancer, and its efficacy is often hampered by the low tolerance of the surrounding normal tissues. Recent advancements have demonstrated the potential to widen the therapeutic window using "very short" radiation treatment delivery (from a conventional dose rate between 0.5 Gy/min and 2 Gy/min to more than 40 Gy/s) causing a significant increase of normal tissue tolerance without varying the tumor effect. This phenomenon is called "FLASH Effect (FE)" and has been discovered by using electrons. Although several physical, dosimetric, and radiobiological aspects need to be clarified, current preclinical "*in vivo*" studies have reported a significant protective effect of FLASH RT on neurocognitive function, skin toxicity, lung fibrosis, and bowel injury. Therefore, the current radiobiological premises lay the foundation for groundbreaking potentials in clinical translation, which could be addressed to an initial application of Low Energy Electron FLASH (LEE) for the treatment of superficial tumors to a subsequent Very High Energy Electron FLASH (VHEE) for the treatment of deep tumors. Herein, we report a clinical investigational scenario that, if supported by preclinical studies, could be drawn in the near future.

KEYWORDS

**FLASH radiotherapy, dose rate, low electron energy, very high electron energy, tumor control probability, normal tissue complication probability**

## Introduction

The success of radiotherapy (RT) in eradicating tumors depends on the total radiation dose delivered to the tumor. The tolerance of surrounding normal tissues often represents the main limitation in achieving the required dose. In recent decades, technological advances have improved the geometric precision of dose delivery by generating highly

conformal dose distributions. However, a significant percentage of tumors remain incurable because of the unacceptable risk-to-benefit ratio (1).

Recently, the possibility of increasing the therapeutic window has been shown through temporal modulation of the beam delivery due to a differential radiobiological effect between normal tissues and tumor, the so called "FLASH Effect" (FE) (2). Specifically, this surprising effect was demonstrated "*in vivo*" on different animal models and organs by delivering the total radiation dose in a very short time (<200 ms), with average dose rates above 40 Gy/s (in comparison with 0.5 Gy/min–20 Gy/min of conventional RT) and leading to a sparing effect on normal tissues without varying tumor effect compared with conventional RT (CONV-RT). As this phenomenon has been discovered using electrons, most preclinical experiments have been performed using this type of radiation source (3–5).

Despite encouraging preclinical findings, the clinical translation of FE is currently in its early experimental phase, primarily owing to significant uncertainties in several key physical, dosimetric, and radiobiological aspects. The design of new devices capable of delivering beam fluences several orders higher than those used for CONV-RT, the availability of new dosimeters, and dosimetric protocols capable of measuring beams at the very high dose per pulse needed to trigger the effect, the dependence of FE on the variations of different temporal beam parameters needs to be clarified before translation to the clinic (6, 7). In addition, a comprehensive understanding of the underlying radiobiological mechanisms driving FE remains to be elucidated.

FE represents a great challenge that could significantly change the paradigm of RT-based treatments in the near future. For this purpose, real brainstorming has been triggered, involving all the specific skills around this issue, from medical physics to biophysics, radiochemists, and radiobiologists to radiation oncologists.

Based on the groundbreaking clinical possibilities associated with FE, we present a detailed overview of the primary oncologic conditions that are particularly suitable for initial clinical investigations of FLASH-RT, from Low Energy Electrons (LEE) (4 MeV–12 MeV) to Very High Energy Electrons (VHEE) (100 MeV–200 MeV) RT.

## Radiobiological premises of clinical translation

The therapeutic window is the dose region interval between the Normal Tissue Complication Probability (NTCP) and the Tumor Control Probability (TCP) curves and represents the milestone for a RT treatment (8). Historically, according to the five principles of radiobiology (5Rs), the use of standard fractionation exploits a differential biological effect favoring the killing of cancer cells more than the killing of healthy ones. Several altered fractionation schemes (such as hyperfractionation or accelerated) have been tested trying to biologically spacing out the two curves but have been gradually abandoned due to controversial risk to benefit ratio (9).

In recent decades, owing to technological advances highly biologically effective hypofractionation schemes have emerged to overcome the intrinsic radioresistance of several tumors, often leading to high curative rates. However, hypofractionation allowed by the geometrical achievement of a very steep spatial dose gradient between the tumor and surrounding healthy tissues remains restricted to limited-sized lesions mostly located in parallel functional organs (such as the lung or liver). Moreover, the use of high linear energy transfer ionizing charged radiation, characterized by a higher relative biological efficacy, has been hampered by the necessity to achieve a subtle balance in the delivery mode to spatially spare the nearest healthy tissues with a subsequent high risk of severe sequelae. These limitations restrict the use of charged particles in clinical practice to very highly selected cases (such as chordoma or non-operable adenoidocystic carcinoma) that must be referred to a few reference centers and often require patients (pts) to be enrolled in clinical trials (10).

Hence, the potential protective effect observed in nonmalignant tissues holds significant promise for novel clinical applications. However, before the translation of FE into clinical practice, several concerns must be addressed through future preclinical studies. First, the determination of the threshold dose per fraction required to trigger the FE, as well as its dependency on various physical beam parameters (such as the total duration of irradiation, average dose rate, dose per pulse, and instantaneous dose per pulse), needs to be resolved. Understanding these dose–response relationships is crucial for optimizing treatment protocols.

Second, the extension of the FE effect to larger irradiation volumes (referred to as the "volume effect") and exploration of multiple treatment fields are important considerations. Currently, FE has only been observed for a single treatment field delivering a high dose per fraction (approximately 6 Gy) without a standardized set of physical beam parameters, resulting in limited reproducibility of the results (11, 12).

In this regard, we believe that a key point will be to test the sparing effect and the corresponding dose-modifying factor (the increased dose factor to cause the same toxicity grade of CONV-RT) for both organs with "serial" (i.e., spinal cord, small bowel, brainstem and brain tissue) and "parallel" (i.e., lung and liver) functional organization, as well as the isoefficacy on different types of tumors compared with CONV-RT.

Since the FE has already been described as a "tissue effect," the majority of data to address the clinical translation will likely come from "*in vivo*" experiments. In this regard, the currently available data seem to agree in recognizing a higher tolerance to FLASH irradiation for the most crucial healthy tissues (such as bowel, brain, and lung) that strongly limit the delivery of tumoricidal doses in clinical practice (3–5). Therefore, these results might realistically widen the therapeutic index for oncological conditions that are currently burdened by a dismal prognosis.

## Clinical perspectives

Based on the radiobiological premises reported above, FE could advantageously be translated to the clinic for three main purposes:

1. Radioresistant tumors located in close proximity to radiosensitive "serial" organs: it is hypothesized that a

higher RT dose could be delivered to the tumor without inducing severe toxicities to the surrounding normal tissues as would be expected following CONV-RT.

2. Large tumors arising in "parallel" organs: the delivery of tumoricidal RT dose is hampered by the size and local extension of the tumor mass, which would lead to low-dose irradiation of a significant portion of organs at risk with a subsequent unacceptable risk of severe toxicity.
3. Reirradiation: Tumor recurrence often occurs within a previously irradiated high-dose region. This means that the dose required for tumor control is often much higher than that required for severe toxicity, leading to an inverted relationship between NTCP and TCP curves. Currently, these situations are evaluated on a case-by-case basis, taking into consideration the availability of advanced technologies (e.g., Cyberknife) that allow for maximal geometric sparing of primary organs at risk.

From a clinical perspective, two different lines of technological developments can be identified: LEE for the treatment of superficial tumors and VHEE for the treatment of deep tumors.

Undoubtedly, LEE might have very few but, at the same time, rapid clinical applications owing to the ease of technological implementation of LEE accelerators for clinical use. In contrast, VHEE would necessitate the design and development of a novel prototype machine that combines the capacity of managing accelerated high-energy electrons for clinical use with the limited size requirements of an RT bunker. Notably, the latter could be applied to many clinical situations that are currently undercured, thus leading to a real "cutting-edge" breakthrough in the RT treatment of cancer.

## Low electron energy FLASH therapy

Three possible areas of clinical implementation can be identified for LEE: skin tumors, uveal melanoma, and intraoperative RT for abdominopelvic tumors.

Skin tumors usually takes advantage of an upfront surgical removal of the primary lesion despite burdened by a high rate of local recurrence due to their frequent unfavorable location (such a canthus, glabella, nasolabial folds, or preauricolar region) that often limits radical resection causing post-surgical "close" or "microscopically positive" margins (13–15). Therefore, low-energy standard RT (plesiotherapy or superficial brachytherapy) is frequently used as exclusive or postoperative treatment to sterilize microscopic neoplastic foci. Surely, the skin would be the ideal target for a preliminary clinical investigation as it represents a bidimensional matrix that makes it easy for both treatment planning and visualization of tumor and normal tissue response. In addition, the treatment of skin with LEE might play a pioneering role in the subsequent implementation of VHEE, as the healthy skin would represent a primary organ at risk for the treatment of deep tumors.

Uveal melanoma is a rare intraocular tumor that can be treated with radical or conservative treatment (16). Radical treatment, performed in approximately 30% of cases, consists of surgical resection, often providing total removal of the ocular globe and is usually offered to patients with greater tumor size and visual impairment at diagnosis. Indeed, conservative treatment that is performed in approximately 70% of cases consists of RT that can be delivered in the presence of small-sized tumors by implantation of intraocular radioactive plaques (ruthenium or iodine) or in the presence of medium-sized tumors by external beam-accelerated protons (17). The key point in performing conservative treatment is represented by the preservation of the optic nerve, whose damage is related to the reduction or loss of vision (18). Thus, the spatial relationship between tumor and optic nerve is crucial and the choice of external beam protons therapy is based on the achievement of a very steep "fall-off" of RT dose outside the clinical target volume (19). In this regard, owing to the proximity of the target to the cutaneous surface (approximately 1 cm–3 cm), LEE might represent a valid alternative to proton therapy as a conservative treatment in the presence of close proximity or tumor infiltration of the optic nerve. In this regard, preclinical studies investigating the effects of FLASH-RT on peripheral nerves are of primary importance.

Finally, malignancies located in the abdomen or pelvis would optimally fit for an early clinical investigation of Intraoperative Electron FLASH RT (20, 21) Primary tumor control, often conditioning survival due to a higher risk of local mortal complications and the development of distant metastases, can be crucial in the presence of non-operated radioresistant malignancies, such as pancreatic tumors or retroperitoneal sarcoma, surrounded by radiosensitive "serial" organs at risk (such as the intestine or stomach) (22). From the beginning, the rationale for intraoperative RT has always been the improvement of local control through the delivery of a dose-escalated hypofractionated boost to the primary gross tumor after standard fractionated external RT. Nevertheless, late small vessel and peripheral nerve injuries caused by large doses per fraction remains a limiting factor that can only be partially overcome by exploiting intraoperative FE.

Although the therapeutic applications of LEE are limited, it will be the first to be implemented as a direct application of *in vivo* experimental evidence performed using a single field of low-energy electron beams, mechanically collimated, and delivered in a single fraction.

## Very high electron energy FLASH therapy

Multiple brain metastases and primary brain tumors (high grade gliomas) are currently associated to a poor "quoad-vitam" prognosis that is caused by the impossibility to eradicate intracranial tumor disease (23, 24). In fact, the large dissemination of small tumoral foci within the brain (multiple metastases) or the presence of a large tumor mass (primary tumors) usually requires very large-volume irradiation (25). This requirement, combined with the radiosensitivity of healthy brain tissue, usually represents the main limitation for the delivery of high tumoricidal doses (26). Therefore, a whole brain palliative

irradiation as well as a "gross tumor" or "tumor surgical bed" involved field with large clinical margins is usually used in the current clinical practice but with suboptimal oncologic results. Although preliminary, currently available preclinical data report promising results in terms of neurocognitive sparing after FLASH compared with conventional irradiation, suggesting a preserving effect on stem hippocampal cells. Specifically, the results of all the cognitive tests performed were statistically indistinguishable between non-irradiated and FLASH irradiated mice, whereas cognition was permanently altered in mice receiving conventional radiation with a dose-modifying factor (DMF) of approximately 1.4 after a single dose of 10 Gy (5). If confirmed, these results could auspiciously pave the way for phase II dose escalation trials aimed at improving the local control of intracranial disease with a subsequent likely improvement in overall survival.

Locally advanced non-small cell lung tumors accounts for approximately 30% of all non-small cell lung tumors (27). Among them, only one-third are suitable for a surgical approach, usually after neoadjuvant chemotherapy. The remaining patients, who are not suitable for surgery, undergo RT-based treatment, either in combination with chemotherapy or as a standalone modality. Although RT represents a fundamental treatment for this subset of tumors, survival is still poor, accounting for approximately 15%–20% of patients alive 5 years after the diagnosis (28). In this case, the dismal prognosis seems to be related to scarce control of the tumor, with a subsequent high risk of life-threatening complications (i.e., hemorrhage) and metastatic dissemination. The real limit is represented by the volume of a healthy uninvolved lung that receives a low radiation dose rather than the maximum dose. In this regard, the life-threatening toxicities that limit the delivery of tumoricidal doses are acute pneumonitis and diffuse late fibrosis (29–31). Again, preclinical "*in vivo*" studies focused on FE in healthy lung tissue reported the occurrence of lung fibrosis after doses much higher than those required with CONV-RT (17 Gy CONV-RT vs. 30 Gy FLASH) (32). These data lay the foundation for a possible and promising translation to the clinic.

Vertebral metastases usually require palliative RT in more than 90% of patients with primary intent to control pain, prevent impending fracture, and avoid intracanal tumor invasion with the subsequent risk of spinal cord compression. Radiation oncologists often fail to reach this goal because of the delivery of suboptimal RT doses. The main drawback is the need to treat the entire vertebra encompassing the spinal cord in the clinical target volume. The spinal cord is a primary radiosensitive "serial" structure and is considered the cornerstone of primary organs at risk in RT, as overcoming the maximum tolerated dose leads to transversal myelitis (33). To date, the preserving effect of FLASH irradiation on the spinal cord has yet to be investigated in preclinical studies, as no data are currently available. Indeed, we do believe that this specific issue should be considered in the planning of the upcoming "*in vivo*" studies as it could rapidly open new perspectives in the clinical translation of FLASH-RT. In fact, the achievement of the maximum tolerated dose in the spinal cord is a major limitation in the RT of vertebral metastases as well as in the reirradiation of locoregional recurrences such as head and neck or lung tumors (34–36). Notably, RT for vertebral metastases might represent an ideal initial clinical application of VHEE due to the necessity of a low-complexity treatment technique.

Finally, pancreatic cancers are notoriously associated with a dismal prognosis due to poor local control and the early occurrence of distant metastases (37). Surgery is the mainstay of treatment, but only 30% of patients are fit, so many of them are treated with chemotherapy or RT. In this regard, the role of RT (mostly in non-surgical patients) has historically been debated because high tumoricidal doses cannot be delivered owing to double limitations. First, in patients affected by tumors located in the head of the pancreas, the duodenum is in close proximity with the primary tumor. Second, the presence of the small bowel, colon, and stomach, surrounding the clinical target volume. Notably, studies focused on investigating the possible role of stereotactic ablative RT in pancreatic cancers failed to prove a clinical benefit owing to the high pattern of severe complications (38) despite the use of a steep-gradient dose delivery technique. Therefore, if the current available data on the preservation of the intestine after FLASH irradiation is proven, it will constitute a good foundation for the potential clinical application of VHEE in pancreatic patients.

The clinical impact of VHEE is extremely important in oncology. However, its clinical implementation requires technological problems to be solved and the radiobiological mechanisms to be properly examined. To date, a clinical VHEE Linac has yet to be implemented. In this regard, high-energy electrons cannot be mechanically collimated (such as low-energy electrons) so that the dose coverage of the irradiated volume can be obtained by using a pencil beam delivery mode. Thus, it is necessary to investigate the "volume effect" by using adjacent and/or overlapping fields. Finally, owing to the necessity of using multiple fields to obtain an acceptable pattern of dose distribution, it is crucial to understand if the time lapse to pass from one field to another could compromise the FE.

## Conclusions

Currently, FLASH-RT has generated a significant interest in the radiation oncology community. Since the inception of RT and its underlying radiobiological principles, it represents the first radiobiological breakthrough that has the potential to revolutionize the treatment paradigm in the field of oncology. It is worth noting that the American Society for Radiation Oncology (ASTRO) membership has acknowledged FLASH-RT as a groundbreaking discovery that warrants prompt translation into clinical practice (39). In this regard, we anticipate an initial phase of limited clinical application involving Low Energy Electron (LEE) radiation, which will hopefully pave the way for a broader clinical implementation of Very High Energy Electron (VHEE) radiation. We believe that the crucial milestones for the exclusive treatment of deep-seated tumors will depend on the sustained manifestation of the FLASH Effect (FE) using low-dose fractions and the application of large, multi-field irradiation techniques. Conversely, FLASH-RT can also be integrated with conventional RT (CONV-RT) in the form of a tumor hypofractionated boost using simple techniques.

## Data availability statement

The original contributions presented in the study are included in the article/supplementary material. Further inquiries can be directed to the corresponding author.

## Author contributions

SU: Conceptualization, Writing – original draft. GG: Writing – review & editing. NG: Writing – review & editing. AG: Writing – review & editing. TF: Writing – review & editing. FD: Conceptualization, Supervision, Validation, Writing – review & editing. FP: Conceptualization, Supervision, Validation, Writing – review & editing.

## Funding

The author(s) declare financial support was received for the research, authorship, and/or publication of this article. This work is supported by the University of Pisa under the "PRA—Progetti di Ricerca di Ateneo" (Institutional Research Grants)—Project no. PRA_2022-2023_63 "DRIFT: DosimetRic and *in vitro* studies of Flash radioTherapy effect".

## Conflict of interest

FM received personal support for attending meetings from SIT-Sordina. FP received personal support for attending meetings from SIT-Sordina and from Thema Sinergie.

The remaining authors declare that the research was conducted in the absence of any commercial or financial relationships that could be construed as a potential conflict of interest.

## Publisher's note



## References

1. Thariat J, Hannoun-Levi JM, Myint AS, Vuong T, Gérard JP. Past, present, and future of radiotherapy for the benefit of patients. *Nat Rev Clin Oncol* (2013) 10(1):52–60. doi: 10.1038/nrclinonc.2012.203

2. Schuler E, Acharya M, Montay-Gruel P, Loo BW, Vozenin MC, Maxim PG. Ultra-high dose rate electron beams and the FLASH effect: From preclinical evidence to a new radiotherapy paradigm. *Med Phys* (2022) 49:2082–95. doi: 10.1002/mp.15442

3. Soto LA, Casey KM, Wang J, Blaney A, Manjappa R, Breitkreutz D. FLASH irradiation results in reduced severe skin toxicity compared to conventional-dose-rate irradiation. *Radiat Res* (2020) 194(6):618–24. doi: 10.1667/RADE-20-00090

4. Levy K, Natarajan S, Wang J, Chow S, Eggold JT, Loo PE, et al. Abdominal FLASH irradiation reduces radiation-induced gastrointestinal toxicity for the treatment of ovarian cancer in mice. *Sci Rep* (2020) 10(1):21600. doi: 10.1038/s41598-020-78017-7

5. Montay-Gruel P, Petersson K, Jaccard M, Boivin G, Germond JF, Petit B, et al. Irradiation in a flash: Unique sparing of memory in mice after whole brain irradiation with dose rates above 100Gy/s. *Radiother Oncol* (2017) 124(3):365–9. doi: 10.1016/j.radonc.2017.05.003

6. Di Martino F, Del Sarto D, Barone S, Bisogni MG, Capaccioli S, Galante F, et al. A new calculation method for the free electron fraction of an ionization chamber in the ultra-high-dose-per-pulse regimen. *Physica Med* (2022) 103:175–80. doi: 10.1016/j.ejmp.2022.11.001

7. Di Martino F, Del Sarto D, Bisogni MG, Capaccioli S, Galante F, Gasperin A, et al. A new solution for UHDP and UHDR (Flash) measurements: Theory and conceptual design of ALLS chamber. *Phys Med* (2022) 102:9–18. doi: 10.1016/j.ejmp.2022.08.010

8. Marks LB, Yorke ED, Jackson A, Ten Haken RK, Constine LS, Eisbruch A, et al. Use of normal tissue complication probability models in the clinic. *Int J Radiat Oncol Biol Phys* (2010) 76:S10–9. doi: 10.1016/j.ijrobp.2009.07.1754

9. Saunders M, Dische S, Barrett A, Harvey A, Gibson D, Parmar M. Continuous hyperfractionated accelerated radiotherapy (CHART) versus conventional radiotherapy in non-small-cell lung cancer: a randomised multicentre trial. *CHART Steering Committee Lancet* (1997) 19(350):161–5. doi: 10.1016/s0140-6736(97)06305-8

10. Mohan R. A review of proton therapy - current status and future directions. *Precis Radiat Oncol* (2022) 6:164–76. doi: 10.1002/pro6.1149

11. Wilson JD, Hammond EM, Higgins GS, Petersson K. Ultra-high dose rate (FLASH) radiotherapy: silver bullet or fool's gold? Front. *Oncol* (2020) 9:1563. doi: 10.3389/fonc.2019.01563

12. Friedl AA, Prise KM, Butterworth KT, Montay-Gruel P, Favaoudon V. Radiobiology of the flash effect. *Med Phys* (2022) 49(3):1993–2013. doi: 10.1002/mp.15184

13. Likhacheva A, Awan M, Barker CA, Bhatnagar A, Bradfield L, Brady MS, et al. Definitive and postoperative radiation therapy for basal and squamous cell cancers of the skin: executive summary of an american society for radiation oncology clinical practice guideline. *Pract Radiat Oncol* (2020) 10(1):8–20. doi: 10.1016/j.prro.2019.10.014

14. Cutaneous melanoma: ESMO clinical practice guidelines. *Ann Oncol* (2019).

15. Brodland DG, Zitelli JA. Surgical margins for excision of primary cutaneous squamous cell carcinoma. *J Am Acad Dermatol* (1992) 27:241–8. doi: 10.1016/0190-9622(92)70178-i

16. Jager MJ, Shields CL, Cebulla CM, Abdel-Rahman MH, Grossniklaus HE, Stern ME, et al. Uveal melanoma. *Nat Rev Dis Primers* (2020) 8:24. doi: 10.1038/s41572-020-0158-0

17. Sayan M, Mamidanna S, Oncel D, Jan I, Vergalasova I, Weiner J, et al. Clinical management of uveal melanoma: a comprehensive review with a treatment algorithm. *Radiat Oncol J* (2020) 38:162–9. doi: 10.3857/roj.2020.00318

18. Zemba M, Dumitrescu OM, Gheorghe AG, Radu M, Ionescu MA, Vatafu A, et al. Ocular complications of radiotherapy in uveal melanoma. *Cancers (Basel)* (2023) 15(2):333. doi: 10.3390/cancers15020333

19. Mishra KK, Daftari IK. Proton therapy for the management of uveal melanoma and other ocular tumors. *Chin Clin Oncol* (2016) 5:50. doi: 10.21037/cco.2016.07.06

20. Krempien R, Roeder F. Intraoperative radiation therapy (IORT) in pancreatic cancer. *Radiat Oncol* (2017) 12:8. doi: 10.1186/s13014-016-0753-0

21. Roeder F, Alldinger I, Uhl M, Ebrahimi LS, Schimmack S, Mechtersheimer G, et al. Intraoperative radiation therapy (IORT) in pancreatic cancer. *Radiat Oncol* (2017) 12:8. Intraoperative Electron Radiation Therapy in Retroperitoneal Sarcoma. Int J Radiat Oncol Biol Phys. 2018 100: 516-527 doi: 10.1186/s13014-016-0753-0. doi: 10.1186/s13014-016-0753-0

22. Gérard JP, Roy P, Cucherat M. Le contrôle local de la tumeur primitive. Étape indispensable de la guérison des cancers. *Cancer/Radiothérapie* (1998) 2(6):668–71. doi: 10.1016/s1278-3218(99)80006-7

23. Achrol AS, Rennert RC, Anders C, Soffietti R, Ahluwalia MS, Nayak L, et al. Brain metastases. *Nat Rev Dis Primers* (2019) 5(1):5. doi: 10.1038/s41572-018-0055-y

24. Rodríguez-Camacho A, Flores Vazquez JG, Moscardini Martelli J, Torres-Rio JA, Olmos-Guzman A, Ortiz-Arce CS, et al. Glioblastoma treatment: state-of-the-art and future perspectives. *Int J Mol Sci* (2022) 23:7207. doi: 10.3390/ijms23137207

25. Kruser TJ, Bosch WR, Badiyan SN, Bovi JA, Ghia AJ, Kim MM. NRG brain tumor specialists consensus guidelines for glioblastoma contouring. *J Neurooncol* (2019) 143(1):157–66. doi: 10.1007/s11060-019-03152-9

26. Zhong X, Huang B, Feng J, Yang W, Liu H. Delayed leukoencephalopathy of non-small cell lung cancer patients with brain metastases underwent whole brain radiation therapy. *J Neurooncol* (2015) 125(1):177–81. doi: 10.1007/s11060-015-1888-9

27. Casal-Mouriño A, Ruano-Ravina A, González ML, Rodríguez-Martínez A, Osorio AG, Lema LV, et al. Epidemiology of stage III lung cancer: frequency, diagnostic characteristics, and survival. *Transl Lung Cancer Res* (2021) 10(1):506–18. doi: 10.21037/tlcr.2020.03.40

28. Nichols L, Saunders R, Knollmann FD. Causes of death of patients with lung cancer. *Arch Pathol Lab Med* (2012) 136(12):1552–7. doi: 10.5858/arpa.2011-0521-OA

29. Käsmann L, Dietrich A, Staab-Weijnitz CA, Manapov F, Behr J, Rimner A, et al. Radiation-induced lung toxicity - cellular and molecular mechanisms of pathogenesis, management, and literature review. *Radiat Oncol* (2020) 15(1):214. doi: 10.1186/s13014-020-01654-9

30. Meng J, Li Y, Wan C, Sun Y, Dai X, Huang J, et al. Targeting senescence-like fibroblasts radiosensitizes non-small cell lung cancer and reduces radiation-induced pulmonary fibrosis. *JCI Insight* (2021) 6(23):e146334. doi: 10.1172/jci.insight.146334

31. Arroyo-Hernández M, Maldonado F, Ruiz FL, Muñoz-Montaño WM, Nuñez-Baez M, Arrieta O. Radiation-induced lung injury: current evidence. *BMC Pulm Med* (2021) 21:9. doi: 10.1186/s12890-020-01376-4

32. Favaudon V, Caplier L, Monceau V, Pouzoulet F, Sayarath M, Fouillade C. Ultrahigh dose-rate FLASH irradiation increases the differential response between normal and tumor tissue in mice. *Sci Transl Med* (2014) 6(245). doi: 10.1126/scitranslmed.3008973

33. Peyraga G, Ducassou A, Arnaud F-X, Lizée T, Pouédras J, Moyal E. Radiothérapie et toxicité médullaire: actualités et perspectives [Radiotherapy and spinal toxicity: News and perspectives]. *Cancer Radiother* (2021) 25(1):55–61. doi: 10.1016/j.canrad.2020.05.017

34. Embring A, Onjukka E, Mercke C, Lax I, Berglund A, Bornedal S, et al. Re-irradiation for head and neck cancer: cumulative dose to organs at risk and late side effects. *Cancers (Basel)* (2021) 13(13):3173. doi: 10.3390/cancers13133173

35. Hunter B, Crockett C, Faivre-Finn C, Hiley C, Salem A. Re-Irradiation of recurrent non-Small cell lung cancer. *Semin Radiat Oncol* (2021) 31(2):124–32. doi: 10.1016/j.semradonc.2020.11.009

36. Gottumukkala S, Srivastava U, Brocklehurst S, Mendel T, Kumar K, Yu F, et al. Fundamentals of radiation oncology for treatment of vertebral metastases. *Radiographics* (2021) 41(7):2136–56. doi: 10.1148/rg.2021210052

37. Park W, Chawla A, Eileen M. O'Reilly pancreatic cancer: A review. *JAMA* (2021) 326(9):851–62. doi: 10.1001/jama.2021.13027

38. Goldsmith C, Plowman PN, Melanie M, Green MM, Dale RG, Price PM, et al. Stereotactic ablative radiotherapy (SABR) as primary, adjuvant, consolidation and re-treatment option in pancreatic cancer: scope for dose escalation and lessons for toxicity. *Radiat Oncol* (2018) 19 13(1):204. doi: 10.1186/s13014-018-1138-3

39. Dominello MM, Sanders T, Anscher M, Bayouth J, Brock KK, Carlson DJ, et al. Responses to the 2018 and 2019 "One big discovery" Question: ASTRO membership's opinions on the most important research question facing radiation oncology … Where are we headed? *Int J Radiat Oncol Biol Phys* (2021) 109(1):38–40. doi: 10.1016/j.ijrobp.2020.08.032

frontiers | Frontiers in Physics

TYPE Original Research
PUBLISHED 08 November 2023
DOI 10.3389/fphy.2023.1274064



OPEN ACCESS

EDITED BY
Claudia Tanja Mierke,
Leipzig University, Germany

REVIEWED BY
Lanchun Lu,
The Ohio State University, United States
Stefan Bartzsch,
Technical University of Munich, Germany

*CORRESPONDENCE
Francesco G. Cordoni,
francesco.cordoni@unitn.it

RECEIVED 07 August 2023
ACCEPTED 10 October 2023
PUBLISHED 08 November 2023

CITATION
Battestini M, Missiaggia M, Attili A, Tommasino F, La Tessa C, Cordoni FG and Scifoni E (2023), Across the stages: a multiscale extension of the generalized stochastic microdosimetric model (MS-GSM$^2$) to include the ultra-high dose rate. *Front. Phys.* 11:1274064. doi: 10.3389/fphy.2023.1274064



# Across the stages: a multiscale extension of the generalized stochastic microdosimetric model (MS-GSM$^2$) to include the ultra-high dose rate

Marco Battestini[1,2], Marta Missiaggia[3], Andrea Attili[4], Francesco Tommasino[1,2], Chiara La Tessa[3], Francesco G. Cordoni[5,2]* and Emanuele Scifoni[2]

[1]Department of Physics, University of Trento, Trento, Italy, [2]National Institute for Nuclear Physics (INFN), Trento Institute for Fundamental Physics and Applications (TIFPA), Trento, Italy, [3]Radiation Oncology Department, University of Miami, Miami, FL, United States, [4]National Institute for Nuclear Physics (INFN), Roma Tre Section, Roma, Italy, [5]Department of Civil, Environmental and Mechanical Engineering, University of Trento, Trento, Italy

Ultra-high dose rate (UHDR) irradiations with different types of radiation have shown a larger sparing of normal tissue and unchanged tumor control with respect to conventional delivery. In recent years, there has been an accumulation of experimental evidence related to the so-called FLASH effect. However, the underpinning mechanism remains, to date, extremely debated and largely unexplained, while the involvement of multiple scales of radiation damage has been suggested. Since it is believed that the chemical environment plays a crucial role in the FLASH effect, this work aims to develop a multi-stage tool, the multiscale generalized stochastic microdosimetric model (MS-GSM$^2$), that can capture several possible effects on DNA damage at the UHDR regime, such as reduction of DNA damage yield due to organic radical recombination, damage fixation due to oxygenation, and spatial and temporal dose deposition effects, allowing us to explore most of the candidate mechanisms for explaining the FLASH effect. The generalized stochastic microdosimetric model (GSM$^2$) is a probabilistic model that describes the time evolution of DNA damage in a cell nucleus using microdosimetric principles, accounting for different levels of spatio-temporal stochasticity. In particular, the GSM$^2$ describes radiation-induced DNA damage formation and kinetic repair in the case of protracted irradiation without considering the Poissonian assumption to treat the number of radiation-induced DNA damage. In this work, we extend the GSM$^2$, coupling the evolution of DNA damage to fast chemical reaction kinetics, described by a system of ordinary differential equations, accounting for an additional level of stochasticity, i.e., in chemistry. We simulate energy deposition by particles in a microscopic volume, which mimics the cell nucleus, in order to examine the combined effects of several chemical species and the time evolution of DNA damage. We assume that UHDR modifies the time evolution of the peroxyl radical concentration, with a consequent reduction in the yield of the indirect DNA damage. This damage reduction emerges only at UHDR and is more pronounced at high doses. Moreover, the indirect damage yield reduction depends on the radiation quality. We show that the MS-GSM$^2$ can describe the empirical trend of dose- and dose rate-dependent cell sensitivity over a broad range, particularly the

larger sparing of healthy tissue occurring at the FLASH regime. The complete generality of the MS-GSM$^2$ also allows us to study the impact of different dose delivery time structures and radiation qualities, including high LET beams.

KEYWORDS

**FLASH effect, ultra-high dose rate biological mechanism, radiation chemistry, multi-stage radiobiological model, multiscale generalized stochastic microdosimetric model**

# 1 Introduction

## 1.1 Ultra-high dose rate irradiation: general context

Ultra-high dose rate (UHDR) irradiation, sometimes also referred to in the literature as FLASH irradiation, is a novel technique based on fast beam delivery, with a total irradiation time < 100 ms and an overall dose rate > 40 Gy/s for a single high enough dose, usually exceeding 10 Gy. It has been extensively demonstrated experimentally [1–5] that FLASH irradiation allows obtaining a higher sparing of normal tissue, e.g., a decrease in memory loss [6, 7] or less intestine necrosis [8], and, at the same time, an unchanged tumor control, e.g., an indistinguishable tumor response for HBCx-12A xenografts [1], with respect to conventional dose rate irradiation (CONV), characterized by a dose rate of 0.03–0.1 Gy/s. Many other experiments confirmed this sparing effect appearing at FLASH regimes, such as in animals, for example, no severe fibro-necrotic lesions on mini pig skin were observed [2] or even in humans, as in the first patient with cutaneous lymphoma, treated using electron beams [9].

In addition to that, the FLASH effect was observed for different radiation qualities [10], i.e., for different particle types, energies, and linear energy transfer (LET): (i) studies with electrons, such as in [11] with a 6 MeV electron beam LINAC, showed the same delayed glioblastoma growth in both CONV and the FLASH regime, while only the FLASH regime significantly spared animals from cognitive deficits in learning and memory; (ii) with protons, as demonstrated in [12], where using IBA *Proteus* Plus at 203 MeV at the FLASH regime, a significant reduction in the loss of proliferating cells in intestinal crypts was observed compared to the CONV regime, or in [13], where a reduction in normal tissue damage (in particular, acute skin damage and radiation-induced fibrosis) was observed for the same tumor control in the case of FLASH with respect to CONV using proton PBS (ProBeam, Varian Medical Systems) at 244 MeV for CONV and 250 MeV for FLASH; and, more recently, (iii) also with carbon ions [14, 15], both *in vitro* at the Heidelberg Ion-Beam Therapy Center (HIT) synchrotron and *in vivo* at the GSI Helmholtz Center in Darmstadt. Moreover, the first clinical trial with protons has already started [16]. Clinical translation is a fundamental step since FLASH radiotherapy, in principle, should allow for an

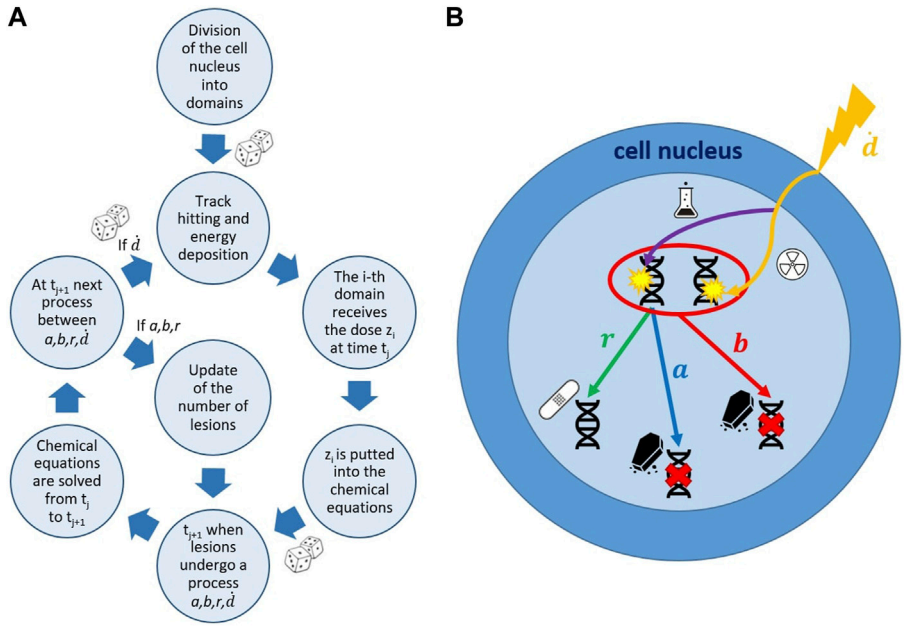


FIGURE 1
Schematic representation of the MS-GSM$^2$ workflow. **(A)** Simulation steps of the MS-GSM$^2$. Energy deposition according to microdosimetry, dose *z* distributed with the amorphous track model; joint evolution of slow biological and fast chemical processes. **(B)** Possible evolution of DNA lesions in a cell nucleus. *a*, *b*, *r*, and $\dot{d}$ are the death, pairwise death, repair, and dose rates, respectively. Both direct and indirect damage actions of ionizing radiation are taken into account.

enhancement of the therapeutic window because it should reduce the normal tissue toxicity for the same tumor control probability.

In recent years, numerous experimental efforts [3] have been dedicated to confirming the FLASH effect. However, the mechanism underlying this effect remains, to date, extremely debated and largely unexplained [5]. Several possible explanations of the FLASH effect have been proposed in the last few years [17], such as (i) transient hypoxia due to $O_2$ depletion [18], (ii) organic radical recombination [19], (iii) intertrack effects [20], or (iv) the immune system-driven effect [21].

(i) The transient hypoxia speculation [18] stems from the well-known effect that $O_2$ is locally consumed due to chemical reactions induced by the interaction between the ionizing radiation and the medium. Although the re-oxygenation phenomenon happens in milliseconds, the oxygen depletion is probably not enough to prompt radiobiological resistance. Therefore, it is not sufficient to explain the differential effect between healthy tissue and tumor, as described in [22]. (ii) The radical recombination hypothesis is based on the concept that a specific radical could accumulate differently between normal tissue and tumor under the UHDR regime. In particular, in [19], it was suggested that the different temporal evolution of the peroxyl radical concentration [$ROO^{\bullet}$] at a high dose rate could explain the sparing effect. The peroxyl radical $ROO^{\bullet}$ is generated from the reaction between the alkyl radical $R^{\bullet}$ and $O_2$, and it is known to be an important source of adverse effects on lipids and DNA [19, 23, 24]. (iii) The conjecture of the intertrack effect arises from the fact that, at a high dose rate, particles could arrive close enough in time and space before heterogeneous chemical reactions end, and this may affect the chemical stage of water radiolysis [20] and, in turn, the chemical environment of the cell. (iv) The last main hypothesis, the immune system-driven effect [21], postulates that UHDR irradiation may change the expression level of immune factors and active immune cells or, in general, influence the immune response.

To date, there are no experimental data that can validate or completely reject only one of these hypotheses; however, the involvement of a combination of multiple scales of radiation damage has been suggested [25]. If we compare the typical time scale to deliver 10 Gy CONV or 10 Gy FLASH with protons, it can be seen that the spatio-temporal window between the homogeneous chemical and biochemical stages of radiation damage could play a crucial role in the FLASH effect [25, 26].

## 1.2 An overview of mechanistic models and the contribution of this work

In the last 3–4 years, several mechanistic models have been developed to understand the underlying mechanism of the FLASH effect, using several different approaches such as molecular dynamics, Monte Carlo methods (e.g., track structure codes), analytical models, and mixed techniques [19, 27–31]. Despite the huge effort of the community, which succeeded in providing several insights into this complex picture, e.g., stressing the minor role of some proposed hypotheses, none of the proposed models seem to be able to fully describe the mechanism at the origin of the FLASH effect. Furthermore, the aforementioned models focus on a single possible mechanism and, thus, do not provide a mechanistically driven interpretation of the FLASH effect that fully includes an interplay of several potential pathways and spatio-temporal scales. This work extends a recently developed stochastic radiobiological model, the *Generalized Stochastic Microdosimetric Model* ($GSM^2$) [32–36].

The $GSM^2$ is a comprehensive mathematical model that encompasses numerous stochastic effects that arise during the creation, repair, and kinetics of radiation-induced DNA damage [34]. The $GSM^2$, based on microdosimetric principles, describes the formation and kinetic repair of two types of DNA lesions, namely, X and Y, which represent lesions that are reparable and lesions that result in cell inactivation, respectively. The $GSM^2$ assumes that lethal and sub-lethal lesions can undergo three different pathways, namely, *r*, *a*, and *b*, which represent, respectively, the repair of a sub-lethal lesion, the conversion of a sub-lethal lesion to a lethal lesion, and the pairwise interaction of two sub-lethal lesions to become a lethal one [32, 33].

Due to the significant role that the chemical environment is believed to play in the FLASH effect, in the present work, we expanded the $GSM^2$ by coupling fast chemical reaction kinetics, as described in [19], to the slow evolution of DNA damage. This led to the development of a multiscale version of the $GSM^2$ (MS-$GSM^2$), which can capture various potential impacts on DNA damage within the UHDR regime. The multiscale nature of the MS-$GSM^2$ emerges from the driving equations, where the slow biological processes are described by discrete stochastic differential equations, whereas the chemical kinetics are continuous ordinary differential equations. Following [19], we hypothesize that the different temporal evolution of the peroxyl radical concentration [$ROO^{\bullet}$] at a high dose rate is at the origin of the FLASH effect. In contrast to [19], we directly link [$ROO^{\bullet}$] to the biological damage as follows: we split the creation of biological damage by an energy deposition into direct and indirect damage. As standard in the literature, we assume that the number of direct damages is proportional to the imparted energy. On the contrary, indirect damage is linked to the chemical environment. In particular, we conjecture that the number of lethal and sub-lethal damages depends on the local peroxyl radical concentration [$ROO^{\bullet}$], since the contribution of [$ROO^{\bullet}$] to the damage of biological structures, including DNA, is well known [19]. Therefore, we show how UHDR regimes that modify the [$ROO^{\bullet}$] evolution can, in turn, change the indirect damage yield that eventually leads to a cell survival reduction. Similar to the approach described in [37], energy depositions are described via a Monte Carlo sampling of particle tracks hitting the target, while the radial dose distribution is described via an amorphous track model [38]. The target considered is bigger than the cell nucleus, so the energy deposited by tracks passing near the cell nucleus, i.e., the ionization penumbra of the tracks, is also accounted for by the MS-$GSM^2$. The resulting model is an extremely general biophysical model, able to provide a mechanistically grounded description of several effects of random processes in space and time [34, 39].

In addition to introducing the MS-$GSM^2$, the present paper investigates the effect of radiation quality on the onset of the FLASH effect. The latter issue is presently largely debated [25], and it is still largely unknown how LET can affect the typical normal tissue sparing encountered in FLASH. For this reason, we consider protons of 18.6 MeV and carbon ions of 149 MeV/u, studying how the different spatio-temporal stochastic patterns of energy

deposition affect the damage yield and, in turn, the resulting cell survival.

The main contributions of the present work are as follows:

(i) Introducing a general stochastic model able to provide a unified framework encompassing physics, chemistry, and biology;
(ii) Proposing a mechanism underpinning the manifestation of the FLASH effect, which includes three of the major potential mechanistic pathways commonly considered for explaining that effect, i.e., organic radical–radical recombination, damage fixation due to oxygenation, and spatial and temporal dose deposition effects;
(iii) Showing how the interplay of the aforementioned different mechanisms can, in turn, produce cell survival sparing at a sufficiently high dose and dose rate.

# 2 Theory and calculations

## 2.1 Generalized stochastic microdosimetric model

The GSM$^2$ is a fully probabilistic model that accurately describes the stochastic nature of energy deposition in volumes of interest for cellular systems. The final goal is to overcome existing models, which most assume a Poissonian distribution of the number of radiation-induced DNA damages, to provide a better prediction of biological endpoints relevant to radiotherapy applications. The GSM$^2$ was first introduced in [32], where a detailed description of its structure can be found. The model assumes that the cell nucleus is divided into $N_d$ independent domains $d$. Within each domain, it is assumed that two types of DNA lesions can be formed: lethal and sub-lethal lesions. The former represents damage that cannot be repaired, leading to cell inactivation, while the latter can be either repaired or become a lethal lesion, leading to cell inactivation.

For modeling the time evolution of the number of lethal and sub-lethal lesions, we will denote the state of the system by $(Y(t), X(t))$ at time $t$, where $X$ and $Y$ are two $\mathbb{N}$–valued random variables representing the number of lethal and sub-lethal lesions, respectively.

A sub-lethal lesion can evolve in three different ways: (i) it can become a lethal lesion at a rate $a$, (ii) it can be repaired at a rate $r$, or (iii) it can combine with another sub-lethal lesion to become a lethal lesion at a rate $b$. This scheme can be represented by the following equations:

$$X \xrightarrow{a} Y, \qquad X \xrightarrow{r} \varnothing, \qquad X + X \xrightarrow{b} Y, \tag{1}$$

where $\varnothing$ represents the ensemble of healthy cells.

Based on Eq. 1, we developed the *microdosimetric master equation* (MME) as follows [32]:

$$\begin{aligned}\frac{\partial}{\partial t}p(t,y,x) &= (E^{-1,2}-1)[x(x-1)bp(t,y,x)] \\ &\quad +(E^{-1,1}-1)[xap(t,y,x)] + (E^{0,1}-1)[xrp(t,y,x)] \\ &= \mathcal{E}^{-1,2}[x(x-1)bp(t,y,x)] + \mathcal{E}^{-1,1}[xap(t,y,x)] \\ &\quad + \mathcal{E}^{0,1}[xrp(t,y,x)],\end{aligned} \tag{2}$$

where the creation operator is defined as

$$\mathcal{E}^{i,j}[f(y,x)] \coloneqq (E^{i,j}-1)[f(y,x)] \coloneqq f(y+i,x+j) - f(y,x),$$

which signifies a transition in the state, defining the number of sub-lethal and lethal damages.

The MME is coupled with an initial damage distribution derived from microdosimetric spectra, providing a comprehensive description of the radiation field quality [40–42]. The single-event distribution of energy deposition on a domain $d$, referred to as $f_{1;d}(z)$ [43], can either be computed numerically with a Monte Carlo code or measured experimentally. Given a cell nucleus domain $d$, the probability that $\nu$ events deposit energy $z$ follows a Poissonian distribution with the mean denoted by $\lambda_n \coloneqq \frac{z_n}{z_F}$, where $z_n$ represents the mean energy deposition on the nucleus domain and $z_F$ is the first moment of the single-event distribution $f_{1;d}$. Then, assuming a Poissonian probability that a domain registers $\nu$ events, the energy deposition distribution is given by

$$f_d(z|z_n) \coloneqq \sum_{\nu=0}^{\infty} \frac{e^{-\frac{z_n}{z_F}}}{\nu!}\left(\frac{z_n}{z_F}\right)^{\nu} f_{\nu;d}(z), \tag{3}$$

where $f_{\nu;d}(z)$ is the energy deposition distribution resulting from $\nu$ depositions. We conventionally assumed that $f_{0;d}(z) = \delta_0(z)$, indicating that no event will result in the deposition specific energy.

Using $p_z(x, y|z)$ to denote the initial joint distributions for the number of sub-lethal and lethal lesions for a given energy deposition $z$, we obtain

$$\begin{aligned}p_0(x,y) = \sum_{\nu=0}^{\infty}\int_0^{\infty}\cdots\int_0^{\infty} p_z(x,y|z_1,\ldots,z_\nu)\frac{e^{-\frac{z_n}{z_F}}}{\nu!}\left(\frac{z_n}{z_F}\right)^{\nu} \\ \times f_{\nu;d}(z_1,\ldots,z_\nu)dz_1\ldots dz_\nu.\end{aligned} \tag{4}$$

In particular, assuming the events to be statistically independent, the distribution resulting from $\nu$ events can be computed by convolving the single-event distribution $\nu$ times [43]. Therefore, the distribution $f_{\nu;d}$ of the imparted energy $z$ is computed iteratively as

$$\begin{aligned}f_{2;d}(z) &\coloneqq \int_0^{\infty} f_{1;d}(\bar{z})f_{1;d}(z-\bar{z})d\bar{z}, \\ &\ldots, \\ f_{\nu;d}(z) &\coloneqq \int_0^{\infty} f_{1;d}(\bar{z})f_{\nu-1;d}(z-\bar{z})d\bar{z}.\end{aligned}$$

It is considered that the quantity $p_z(x, y|z_1, \ldots, z_\nu)$ gives the probability of observing $x$ sub-lethal lesions and $y$ lethal lesions resulting from the energy depositions $z_1, \ldots, z_\nu$. The average yields of sub-lethal and lethal lesions are denoted by $\kappa(z_1, \ldots, z_\nu)$ and $\lambda(z_1, \ldots, z_\nu)$, respectively, for the energy depositions $z_1, \ldots, z_\nu$. The formation of lesions by different deposition events is statistically independent because the events are independent. The formation of lesions by a single energy deposition event is approximately statistically independent. It follows that the distribution of the number of lesions that result from the $i$-th deposition event is approximately Poissonian, i.e.,

$$\begin{aligned}p_z(x_\nu, y_\nu|z_1,\ldots,z_\nu) \coloneqq e^{-\kappa(z_1,\ldots,z_\nu)}\frac{(\kappa(z_1,\ldots,z_\nu))^{x_\nu}}{x_\nu!} \\ \times e^{-\lambda(z_1,\ldots,z_\nu)}\frac{(\lambda(z_1,\ldots,z_\nu))^{y_\nu}}{y_\nu!}.\end{aligned}$$

The probability that $x$ and $y$ total lesions will be produced if energy depositions $z_1, \dots, z_\nu$ occur is

$$p_z(x, y|z_1, \dots, z_\nu) \coloneqq \sum_{\substack{x_1,\dots,x_\nu \\ y_1,\dots,y_\nu}} p_z^X(x_1, y_1|z_1) p_z^X(x_2, y_2|z_1, z_2) \dots \times p_z^X(x_\nu, y_\nu|z_1, \dots, z_\nu),$$

where the aforementioned summation runs over $x_1, \dots, x_\nu$ and $y_1, \dots, y_\nu$ such that $x_1 + \dots + x_\nu = x$ and $y_1 + \dots + y_\nu = y$. In short, we can denote as

$$\bar{\kappa}(z_1, \dots, z_\nu) \coloneqq \sum_{i=1}^{\nu} \kappa(z_1, \dots, z_i), \quad \bar{\lambda}(z_1, \dots, z_\nu) \coloneqq \sum_{i=1}^{\nu} \lambda(z_1, \dots, z_i),$$

and the probability of $x$ and $y$ lesions is given by

$$p_z(x, y|z_1, \dots, z_\nu) = e^{-\bar{\kappa}(z_1,\dots,z_\nu)} \frac{(\bar{\kappa}(z_1, \dots, z_\nu))^x}{x!} e^{-\bar{\lambda}(z_1,\dots,z_\nu)} \frac{(\bar{\lambda}(z_1, \dots, z_\nu))^y}{y!}.$$

The standard assumption is that the average yield of lesions is proportional to the dose, i.e.,

$$\bar{\kappa}(z_1, \dots, z_\nu) = \kappa(z_1 + \dots + z_\nu) = \kappa z,$$
$$\bar{\lambda}(z_1, \dots, z_\nu) = \lambda(z_1 + \dots + z_\nu) = \lambda z,$$

for positive constants $\kappa > 0$ and $\lambda > 0$. In [32, 33], the same choice has been made, implying that the average yield of the lesion for a given dose $D$ is given by

$$\sum_{x \geq 0} x p_0(x, y) = \kappa D.$$

The quantity $\kappa(z_1, \dots, z_\nu)$ is generally taken to be either a linear or quadratic function that summarizes several physical, chemical, and biological effects. It is a function of the type of ionizing particle, LET, details of the track structure, radical diffusion and reaction rates, the phase in the cell cycle, and the chemical environment of the cell. Additionally, as it is widely acknowledged that the temporal and spatial distribution of various particle tracks and energy deposition significantly influence the emergence of the FLASH effect, our forthcoming approach is geared toward explicitly incorporating both temporal and spatial stochasticity. This will be achieved by closely coupling the energy deposition with a rapid chemical characterization of the surrounding environment. We will formally introduce a fast component that describes the evolution of the chemical environment. To further explicitly model the dose rate effect, we will assume that the function $\kappa$ depends on the chemical environment modified by radiation.

## 2.2 Multiscale GSM$^2$

In order to generalize the GSM$^2$ to the multiscale GSM$^2$ (MS-GSM$^2$), including the fast chemical reactions, as schematized in Figure 1, we first reformulate the model along two main directions: on one side, we provide a general multi-domain cell nucleus description along the lines of [32], and on the other side, we give a pathwise description for the MME (2) in terms of jump-type *stochastic differential equations* (SDEs).

In particular, it can be seen [44, Chapter 13] that Eq. 2 describes the time evolution for the probability density function associated with the following SDE for the domain $d$ of the cell $c$:

$$\Sigma^c: \begin{cases} Y^{(c,d)}(t) & = Y_0^{(c,d)} + \mathrm{P}_a^{(c,d)}\left(\int_0^t aX^{(c,d)}(s)ds\right) + \mathrm{P}_b^{(c,d)}\left(\int_0^t bX^{(c,d)}(s)\left(X^{(c,d)}(s) - 1\right)ds\right), \\ X^{(c,d)}(t) & = X_0^{(c,d)} - \mathrm{P}_a^{(c,d)}\left(\int_0^t aX^{(c,d)}(s)ds\right) - \mathrm{P}_r^{(c,d)}\left(\int_0^t rX^{(c,d)}(s)ds\right) + \\ & \quad -2\mathrm{P}_b^{(c,d)}\left(\int_0^t bX^{(c,d)}(s)\left(X^{(c,d)}(s) - 1\right)ds\right), \\ d & = 1, \dots, N_d. \end{cases} \tag{5}$$

In Eq. 5, the terms $\mathrm{P}_h^{(c,d)}$, with $h \in \{a, b, r\}$, are independent unitary Poisson jump processes [45]. In order to include the effect of UHDR in the GSM$^2$, as briefly mentioned above, we will suitably modify here how the energy depositions $z$ create lethal and sub-lethal lesions. In particular, we introduce several improvements to the presently available version of GSM$^2$. First, as already carried out in [32], (i) we include a protracted dose-rate term that accounts for the energy deposition events and subsequent lesion creation; such a term explicitly models the series of energy depositions in the whole cell nucleus $z_1, \dots, z_\nu$, where $\nu$, in this case, is the number of events on the nucleus. Then, (ii) we split the creation of direct and indirect DNA damage, where the former happens instantaneously at the energy deposition and the latter depends on the chemical environment and how organic radicals recombine in a suitable time interval $[0, T_I]$. At last, (iii) to describe the formation of indirect DNA damage, following [19], we include a set of differential equations that model the time evolution and reaction of radicals and other molecular species.

Thus, we get to the following MS-GSM$^2$ system of equations:

$$\Sigma^c_{\mathrm{MS}}: \begin{cases} Y^{(c,d)}(t) & = \mathrm{P}_a^{(c,d)}\left(\int_0^t aX^{(c,d)}(s)ds\right) + \mathrm{P}_b^{(c,d)}\left(\int_0^t bX^{(c,d)}(s)\left(X^{(c,d)}(s) - 1\right)ds\right) + \\ & \quad + Z_{Y;d}^{(c,d)} \mathrm{P}_{\dot{d}}^{(c)}\left(\int_0^t \dot{d}\, ds\right) + Z_{Y;i}^{(c,d)} \mathrm{P}_\rho^{(c,d)}\left(\int_0^t \rho(\xi_s)\, ds\right) \\ X^{(c,d)}(t) & = -\mathrm{P}_a^{(c,d)}\left(\int_0^t aX^{(c,d)}(s)ds\right) - \mathrm{P}_r^{(c,d)}\left(\int_0^t rX^{(c,d)}(s)ds\right) + \\ & \quad -2\mathrm{P}_b^{(c,d)}\left(\int_0^t bX^{(c,d)}(s)\left(X^{(c,d)}(s) - 1\right)ds\right) + \\ & \quad + Z_{X;d}^{(c,d)} \mathrm{P}_{\dot{d}}^{(c)}\left(\int_0^t \dot{d}\, ds\right) + Z_{X;i}^{(c,d)} \mathrm{P}_\rho^{(c,d)}\left(\int_0^t \rho(\xi_s)\, ds\right), \\ \frac{d}{dt}\left[\mathrm{e}^-_{\mathrm{aq}}\right]^d(t) & = f_{\mathrm{e}^-_{\mathrm{aq}}}\left(\xi^d(t)\right) + c_{\mathrm{e}} \dot{z}^d, \\ \frac{d}{dt}[\mathrm{O}_2]^d(t) & = f_{\mathrm{O}_2}\left(\xi^d(t)\right), \\ \frac{d}{dt} C^d_{\mathrm{H_2O_2}}(t) & = f_{\mathrm{H_2O_2}}\left(\xi^d(t)\right) + c_{\mathrm{H_2O_2}} \dot{z}^d, \\ \frac{d}{dt} C^d_{\mathrm{OH^\bullet}}(t) & = f_{\mathrm{OH^\bullet}}\left(\xi^d(t)\right) + c_{\mathrm{OH^\bullet}} \dot{z}^d, \\ \frac{d}{dt}[\mathrm{H^\bullet}]^d(t) & = f_{\mathrm{H^\bullet}}\left(\xi^d(t)\right) + c_{\mathrm{H^\bullet}} \dot{z}^d, \\ \frac{d}{dt}[\mathrm{H_2}]^d(t) & = f_{\mathrm{H_2}}\left(\xi^d(t)\right) + c_{\mathrm{H_2}} \dot{z}^d, \\ \frac{d}{dt} C^d_{\mathrm{O_2^{\bullet-}}}(t) & = f_{\mathrm{O_2^{\bullet-}}}\left(\xi^d(t)\right), \\ \frac{d}{dt}[\mathrm{R^\bullet}]^d(t) & = f_{\mathrm{R^\bullet}}\left(\xi^d(t)\right) + c_{\mathrm{R^\bullet}} \dot{z}^d, \\ \frac{d}{dt}[\mathrm{ROO^\bullet}]^d(t) & = f_{\mathrm{ROO^\bullet}}\left(\xi^d(t)\right), \\ \xi^d(t) & = \left(\left[\mathrm{e}^-_{\mathrm{aq}}\right]^d, [\mathrm{O}_2]^d, C^d_{\mathrm{H_2O_2}}, C^d_{\mathrm{OH^\bullet}}, [\mathrm{H^\bullet}]^d, [\mathrm{H_2}]^d, C^d_{\mathrm{O_2^{\bullet-}}}, [\mathrm{R^\bullet}]^d, [\mathrm{ROO^\bullet}]^d\right)(t), \\ d & = 1, \dots, N_d. \end{cases} \tag{6}$$

The reaction network is schematized in Figure 1 of [19], while the specific reactions and the rate constants considered in this work are reported in Sections S.1 and S.2 of [19].

The key aspects worth highlighting regarding the MS-GSM$^2$ (6) are the following:

(i) Compared to the system $\Sigma^c$ in Eq. 5, the MS-GSM$^2$ system $\Sigma^c_{\mathrm{MS}}$ in Eq. 6 is driven by two more unitary Poisson processes: $\mathrm{P}_{\dot{d}}^{(c)}$ and $\mathrm{P}_\rho^{(c,d)}$. It should be noted that $\mathrm{P}_\rho^{(c,d)}$ is similar to $\mathrm{P}_h^{(c,d)}$, where $h \in \{a, b, r\}$, and it is a Poisson process acting on a single domain,

whereas $\mathrm{P}_{\dot{d}}^{(c)}$ accounts for energy deposition and is, therefore, an inter-domain process that can affect more than one domain at once. Each single energy deposition can induce a random number $Z_{Y;d}^{(c,d)}$ and $Z_{X;d}^{(c,d)}$ of direct lethal and sub-lethal lesions, respectively, on each domain $d = 1, \ldots, N_d$; a similar argument holds for $Z_{Y;i}^{(c,d)}$ and $Z_{X;i}^{(c,d)}$ concerning indirect damages.

(ii) The Poisson jump process $\mathrm{P}_{\rho}^{(c,d)}$ describes the formation of indirect damages. It depends explicitly on the chemical environment and energy depositions. In doing so, we assume that the effect of the chemical environment on the creation of DNA damage is not instantaneous but depends on the concentration of radicals in a time interval $[t - T_I, t]$. Therefore, we employed the shorthand notation $\xi_t$ to denote

$$\xi_t := \int_{-T_I}^{0} \xi(t+\theta)d\theta.$$

In the present work, we choose the rate

$$\rho(\xi_t) := \varrho \int_{-T_I}^{0} e^{-T_{irr}} \xi(t+\theta)d\theta, \tag{7}$$

for a suitable constant $\varrho > 0$, where $T_{irr}$ is the irradiation time.

(iii) The random variables $Z_{Y;d}^{(c,d)}$ and $Z_{X;d}^{(c,d)}$ describe the number of direct lethal and sub-lethal lesions, respectively, created on each domain $d = 1, \ldots, N_d$, whereas $Z_{Y;i}^{(c,d)}$ and $Z_{X;i}^{(c,d)}$ are random variables describing the number of indirect lethal and sub-lethal lesions, respectively, created on each domain $d = 1, \ldots, N_d$. As mentioned previously, the distinction has been made to account for the UHDR effects. According to the aforementioned description, we first assume that, given an energy deposition $z$ subsequent to a track deposition, a certain number of direct DNA damages are created within the cell nucleus, $Z_Y^{(c,d)}$ and $Z_X^{(c,d)}$. These random variables follow a distribution

$$\begin{aligned} p(x|z) &= e^{-\kappa(z)} \frac{(\kappa(z))^x}{x!} \\ p(y|z) &= e^{-\lambda(z)} \frac{(\lambda(z))^y}{y!}. \end{aligned} \tag{8}$$

Thus, we explicitly include in the functions $\kappa(z)$ and $\lambda(z)$ the effects that the chemical environment and LET have on the number of damages created. In particular, we assume that the average yield of sub-lethal lesions per unit Gy under the conventional dose rate is $\kappa > 0$. Then, we assume that a fraction $q \in [0, 1]$ of $\kappa$ is due to indirect damage, i.e., radical-mediated. In contrast, the remaining $1 - q$ is due to direct damages, and this fraction depends on LET, according to several experimental data such as in [46]; we assume that only the number of indirect damages created depends on the chemical environment. Summarizing, after an energy deposition event $z$ is registered at a certain time $t$, we assume first that a random number of direct sub-lethal or lethal lesions can be created at rates $\kappa(1 - q)z$ and $\lambda(1 - q)z$, respectively.

(iv) The chemical system $\xi$ evolves according to [19]; nonetheless, in contrast to [19], we do not assume a continuous dose-rate effect, but the effect of energy deposition is modulated by the track's arrival time as prescribed by $\mathrm{P}_{\dot{d}}^{(c)}$. In particular, $\dot{z}^d$ is a purely discontinuous jump process that describes the energy deposition in the domain $d$. This allows extreme flexibility in the modelization of the effect of dose rate so that any dose-rate structure can be implemented into the MS-GSM$^2$.

## 2.3 Stepwise construction of the MS-GSM$^2$

In Algorithm 1, we describe in detail how to construct and simulate stepwise the solution of the MS-GSM$^2$ (6), as also summarized in Figure 1. Such construction is based on the joint usage of a standard *stochastic simulation algorithm* (SSA) [45], together with a solver of ordinary differential equations (ODEs) for the chemical system. In the following, we assume irradiation in the time interval $[0, T_{\mathrm{irr}}]$ so that we have $\dot{d} = 0$ for $t > T_{\mathrm{irr}}$ and a terminal time $T > T_{\mathrm{irr}} + T_I$ sufficiently large so that the system $\Sigma_{\mathrm{MS}}^c$ reaches convergence.

Notation:
$h_{1+4(d-1)}(x,\xi) = rx^d$, $h_{2+4(d-1)}(x,\xi) = ax^d$, $h_{3+4(d-1)}(x,\xi) = bx^d\left(x^d - 1\right)$,
$h_{4+4(d-1)}(x,\xi) = \rho\left(\xi^d\right)$, $h_{1+4N_d}(x,\xi) = \dot{d}$, $h(x,\xi) := \sum_{i=1}^{1+4N_d} h_i(x,\xi)$.

Start with an initial chemical environment $\xi(t) = \xi_0$, biological system $X(t) = Y(t) = 0$, and initial time $t = 0$;
  set $T_i = 0$, for $i = 1, \ldots, 1 + 4N_d$;
  **while** $t < T$ **do**
    **for all** $h_i$, $i = 1, \ldots, 1 + 4N_d$ **do**
generate a random number $R_i \sim U(0, 1)$ and set $U_i := \log\frac{1}{R_i}$;
      compute $\tau_i$ solving

$$\int_t^{t+\tau_i} h_i(X(s), \xi_s)ds = S_i - T_i.$$

We use the convention that if $h_i(X(t), \xi_s) = 0$, then $\tau_i = \infty$;
    **end for**
    select $\tau := \min_{(i=1,\ldots,1+4N_d)} \tau_i$;
    select the corresponding rate $h_i$ at which the minimum is attained;
    solve the chemical system for $\xi$ in the time interval $[t, t + \tau]$;
    **for all** $h_i$, $i = 1, \ldots, 1 + 4N_d$ **do**
      set

$$T_i = T_i + \int_t^{t+\tau} h_i(X(s), \xi_s)ds,$$

      update $t = t + \tau$;
    **if** $i = 1 + 4(d - 1)$, for some $d = 1, \ldots, N_d$, **then**
      update $X(t) = X(t) - 1$, $Y(t) = Y(t)$, and $\xi(t) = \xi(t)$;
    **else if** $i = 2 + 4(d - 1)$, for some $d = 1, \ldots, N_d$, **then**
      update $X(t) = X(t) - 1$, $Y(t) = Y(t) + 1$, and $\xi(t) = \xi(t)$;
    **else if** $i = 3 + 4(d - 1)$, for some $d = 1, \ldots, N_d$, **then**
      update $X(t) = X(t) - 2$, $Y(t) = Y(t) + 1$, and $\xi(t) = \xi(t)$;
    **else if** $i = 4 + 4(d - 1)$, for some $d = 1, \ldots, N_d$, **then**
      simulate $Z_{Y;i}^{(c,d)}$ and $Z_{X;i}^{(c,d)}$;
      update $X(t) = X(t) + Z_{X;i}^{(c,d)}$, $Y(t) = Y(t) + Z_{Y;i}^{(c,d)}$, and $\xi(t) = \xi(t)$;

```
    else if i = 4N_d, then
      simulate the position where the track hits;
      compute the total specific energy deposition z
      according to microdosimetric spectra;
      for d = 1 to N_d do
        compute the specific energy deposition z^d
        according to an amorphous track model;
        simulate Z_{Y;d}^{(c,d)} and Z_{X;d}^{(c,d)} according to Eq. 8;
        update X(t) = X(t) + Z_{X;d}^{(c,d)}, Y(t) = Y(t) + Z_{Y;d}^{(c,d)}, and
        ξ(t) = ξ(t) + G_ξ ρ z^d;
      end for
    end if
    end for
  end while
  end the system.
```

Algorithm 1. The MS-GSM².

## 2.4 MS-GSM² simulations

We consider a microscopic volume consisting of a water cylinder of radius $R_N = 8\ \mu m$ ($xy$-plane) and length $2R_N$ ($z$-direction), divided into $N_d = 64 \times 8$ cubic domains to mimic a cell nucleus. The impact point of the particle is simulated by sampling randomly from a uniform distribution on a circle of radius $R_N + R_{80}$ on the $xy$-plane, where

$$R_{80} = R_c \exp\left(\frac{0.8\left(1 + 2\ln\left(R_p/R_c\right) - 1\right)}{2}\right)$$

is the radius corresponding to 80% of the dose deposited by the track, according to the amorphous track model description mentioned in [25]. The choise of $R_N + R_{80}$ is made in such a way as to take into account for dose depositions due to particles passing outside the cell nucleus but delivering a significant contribution inside it. We use the following parameters: $R_c = 0.01\ \mu m$ is the core radius and $R_p = 0.05\ (E/A)^{1.7}$ is the penumbra radius of the track, according to [47], where $E/A$ is the energy per nucleon. The choice of approximating the penumbra radius $R_p$ with $R_{80}$ is a compromise between the accuracy of the description of the amorphous track and computational reasons (long time and large memory consumption). The average number of simulated particles $N_p$ is defined by the dose–LET relation, considering $\pi(R_N + R_{80})^2$ as the hitting surface. The actual number of simulated particles is obtained by summing the number of deposition events up to the irradiation time $T_{irr} = D/\dot{D}$ according to Algorithm 1, where $D$ is the imparted macroscopic dose and $\dot{D}$ is the mean dose rate. The time $\tau$ between one deposition and the next is sampled as described in Algorithm 1. The absorbed dose of a single event $z$ is distributed on the $N_d$ domains of the $xy$-plane according to the amorphous track model described in [47], i.e.,

$$D_c = \frac{1}{\pi R_c^2}\left(\frac{LET}{\rho\left(1 + 2\ln\left(R_p/R_c\right)\right)}\right)$$
$$D_p(r) = \frac{1}{\pi r^2}\left(\frac{LET}{\rho\left(1 + 2\ln\left(R_p/R_c\right)\right)}\right),$$

where $r$ is the track radius and $\rho$ is the water density. The path of the ion is considered parallel to the cylinder axis, and variations in trajectory and speed are neglected along the $z$-direction, i.e., the LET is constant within the cylinder ("track-segment conditions"), in analogy to [38].

The chemical system is described by a set of nine ordinary differential equations (Eq. 6), considering the reactions and their rate constants and initial concentrations according to [19]. The evolution of the chemical species is followed up to a time $T = T_{irr} + T_{off} > 500$ s, where $T_{off}$ is the time for the relaxation of the chemical system once the irradiation is finished, i.e., $\dot{d} = 0$. The indirect DNA damage yield $\kappa$, described in the previous paragraph (i.e., in Eq. 8), is modulated, in particular, by the time evolution of the peroxyl radical concentration [$ROO^{\bullet}$], according to Eq. 7. This organic radical is crucial for DNA damage, as described in [19]. The number of sub-lethal and lethal lesions is calculated from Eq. 6, while the cell survival fraction is estimated according to [32, 33], considering common values for the pathway rates, i.e., $a = 0.01$, $b = 0.01$, and $r = 4$.

Given a certain particle, characterized by type, energy, and LET, the simulation is repeated over a wide range of macroscopic doses $D$, from 1 Gy to 30 Gy, and the average dose rate $\dot{D}$, from 0.03 Gy/s (CONV) to 100 Gy/s (UHDR). The time evolution of the instantaneous dose rate depends on the deposition time structure described previously. The simulation is also repeated for different radiation qualities; specifically, we report the results for protons at 18.6 MeV and carbon ions at 149 MeV/u.

To summarize, all the parameters considered in our simulations are shown in Table 1. Moreover, as mentioned previously, the MS-GSM² accounts for several stages of radiation damage, including the physical, homogeneous chemical, and biological stages, as well as different levels of stochasticity, particularly in ionizing radiation, chemistry, and DNA damage formation and time evolution, as reported in Table 2. Finally, following Algorithm 1, all the simulations reported in this work were performed using MATLAB; specifically, we used the function `ode15s.m` for the numerical integration of the ODEs that describe the chemical system shown in Eq. 6.

**TABLE 1** Summary of the parameters considered in this work.

| Parameter | Description | Value/range |
|---|---|---|
| $R_N$ | Nucleus radius | 8 $\mu m$ |
| $N_d$ | Number of cubic domains | 64 × 8 |
| ${}^{A}X$ | Particle type | p and ${}^{12}C$ |
| $E/A$ | Particle energy | 18.6 MeV and 149 MeV/u |
| $R_{80}$ | Radius at 80% of the dose | 1.75 $\mu m$ and 29.60 $\mu m$ |
| $D$ | Dose | 1–30 Gy |
| $\dot{D}$ | Dose rate | 0.03–100 Gy/s |
| $\{\xi_0\}$ | Initial concentrations | Reported in [19] |
| $\{k_\xi\}$ | Rate constants | Reported in [19] |
| $q$ | Indirect damage fraction | 0.8 and 0.65 [45] |
| $a$, $b$, and $r$ | Pathway rates | 0.01, 0.01, and 4 |

**TABLE 2** Stages and corresponding spatio-temporal scales of radiation damage considered in this work and related levels of stochasticity taken into account by the MS-GSM$^2$.

| Stage | Temporal scale | Spatial scale | Stochasticity |
|---|---|---|---|
| Physics | Instantaneous | $10^{-6}$–$10^{-5}$ $m$ | Track hitting and energy deposition |
| Homogeneous chemistry | $10^{-6}$–$10^{0}$ $s$ | $10^{-6}$ $m$ | Time $\tau$ for next deposition event $\dot{d}$ |
| Direct damage formation | Instantaneous | $10^{-6}$ $m$ | $Z_{Y;d}^{(c,d)}$ and $Z_{X;d}^{(c,d)}$ according to (8) |
| Indirect damage formation | $10^{-6}$–$10^{0}$ $s$ | $10^{-6}$ $m$ | $Z_{Y;i}^{(c,d)}$ and $Z_{X;i}^{(c,d)}$ according to (8) |
| Damage evolution | $10^{0}$–$10^{5}$ $s$ | $10^{-6}$ $m$ | Processes $a$, $b$, and $r$ according to (6) |
| Cellular endpoint | $>10^{5}$ $s$ | $10^{-5}$ $m$ | – |

# 3 Results

Figure 2 shows the microscopic absorbed dose for protons at 18.6 MeV over the cell nucleus in different domains for different (macroscopic) average doses: the top row reports 1 Gy, the bottom row reports 30 Gy, the left column reports 0.03 Gy/s (CONV), and the right column reports 100 Gy/s (UHDR). Figure 3 shows the same results for the case of carbon ions at 149 MeV/u. Both Figures 2, 3 highlight how the case of 1 Gy is characterized by a more spatially heterogeneous dose distribution over the cell nucleus; on the contrary, at 30 Gy, the dose distribution is more homogeneously distributed. Furthermore, differences in the absorbed dose over cell domains are more significant in the case of carbon ions, characterized by high local energy deposition in a single domain even at 30 Gy, with a non-uniform dose distribution. Specifically, in the case of 1 Gy, the impact of the energy deposited by a single track depositing almost 3 Gy in a single domain is evident, as opposed to an overall dose deposition of 1 Gy in the cell nucleus. Furthermore, it is clear from both figures that the dose rate has no impact on the total dose distribution, as expected.

Figure 4 shows the cumulative absorbed dose in a single domain over time for different dose rates. Both panels report the case of a total dose of 1 Gy in the domain; the top panel shows the case of protons at 18.6 MeV, whereas the bottom panel considers the case of carbon ions at 149 MeV/u. The figure shows how the pattern of local energy deposition is different for the two ions considered. Protons are characterized by a higher amount of energy deposition, each of which releases a small amount of energy. On the contrary, carbon ions exhibit fewer depositions, with a clear impact of single tracks hitting the nucleus. Jumps in the cumulative absorbed dose due to high energy depositions are clearly visible.

Figure 5 shows the $ROO^{\bullet}$ concentration over time for a single domain for proton at 18.6 MeV at 1 Gy (top panel) and 30 Gy (bottom panel) for different dose rates. From Figure 5, it is visible how both dose and dose rate play a crucial role in the peroxyl radical concentration evolution. The higher-dose case is characterized by a higher concentration of $ROO^{\bullet}$. In addition, high dose rates show an almost continuous pattern of energy deposition, whereas on the contrary, low dose rates are characterized by more jagged behavior due to the longer time elapsing between consecutive energy depositions. Moreover, $ROO^{\bullet}$ concentrations at 1 Gy are more similar for the different dose rates, while in the 30 Gy case, there is a clearly different time evolution of $[ROO^{\bullet}]$ for the dose rates considered, both in terms of maximum concentration and in terms of growth and relaxation rate of the chemical species.

Figure 6 reports the relative reduction in indirect damage per unit Gy versus dose rate for different doses. The top panel shows the case of protons at 18.6 MeV, whereas the bottom panel shows the case of carbon ions at 149 MeV/u. A more severe reduction is evident in the case of protons, where at 30 Gy and 100 Gy/s, the indirect damage yield is reduced to 30% compared to the conventional dose rate of 0.03 Gy/s. In the case of carbon ions, the relative reduction reaches at most 12% in the same situation. This is consistent with what was predicted in [25], pointing to a lower entity of the FLASH effect for higher-LET beams. Furthermore, in both ions considered, there is a clear pattern of reversed behavior, where increasing the imparted dose up to 10 Gy/s yields a higher amount of indirect damage, whereas after this dose rate, the pattern is the opposite. For dose rates exceeding 50 Gy/s, higher doses are associated with less damage induced. In general, low doses are characterized by a steady low reduction of damage yields, whereas high doses show almost no reduction up to 10 Gy/s, followed by a sharp fall-off with high indirect damage yield reduction.

Figure 7 shows the survival fraction of the human salivary gland (HSG) cells computed with the MS-GSM$^2$ versus dose rate at different doses in the case of protons at 18.6 MeV. Figure 8 reports the same result in the case of carbon ions at 149 MeV/u. Both figures are characterized by a steady, flat surviving fraction from the conventional dose rates up to 10 Gy/s, after which an increase in the surviving fraction is visible. The sparing effect emerges only at high doses: for protons, this effect is slightly visible at 10 Gy and severe at 30 Gy, whereas for carbon ions, the effect clearly emerges after 20 Gy and is more attenuated.

# 4 Discussion

## 4.1 Analysis of the results

It is worth stressing, first, how different stochastic effects and time scales are included in the MS-GSM$^2$ derived in this study, as summarized in Table 2. The MS-GSM$^2$ construction highlights the several stochasticities that are taken into account in the MS-GSM$^2$. First, the time between consecutive energy depositions is stochastic, so both the evolution of the chemical environment and the yield of

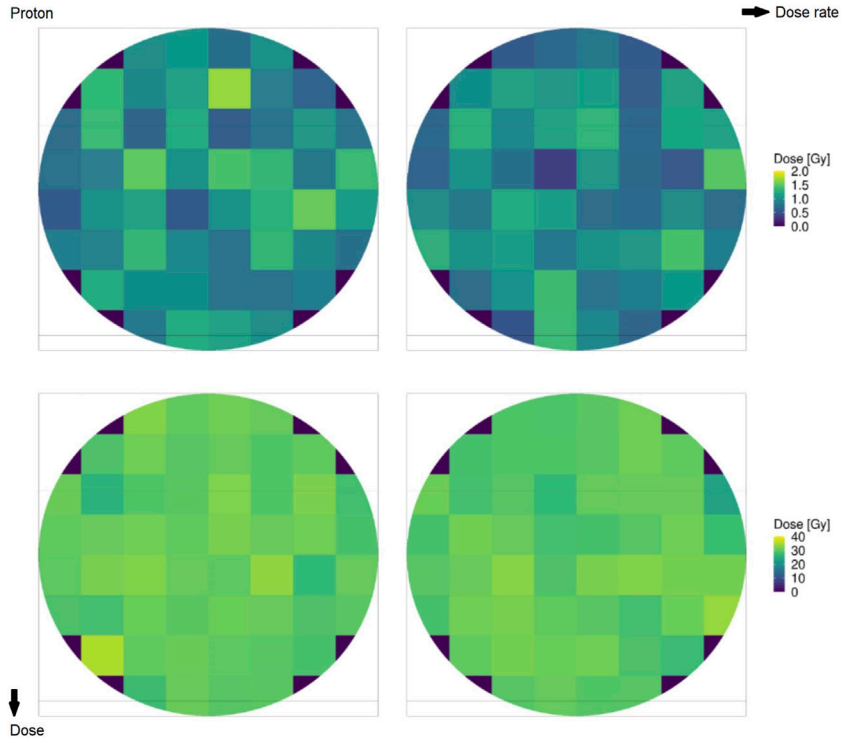


FIGURE 2
Domain distribution of the absorbed dose by the cell nucleus for protons of 18.6 MeV at 1 Gy (top row) and 30 Gy (bottom row) and overall doses for rates of 0.03 Gy/s (left column) and 100 Gy/s (right column).

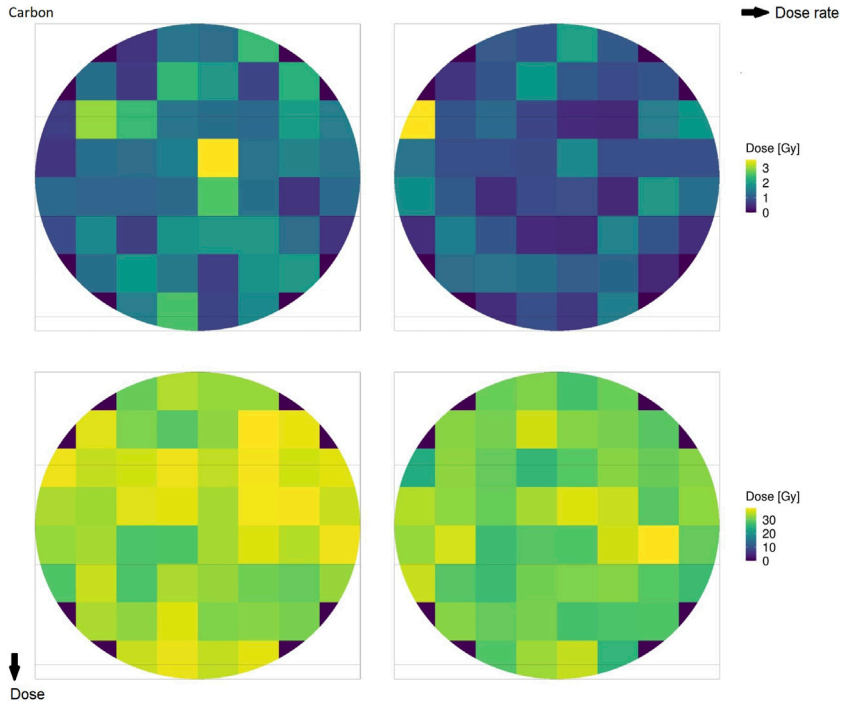


FIGURE 3
Absorbed dose by the cell nucleus for carbon ions of 149 MeV/u at 1 Gy (top row) and 30 Gy (bottom row) for rates of 0.03 Gy/s (left column) and 100 Gy/s (right column).

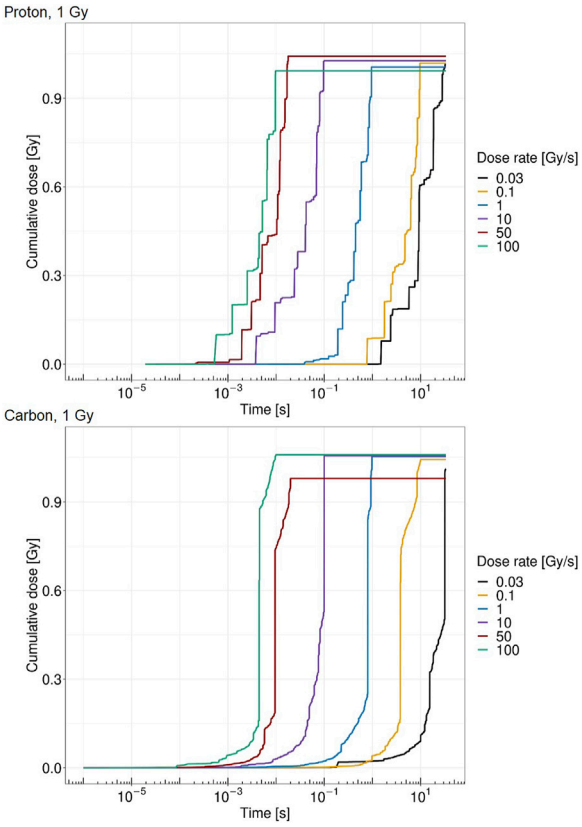


FIGURE 4
Cumulative absorbed dose by the cell nucleus for protons of 18.6 MeV over time for a single domain at 1 Gy (top panel) and carbon ions of 149 MeV/u over time for a single domain at 1 Gy (bottom panel) at 0.03 Gy/s (black), 0.1 Gy/s (yellow), 1 Gy/s (blue), 10 Gy/s (purple), 50 Gy/s (red), and 100 Gy/s (green).

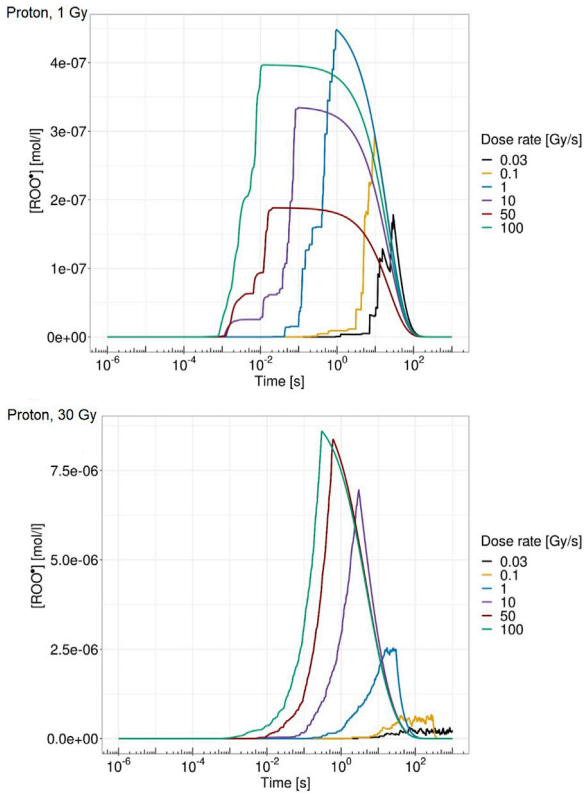


FIGURE 5
$ROO^{\bullet}$ concentration over time for a single domain for proton of 18.6 MeV at 1 Gy (top panel) and 30 Gy (bottom panel) at 0.03 Gy/s (black), 0.1 Gy/s (yellow), 1 Gy/s (blue), 10 Gy/s (purple), 50 Gy/s (red), and 100 Gy/s (green).

DNA damage depend on the time elapsing between two consecutive energy deposition events. Furthermore, the spatial position of the track hitting the biological target, which, in complete generality, is larger than the cell nucleus, is again stochastic; consequently, each domain of the cell nucleus experiences a different amount of energy imparted at any deposition event. It is worth noticing that, mostly in the case of high-LET radiation, some domains could also have null energy deposited. Then again, both the chemical environment and the damage yield are affected by stochastic energy deposition; this implies that not only the time elapsed between consecutive tracks is stochastic but also the actual energy imparted is a random variable. Moreover, the indirect damage yield depends on the chemical environment, thus accounting for a further stochasticity. At last, after the chemical environment reaches stability after irradiation, only the biological pathways of repair and clustering, as described by the GSM$^2$ via $r$, $a$, and $b$, remain, which allows for the computation of the predicted cell survival probability.

The obtained results, summarized in Figures 7, 8, show a cell survival increase with a consequent tissue sparing at sufficiently high doses and dose rates; specifically, it is worth highlighting how both the dose and the dose rate play a crucial role in the sparing effect at the UHDR regime, consistent with most preclinical literature, interestingly collected as a general trend in [48]. In this regard, in the proposed model, several results point toward the conclusion that the dose and the dose rate play a different role in inducing the FLASH effect: (i) a sufficiently high dose rate allows for close enough energy depositions over time so that the chemical environment is modified appropriately, whereas (ii) a sufficiently high dose permits spatial interaction of subsequent energy depositions. Relevant enough, as expected, the ion and its energy play a role in both dose- and dose rate-related effects, and as shown in the results in Figures 7, 8, the dose and dose rate at which the FLASH effect emerges and the magnitude of the sparing shown depend strongly on the quality of the radiation considered. For both ions considered and more clearly in the case of carbon ions (Figures 2, 3), it is evident that high local dose deposition is not sufficient to trigger the FLASH effect, whereas on the contrary, a uniform dose must be reached over the cell nucleus in order to give rise to the FLASH effect. In other words, enough domains must be above a certain dose threshold to have a significant response, since the FLASH effect is not linear. Energy depositions happen not only due to the direct hit of tracks of the cell nucleus but also due to tracks passing nearby. This translates into more localized energy deposition for high LET and a more spatially homogeneous dose pattern for lower LET. This is evident in Figures 2, 3, where carbon ions are characterized by high local energy deposition. The same effect emerges in Figure 4, with sudden jumps in the cumulative deposited dose due to tracks hitting the cell nucleus.

Regarding the chemical environment, again, it emerges from Figure 5 how both dose and dose rate concur to trigger the FLASH

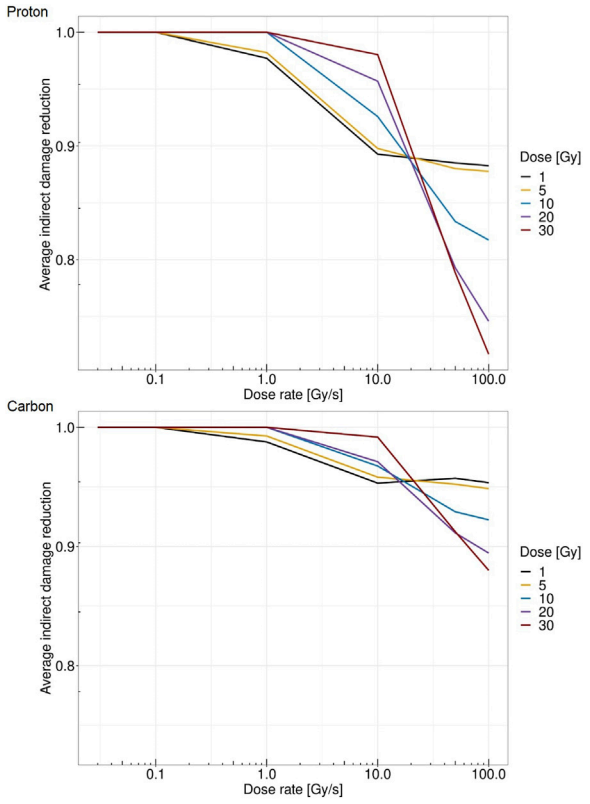


FIGURE 6
Dose rate versus average relative reduction in indirect damage per unit Gy for protons of 18.6 MeV (top panel) and for carbon ions of 149 MeV/u (bottom panel) at 1 Gy (black), 5 Gy (yellow), 10 Gy (blue), 20 Gy (purple), and 30 Gy (red).

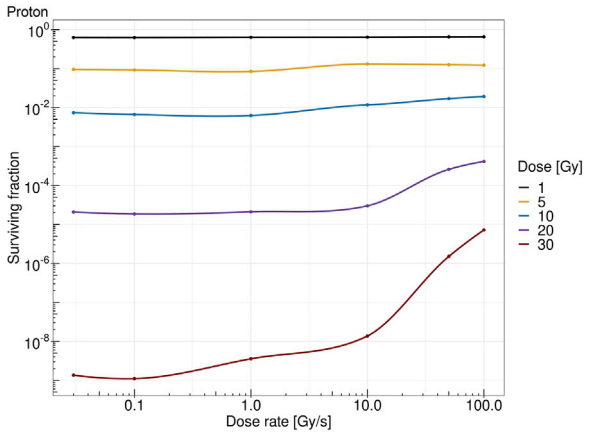


FIGURE 7
Dose rate versus survival fraction for protons of 18.6 MeV at 1 Gy (black), 5 Gy (yellow), 10 Gy (blue), 20 Gy (purple), and 30 Gy (red).

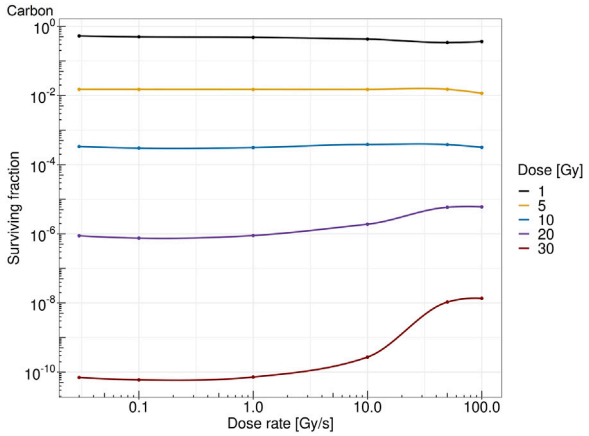


FIGURE 8
Dose rate versus survival fraction for carbons ion of 149 MeV/u at 1 Gy (black), 5 Gy (yellow), 10 Gy (blue), 20 Gy (purple), and 30 Gy (red).

effect. Heuristically speaking, the main idea of the proposed model is, following the main mechanism already proposed in [19], to relate cell survival sparing to the peroxyl radical concentration $ROO^{\bullet}$ evolution. Therefore, the dose rate concurs to increase $[ROO^{\bullet}]$ in a short time so that, if the absorbed dose is sufficiently high, causing $[ROO^{\bullet}]$ to be high enough, organic radical–radical recombination during the chain termination in the homogeneous chemical stage is more likely to happen with a consequently lower probability of interaction with the DNA. This reduced radical interaction probability with the DNA has a consequent DNA damage yield reduction, as emerges in Figure 6. This combined effect of dose and dose rate is also coherent with the inversion of the indirect damage yield pattern that emerges between 10 Gy/s and 50 Gy/s. At a chemical level, a higher dose corresponds to a higher production of $ROO^{\bullet}$, which is more marked at high dose rates. Indeed, only the combined effect of high dose and high dose rate leads to a different temporal evolution of $[ROO^{\bullet}]$; specifically, the high dose rate allows faster growth of $[ROO^{\bullet}]$ but, at the same time, also a more rapid decrease due to the recombination of these chemical species. At high dose rates, the dose deposition events are much closer to each other in time, and therefore, this leads to competition with radical recombination effects. On the contrary, if the dose rate is not high enough, increasing the dose would only increase the rate of damage induction per unit Gy, i.e., the standard trend of damage dependence on the dose, which, due to the well-known linear quadratic behavior, will result in an increasing derivative at a larger dose. This is because at a low dose rate, the cell exposure to a high concentration of this harmful organic radical takes place for a prolonged time; this effect is similar to what occurs with drugs [44], as described in [19]. On the contrary, if a sufficiently high dose is imparted over a short time, organic radical–radical recombination is favored over interaction with DNA. This leads to cell tissue sparing, implying that a high dose rate will trigger an additional quenching effect on the dose, in addition to the previously described standard effect, while with conventional radiation, this latter effect will not occur. Again, the sparing effect is more pronounced in the low-LET case, whereas as the LET increases, the highly localized dose deposition pattern implies that a local disappearance of some harmful chemical species occurs. However, this process does not happen on the whole cell, i.e., a higher dose is required to reach the sufficiently spatially uniform dose needed to trigger the FLASH effect.

The aforementioned points also highlight some key differences between the originally proposed model in [19] and the generalization proposed in the current research. The main novelty, compared to [19], is to provide a more direct link from the chemical environment to its biological effect. Radical concentration is, thus, related to indirect damage induction. Therefore, the general linear or quadratic relation between energy deposition and damage yield, already proposed decades ago in [49], is generalized in the present work so that a more direct link between the concentration of the radical and the consequent damage yield is considered. In addition, the multiscale nature of the proposed model clearly emerges in several plots (Figures 4, 5). A purely discontinuous time pattern in energy deposition is evident. This translates into highly jagged radical concentrations at low dose rates, which naturally turn continuous as the dose rate increases, differing from what is considered in [19].

Therefore, with the proposed approach, we can directly link the radical concentration, which is directly modified by the energy deposition pattern depending on both dose and dose rate, to the DNA damage formation. It should be noted that conventional dose rates do not provide any changes in the indirect damage yield, whereas as the dose rates increase, a reduction in the damage occurs. The magnitude of damage reduction depends on the absorbed dose. Moreover, the overall pattern of indirect damage yield reduction strongly depends on the radiation quality. In this regard, it is worth stressing that, Figure 6 reports the relative reduction in the indirect damage yield per unit Gy. Therefore, since the proportion of indirect damage compared to direct damage in the high-LET radiation is lower than in the low-LET case, the overall reduction in the total damage yields would be even higher.

All the previously mentioned discussions eventually emerge in the different sparing at the cell survival level. Both Figures 7, 8 show that a sufficiently high dose and dose rate result in cell survival sparing. Furthermore, the highly localized energy deposition of high LET results in a less sparing at 30 Gy compared to protons. The magnitude of the sparing of carbon ions at FLASH dose rates at 30 Gy is in the order of the sparing at FLASH dose rates for protons at 20 Gy. This is in agreement with the discussion that emerged previously, considering how the local pattern of energy deposition affects the chemical environment. It is worth stressing that the surviving fraction remains almost constant up to 10 Gy/s, after which there is an increase in the surviving fraction. For protons, a slight increase in the surviving fraction emerges at 10 Gy, and it is clear at higher doses, such as 30 Gy; this is in agreement with what was experimentally observed in [48]. On the contrary, carbon ions require a higher dose to observe the FLASH effect, which is in agreement with [25]. Differently from the results derived in [29], where the predicted surviving fraction steadily decreases in the conventional dose rate regimes, reaching a minimum of approximately 1 Gy/s, the predicted surviving fraction of the MS-GSM$^2$ remains almost unchanged in the range below 10 Gy/s, after which the FLASH effect is triggered.

## 4.2 Current limitations of the MS-GSM$^2$ and future perspectives

Although the presently developed model is general enough in the sense that it includes several effects of random processes in space and time inherent to three different domains, such as physics, chemistry, and biology, it also presents some limitations. Subsequently, we discuss some possible future lines of research to strengthen the developed model.

It is worth stressing that 100 Gy/s represents a limit for the proposed model. Above 100 Gy/s, the time elapsed by two consecutive energy depositions significantly overlaps with the heterogeneous chemical stage. Therefore, accurately considering high dose rates would require a more sophisticated chemical treatment that goes beyond the homogeneous chemical stage as considered in the current approach, e.g., including diffusion during the heterogeneous chemical stage. Finally, as previously described, this model allows us to consider single deposition events. This, in principle, would allow us to consider any temporal structure of dose delivery to study the effect that an intra-pulse dose rate could have on the triggering of the FLASH effect. Both of these aspects are currently under investigation and will be analyzed in future work.

As is well known, the FLASH biological effect can be described by two different and presently unexplained aspects, i.e., the sparing effect of healthy tissues and the differential effect between normal tissues and tumors. In this work, we chose to focus on the first aspect of UHDR irradiation, i.e., the higher sparing of healthy tissues at high doses and high dose rates with respect to conventional irradiation; nevertheless, our model is not in contradiction with some of the most accredited hypotheses that try to explain the differential effect between normal tissues and tumors. The first hypothesis is based on a combination of two mechanisms linked to DNA damage, i.e., a different damage formation due to the reduction of a specific oxygen-dependent DNA damage, which is consistent with a decrease in the organic peroxyl radical concentration, and a defective repair process, such as pathologic chromosome rearrangements due to an aberrant DNA double-strand break (DSB) repair, as described in [19]. The second conjecture postulates that a different accumulation of a specific chemical species between normal tissue and tumor is the basis for the differential effect, as proposed in [50]. Specifically, this hypothesis states that normal tissues have a greater ability to detoxify from reactive oxygen species, reducing oxidative injury with respect to tumors, as described in [23]. In fact, normal cells have a more rapid elimination, mediated by enzymes, of peroxidized compounds compared to tumor cells [50]. We may test these hypotheses in future work.

Last, a critical aspect that we decided not to address in this work is the experimental validation of our model. As stated at the beginning of this paper, the aim of this work is to develop a multiscale model, merging the homogeneous chemical stage, described by a reaction kinetic model, with the formation and time evolution of DNA damage, accounted for by the GSM$^2$. The aim of this study is to show the mathematical framework of this novel tool that allows, among many biological effects of radiation, to capture possible effects of DNA damage during UHDR irradiation. The goal of the calculations that we report here is to show how, in principle, this tool is able to describe the sparing effect of healthy tissues at high doses and high dose rates—an effect contradicting conventional radiobiological modeling outcomes, which typically may explain larger damage in occurrence on a more temporally dense dose-delivery basis—and not explain the FLASH effect. For this reason, considering the great importance of this aspect and the complexity due to the presence of several parameters that play a role in this context, we decided to dedicate a specific future work

regarding the comparison with the experimental data. At this stage, we want to underline how the trend of the survival curves that we obtained is, in any case, in agreement with the few experimental *in vitro* data currently available, such as in [14].

## 5 Conclusion

In this paper, we extended the GSM$^2$ by coupling biological DNA damage repair and kinetics to the radiation-induced chemical environment. Specifically, by introducing a proper mathematical formulation of the homogeneous chemical stage, we establish a link between the organic radical concentration and the formation of indirect damage. The resulting model is a universal multiscale stochastic model able to treat in a complete general formulation the stochastic effects inherent to physics, chemistry, and biology. Different temporal and spatial scales are efficiently included in the model. We showed how the proposed model is able to describe the normal tissue sparing arising at ultra-high dose rates. Relevant enough, this sparing typical of the FLASH effect emerges at the interplay of many mechanisms: oxygen concentration is involved in driving the effect so that spatial and temporal dose deposition effects favor organic radical–radical recombination, such as $R^{\bullet}$ and $ROO^{\bullet}$, during the homogeneous chemical stage, that eventually reduces the indirect damage yield, causing tissue sparing. A natural generalization of the model developed will be to include the heterogeneous chemical stage in order to provide a more mechanistically grounded analysis of the phenomena involved in the FLASH effects, opening up further investigation of higher dose rates than the one considered in the current research. Such a generalization will require a more advanced spatial description of the physical, chemical, and biological processes involved, thus abandoning a domain-like formulation in favor of a true full spatial description [35]. Such a model, adequately tuned with *in vitro* and *in vivo* experimental data and coupled with advanced biologically driven treatment plan optimization [51], can, on the one hand, help understand the main biological mechanism underlying the FLASH effect and, on the other hand, favor the full exploitation of such an effect in clinical practice.

## Data availability statement

The raw data supporting the conclusion of this article will be made available by the authors, without undue reservation.

## Author contributions

MB: conceptualization, data curation, formal analysis, investigation, methodology, software, validation, writing–original draft, and writing–review and editing. MM: conceptualization, methodology, and writing–review and editing. AA: conceptualization, writing–review and editing. FT: conceptualization, writing–review and editing. CLT: funding acquisition and writing–review and editing. FGC: conceptualization, data curation, formal analysis, investigation, methodology, supervision, writing–original draft, and writing–review and editing. ES: conceptualization, formal analysis, funding acquisition, methodology, supervision, validation, writing–original draft, and writing–review and editing.

## Funding

The authors declare that financial support was received for the research, authorship, and/or publication of this article. This work was partially supported by the INFN CSN5 project FRIDA.

## Acknowledgments

Rudi Labarbe and Lucian Hotoiu are gratefully acknowledged for multiple fruitful discussions and for providing their code. Martina Fuss, Michael Krämer, Gianmarco Camazzola, and Daria Boscolo are thanked for inspiring discussions.

## Conflict of interest

The authors declare that the research was conducted in the absence of any commercial or financial relationships that could be construed as a potential conflict of interest.

## Publisher's note



## References

1. Favaudon V, Caplier L, Monceau V, Pouzoulet F, Sayarath M, Fouillade C, et al. Ultrahigh dose-rate flash irradiation increases the differential response between normal and tumor tissue in mice. *Sci Transl Med* (2014) 6:245ra93. doi:10.1126/scitranslmed.3008973

2. Vozenin M, De Fornel P, Petersson K, Favaudon V, Jaccard M, Germond J, et al. The advantage of flash radiotherapy confirmed in mini-pig and cat cancer patients. *Clin Cancer Res* (2019) 25:35–42. doi:10.1158/1078-0432.CCR-17-3375

3. Schüler E, Acharya M, Montay-Gruel P, Loo BW, Jr., Vozenin M-C, Maxim PG. Ultra-high dose rate electron beams and the flash effect: from preclinical evidence to a new radiotherapy paradigm. *Med Phys* (2022) 49:2082–95. doi:10.1002/mp.15442

4. Adrian G, Ruan J-L, Paillas S, Cooper CR, Petersson K. *In vitro* assays for investigating the flash effect. *Expert Rev Mol Med* (2022) 24:e10. doi:10.1017/erm.2022.5

5. Limoli CL, Vozenin M-C. Reinventing radiobiology in the light of flash radiotherapy. *Annu Rev Cancer Biol* (2023) 7:1–21. doi:10.1146/annurev-cancerbio-061421-022217

6. Montay-Gruel P, Petersson K, Jaccard M, Boivin G, Germond J, Petit B, et al. Irradiation in a flash: unique sparing of memory in mice after whole brain irradiation with dose rates above 100gy/s. *Radiother Oncol* (2017) 124:365–9. doi:10.1016/j.radonc.2017.05.003

7. Montay-Gruel P, Acharya M, Petersson K, Alikhani L, Yakkala C, Allen B, et al. Long-term neurocognitive benefits of flash radiotherapy driven by reduced reactive oxygen species. *Proc Natl Acad Sci USA* (2019) 116:10943–51. doi:10.1073/pnas.1901777116

8. Loo B, Schuler E, Lartey F, Rafat M, King G, Trovati S, et al. (P003) delivery of ultra-rapid flash radiation therapy and demonstration of normal tissue sparing after

abdominal irradiation of mice. *Int J Radiat Oncol Biol Phys* (2017) 98:E16. doi:10.1016/j.ijrobp.2017.02.101

9. Bourhis J, Sozzi WJ, Jorge PG, Gaide O, Bailat C, Duclos F, et al. Treatment of a first patient with flash-radiotherapy. *Radiother Oncol* (2019) 139:18–22. doi:10.1016/j.radonc.2019.06.019

10. Bourhis J, Montay-Gruel P, Jorge PG, Bailat C, Petit B, Ollivier J, et al. Clinical translation of flash radiotherapy: why and how? *Radiother Oncol* (2019) 139:11–7. doi:10.1016/j.radonc.2019.04.008

11. Montay-Gruel P, Acharya MM, Gonçalves Jorge P, Petit B, Petridis IG, Fuchs P, et al. Hypofractionated flash-rt as an effective treatment against glioblastoma that reduces neurocognitive side effects in mice. *Clin Cancer Res* (2021) 27:775–84. doi:10.1158/1078-0432.CCR-20-0894

12. Diffenderfer ES, Verginadis II, Kim MM, Shoniyozov K, Velalopoulou A, Goia D, et al. Design, implementation, and *in vivo* validation of a novel proton flash radiation therapy system. *Int J Radiat Oncology*Biology*Physics* (2020) 106:440–8. doi:10.1016/j.ijrobp.2019.10.049

13. Sørensen BS, Sitarz MK, Ankjærgaard C, Johansen JG, Andersen CE, Kanouta E, et al. Pencil beam scanning proton flash maintains tumor control while normal tissue damage is reduced in a mouse model. *Radiother Oncol* (2022) 175:178–84. doi:10.1016/j.radonc.2022.05.014

14. Tinganelli W, Sokol O, Quartieri M, Puspitasari A, Dokic I, Abdollahi A, et al. Ultra-high dose rate (flash) carbon ion irradiation: dosimetry and first cell experiments. *Int J Radiat Oncology*Biology*Physics* (2022) 112:1012–22. doi:10.1016/j.ijrobp.2021.11.020

15. Tinganelli W, Weber U, Puspitasari A, Simoniello P, Abdollahi A, Oppermann J, et al. Flash with carbon ions: tumor control, normal tissue sparing, and distal metastasis in a mouse osteosarcoma model. *Radiother Oncol* (2022) 175:185–90. doi:10.1016/j.radonc.2022.05.003

16. Daugherty E, Mascia A, Zhang Y, Lee E, Xiao Z, Sertorio M, et al. Flash radiotherapy for the treatment of symptomatic bone metastases (fast-01): protocol for the first prospective feasibility study. *JMIR Res Protoc* (2023) 12:e41812. doi:10.2196/41812

17. Friedl AA, Prise KM, Butterworth KT, Montay-Gruel P, Favaudon V. Radiobiology of the flash effect. *Med Phys* (2022) 49:1993–2013. doi:10.1002/mp.15184

18. Wilson JD, Hammond EM, Higgins GS, Petersson K. Ultra-high dose rate (flash) radiotherapy: silver bullet or fool's gold? *Front Oncol* (2020) 9:1563–12. doi:10.3389/fonc.2019.01563

19. Labarbe R, Hotoiu L, Barbier J, Favaudon V. A physicochemical model of reaction kinetics supports peroxyl radical recombination as the main determinant of the flash effect. *Radiother Oncol* (2020) 153:303–10. doi:10.1016/j.radonc.2020.06.001

20. Ramos-Méndez J, Domínguez-Kondo N, Schuemann J, McNamara A, Moreno-Barbosa E, Faddegon B. Let-dependent intertrack yields in proton irradiation at ultra-high dose rates relevant for flash therapy. *Radiat Res* (2020) 194:351–62. doi:10.1667/RADE-20-00084.1

21. Zhou G. Mechanisms underlying flash radiotherapy, a novel way to enlarge the differential responses to ionizing radiation between normal and tumor tissues. *Radiat Med Prot* (2020) 1:35–40. doi:10.1016/j.radmp.2020.02.002

22. Boscolo D, Scifoni E, Durante M, Krämer M, Fuss MC. Oxygen depletion explain the flash effect? a chemical track structure analysis. *Radiother Oncol* (2021) 162:68–75. doi:10.1016/j.radonc.2021.06.031

23. Favaudon V, Labarbe R, Limoli CL. Model studies of the role of oxygen in the flash effect. *Med Phys* (2022) 49:2068–81. doi:10.1002/mp.15129

24. von Sonntag C. *The chemical basis of radiation biology*. Taylor & Francis (1987).

25. Weber UA, Scifoni E, Durante M. Flash radiotherapy with carbon ion beams. *Med Phys* (2022) 49:1974–92. doi:10.1002/mp.15135

26. Wardman P. Radiotherapy using high-intensity pulsed radiation beams (flash): a radiation-chemical perspective. *Radiat Res* (2020) 194:607–17. doi:10.1667/RADE-19-00016

27. Abolfath R, Grosshans D, Mohan R. Oxygen depletion in flash ultra-high-dose-rate radiotherapy: a molecular dynamics simulation. *Med Phys* (2020) 47:6551–61. doi:10.1002/mp.14548

28. Abolfath R, Peeler C, Mirkovic D, Mohan R, Grosshans D. A dna damage multiscale model for ntcp in proton and hadron therapy. *Med Phys* (2020) 47:2005–12. doi:10.1002/mp.14034

29. Liew H, Mein S, Dokic I, Haberer T, Debus J, Abdollahi A, et al. Deciphering time-dependent dna damage complexity, repair, and oxygen tension: a mechanistic model for flash-dose-rate radiation therapy. *Int J Radiat Oncology* Biology* Phys* (2021) 110:574–86. doi:10.1016/j.ijrobp.2020.12.048

30. Petersson K, Adrian G, Butterworth K, McMahon SJ. A quantitative analysis of the role of oxygen tension in flash radiation therapy. *Int J Radiat Oncology* Biology* Phys* (2020) 107:539–47. doi:10.1016/j.ijrobp.2020.02.634

31. Abolfath R, Baikalov A, Rahvar S, Fraile A, Bartzsch S, Schüler E, et al. *Differential tissue sparing of flash ultra high dose rates: an in-silico study* (2022). *arXiv preprint arXiv:2210.03565*.

32. Cordoni F, Missiaggia M, Attili A, Welford S, Scifoni E, La Tessa C. Generalized stochastic microdosimetric model: the main formulation. *Phys Rev E* (2021) 103:012412. doi:10.1103/PhysRevE.103.012412

33. Cordoni FG, Missiaggia M, Scifoni E, La Tessa C. Cell survival computation via the generalized stochastic microdosimetric model (gsm2); part i: the theoretical framework. *Radiat Res* (2022) 197:218–32. doi:10.1667/RADE-21-00098.1

34. Cordoni FG, Missiaggia M, La Tessa C, Scifoni E. Multiple levels of stochasticity accounted for in different radiation biophysical models: from physics to biology. *Int J Radiat Biol* (2022) 1:807–22. doi:10.1080/09553002.2023.2146230

35. Cordoni FG. *A spatial measure-valued model for radiation-induced dna damage kinetics and repair under protracted irradiation condition* (2023). *arXiv preprint arXiv:2303.14784*.

36. Missiaggia M, Cordoni FG, Scifoni E, La Tessa C. *Cell survival computation via the generalized stochastic microdosimetric model (gsm2); part ii: numerical results* (2023). *(submitted)*.

37. Manganaro L, Russo G, Cirio R, Dalmasso F, Giordanengo S, Monaco V, et al. A Monte Carlo approach to the microdosimetric kinetic model to account for dose rate time structure effects in ion beam therapy with application in treatment planning simulations. *Med Phys* (2017) 44:1577–89. doi:10.1002/mp.12133

38. Kase Y, Kanai T, Matsufuji N, Furusawa Y, Elsässer T, Scholz M. Biophysical calculation of cell survival probabilities using amorphous track structure models for heavy-ion irradiation. *Phys Med Biol* (2007) 53:37–59. doi:10.1088/0031-9155/53/1/003

39. Cordoni FG. On the emergence of the deviation from a Poisson law in stochastic mathematical models for radiation-induced dna damage: a system size expansion. *Entropy* (2023) 25:1322. doi:10.3390/e25091322

40. Missiaggia M, Cartechini G, Scifoni E, Rovituso M, Tommasino F, Verroi E, et al. Microdosimetric measurements as a tool to assess potential in-field and out-of-field toxicity regions in proton therapy. *Phys Med Biol* (2020) 65:245024. doi:10.1088/1361-6560/ab9e56

41. Missiaggia M, Pierobon E, Castelluzzo M, Perinelli A, Cordoni F, Centis Vignali M, et al. A novel hybrid microdosimeter for radiation field characterization based on the tissue equivalent proportional counter detector and low gain avalanche detectors tracker: a feasibility study. *Front Phys* (2021) 8:578444. doi:10.3389/fphy.2020.578444

42. Missiaggia M, Cartechini G, Tommasino F, Scifoni E, La Tessa C. Investigation of in-field and out-of-field radiation quality with microdosimetry and its impact on relative biological effectiveness in proton therapy. *Int J Radiat Oncology* Biology* Phys* (2023) 115:1269–82. doi:10.1016/j.ijrobp.2022.11.037

43. Zaider M, Rossi BHH, Zaider M. *Microdosimetry and its applications*. Springer (1996).

44. Scheff JD, Almon RR, Dubois DC, Jusko WJ, Androulakis IP. Assessment of pharmacologic area under the curve when baselines are variable. *Pharm Res* (2011) 28:1081–9 (2022) 114:1032–44. doi:10.1007/s11095-010-0363-8

45. Weinan E, Li T, Vanden-Eijnden E. *Applied stochastic analysis*, 199. American Mathematical Soc. (2019).

46. Hirayama R, Ito A, Tomita M, Tsukada T, Yatagai F, Noguchi M, et al. Contributions of direct and indirect actions in cell killing by high-let radiations. *Radiat Res* (2009) 171:212–8. doi:10.1667/RR1490.1

47. Scholz M, Kraft G. Track structure and the calculation of biological effects of heavy charged particles. *Adv Space Res* (1996) 18:5–14. doi:10.1016/0273-1177(95)00784-C

48. Böhlen TT, Germond J-F, Bourhis J, Vozenin M-C, Ozsahin EM, Bochud F, et al. Normal tissue sparing by flash as a function of single-fraction dose: a quantitative analysis. *Int J Radiat Oncology*Biology*Physics* (2022) 114:1032–44. doi:10.1016/j.ijrobp.2022.05.038

49. Kellerer AM, Rossi HH. A generalized formulation of dual radiation action. *Radiat Res* (1978) 75:471–88. doi:10.2307/3574835

50. Spitz DR, Buettner GR, Petronek MS, St-Aubin JJ, Flynn RT, Waldron TJ, et al. An integrated physico-chemical approach for explaining the differential impact of flash versus conventional dose rate irradiation on cancer and normal tissue responses. *Radiother Oncol* (2019) 139:23–7. doi:10.1016/j.radonc.2019.03.028

51. Battestini M, Schwarz M, Krämer M, Scifoni E. Including volume effects in biological treatment plan optimization for carbon ion therapy: generalized equivalent uniform dose-based objective in trip98. *Front Oncol* (2022) 12:826414. doi:10.3389/fonc.2022.826414

frontiers | Frontiers in Physics

TYPE Original Research
PUBLISHED 16 November 2023
DOI 10.3389/fphy.2023.1269495



OPEN ACCESS

EDITED BY
Paweł Moskal,
Jagiellonian University, Poland

REVIEWED BY
Karol Lang,
The University of Texas at Austin, United States
Ewa L. Stepien,
Jagiellonian University, Poland

*CORRESPONDENCE
Francesco Romano,
francesco.romano@ct.infn.it

RECEIVED 30 July 2023
ACCEPTED 03 November 2023
PUBLISHED 16 November 2023

CITATION
Pensavalle JH, Romano F, Celentano M, Sarto DD, Felici G, Franciosini G, Masturzo L, Milluzzo G, Patera V, Prezado Y and Di Martino F (2023), Realization and dosimetric characterization of a mini-beam/flash electron beam.
*Front. Phys.* 11:1269495.
doi: 10.3389/fphy.2023.1269495



# Realization and dosimetric characterization of a mini-beam/flash electron beam

Jake Harold Pensavalle[1,2,3], Francesco Romano[4,5]*, Mariagrazia Celentano[1,3], Damiano Del Sarto[1,3], Giuseppe Felici[2], Gaia Franciosini[6], Luigi Masturzo[1,2,3], Giuliana Milluzzo[4], Vincenzo Patera[6], Yolanda Prezado[7] and Fabio Di Martino[1,3,8,9]

[1]Centro Pisano Multidisciplinare Sulla Ricerca e Implementazione Clinica Della Flash Radiotherapy (CPFR), Pisa, Italy, [2]Sordina IORT Technologies S.p.A., Research and Development, Aprilia, Italy, [3]Department of Physics, University of Pisa, Pisa, Italy, [4]Istituto Nazionale di Fisica Nucleare, Sezione di Catania, Catania, Italy, [5]Particle Therapy Research Center (PARTREC), Department of Radiation Oncology, University Medical Center Gro-Ningen, University of Groningen, Groningen, Netherlands, [6]Dipartimento di Fisica, Sapienza Università di Roma, Roma, Italy, [7]Université Paris-Saclay, Centre national de la recherche scientifique UMR3347, Inserm U1021, Signalisation Radiobiologie et Cancer, Orsay, France, [8]Azienda Ospedaliero Universitaria Pisa (AOUP), Fisica Sanitaria, Pisa, Italy, [9]Istituto Nazionale di Fisica Nucleare, Sezione di Pisa, Pisa, Italy

The use of the flash effect and mini-beams have demonstrated the ability to spare healthy tissue while maintaining the same effectiveness in controlling tumors. In this study, we present the implementation and comprehensive dosimetric characterization of low-energy mini-beam radiation therapy at both conventional and ultra-high dose rates. These beams possess important features that allow for a wide range of spatial and temporal parameter variations, independently or simultaneously, for both effects. This novel capability enables the performance of *in vivo*/*vitro* radiobiological experiments, which are crucial for understanding the underlying mechanisms and quantitative dependencies of these effects on their respective parameters. This understanding is essential for evaluating the potential clinical applications of the two effects both individually and in terms of their potential synergistic actions.

KEYWORDS

**mini-beam, flash, UHDR, UHDP, SFRT, passive collimation**

## 1 Introduction

The initial intuition that led to the development of spatially fractionated radiotherapy (SFRT) was credited to Dr. Alban Köhler in 1909. Köhler discovered that by introducing a grid-shaped shielding system for X-ray beams (at that time, X-ray tubes were the only radiation source), he was able to treat skin tumors more effectively while significantly reducing damage to healthy tissue. Erythema and necrosis healed within a few weeks, leaving the new epidermal tissue completely healthy [1]. Although this approach was initially used for the treatment of some superficial tumors, it remained on the sidelines of radiotherapy development for a long time. However, since the 1990s, several research groups in Europe and the United States have begun to consider the possibility of implementing spatial fractionation in radiotherapy. Multiple radiobiology studies were conducted, initially using X-rays, including synchrotron light [2–5] and later with proton beams [2, 3, 6–10]. These studies have demonstrated that this highly unconventional approach has the potential to be revolutionary, allowing significant sparing of healthy tissue while

maintaining local tumor control. This outcome presents evident clinical prospects once radiation therapy accelerators (medical devices) capable of delivering such treatment become available. Most SFRT techniques spare normal tissues with conventional dose rates [11, 12]. Experiments combining Ultra High Dose Rates (UHDR) with SFRT using Microbeam Radiotherapy (MRT) and mini-beam Radiotherapy (MBRT) have been conducted [13, 14], however, establishing the additive or synergistic effects of combining these techniques is still pending, and separating the flash effect from spatial fractionation in MRT studies has yielded inconclusive results [15].

Conventional radiotherapy has always followed the paradigm of using a uniform beam to deliver the same dose to the target. In contrast, SFRT proposes the possibility of achieving a spatially periodic structure where the transverse profile is articulated in a recurring series of "peaks and valleys" [3]. The optimal structure of this pattern, which refers to the peak-to-valley dose ratio (PVDR) and the spatial extent of the "light and shadow" regions, is still the subject of ongoing research. SFRT can be implemented in two different modes, irrespective of the radiation source employed. The first mode involves using a spatially homogeneous beam and positioning a periodic screen with alternating slits and solid elements, known as the GRID technique [16–19], between the source and the target. This approach, initially proposed by Köhler in 1909 and replicated in experiments using synchrotron light with microbeams, has demonstrated promising results. The second mode utilizes the pencil beam technique, wherein multiple narrow beams, referred to as "pencil beams," are employed to paint the desired dose distribution pattern. This requires charged particles. Proton accelerators have been particularly suitable for implementing this approach, even though most radiobiological studies have used passive collimation [20–25].

While GRID therapy has found clinical success in palliative applications and mini beam RT is approaching clinical trials with enormous potential, SFRT has not gained widespread adoption not only due to technological limitations of current available devices, as detailed in [21], but also due to the high heterogeneity of tumor coverage, which is in stark contrast to conventional radiotherapy.

Furthermore, it is important to emphasize that the optimal use of SFRT with low energy electron beams is limited to the context of potential flash delivery, as extensively discussed in [2]. Therefore, the study of the combined flash and mini-beam effect is a key aspect, and this present work serves as a foundation for future research.

A dedicated beam with the ability to independently adjust its parameters is essential not only for advancing radiobiology research but also for facilitating accurate dosimetric studies, as was the case of flash [26]. This capability has been demonstrated to be valuable in previous research involving electron Ultra High Dose per Pulse (UHDP) beams, where fundamental dosimetry solutions have been developed [27–30].

In fact, for low energy electrons an immediate application in the clinic would be Intra Operative Radiotherapy (IORT). However, the study of the mini-beam effect is fundamental in the perspective of Very High Energy Electron (VHEE) irradiation, since the mini-beam effect may play a major role since VHEE will most likely be delivered via pencil beams, that allow the possibility of "painting" the spatial dose distribution [18].

In this paper, we explore the potential of using electron mini-beams in conjunction with flash irradiation. The flash effect, as described in previous studies [31–33], is observed when irradiation times are shorter than 0.1–0.2 s, and the average dose rate exceeds 40–100 Gy/s. The mini-Beam distribution, correlated to a tissue sparing effect [3], is characterized by a spatial dose distribution with alternating peaks and valleys, where the full width at half maximum (FWHM) of the peaks is less than 1 mm, and the distance between successive peaks is 2–4 times the FWHM. Although the combination of these two techniques has not been experimentally evaluated yet, it has the potential for a synergistic action, resulting in a significant reduction in the side effects of radiation therapy while maintaining therapeutic efficacy. Therefore, we can deliver irradiation in four different modalities (Conventional, flash, mini-Beam, and mini-beam-flash), independently varying their main parameters, to study the individual and combined effects of these techniques.

# 2 Materials and methods

## 2.1 Mini-beam design and generation

To explore the possibility of creating UHDR mini beams, Monte Carlo simulations were carried out reproducing different devised suitable collimator templates, which are passive spatial distribution modulators. These templates are integrated into the beam optic system to achieve mini-beam spatial distributions.

The mini-beam templates have been designed with the GEANT4 [34] version 10.7.2 Monte Carlo code. In particular, the Sordina IORT Technologies S.p.A. (SIT, Italy) ElectronFlash linear accelerator (linac) available at the Centro Pisano for Flash Radiotherapy (CPFR) was fully modelled, in terms of beam optics, geometry and input energy spectra with the Geant4 code, and a dedicated application was recently inserted within the official advanced examples of the Geant4 distribution with the name "eFLASH_radiotherapy." For each simulation, the GEANT4 standard_opt4 physics list with $10^8$ primary particles and 0.1 mm production cuts were set. A water phantom was implemented just after the template to score the dose, using a $0.125 \times 0.125 \times 0.5$ mm$^3$ voxel size.

A fundamental requisite for a useful mini-beam structure, defined as having distinct peaks and valleys with high peak-to-valley dose ratio, is avoiding bleed-through of electrons through the septa, thus high Z materials are needed. In fact, by keeping the thickness equal to the practical range of the electron energy (9 MeV nominal energy), we noticed a significant reduction of PVDR for plastic materials, such as Teflon, as opposed to Tungsten due to septa bleed-through, as shown in Figure 1. Similar results have been reported also in [35] in the context of experimental IORT beam limiting devices.

Thus, we designed the collimators to have a thickness of 5 mm and be made of Tungsten. Each of the designed templates differs mainly in hole structure (grid or planar slits) and center-to-center distance (ctc), so that it is possible to study the effect of varying these parameters.

## 2.2 Monte Carlo simulations

To further strengthen the reliability of dose evaluations in terms of spatial distribution, we compared the Monte Carlo

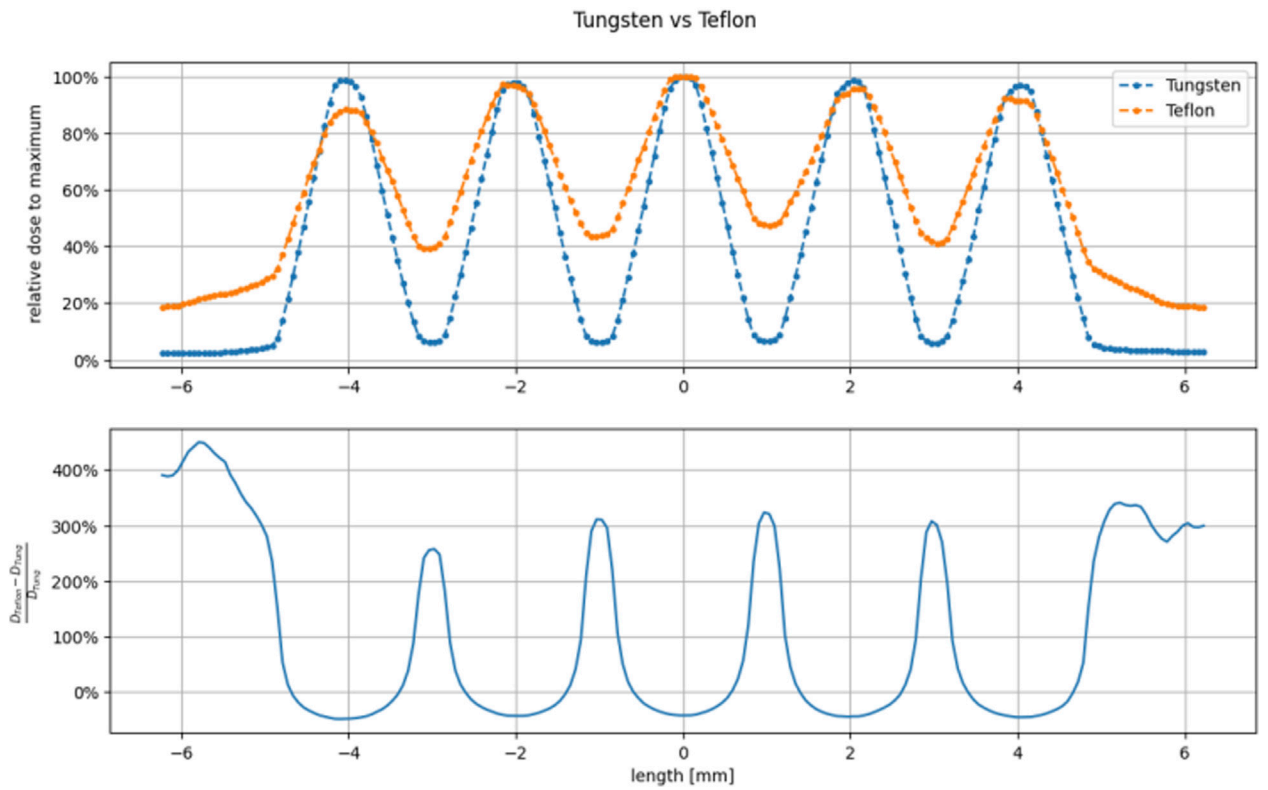


FIGURE 1
Comparison between Tungsten (thickness 5 mm) and Teflon (thickness 25 mm) grid-hole template superficial dose profiles. The thickness has been calculated as the practical range extrapolated from the PDD in the selected material. We can see that Teflon cannot achieve useful peak to valley ratio since the thickness of the walls of the holes (1 mm) are much smaller than the practical range.

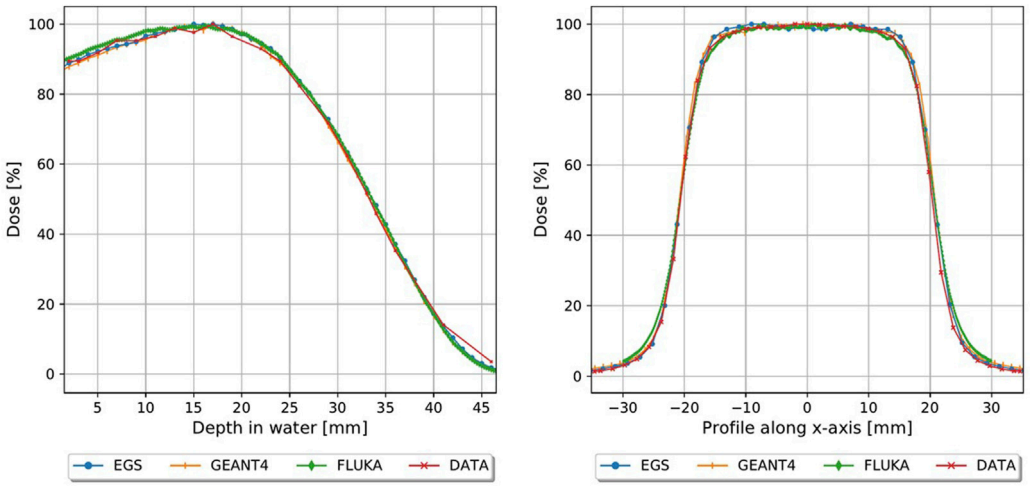


FIGURE 2
Monte carlo simulations plotted with FlashDiamond measurements, PDD **(left)** and profiles at R100 **(right)**.

simulations with experimental data acquired with radiochromic gafchromic films, which are currently considered the most suitable dosimeters with high spatial resolution (below 25 µm [36]). However, it is important to acknowledge that these dosimeters have certain limitations, mostly related to the accuracy of dose reading [37]. To address this, we conducted a comparative analysis by comparing the gafchromic data with results obtained from three independent Monte Carlo simulation

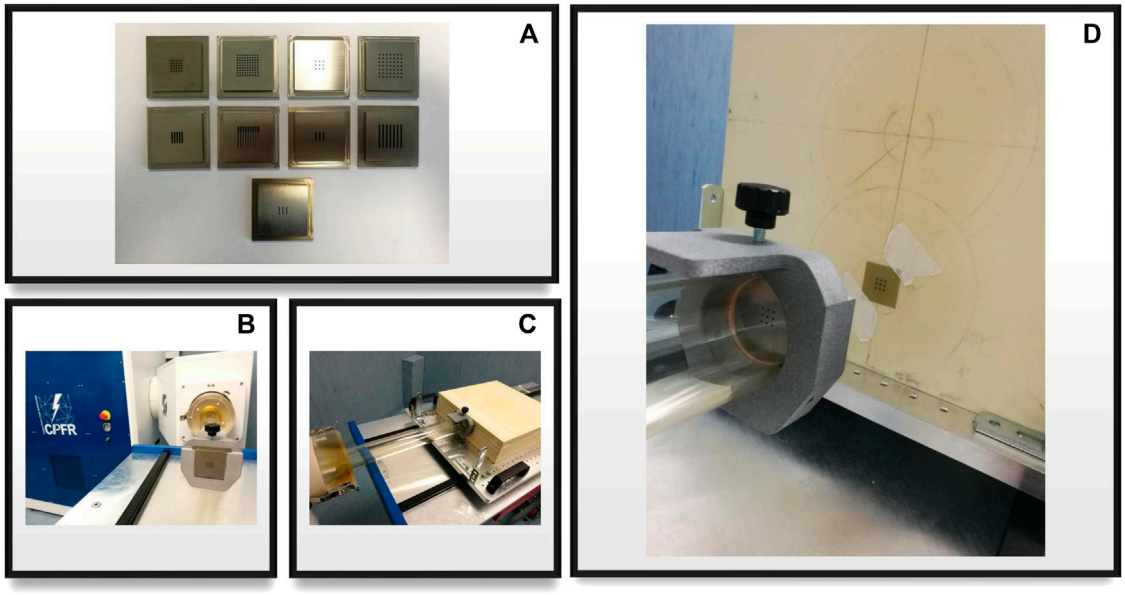


FIGURE 3
**(A)** All nine template configurations for grid and planar collimators; **(B)** template mounted on the accelerator's applicator with a nylon 3d printed holder; **(C)** experimental setup close-up, applicator, template and phantom are shown; **(D)** close-up of the beam optics, template and irradiated gafchromic film after dose delivery with a visible mini-beam pattern.

**TABLE 1 Mini-beam template geometric parameters.**

| Configuration name | Hole/slit dimensions ($mm^2$) | # of holes/slits | Center to center distance (ctc) (mm) |
|---|---|---|---|
| Grid_conf1 | 1 × 1 | 25 | 2 |
| Grid_conf2 | 1 × 1 | 9 | 3 |
| Grid_conf3 | 1 × 1 | 81 | 2 |
| Grid_conf4 | 1 × 1 | 49 | 3 |
| Planar_conf1 | 1 × 9 | 5 | 2 |
| Planar_conf2 | 1 × 7 | 3 | 3 |
| Planar_conf3 | 1 × 17 | 9 | 2 |
| Planar_conf4 | 1 × 17 | 7 | 3 |
| Planar_conf5 | 0.5 × 6 | 3 | 3 |

codes: Electron Gamma Shower by the National Research Council Canada (EGSnrc) [38], Geant4, and FLUKA [39, 40]. The realistic input energy spectrum and spatial distribution before the Titanium window were provided by SIT Sordina company. To validate the accuracy of the simulations, we compared them with measurements obtained using the FlashDiamond [41] detector, including PDD and dose profile measurements. In order to obtain absolute dose values from the simulations, we normalized the mini-beam dose percentage with respect to an open field measurement at the buildup region. This normalization was then scaled to the desired depth using the PDD curve.

### 2.2.1 EGSnrc

The simulations performed using EGSnrc consisted of two parts, using the beamline simulation code (BEAMnrc) and the dose deposition simulation code (DOSXYZnrc). At first, a phase space was obtained using BEAMnrc, then the dose was calculated using DOSXYZnrc in the water phantom. The voxel size was adjusted to closely match the dots per inch (DPI) scan setting of the gafchromic film and the film thickness. With BEAMnrc, we modeled the accelerator optics starting from the titanium window down to the tungsten template. To include all the beam optic materials, we expanded the default International Commission on Radiation Units and Measurements (ICRU) material data file (ICRU521) using the EGSnrc graphic interface.

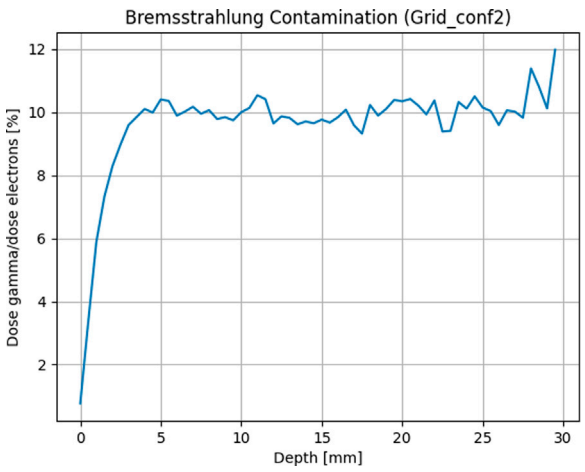


FIGURE 4
Bremsstrahlung photons evaluated as average dose contribution along the depth of a water phantom by separating particles in the phase space after the template.

### 2.2.2 GEANT4

We also recreated the EGSnrc setup using GEANT4 to compare it with the gafchromic measurements. We used the same input spectrum and designed the simulated setup to mimic the modeling approach in EGSnrc. However, in GEANT4, we directly calculated the dose in a water phantom without generating a phase space.

### 2.2.3 FLUKA

In addition, we replicated the EGSnrc configuration using FLUKA as an alternative comparison to the measurements. Keeping the input spectrum unchanged, the simulated setup closely emulates the modeling methodology employed in EGSnrc. Like in GEANT4, in FLUKA, the dose calculation was performed directly in a water phantom, eliminating the need for generating a phase space.

## 2.3 UHDP-mini-beam by using the triode-gun electronflash linac

The flash linac adopted is the Triode-Gun equipped ElectronFlash manufactured by SIT, available at the CPFR in Pisa, Italy. It operates at energies of 7 and 9 MeV, delivering a dose-rate of up to 5,000 Gy/s. Field size and Normal Treatment Distance (NTD) is achieved by means of passive collimation with polymethyl methacrylate (PMMA) cylindrical tubes, called applicators. Each applicator is uniquely identified by its diameter (ex. Applicator 100 mm, 50 mm, 40 mm, etc.). With this linac it's possible to achieve flash conditions and vary the main parameters (Dose per pulse, pulse width, pulse repletion frequency ecc.) independently from one and another, without changing experimental setup or beam collimation [42].

## 2.4 Experimental setup

Measurements were performed using the ElectronFlash linac in 9 MeV mode with a 40 mm diameter applicator. For electron flash, beam monitoring is critical as conventional systems based on ionization chambers are not compatible with the high beam current [43]. As in the case of flash with protons [44], beam monitoring is a topic of great interest which requires non-conventional solution. In fact, ElectronFlash comes equipped with a IEC 60601-2-1 [45] compliant beam current transformer (ACCT) based monitoring system, which correlates the beam current to delivered dose in the form of monitor units (MU) displayed on the machine human interface (HMI) system. After an initial MU calibration check without the mini-beam template, we fixed the pulse width ($t_p$), pulse repetition frequency (PRF), and dose per pulse to ensure each gafchromic film received the same dose at the open field electron beam build up depth (R100). The EBTXD gafchromic films [36] were analyzed with an Epson Expression scanner 10000XL after 48 h, 254 DPI with the background subtracted from a pre-irradiation scan. From the scan, we converted the optical density (OD) to dose with previously measured dose calibration curves. Each film was irradiated accumulating a total dose of 23.5 Gy at R100, using a dose per pulse of about 0.2 Gy/p, $t_p$ of 4 μs and a PRF of 50 Hz.

The mini-beam templates were attached to the applicator using a 3D-printed nylon holder, and the films were placed between slabs of a plastic water phantom to measure the dose profile at each depth. The total phantom dimensions are 30 × 30 × 15 $cm^3$, with singular slab thickness ranging from 1 mm to 1 cm. For each template we evaluated the main characteristics, such as ctc, PVDR, irradiated surface, and the effect of hole type and dimensions.

As by design, the nylon holder does not extend beyond the template, ensuring that only the tungsten is in contact with the phantom. For each template, we measured the dose profile at various depths ranging from 0 up to 4 mm water depth, using 25.6 × 25.6 $mm^2$ films positioned perpendicular to the beam axis in the water equivalent phantom. In the case of GRID templates, we sampled additional points along the depth to evaluate the PDD (percentage depth dose). For the PLANAR templates, a 51.2 × 51.2 $mm^2$ film was placed parallel to the beam axis at a depth of 4 mm, with normalization to the entrance dose measured using a 25.6 × 25.6 $mm^2$ film positioned perpendicular to the beam axis during the same irradiation.

# 3 Results

## 3.1 Monte Carlo validation

Each of the Monte Carlo codes show good agreement with the open field experimental data in the water phantom, as shown in Figure 2. Gamma index analysis [46] was performed for the Monte Carlo curves, comparing each one with the FlashDiamond data. With a Dose Difference (DD) of 3% and a Distance to Agreement (DTA) of 3 mm, we have obtained over a 90% agreement for the curves across all Monte Carlo codes. We decided on these values of DD and DTA due to the dose response and spatial resolution of the FlashDiamond detector [41]. Thus, we can reasonably use the Monte Carlo codes for a comparison with the experimental data.

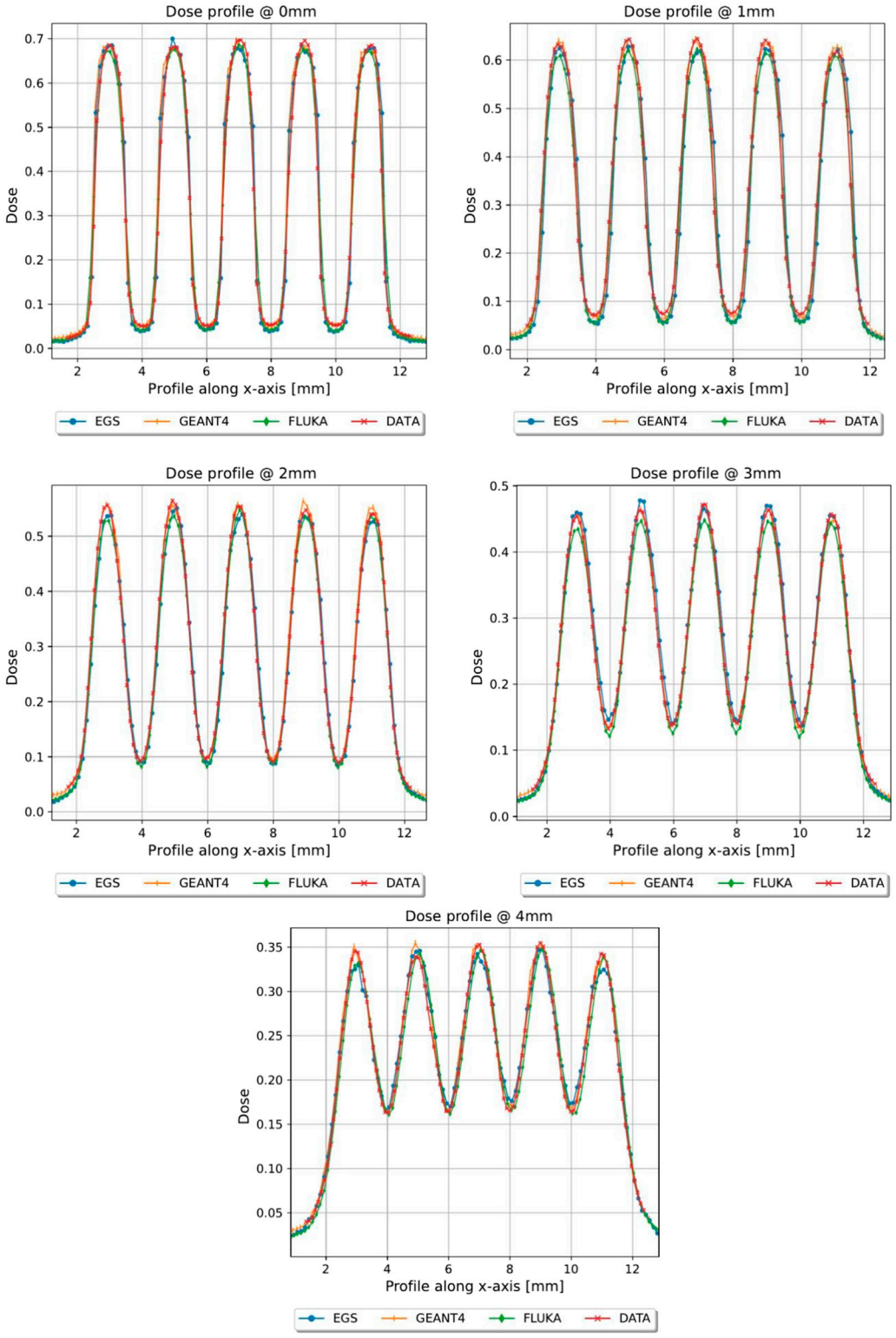


FIGURE 5
Dose profiles, normalized to the dose value of the open field at R100, of the first 4 mm in depth of grid conf1, Monte Carlo vs. Gafchromic film.

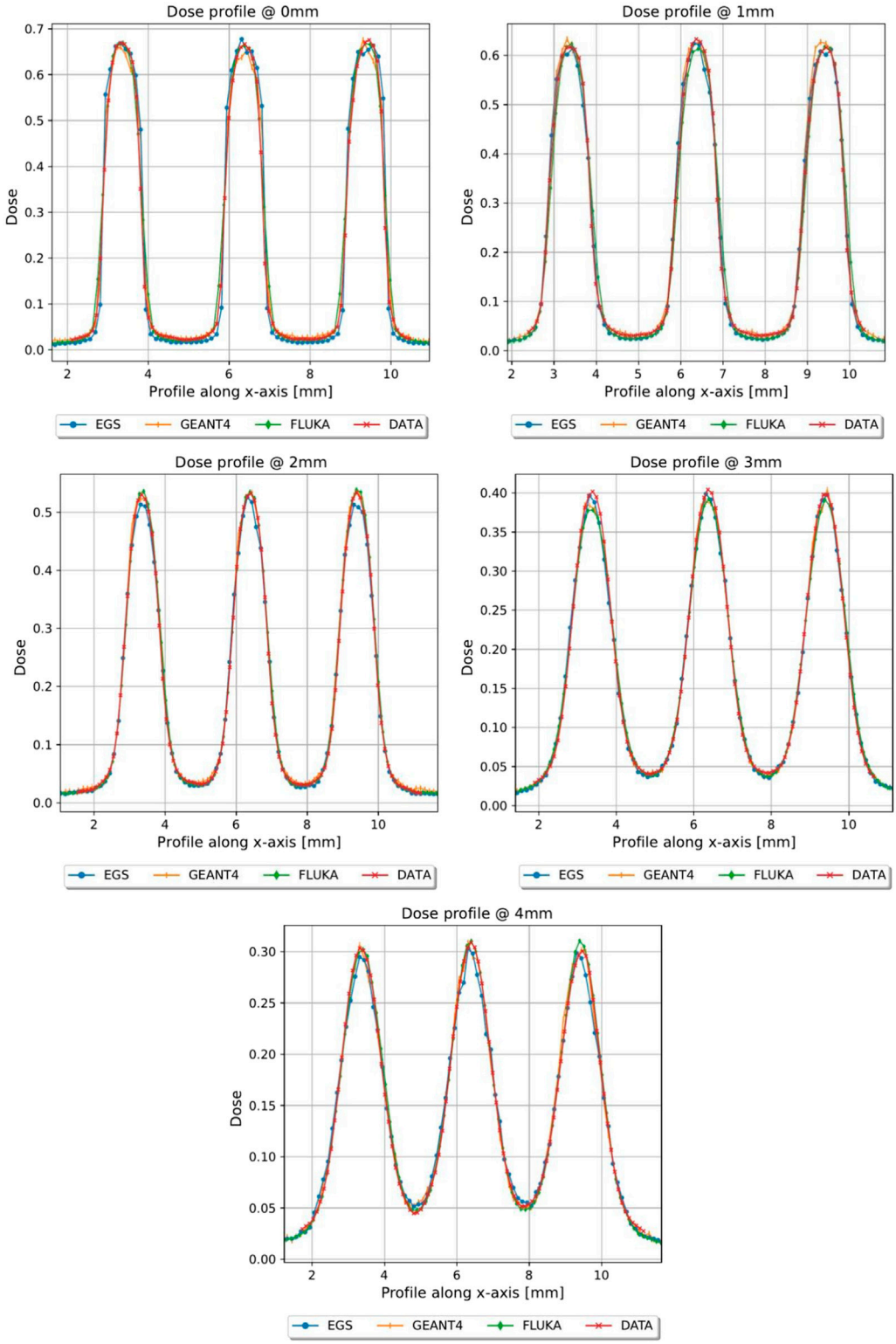


FIGURE 6
Dose profiles, normalized to the dose value of the open field at R100, of the first 4 mm in depth of grid conf2, Monte Carlo vs. Gafchromic film.

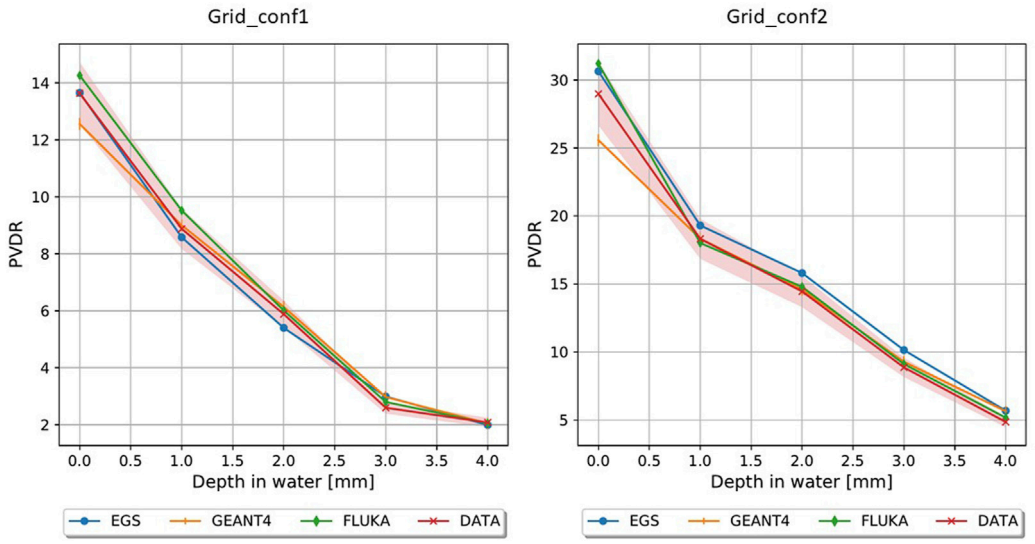


FIGURE 7
PVDR for grid_conf1 **(left)** and grid_conf2 **(right)**.

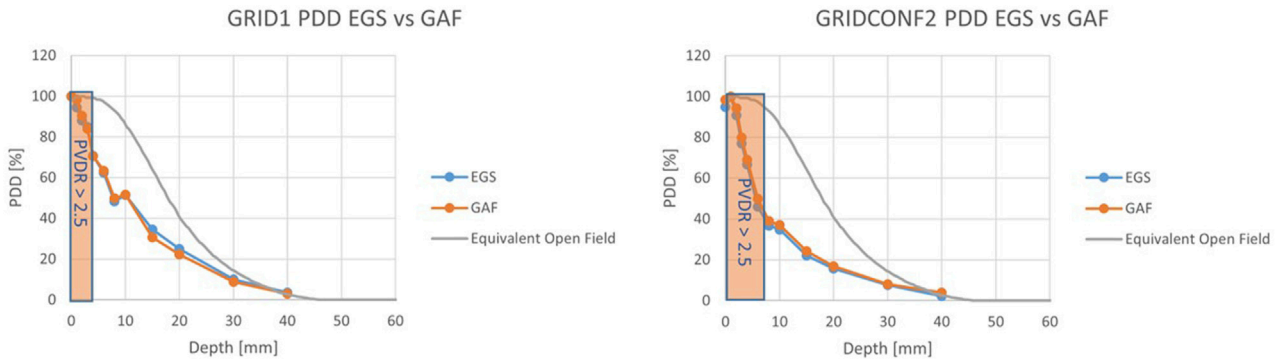


FIGURE 8
PDDs for the grid configurations. For grid_conf1 **(left)** the "mini-beam zone" extends up to 3 mm, while for grid_conf2 **(right)** the zone extends to 6 mm.

## 3.2 Template construction and characteristics

The final collimators which have been constructed are shown in Figure 3, which also shows a picture of the template attachment on the PMMA applicator and a close-up of the setup, and in Table 1 the main geometric characteristics of each one is summarized. Each one is $5 \times 5 \times 0.5\,cm^3$ and is made of Tungsten, to ensure minimal electron septa bleed-through and maintain a useful mini-beam structure. Since the templates are made of a high Z material, it is useful to evaluate secondary radiation and its effect on the mini-beam distribution. As shown in Figure 4, Bremsstrahlung photons, evaluated in the worst-case scenario of the grid_conf2 template (the one with least open volume), constitute less than 10% for depth up to 5 mm of the dose, which is deposited mostly at depths beyond the desired mini-beam structure. A rough approximation can be made by utilizing the radiative stopping powers listed in the National Institute of Standards and Technology (NIST) tables for Tungsten [47]. This calculation overlooks any directional or geometric aspects of the beam and yields an estimate of approximately 10% of the maximum dose attributable to radiative loss.

## 3.3 Experimental measurements and comparison with Monte Carlo simulations

The templates used for measurement, referenced in Table 1, are as follows:

1. Grid_conf1
2. Grid_conf2
3. Planar_conf1
4. Planar_conf3

In Figures 5, 6, the transversal dose profiles obtained experimentally, at the center of the beam from 0 mm up to

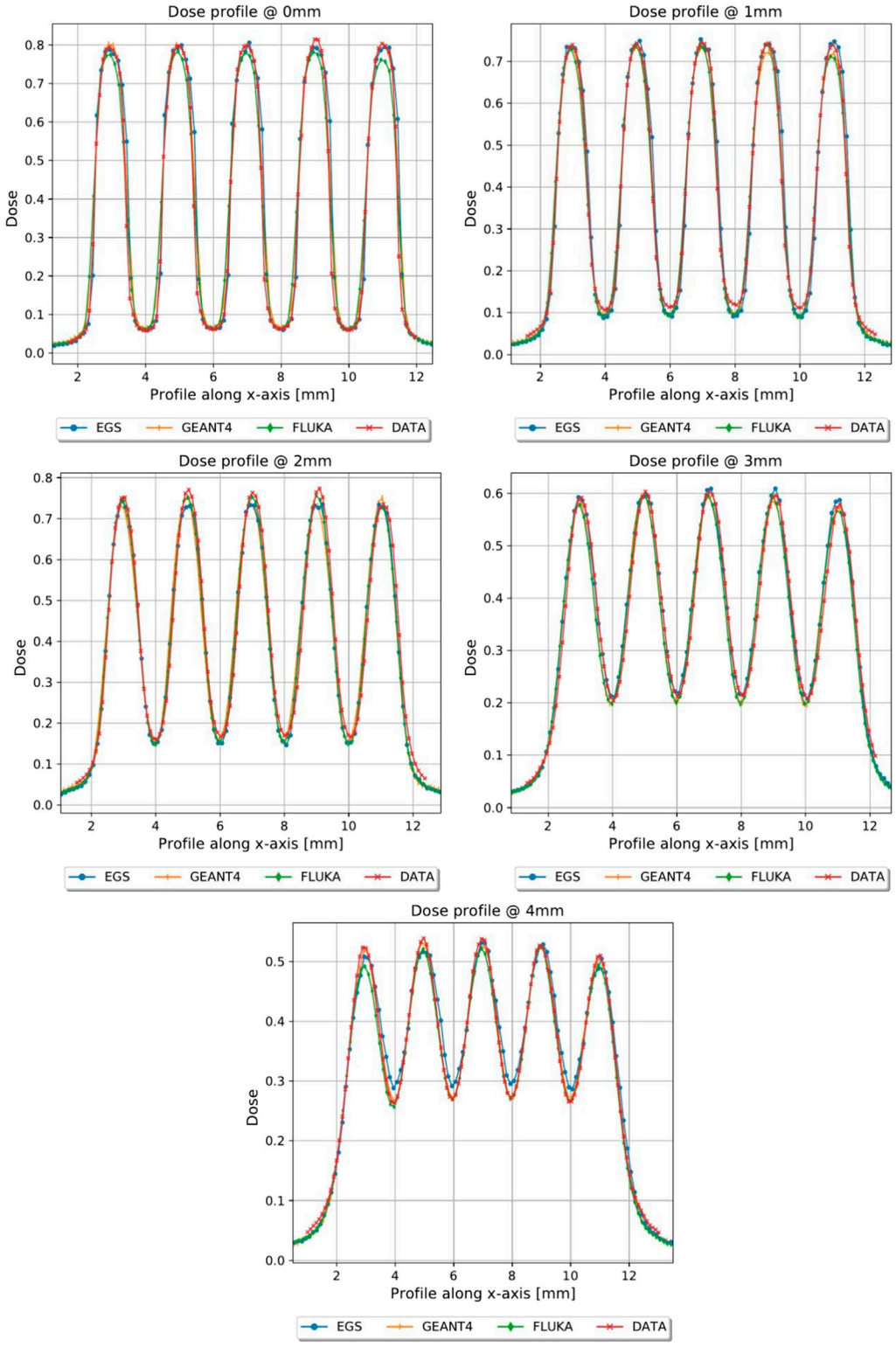


FIGURE 9
Dose profiles, normalized to the dose value of the open field at R100, of the first 4 mm in depth of planar_conf1, MC vs. GAF.

4 mm in water depth are presented for the grid configurations, grid1 and grid2, along with the expected values from the Monte Carlo (MC) simulations. For all profiles, the dose is normalized to the dose at R100 of the open 40 mm field. To evaluate the agreement of the Monte Carlo simulations, we used gamma index analysis with DD of 6% and DTA of 2 mm to achieve an agreement greater than 93% with the experimental data at each depth. The choice of DD and DTA is due to the high dose uncertainty and high spatial resolution

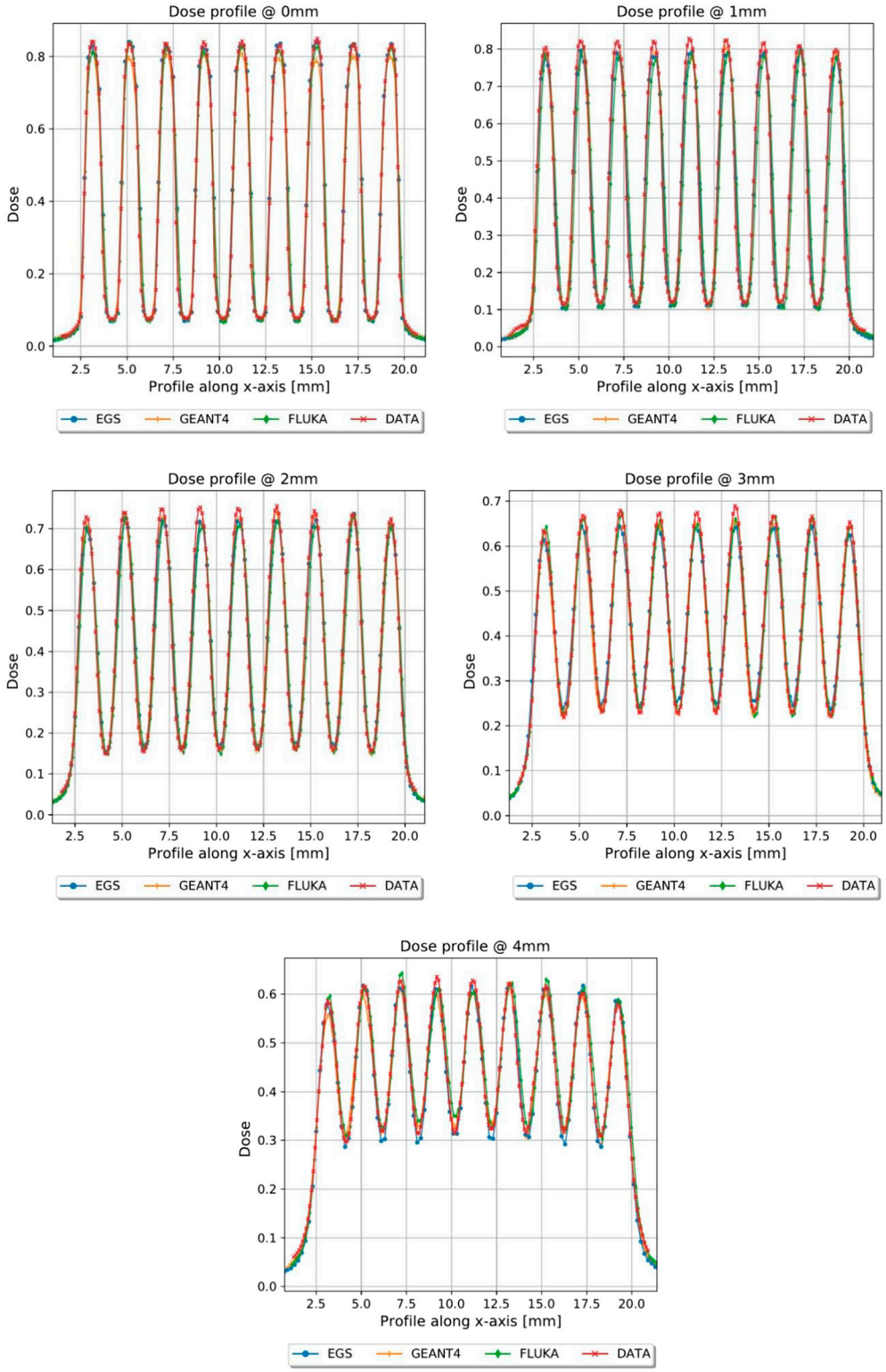


FIGURE 10
Dose profiles, normalized to the dose value of the open field at R100, of the first 4 mm in depth of planar_conf3, MC vs. GAF.

of gafchromic films, as pointed out in [36, 37, 41]. The agreement is further observed in the PVDR values reported as function of the depth depicted in Figure 7. As anticipated, a higher ctc results in a significantly greater PVDR, as the increased septa blocks adjacent hole contamination, leading to a substantial decrease in the valley dose at the expense of a lower average dose. Figure 8 illustrates the average dose PDDs (percentage depth dose) and the depth at which PVDR > 2.5 for the grid templates. As comparison, also the

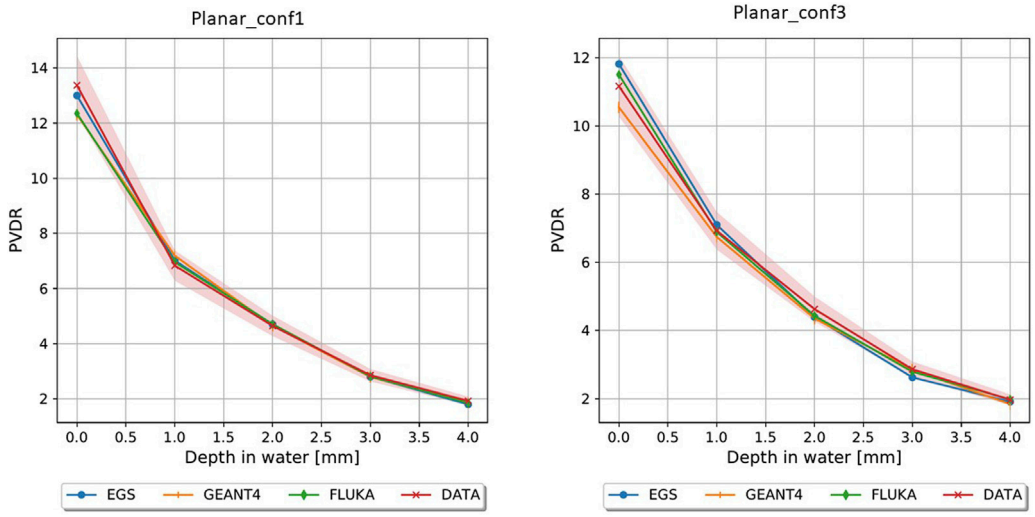


FIGURE 11
PVDR planar_conf1 **(left)** and planar_conf3 **(right)**.

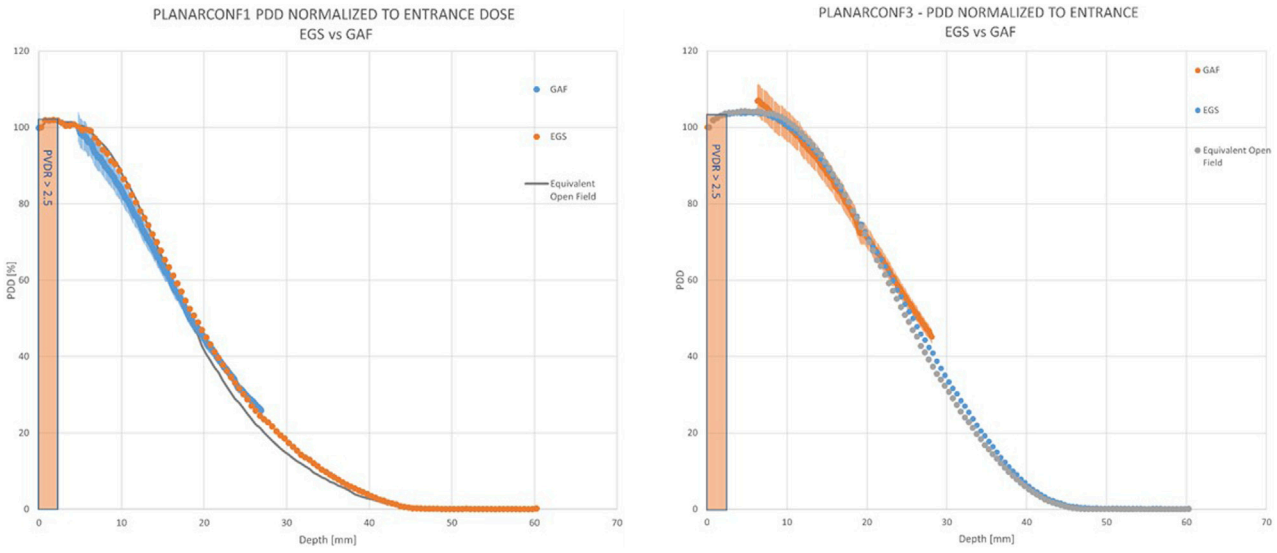


FIGURE 12
PDDs for the planar configurations. For planar_conf1 **(left)** the "mini-beam zone" extends up to 3 mm, which is the same as planar_conf3 **(right)**.

equivalent open field (obtained as EGSnrc simulated tungsten slab of 5 mm with an aperture of the dimensions of the hole distribution, in this case 1 cm) is shown. We can observe that a greater ctc considerably expands the "mini-beam zone" (PVDR > 2.5) while creating a steeper PDD. This mini-beam structure covers a zone up to the depth of the 50% dose deposition (R50) in water, while reducing the total penetration of the dose distribution for greater depth. This makes the grid template particularly interesting, as it is possible to obtain a large area of "mini-beam" characteristics, with the possibility of performing *in vivo* experiments on organs and tissues of dimensions of 5–6 mm. Figures 9, 10 present the profiles for the planar templates, showing a good agreement also above 93% of gamma index with DD 6% and DTA 2 mm. In Figure 11, the PVDR as a function of depth for the planar configuration is displayed. Apart from a slight discrepancy (15%) at the entrance, where a small increase in the valley dose can significantly impact the PVDR, the greater field size does not affect significantly the mini-beam distribution along the depth. Figure 12 shows the PDDs normalized to the entrance dose and "mini-beam zone" (PVDR > 2.5) for the templates, compared to the equivalent open beam configuration (2 × 2 $cm^2$ field). Since the positioning of the film parallel to the beam resulted in an underexposure after the R50 beyond the constructor's tolerances, that part is omitted on the graph. As expected, with an increase in field size, we approach an

**TABLE 2 Mini-beam characteristics for each template.**

| Template | Depth (mm) | PVDR | D_p/ D_open (%) | D_v/ D_open (%) | D_avg/ D_open (%) | Ctc (mm) | FWHM (mm) | R50 (mm) |
|---|---|---|---|---|---|---|---|---|
| Grid_conf1 | 0 | 13.6 | 70.8 | 5.2 | 37.9 | 2 | 0.9 | 9 |
| | 1 | 8.9 | 63.9 | 7.2 | 35.8 | 2 | 1 | |
| | 2 | 5.9 | 56.5 | 9.6 | 33.2 | 2 | 1.1 | |
| | 3 | 2.6 | 47.4 | 18.2 | 31.6 | 2 | 1.2 | |
| | 4 | 2.1 | 30.9 | 14.7 | 25.1 | 2 | 1.5 | |
| Grid_conf2 | 0 | 28.9 | 68.9 | 2.4 | 25.1 | 3 | 0.9 | 6 |
| | 1 | 18.3 | 60.9 | 3.3 | 24.5 | 3 | 1 | |
| | 2 | 15.3 | 49.7 | 3.5 | 23.7 | 3 | 1 | |
| | 3 | 9.5 | 54.7 | 4.3 | 20.1 | 3 | 1.2 | |
| | 4 | 6.5 | 40.2 | 4.6 | 17.1 | 3 | 1.3 | |
| Grid_conf3 | 0 | 14 | 69.2 | 4.9 | 38.5 | 2 | 1 | 10 |
| | 1 | 9.6 | 58.5 | 6.1 | 33.9 | 2 | 1 | |
| | 2 | 5.7 | 51.1 | 9.0 | 29.4 | 2 | 1.1 | |
| | 3 | 3 | 39.3 | 13.1 | 26.0 | 2 | 1.2 | |
| | 4 | 1.9 | 30.2 | 15.9 | 22.9 | 2 | 1.5 | |
| Grid_conf4 | 0 | 32.8 | 64.1 | 2.0 | 22.3 | 3 | 1 | 6 |
| | 1 | 24.2 | 53.5 | 2.2 | 19.8 | 3 | 1 | |
| | 2 | 16.6 | 47.2 | 2.8 | 19.0 | 3 | 1.1 | |
| | 3 | 9.6 | 35.7 | 3.7 | 16.5 | 3 | 1.2 | |
| | 4 | 5.4 | 26.1 | 4.8 | 14.2 | 3 | 1.5 | |
| Planar_conf1 | 0 | 13.4 | 81.8 | 6.1 | 39.9 | 2 | 0.9 | 19 |
| | 1 | 6.8 | 72.9 | 10.7 | 39.6 | 2 | 1 | |
| | 2 | 4.7 | 73.6 | 15.7 | 39.4 | 2 | 1.1 | |
| | 3 | 2.9 | 59.2 | 20.4 | 38.2 | 2 | 1.3 | |
| | 4 | 1.9 | 52.2 | 27.5 | 37.8 | 2 | 1.6 | |
| Planar_conf2 | 0 | 28.4 | 84.0 | 3.0 | 32.9 | 3 | 1 | 15 |
| | 1 | 18.6 | 74.8 | 4.0 | 31.0 | 3 | 1 | |
| | 2 | 13.7 | 66.3 | 4.8 | 29.7 | 3 | 1.1 | |
| | 3 | 8 | 64.0 | 8.0 | 29.0 | 3 | 1.3 | |
| | 4 | 4.7 | 53.2 | 11.3 | 27.8 | 3 | 1.5 | |
| Planar_conf3 | 0 | 11.2 | 84.3 | 7.5 | 41.3 | 2 | 0.9 | 26 |
| | 1 | 6.9 | 81.9 | 11.9 | 43.7 | 2 | 1 | |
| | 2 | 4.6 | 74.0 | 16.1 | 43.1 | 2 | 1.1 | |
| | 3 | 2.9 | 67.6 | 23.3 | 42.1 | 2 | 1.3 | |
| | 4 | 2 | 63.1 | 31.6 | 42.8 | 2 | 1.5 | |
| Panar_conf4 | 0 | 25 | 82.0 | 3.3 | 31.4 | 3 | 0.8 | 15 |
| | 1 | 15.1 | 78.6 | 5.2 | 32.4 | 3 | 0.9 | |
| | 2 | 10.2 | 70.5 | 6.9 | 31.2 | 3 | 1 | |

(Continued on following page)

**TABLE 2 (*Continued*) Mini-beam characteristics for each template.**

| Template | Depth (mm) | PVDR | D_p/ D_open (%) | D_v/ D_open (%) | D_avg/ D_open (%) | Ctc (mm) | FWHM (mm) | R50 (mm) |
|---|---|---|---|---|---|---|---|---|
| | 3 | 6.8 | 64.5 | 9.5 | 28.8 | 3 | 1.1 | |
| | 4 | 4 | 55.3 | 13.8 | 28.8 | 3 | 1.3 | |
| Planar_conf5 | 0 | 28 | 60.5 | 2.2 | 14.9 | 3 | 0.5 | 17 |
| | 1 | 20.1 | 52.0 | 2.6 | 14.8 | 3 | 0.6 | |
| | 2 | 15.1 | 38.9 | 2.6 | 12.7 | 3 | 0.7 | |
| | 3 | 10.3 | 31.6 | 3.1 | 9.5 | 3 | 0.9 | |
| | 4 | 6.3 | 25.7 | 4.1 | 9.1 | 3 | 1.2 | |

**TABLE 3 MINI-BEAM-CONV and MINI-BEAM-FLASH characteristics for PEAK and AVERAGE dose points.**

| Template | Average DR @peak (Gy/s) | DPP@peak (Gy/p) | DR_pulse@peak (kGy/s) | Average DR @average (Gy/s) | DPP@average (Gy/p) | DR_pulse@average (kGy/s) |
|---|---|---|---|---|---|---|
| Grid_conf1 | (0.09, 1404.36) | (0.09, 5.73) | (21.36, 1431.70) | (0.05, 787.44) | (0.05, 3.21) | (11.98, 802.77) |
| Grid_conf2 | (0.08, 1346.26) | (0.08, 5.49) | (20.48, 1372.48) | (0.03, 541.49) | (0.03, 2.21) | (8.24, 552.04) |
| Grid_conf3 | (0.08, 1301.5) | (0.08, 5.31) | (19.8, 1326.85) | (0.05, 760.0) | (0.05, 3.1) | (11.56, 774.8) |
| Grid_conf4 | (0.07, 1206.5) | (0.07, 4.92) | (18.35, 1230.00) | (0.03, 446.5) | (0.03, 1.82) | (6.79, 455.2) |
| Planar_conf1 | (0.10, 1613.58) | (0.10, 6.58) | (24.54, 1645.00) | (0.05, 876.43) | (0.05, 3.57) | (13.33, 893.50) |
| Planar_conf2 | (0.10, 1649.20) | (0.10, 6.73) | (25.09, 1681.32) | (0.04, 684.00) | (0.04, 2.79) | (10.40, 697.32) |
| Planar_conf3 | (0.11, 1746.27) | (0.11, 7.12) | (26.56, 1780.28) | (0.06, 930.08) | (0.06, 3.79) | (14.15, 948.20) |
| Planar_conf4 | (0.10, 1683.4) | (0.10, 6.87) | (25.61, 1716.18) | (0.04, 693.50) | (0.04, 2.83) | (10.55, 707.01) |
| Planar_conf5 | (0.07, 1178.00) | (0.07, 4.81) | (17.92, 1200.94) | (0.02, 334.40) | (0.02, 1.36) | (5.09, 340.91) |

open field configuration, resulting in greater penetration, as precedingly reported by [18]. Furthermore, in comparison to the grid configuration, the PDD does not significantly differ from the equivalent open field. This makes the planar template interesting from a clinical point of view, as it has a PDD practically identical to that of the conventional beam of equal energy (same depth of treatment) with the possibility of having a mini-beam effect, for example, on the skin, potentially reducing the collateral effects to this organ.

## 3.4 Mini-beam characteristics for each template

In Table 2, the main mini-beam characteristics are reported for each constructed template. We reported, for each template and each depth, the PVDR, the ratio of the dose at the peak (D_p) and the dose at the buildup depth without the template (D_open, which is to be considered a reference dose value), the ratio of the dose at the valley (D_v) and D_open, the ratio of the average dose (D_avg) and D_open, the ctc, the FWHM and finally the R50 (which is the same for each template). For the sake of legibility, uncertainties on single dose measurements are assumed to be 4%, to be appropriately propagated for each derived quantity.

## 3.5 Mini-beam-flash irradiation parameters

Finally, we present in Table 3 the possible parameters for mini-beam-conv and mini-beam-UHDR irradiation (Average dose rate (DR), dose per pulse (DPP) and dose rate within the pulse (DR_PULSE) at the peak and average mini-beam dose), at the reference depth of 1 mm, for the peak and average dose. All values are reported as ranges in square brackets, indicating the minimum (CONV) and maximum (FLASH) values achievable. These parameters are to be considered indicative, since we can tune the ElectronFlash to obtain a wide range of characteristics in a continuous way, within the limits of proper linac function.

# 4 Discussion and conclusion

In this study, we have designed, simulated, and finally realized mini-beam and UHDR-mini-beams by using the triode-gun ElectronFlash low energy electrons linac and special tungsten passive template; we have then completely characterized dosimetrically our beams by means of radiochromic films. We have observed a good agreement between film measurements and Monte Carlo simulations. Due to the nature of radiochromic films, a greater discrepancy is the valley is to be expected with respect to the peaks, since the dose is much lower and the region

of interest in which the dose is calculated is quite small. Nevertheless, the comparison with the simulations with various codes gave additional robustness to the experimental measurements. Across all Monte Carlo codes, the obtained results exhibited comparable outcomes with only minor discrepancies in valley dose. The relative dose values and PVDR measurements were in almost all cases within the uncertainty range of the gafchromic films, with discrepancies most likely due to different statistics and variation between the unique code parameters. Nevertheless, these findings affirm the capability of each of the evaluated codes to accurately simulate the linac geometry and templates. We have observed that increasing the ctc results in a decrease in the valley dose, leading to higher PVDR and a larger mini-beam zone. Having both grid and planar configurations at our disposal allows for great versatility in experiments. A grid configuration reduces dose deposition along the depth and enables a higher PVDR and mini-beam zone with fixed template parameters. This can be beneficial for *in vivo* irradiations for target up to 5–6 mm of size. On the other hand, the planar geometry diminishes the PVDR but achieves a higher peak dose and deeper dose penetration. This may be promising from a clinical perspective, as the beam does not lose penetration compared to the open field and has a mini-beam component in the first few mm of depth, which could substantially reduce side effects on the skin. Regarding bremsstrahlung contamination, even in the worst-case scenario, it is not significant within the mini-beam zone, and an appropriate mini-beam structure is maintained. This allows for the use of tungsten as the material of choice, at least in the case of low-energy electrons, as the main cause of mini-beam loss is primarily electron septa crossing, which is avoided due to the high atomic number (Z) of the material. Thus, the proposed method of generating a mini-beam structure offers great versatility. This versatility is particularly important when combined with the flash capabilities of our triode-gun ElectronFlash linac, as it enables the study of both mini-beam and flash effects by independently varying the fundamental spatial and temporal parameters involved in the two effets. This is fundamental for quantitative mini-beam and flash experiments, since we can vary all the fundamental parameters independently one from the other and without altering the experimental setup, guaranteeing a wide range of investigations and great reproducibility. The mini-beam and mini-beam-flash operating beams that we have realized, can be used to carry out radiobiological experiments necessary to study the quantitative dependencies of the flash and mini-beam effects and the beam parameters that characterize them, and to understand their underlying radiobiological mechanisms. These experiments are aimed at optimizing the clinical implementation of flash, mini-beam and possibly mini-beam flash radiotherapy. This will be fundamental also for the future transition to VHEE [48, 49], as mini-beams and the flash effect will play a crucial role. We are thus able to continue working towards a robust clinical protocol and evaluate the biological modifying factors necessary for a treatment planning system, both pre-clinical and clinical.

## Data availability statement

The original contributions presented in the study are included in the article/Supplementary Material, further inquiries can be directed to the corresponding author.

## Author contributions

JP: Writing–original draft, Writing–review and editing. FR: Writing–review and editing. MC: Writing–review and editing. DS: Writing–review and editing. GFe: Writing–review and editing. GFr: Writing–review and editing. LM: Writing–review and editing. GM: Writing–review and editing. VP: Writing–review and editing. YP: Writing–review and editing. FD: Writing–review and editing.

## Funding

The author(s) declare financial support was received for the research, authorship, and/or publication of this article. We thank Fondazione Pisa for funding CPFR with the grant "prog. n. 134/2021." The research is also partially supported by INFN CSN5 funded project "FRIDA." Additionally, the research has received funding from the European Union—NextGenerationEU through the Italian Ministry of University and Research under PNRR—M4C2-I1.3 Project PE_00000019 "HEAL ITALIA."

## Conflict of interest

Authors JP, GFe, and LM were employed by Sordina IORT Technologies S.p.A.

The remaining authors declare that the research was conducted in the absence of any commercial or financial relationships that could be construed as a potential conflict of interest.

## Publisher's note



## Author disclaimer

The views and opinions expressed are those of the authors only and do not necessarily reflect those of the European Union or the European Commission. Neither the European Union nor the European Commission can be held responsible for them.

# References


1. Laissue JA, Blattmann H, Slatkin DN. "Alban Köhler (1874–1947): Erfinder der Gittertherapie." *Zeitschrift für Medizinische Physik* (2012) 22 (2):90–99.

2. Schneider T, Prezado Y, Bertho A, Fazzari J, Iturri L, Martin OA, et al. Combining FLASH and spatially fractionated radiation therapy: the best of both worlds. *Radiother Oncol* (2022) 175(1):169–77. doi:10.1016/j.radonc.2022.08.004

3. Prezado Y. Divide and conquer: spatially fractionated radiation therapy. *Expert Rev Mol Med* (2022) 24:e3. doi:10.1017/erm.2021.34

4. Yan W, Khan MK, Wu X, Simone CB, Fan J, Gressen E, et al. Spatially fractionated radiation therapy: history, present and the future. *Clin translational Radiat Oncol* (2020) 20:30–8. doi:10.1016/j.ctro.2019.10.004

5. Bräuer-Krisch E, Serduc R, Siegbahn EA, Le Duc G, Prezado Y, Bravin A, et al. Effects of pulsed, spatially fractionated, microscopic synchrotron X-ray beams on normal and tumoral brain tissue. *Mutat Research/Reviews Mutat Res* (2010) 704(1-3):160–6. doi:10.1016/j.mrrev.2009.12.003

6. Prezado Y, Jouvion G, Hardy D, Patriarca A, Nauraye C, Bergs J, et al. Proton mini-beam radiation therapy spares normal rat brain: long-Term Clinical, Radiological and Histopathological Analysis. *Scientific Rep* (2017) 7:14403. doi:10.1038/s41598-017-14786-y

7. Prezado Y, Jouvion G, Guardiola C, Gonzalez W, Juchaux M, Bergs J, et al. Tumor control in RG2 glioma-bearing rats: a comparison between proton mini-beam therapy and standard proton therapy. *Int J Radiat Oncology* Biology* Phys* (2019) 104:266–71. doi:10.1016/j.ijrobp.2019.01.080

8. Girst S, Greubel C, Reindl J, Siebenwirth C, Zlobinskaya O, Walsh DW, et al. Proton mini-beam radiation therapy reduces side effects in an *in vivo* mouse ear model. *Int J Radiat Oncology* Biology* Phys* (2016) 95:234–41. doi:10.1016/j.ijrobp.2015.10.020

9. Lamirault C, Doyère V, Juchaux M, Pouzoulet F, Labiod D, Dendale R, et al. Short and long-term evaluation of the impact of proton mini-beam radiation therapy on motor, emotional and cognitive functions. *Scientific Rep* (2020) 10:13511. doi:10.1038/s41598-020-70371-w

10. Bertho A, Ortiz R, Juchaux M, Gilbert C, Lamirault C, Pouzoulet F, et al. First evaluation of temporal and spatial fractionation in proton mini-beam radiation therapy of glioma-bearing rats. *Cancers* (2021) 13:4865. doi:10.3390/cancers13194865

11. Mohiuddin M, Fujita M, Regine WF, Megooni AS, Ibbott GS, Ahmed MM. High-dose spatially-fractionated radiation (GRID): a new paradigm in the management of advanced cancers. *Int J Radiat Oncol Biol Phys* (1999) 45:721–7. doi:10.1016/s0360-3016(99)00170-4

12. Steel H, Brüningk SC, Box C, Oelfke U, Bartzsch SH. Quantification of differential response of tumour and normal cells to microbeam radiation in the absence of FLASH effects. *Cancers (Basel)* (2021) 13:3238. doi:10.3390/cancers13133238

13. Bouchet A, Brauer-Krisch E, Prezado Y, El Atifi M, Rogalev L, Le Clec'h C, et al. Better efficacy of synchrotron spatially microfractionated radiation therapy than uniform radiation therapy on glioma. *Int J Radiat Oncol Biol Phys* (2016) 95:1485–94. doi:10.1016/j.ijrobp.2016.03.040

14. Prezado Y, Deman P, Varlet P, Jouvion G, Gil S, Le Clec'H C, et al. Tolerance to dose escalation in mini-beam radiation therapy applied to normal rat brain: long-term clinical, radiological and histopathological analysis. *Radiat Res* (2015) 184:314–21. doi:10.1667/rr14018.1

15. Smyth LML, Donoghue JF, Ventura JA, Livingstone J, Bailey T, Day LRJ, et al. Comparative toxicity of synchrotron and conventional radiation therapy based on total and partial body irradiation in a murine model. *Sci Rep* (2018) 8:12044. doi:10.1038/s41598-018-30543-1

16. Martínez-Rovira I, Puxeu-Vaqué J, Prezado Y. Dose evaluation of Grid Therapy using a 6 MV flattening filter-free (FFF) photon beam: a Monte Carlo study. *Med Phys* (2017) 44(10):5378–83. doi:10.1002/mp.12485

17. Reiff JE, Huq MS, Mohiuddin M, Suntharalingam N. Dosimetric properties of megavoltage grid therapy. *Int J Radiat Oncol Biol Phys* (1995) 33(4):937–42. doi:10.1016/0360-3016(95)00114-3

18. Martínez-Rovira I, Fois G, Prezado Y. Dosimetric evaluation of new approaches in GRID therapy using nonconventional radiation sources. *Med Phys* (2015) 42(2):685–93. doi:10.1118/1.4905042

19. Tenzel WV. Experience with grid therapy. *Radiology* (1952) 59(3):399–408. doi:10.1148/59.3.399

20. Prezado Y, Fois GR. Proton-mini-beam radiation therapy: a proof of concept. *Med Phys* (2013) 40:031712. doi:10.1118/1.4791648

21. Wright MD. Microbeam radiosurgery: an industrial perspective. *Physica Med* (2015) 31:601–6. doi:10.1016/j.ejmp.2015.04.003

22. Patriarca A, Fouillade C, Auger M, Martin F, Pouzoulet F, Nauraye C, et al. Experimental set-up for FLASH proton irradiation of small animals using a clinical system. *Int J Radiat Oncology* Biology* Phys* (2018) 102:619–26. doi:10.1016/j.ijrobp.2018.06.403

23. Peucelle C, Nauraye C, Patriarca A, Hierso E, Fournier-Bidoz N, Martínez-Rovira I, et al. Proton mini-beam radiation therapy: experimental dosimetry evaluation. *Med Phys* (2015) 42:7108–13. doi:10.1118/1.4935868

24. Schneider T. Technical aspects of proton mini-beam radiation therapy: mini-beam generation and delivery. *Physica Med* (2022) 100:64–71. doi:10.1016/j.ejmp.2022.06.010

25. Mohiuddin M, Lynch C, Gao M, Hartsell W. Early clinical results of proton spatially fractionated GRID radiation therapy (SFGRT). *Br J Radiol* (2020) 93:20190572. doi:10.1259/bjr.20190572

26. Felici G, Barca P, Barone S, Bortoli E, Borgheresi R, De Stefano S, et al. Transforming an IORT linac into a FLASH research machine: procedure and dosimetric characterization. *Front Phys* (2020) 8:374. doi:10.3389/fphy.2020.00374

27. Di Martino F, Del Sarto D, Giuseppina Bisogni M, Capaccioli S, Galante F, Gasperini A, et al. A new solution for UHDP and UHDR (Flash) measurements: theory and conceptual design of ALLS chamber. *Physica Med* (2022) 102:9–18. doi:10.1016/j.ejmp.2022.08.010

28. Marinelli M, di Martino F, Del Sarto D, Pensavalle JH, Felici G, Giunti L, et al. A diamond detector based dosimetric system for instantaneous dose rate measurements in FLASH electron beams. *Phys Med Biol* (2023) 68:175011. doi:10.1088/1361-6560/acead0

29. Morrocchi M, Pensavalle JH, Ciarrocchi E, Di Martino F, Felici G, Galante F, et al. Experimental characterization and Monte Carlo simulation of scintillator detectors in online electron FLASH radiotherapy dosimetry. *J Instrumentation* (2022) 17:P09005. doi:10.1088/1748-0221/17/09/p09005

30. Romano F, Milluzzo G, Di Martino F, D'Oca MC, Felici G, Galante F, et al. First characterization of novel silicon carbide detectors with ultra-high dose rate electron beams for FLASH radiotherapy. *Appl Sci* (2023) 13:2986. doi:10.3390/app13052986

31. Favaudon V, Caplier L, Monceau V, Pouzoulet F, Sayarath M, Fouillade C, et al. Ultrahigh dose-rate FLASH irradiation increases the differential response between normal and tumor tissue in mice. *Sci translational Med* (2014) 6(245):245ra93. doi:10.1126/scitranslmed.3008973

32. Vozenin MC, De Fornel P, Petersson K, Favaudon V, Jaccard M, Germond JF, et al. The advantage of FLASH radiotherapy confirmed in mini-pig and cat-cancer patients. *Clin Cancer Res* (2019) 25(1):35–42. doi:10.1158/1078-0432.ccr-17-3375

33. Montay-Gruel P, Petersson K, Jaccard M, Boivin G, Germond JF, Petit B, et al. Irradiation in a flash: unique sparing of memory in mice after whole brain irradiation with dose rates above 100 Gy/s. *Radiother Oncol* (2017) 124(3):365–9. doi:10.1016/j.radonc.2017.05.003

34. Agostinelli S, Allison J, Amako K, Apostolakis J, Araujo H, Arce P, et al. Geant4—a simulation toolkit. *Nucl Instr Methods Phys Res Section A: Acc Spectrometers, Detectors Associated Equipment* (2003) 506(3):250–303. ISSN 0168-9002. doi:10.1016/S0168-9002(03)01368-8

35. Soriani A, Iaccarino G, Felici G, Ciccotelli A, Pinnarò P, Giordano C, et al. Development and optimization of a beam shaper device for a mobile dedicated IOERT accelerator. *Med Phys* (2012) 39:6080–9. doi:10.1118/1.4749968

36. Ashland. EBTXD. https://www.ashland.com/industries/medical/radiotherapy-films/ebtxd (Accessed November 8, 2023).

37. Niroomand-Rad A, Chiu-Tsao S, Grams MP, Lewis DF, Soares CG, Van Battum LJ, et al. Report of AAPM task group 235 radiochromic film dosimetry: an update to TG-55. *Med Phys* (2020) 47:5986–6025. doi:10.1002/mp.14497

38. Kawrakow I, Rogers DWO, Mainegra-Hing E, Tessier F, Townson RW, Walters BRB. *EGSnrc toolkit for Monte Carlo simulation of ionizing radiation transport* (2000). [release v2021]. doi:10.4224/40001303

39. Böhlen TT, Cerutti F, Chin MPW, Fassò A, Ferrari A, Ortega PG, et al. The FLUKA code: developments and challenges for high energy and medical applications. *Nucl Data Sheets* (2014) 120:211–4. doi:10.1016/j.nds.2014.07.049

40. Ferrari A, Sala PR, Fasso` A, Ranft J. *FLUKA: a multi-particle transport code* (2005). **CERN-2005-10, INFN/TC_05/11**, **SLAC-R-773**.

41. Gianluca VR, Felici G, Galante F, Gasparini A, Kranzer R, Mariani G, et al. Application of a novel diamond detector for commissioning of FLASH radiotherapy electron beams. *Med Phys* (2022) 49:5513–22. doi:10.1002/mp.15782

42. Di Martino F, Del Sarto D, Bass G, Capaccioli S, Celentano M, Coves D, et al. Architecture, flexibility and performance of a special electron Linac dedicated to FLASH Radiotherapy research: ElectronFlash with a triode gun of the Centro Pisano Flash radiotherapy (CPFR). *Front. Phys.* (2023) 11:1268310. Accepted on 26 Oct 2023.

43. Di Martino F, Barca P, Barone S, Bortoli E, Borgheresi R, De Stefano S, et al. FLASH radiotherapy with electrons: issues related to the production, monitoring, and dosimetric characterization of the beam. *Front Phys* (2020) 8:570697. doi:10.3389/fphy.2020.570697

44. Abouzahr F, Cesar JP, Crespo P, Gajda M, Hu Z, Kaye W, et al. The first PET glimpse of a proton FLASH beam. *Phys Med Biol* (2023) 68:125001. doi:10.1088/1361-6560/acd29e

45. IEC 60601-2-1:2020. *Medical electrical equipment - Part 2-1: particular requirements for the basic safety and essential performance of electron accelerators in the range 1 MeV to 50 MeV* (2020). https://webstore.iec.ch/publication/31388 (Accessed November 8, 2023).

46. Low DA, Harms WB, Mutic S, Purdy JA. A technique for the quantitative evaluation of dose distributions. *Med Phys* (1998) 25:656–61. doi:10.1118/1.598248

47. NIST. National Institute of standards and Technology. https://physics.nist.gov/PhysRefData/Star/Text/ESTAR.html (Accessed November 8, 2023).

48. Sarti A, De Maria P, Battistoni G, De Simoni M, Di Felice C, Dong Y, et al. Deep seated tumour treatments with electrons of high energy delivered at FLASH rates: the example of prostate cancer. *Front Oncol* (2021) 11:777852. doi:10.3389/fonc.2021.777852

49. Muscato A, Arsini L, Battistoni G, Campana L, Carlotti D, De Felice F, et al. Treatment planning of intracranial lesions with VHEE: comparing conventional and FLASH irradiation potential with state-of-the-art photon and proton radiotherapy. *Front Phys* (2023) 11:1185598. doi:10.3389/fphy.2023.1185598

frontiers | Frontiers in Physics

TYPE Original Research
PUBLISHED 16 November 2023
DOI 10.3389/fphy.2023.1268310



OPEN ACCESS

EDITED BY
Roy Clarke,
University of Michigan, United States

REVIEWED BY
Ibrahim Oraiqat,
Moffitt Cancer Center, United States
Lanchun Lu,
The Ohio State University, United States

*CORRESPONDENCE
D. Del Sarto,
damiano.delsarto@unipi.it

RECEIVED 27 July 2023
ACCEPTED 26 October 2023
PUBLISHED 16 November 2023

CITATION
Di Martino F, Del Sarto D, Bass G, Capaccioli S, Celentano M, Coves D, Douralis A, Marinelli M, Marrale M, Masturzo L, Milluzzo G, Montefiori M, Paiar F, Pensavalle JH, Raffaele L, Romano F, Subiel A, Touzain E, Verona Rinati G and Felici G (2023), Architecture, flexibility and performance of a special electron linac dedicated to Flash radiotherapy research: electronFlash with a triode gun of the centro pisano flash radiotherapy (CPFR). *Front. Phys.* 11:1268310. doi: 10.3389/fphy.2023.1268310



# Architecture, flexibility and performance of a special electron linac dedicated to Flash radiotherapy research: electronFlash with a triode gun of the centro pisano flash radiotherapy (CPFR)

F. Di Martino[1,2,3], D. Del Sarto[2,3,4]*, G. Bass[5], S. Capaccioli[2,6], M. Celentano[2,3], D. Coves[7], A. Douralis[5], M. Marinelli[8], M. Marrale[9,10,11], L. Masturzo[2,12], G. Milluzzo[11], M. Montefiori[3,6], F. Paiar[2,13], J. H. Pensavalle[2,12], L. Raffaele[14], F. Romano[11], A. Subiel[5], E. Touzain[7], G. Verona Rinati[8] and G. Felici[12]

[1]Azienda Ospedaliero Universitaria Pisana, Pisa, Italy, [2]Centro Pisano Multidisciplinare Sulla Ricerca e Implementazione Clinica Della Flash Radiotherapy (CPFR@CISUP), Pisa, Italy, [3]National Institute of Nuclear Physics (INFN), Section of Pisa, Pisa, Italy, [4]Center for Instrument Sharing of the University of Pisa (CISUP), University of Pisa, Pisa, Italy, [5]National Physical Laboratory, Medical Radiation Science, Teddington, United Kingdom, [6]Department of Physics, University of Pisa, Pisa, Italy, [7]Bergoz Instrumentation, Saint-GenisPouilly, France, [8]Department of Industrial Engineering, University of Rome "Tor Vergata", Rome, Italy, [9]Department of Physics and Chemistry "Emilio Segrè" (DIFC), University of Palermo, Palermo, Italy, [10]Advanced Technologies Network (ATeN) Center, University of Palermo, Palermo, Italy, [11]National Institute of Nuclear Physics (INFN), Section of Catania, Catania, Italy, [12]SIT Sordina IORT Technologies, Aprilia (LT), Italy, [13]Azienda Ospedaliero Universitaria Pisana, U. O. Radioterapia Universitaria, Pisa, Italy, [14]National Institute of Nuclear Physics (INFN), Laboratori Nazionali Del SUD (LNS), Catania, Italy

The FLASH effect is a radiobiological phenomenon that has garnered considerable interest in the clinical field. Pre-clinical experimental studies have highlighted its potential to reduce side effects on healthy tissues while maintaining isoeffectiveness on tumor tissues, thus widening the therapeutic window and enhancing the effectiveness of radiotherapy. The FLASH effect is achieved through the administration of the complete therapeutic radiation dose within a brief time frame, shorter than 200 milliseconds, and, therefore, utilizing remarkably high average dose rates above at least 40 Gy/s. Despite its potential in radiotherapy, the radiobiological mechanisms governing this effect and its quantitative relationship with temporal parameters of the radiation beam, such as dose-rate, dose-per-pulse, and average dose-rate within the pulse, remain inadequately elucidated. A more profound comprehension of these underlying mechanisms is imperative to optimize the clinical application and translation of the FLASH effect into routine practice. Due to the aforementioned factors, the undertaking of quantitative radiobiological investigations becomes imperative, necessitating the utilization of sophisticated and adaptable apparatus capable of generating radiation beams with exceedingly high dose-rates and dose-per-pulse characteristics. This study presents a comprehensive account of the design and operational capabilities of a Linear Accelerator (LINAC) explicitly tailored for FLASH radiotherapy research

10.3389/fphy.2023.1268310

purposes. Termed the "ElectronFlash" (EF) LINAC, this specialized system employs a low-energy configuration (7 and 9 MeV) and incorporates a triode gun. The EF LINAC is currently operational at the Centro Pisano FLASH Radiotherapy (CPFR) facility located in Pisa, Italy. Lastly, this study presents specific instances exemplifying the LINAC's adaptability, enabling the execution of hitherto unprecedented experiments. By enabling independent variations of the temporal parameters of the radiation beam implicated in the FLASH effect, these experiments facilitate the acquisition of quantitative data concerning the effect's dependence on these specific parameters. This novel approach hopefully contributes to a more comprehensive understanding of the FLASH effect, shedding light on its intricate radiobiological behavior and offering valuable insights for optimizing its clinical implementation.

KEYWORDS

**FLASH radiotherapy, ultra-high-dose-per-pulse beams, temporal structure of the beam, LINAC architecture, FLASH research LINAC**

# 1 Introduction

FLASH Radiotherapy (FLASH-RT) is a promising radiotherapy technique that involves delivering the entire radiation dose at an extremely high dose rate, much higher than conventional methods. The technique has been tested in various preclinical experiments using different animals and organs, and results have shown a significant reduction in side effects on healthy tissues while preserving its therapeutic efficacy on tumor tissue. This has generated considerable excitement in the radiotherapy community as FLASH-RT may provide a way to effectively treat tumors that are currently non efficiently treated with conventional radiotherapy [1–7]; in particular:

1. Radioresistant tumors located in close proximity to radiosensitive "serial" organs: it is hypothesized that a higher RT dose could be delivered to the tumor without inducing severe toxicities to the surrounding normal tissues as would be expected following CONV-RT.
2. Large tumors arising in "parallel" organs: the delivery of tumoricidal RT dose is hampered by the size and local extension of tumor mass that would lead to a low-dose irradiation of a significant portion of organ at risk with a subsequent unacceptable risk of severe toxicity.
3. Reirradiation: tumor recurrence often occurs within a previously irradiated high-dose region. This means that the dose required for tumor control is often much higher than that required for severe toxicity leading to an inverted relationship between NTCP and TCP curves.

Despite the very promising results, there are still many unanswered questions regarding the FLASH radiobiological mechanisms: there is still no consensus on its physical mechanism [8,9], and both its dependence on the various beam parameters and the effect on the irradiated tissues remain to be fully understood. One of the biggest challenges has been obtaining quantitative radiobiological data from *in vitro*/vivo experiments, which is essential to understanding the FLASH effect's dependencies on the different beam parameters.

Currently, there are two conditions which seems to trigger the FLASH effect: average dose rate greater than 40 Gy/s and a total irradiation time less than 0.2 s [10–15]. Nevertheless, the beam temporal structure is quite complex, and these two parameters are not enough to fully describe it. An exhaustive representation of the temporal structure is reported in Figure 1: Where

- $d_{MAX}$ depth of maximum dose on beam axis
- $D_p^{(n),k}$ dose of *n*th pulse in the *k*th irradiation at $D_{MAX}$ [Gy]
- $t_p^k$ time width of a single pulse in the *k*th irradiation [s]
- $t_r^k$ time between two pulses in the *k*th irradiation [s]
- $PRF^k$ Pulse Repetition Frequency in the *k*th irradiation [$s^{-1}$]
- $n_{p,k}$ Number of pulses of the *k*th irradiation
- $t_{FL}^k$ irradiation time of the *k*th irradiation [s]
- $t_D^k$ time separation between the end *k*th and the beginning of (k+1)th irradiations [s]
- $TD^k$ total delivered dose at $d_{MAX}$ during $t_{FL}^k$ [Gy]
- $t_{IRR}$ Total irradiation time [s]
- TD total delivered dose at$dD_{MAX}$ during $t_{IRR}$ [Gy]
- $ADR^k$ Average Dose Rate during the *k*th irradiation at $d_{MAX}$ [Gy $s^{-1}$]
- $ADR_p^{i,k}$ Average Dose rate within the *i*th pulse during the *k*th irradiation at $d_{MAX}$ [Gy $s^{-1}$]
- $IDR^{i,k}$ Instantaneous Dose Rate within the *i*th pulse during the *k*th irradiation at $d_{MAX}$ [Gy $s^{-1}$]

In case of a single irradiation, the following relations hold:

$$PRF = \frac{1}{t_r}\left[s^{-1}\right] \tag{1}$$

$$t_{Fl} = \frac{n_p - 1}{PRF} + t_p \cong \frac{n_p - 1}{PRF}\ [s] \tag{2}$$

$$TD = \sum_{i=1}^{n_p} D_p^i = n_p \cdot \overline{D_p}, where \overline{D_p} = \frac{1}{n_p}\sum_{i=1}^{n_p} D_p^i [Gy] \tag{3}$$

$$ADR = \frac{TD}{t_{FL}} = \frac{1}{t_{FL}}\sum_{i=1}^{n_p} D_p^i \cong PRF \cdot \overline{D_p}\left[\frac{Gy}{s}\right] \tag{4}$$

$$ADR_p = \frac{D_p}{t_p}; ADR_p = \frac{t_r}{t_p} ADR\left[\frac{Gy}{s}\right] \tag{5}$$

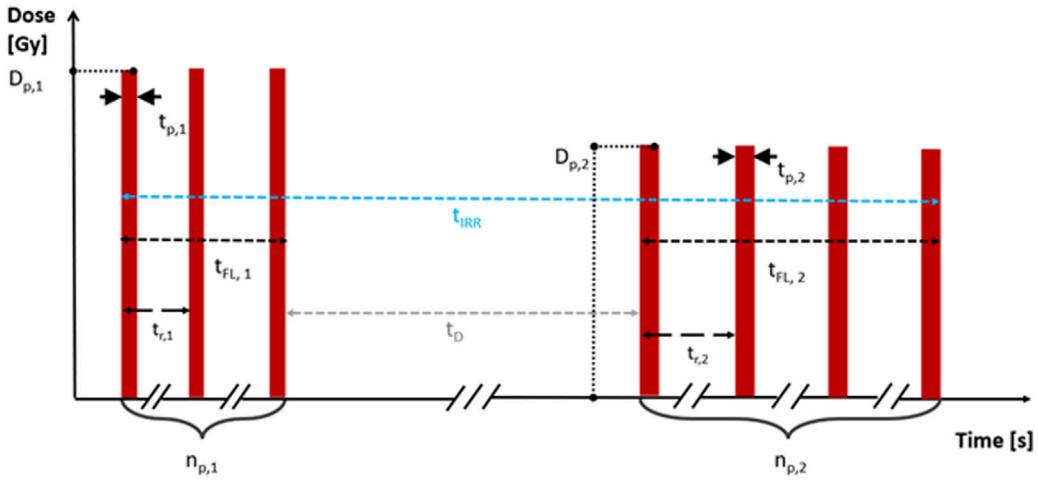


FIGURE 1
Temporal beam structure with all the relevant parameters.

$$D_p = \int_0^{t_p} IDR(t)dt\,[\mathrm{Gy}] \tag{6}$$

If the irradiation consists of multiple sub-irradiations, the previous equations can be easily generalized and the additional relations hold:

$$t_{IRR} = {t_{FL}}^1 + {t_D}^1 + \ldots + {t_D}^{N-1} + {t_{FL}}^N\ [\mathrm{s}] \tag{7}$$

$$TD = \sum_{i=1}^{N} TD^i\ [\mathrm{Gy}] \tag{8}$$

with N being the total number of irradiations. It was chosen to start from the definition of dose per pulse and pulse duration (instead of introducing the dose rate directly) because these two parameters can be measured precisely and independently from each other.

Additionally, if the dose is delivered with two or more train of pulses, also the time lapse between the trains of pulses may play a relevant role. Until now, due the technological limits of the electron LINACs available, no detailed study on the impact of the different parameters is available; nevertheless, there is a large consensus about the need of such investigations, both for electrons and protons [16–22].

FLASH research until today has been substantially slowed by the absence of a specifically designed technological platform, both in terms of beam sources and in terms of beam monitoring systems and dosimeters [23–25]. More specifically, the electron accelerators adopted for FLASH radiobiological experiments are not provided with real-time monitoring of beam parameters, which makes it impossible to take output variation into account. These accelerators are typically electron accelerators designed for industrial use or modified medical accelerators, where diffuser filters and monitor chambers have been removed from the beam path [26]. This fact has somehow limited the researchers' ability to obtain accurate and fully reproducible data on the radiobiological impact of the various beam time structure parameters potentially impacting FLASH effect.

Although the FLASH effect's robustness has been validated by various animal models, organs, and radiobiology research works, the radiobiological mechanism underlying the effect is still unknown. While oxygen consumption has been proposed as a possible explanation [27], other works have highlighted the limits of this explanation and emphasized the need for further investigations [28]. Additionally, the dependence of the FLASH effect on the Linear Energy Transfer (LET) of the radiation used is still unknown.

A better understanding of the complexity of FLASH effect is also mandatory for the VHEE development and its clinical translation.

VHEE would allow to treat even deep-seated tumors. Different national and international research projects are aimed at the realization of Very-High-Energy-Electrons "FLASH" LINAC, with energy up to or greater than 100 MeV. However, this raises new radiobiological questions: such high energy electron beams cannot be collimated mechanically yet, like the low energy ones, but the dose to the target volume is deposited uniformly employing pencil beam scanning technique, requiring to use more fields of view to reach the desired dose conformation. It is therefore essential, before the clinical translation, to quantify any dependence of the entity of the FLASH effect on the beam volume (dimension of the beam) and on the dose fractionation, since the movement of the gantry to pass from one field of view to another is not temporally compatible with the times need to trigger the FLASH effect (<0.1–0.2 s).

In summary, while FLASH-RT has shown promising results, there are still many uncertainties and many issues that need to be addressed before it can be used in clinical practice. Further research is necessary to determine the radiobiological mechanism underlying the FLASH effect and to investigate the dependence of the effect on various beam parameters on the irradiated tissues. Advances in accelerator technology and dosimetry may provide a way to overcome the current limitations and enable researchers to obtain quantitative radiobiological data from *in vitro*/vivo experiments.

A specifically designed LINAC would represent a powerful tool for understanding the mechanism and exploiting the promising radiobiological findings associated with the FLASH effect. Such LINAC should provide the full capability to vary, set and monitor the whole temporal beam structure, as reported in [29]. The discussion between some of the authors of this article, led to the

development of the new design of Electron Flash with a triode e-gun and its power and piloting electronics. The availability of a triode gun enables to adjust the electron fluence (and thus the dose per pulse) in a wide range maintaining the time pulse width and beam optics unchanged.

Such LINAC allows the study of the whole set of beam parameters which could impact FLASH effect: dose per pulse, pulse width, pulse repetition frequency, number of pulses, irradiation time and consequently Average and instantaneous dose rate. All these parameters can be varied independently and without altering the experimental setup, thereby minimizing experimental errors.

Thanks to special funding from Fondazione Pisa, the newly designed system has been installed in July 2022, at the Centro Pisano FLASH Radiotherapy (CPFR) in Pisa, Italy.

# 2 Materials and methods

## 2.1 Characteristics of the research LINAC system

The research LINAC described in the study is the ElectronFlash (indicated as EF in the following) produced by SIT S.p.A. (https://www.soiort.com/flash-rt-technology/[29,30]). and installed in Pisa A.O.U.P., S. Chiara Hospital.

Even though EF is a research LINAC, it has been designed in order to comply with the requirements of IEC 60601-two to one, Medical electrical equipment - Part 2–1: Particular requirements for the basic safety and essential performance of electron accelerators in the range 1 MeV–50 MeV [31]. Furthermore, as long as FLASH treatment requires even additional monitoring in order to guarantee the essential performance, novel monitoring techniques have been devised and integrated [29].

The system operates in electron mode only, with energies of 7 and 9 MeV; e-beam is collimated by means of a purely passive beam optics and several radiation fields are available (see Results section).

The accelerating waveguide is a S band standing wave accelerating guide, operating at 2.998 GHz in the $\pi/2$ mode; the electrostatic radial focusing technique is implemented, in order to avoid the use external solenoid. Such implementation guarantees the stability over time of radial beam dynamics, and therefore also beam symmetry and flatness.

The LINAC features a triode thermionic e-gun composed of an indirectly heated cathode, a control grid, and an anode. The e-gun generates an electron current in a temporal range variable from 0.2 to 4 μs with a peak accelerated current ranging from 1 up to 100 mA, which is adjustable using by means of the grid voltage. The LINAC is powered by an S-band magnetron (model MG6090 produced by E2V) delivering up to 3.1 MW. It is powered by a Solid-State Modulator (model M100 produced by Scandinova).

Beam collimation is achieved through a purely passive scattering system, and the beam is conformed into different fields thanks to different applicators, ranging from diameter 1 cm up to 12 cm.

EF is equipped with a real "dose monitoring system", as defined in IEC 60601-2-1, § 201.3.212 [31]: "system of devices for the measurement and display of a radiation quantity directly related to the absorbed dose".

The dose monitoring system comprises several components, each fulfilling a crucial role in signal processing. The initial stage involves the precise and linear measurement of beam current. This is accomplished using two independent Beam Current Transformers (referred to as ACCTs), designed and manufactured by Bergoz Instrumentation [32]. Previous research has demonstrated the effectiveness of this system in accurately estimating absorbed dose [33,34]. Although alternative devices have been explored [35], ACCTs now function as non-invasive sensors, safeguarding the integrity of the beam and ensuring consistent measurement precision and linearity in both conventional and UHDR modes.

Subsequently, the current waveform is digitized to facilitate charge calculation through integration. Lastly, this computed charge is converted into Monitor Units, normalized as desired by the final user. These Monitor Units are then displayed on the user interface and utilized for treatment control purposes.

ACCT are currently considered as an optimal solution for the beam monitoring in UHDR modality [25,29,36,37], it is however important to stress that a dose monitoring system is much more than the radiation detectors itself: it is a system at least capable of:

- transforming the measurement of the single pulse into a quantity proportional to the absorbed dose ([31] § 201.10.101.1.1.2) and properly visualizing such quantity in terms of MU ([31]§ 201.10.101.1.1.2);
- halting the irradiation when the programmed MU have been delivered ([31] § 201.10.101.1.1.5);
- halting the irradiation if anomalies occur in the monitoring process and/or a given threshold is trespassed [31] (§ 201.10.101.1.3 and [31] § 201.10.101.1.3).

Monitoring system reading can be normalized as desired by the final user. All such features have been implemented in EF. The monitoring system performances (linearity, long and short-term stability) are described in the Results section. A schematic of the beam optic, including the ACCT, is reported in Figure 2.

Two screenshots reporting the monitoring system interface are presented in Figure 3. The reading of both channels for each pulse, the integral dose delivered and the temporal structure of the beam is clearly visible; in the left image an irradiation stopped by the MU limit is reported (500 MU limit set, 2 pulses lasting 4.5 μs, PRF 200 Hz, total irradiation time ≈5 m and total MU1 delivered 530) while in the right one an irradiation stopped by the number of pulses is reported (10 pulses at 200 Hz, each lasting 2.5 μs, PRF 200 Hz, total irradiation time ≈45 m).

EF can also deliver two different trains of pulses, with a time interval between the two trains in the range 0.05 s–60 s. Such feature allows the delivery of two irradiation separated by a time interval, and it is provided in order to study the possibility such dose delivery modality could enhance Flash effect.

EF is designed in a way that the user can vary independently each parameter of the beam temporal structure; notably it allows, by opportunely varying the beam current, to deliver the same dose per pulse even when varying the time width of the pulse in a large range.

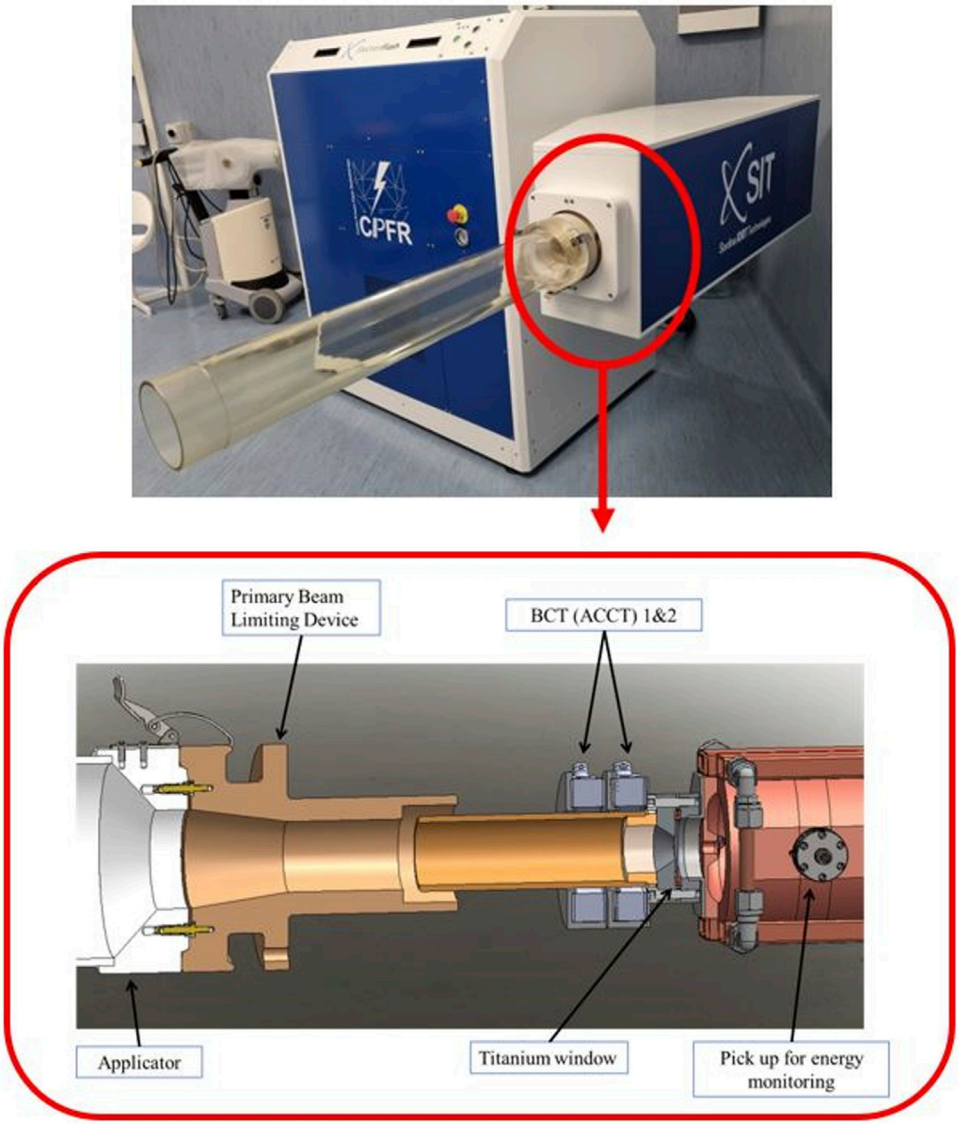


FIGURE 2
Schematic of the beam optic including ACCT.

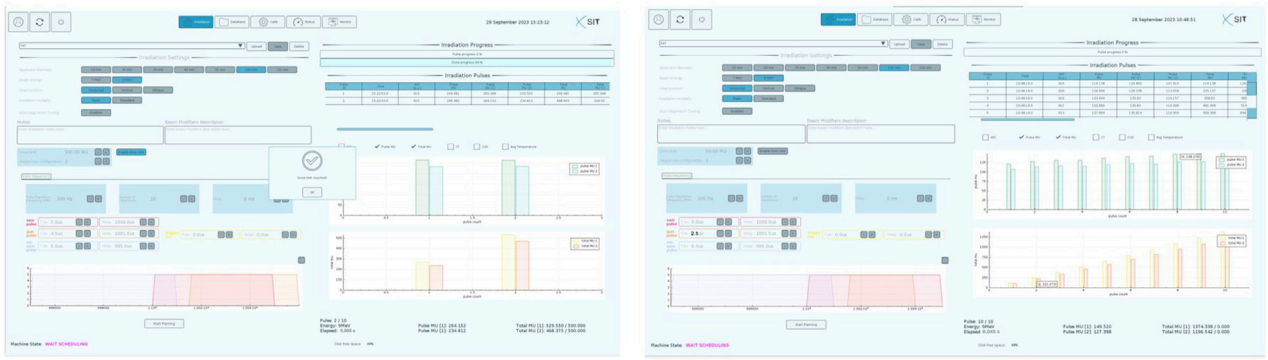

FIGURE 3
System interface of the EF LINAC.

**TABLE 1 Definition of parameters used to characterize the system.**

| PDD | | |
|---|---|---|
| Parameter | Abbreviation | Definition |
| Depth of dose max | R100 [mm] | Depth corresponding to the maximum dose |
| Depth of 90% of dose value | R90 [mm] | Depth corresponding to the 90% of the maximum dose |
| Depth of 50% of dose value | R50 [mm] | Depth corresponding to the 50% of the maximum dose |
| Practical range | Rp [mm] | The depth at which the tangent plotted through the steepest section of the PDD curve intersects with the extrapolation line of the bremsstrahlung background |
| Flatness | Flat [%] | Max. variation $(D_{max}—D_{min})/2$ within the flattened region |
| Symmetry | Sym [%] | Maximum dose ratio $(D(x)/D(-x))_{max}$ * 100% within the flattened region |
| Most probable energy at the phantom surface | Ep0 [MeV] | $0.22 + 1.98R_p + 0.0025R_p^2$ |

The ElectronFlash can therefore adjust its average dose-per-pulse, average dose rate and its average instantaneous dose rate. This is achieved by modifying various parameters such as:

- the E-gun peak current, which leads to an accelerated current between 1 and 100 mA;
- E-gun pulse duration, which can be set between 0.2 μs and 4 μs;
- Pulse Repetition Frequency (PRF), which can be set between 1 Hz and 250 Hz with 1 Hz increments. Higher PRF are achievable, up to 400 Hz, but with a shorter radiofrequency pulse duration down to 2.5 μs instead of the standard 5 μs?

Electron beam is collimated into the target by means of PMMA cylindrical tubes, called applicators. These applicators determine the uniform field dimensions and establish an upper limit on the achievable dose per pulse by modulating the incident electron spectrum and fluence. Since the beam collimation is entirely passive, its performance remains constant over time. Consequently, real-time monitoring is not necessary for ensuring beam flatness, as the uniformity of the dose distribution at a specific depth is primarily influenced by the multiple scattering of electrons with the collimator wall.

## 2.2 LINAC dosimetric characterization

The dosimetric characterization of a LINAC with the illustrated characteristics pose a challenge for commercial dosimetric devices due to very high charge density generated by dose per pulse, which is three orders of magnitude greater than in conventional radiotherapy LINACs [29]. Corrective methods are not sufficient to use standard detectors for the absolute dosimetry needed for commissioning the ElectronFlash [38]. Several FLASH dedicated dosimeters are currently being developed and tested, mainly ionization chambers [22,39] and semiconductor detectors [40,41]. In this study, we used a PTW flashDiamond as the active dosimeter for both relative and absolute dosimetry. The linearity of the employed dosimeter was tested up to 18 Gy per pulse with a graphite calorimeter [42] and alanine pellets.

Additionally, we used EBT-XD Gafchromic films [43] to measure the beam profiles given their high spatial resolutions. Prior to use, we calibrated the EBT-XD films in a plastic phantom by delivering doses ranging from 0.5 to 60 Gy. The dose was delivered with a $D_p$ of approximately 0.02 Gy, a pulse duration $t_p$ of 4 μs, and a PRF of 1 Hz. The total dose delivered was measured using an Advanced Markus ionization chamber connected to a PTW UNIDOS electrometer with a +400 V polarization. The chamber was able to correctly operate with the standard two voltage saturation correction at the polarization and dose per pulse employed. The dose values were obtained following the standard dosimetry protocol for absolute dosimetry in water TRS-398 [44], with a correction factor for the use of a plastic phantom. After a 48-h waiting period, all the films were scanned using an Epson Expression 10000XL scanner and the netOD values were converted to dose values via the calibration curves [45].

We started the dosimetric characterization by performing relative dosimetry measurements, which involved acquiring percentage depth dose (PDD) curves and lateral beam profiles. We obtained these measurements using different applicators, and also carried out measurements without any applicator, directly at the head hosing exit. The measurements were taken for both energies and three (low, mid, high) selected beam current values ((4, 60, 100 mA for 9 MeV; (15, 51, 85 mA) for 7 MeV).

To obtain the PDD curves, we measured the absorbed dose to water using the flashDiamond detector positioned in a modified MP3-XS water phantom that was adapted for horizontal irradiation by cutting a hole in one of the vertical sides and replacing it with a 1 mm thick water-tight carbon window.

The dose was delivered as train of 4μs pulses with 5 Hz PRF and evaluated moving, every 10 s, the flashDiamond detector in increments of 1 mm in the buildup region and 2 mm thereafter. Starting from the PDDs curves data, we evaluated the invariance of the R100, R90, R50 and $R_p$ parameters (see Table 1 for definitions) for each energy, applicator, and beam current combination.

To measure the beam profiles, we positioned gafchromic films between slabs of RW3 plastic phantom at a depth equivalent to the R100. The films were irradiated with the same dose, and we evaluated the beam flatness, symmetry, and the width at the 95% isodose.

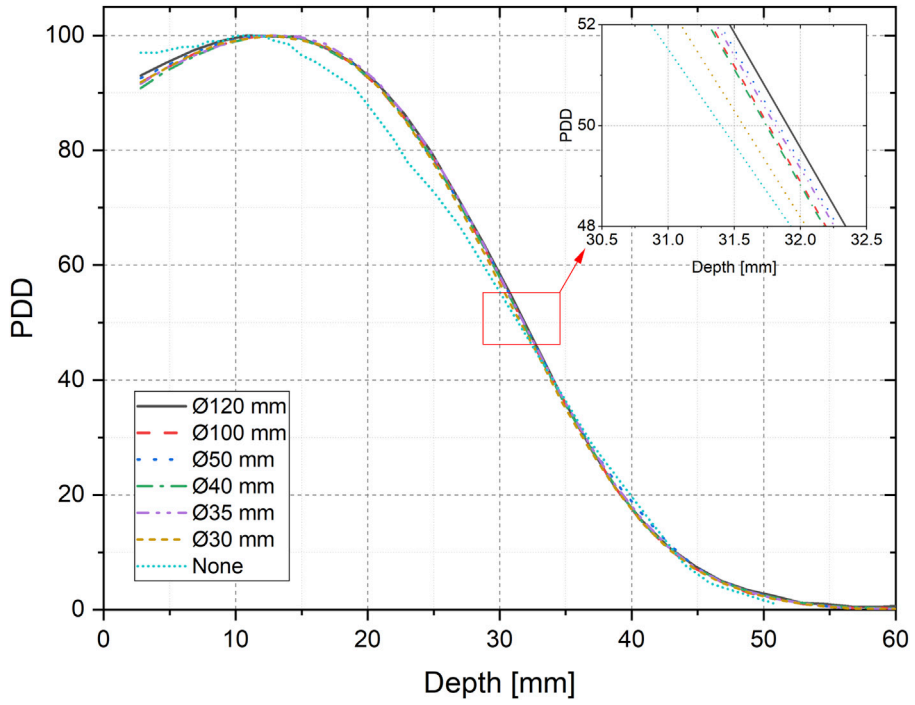


FIGURE 4
9 MeV PDDs for various applicators.

**TABLE 2 PDD characteristics for the 9 MeV beam for different applicators.**

| Applicator internal diameter [mm] | $R_{100}$ [mm] | $R_{90}$ [mm] | $R_{50}$ [mm] | $R_p$ [mm] |
|---|---|---|---|---|
| 30–120 | 13.0 ± 0.5 | 21.0 ± 0.5 | 31.8 ± 0.2 | 42.0 ± 1 |
| Uncollimated | 10.8 | 18.8 | 31.4 | 43.2 |

For absolute dose measurements, we irradiated the flashDiamond at the $d_{MAX}$ depth in a water phantom using 4 μs pulses and a PRF of 5 Hz. The dose per pulse for each irradiation combination was calculated by dividing the total dose by the number of delivered pulses. To ensure sufficient statistical accuracy, we delivered a minimum of 20 pulses for the highest beam current and 200 pulses for the lowest beam current. From this data, we determined the maximum $ADR_p$ for each irradiation condition.

We then assessed the linearity of the total dose with respect to the number of pulses. This was done by delivering a different number of pulses, ranging from 1 to 60, and measuring the total dose delivered. The procedure was repeated 5 times to estimate the output variability.

Next, we evaluated the variation in LINAC output with respect to the PRF in the range of 1–245 Hz while delivering a fixed number of pulses at 9 MeV and a beam current of 60 mA. Additionally, we measured the achievable dose rate ranges by measuring the dose at PRF values of 1 Hz and 245 Hz for each beam current.

To characterize the temporal properties of the pulse, we investigated the dose dependence with respect to the pulse width for the 9 MeV beam. We measured the reproducibility of the pulse width using the signal obtained from the ACCT current transformer. This involved delivering 20 pulses and measuring the resulting pulse duration. We then varied the pulse width from approximately 4 μs–0.38 μs while recording the dose with the flashDiamond for three consecutive pulses.

# 3 Results

## 3.1 Customer Acceptance Test measurements

To evaluate the performance of the LINAC system, a set of procedures was developed in accordance with the Customer Acceptance Test (CAT). These procedures were categorized into two groups: beam properties and beam output.

For the beam properties evaluation, PDD curves were measured for both available energies (7 and 9 MeV) and for three different current values (low, medium, high) using the 40 mm diameter applicator. The PDDs were analysed to measure values such as, $R_{100}$, $R_{90}$, $R_{50}$ and $R_p$ as defined in Table 1. The stability of the LINAC was assessed over 3 days by checking the $R_{50}$ values, which were required to be within a 1 mm tolerance using the 40 mm applicator. Furthermore, measurements of PDD

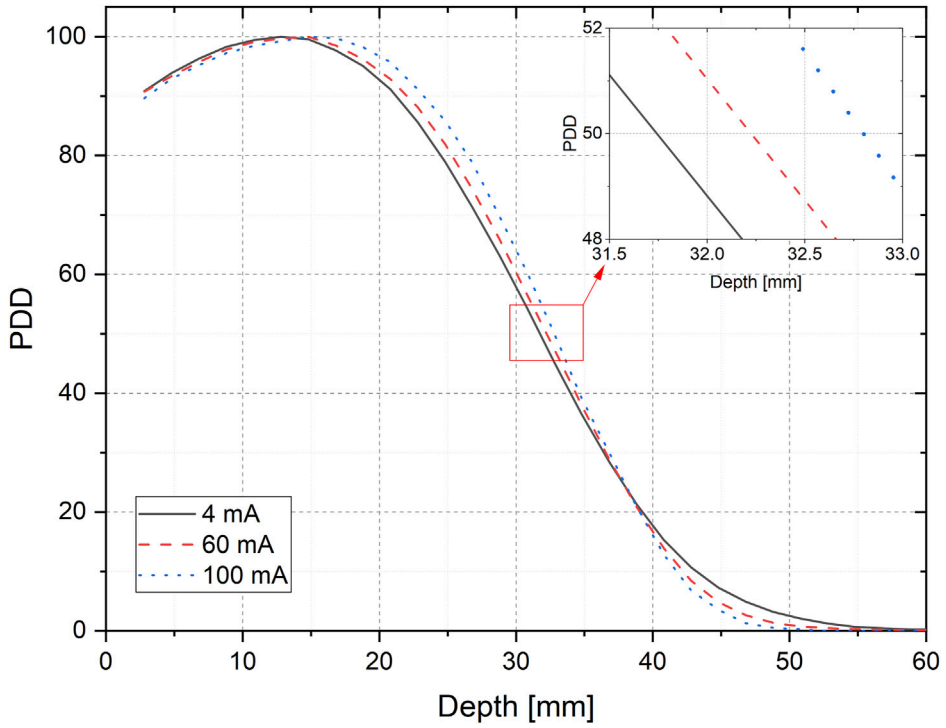


FIGURE 5
9 MeV PDDs for different beam currents.

**TABLE 3 PDD characteristics for the 9 MeV beam for different beam currents.**

| Beam current [mA] | $R_{100}$ [mm] | $R_{90}$ [mm] | $R_{50}$ [mm] | $R_p$ [mm] |
|---|---|---|---|---|
| 4 | 12.9 | 20.8 | 31.5 | 42.7 |
| 60 | 14.5 | 21.8 | 32.2 | 42.9 |
| 100 | 15 | 23.2 | 32.8 | 42.2 |

were conducted using different applicators to verify the position of $R_{50}$ and, consequently, the stability of PDD among the different fields. The beam profiles were also evaluated by measuring flatness symmetry and 95% isodose width for all available applicators.

Regarding the beam output, measurements were performed with both energies (7 and 9 MeV) and for 2 dose-per-pulses (high and low), setting the flashDiamond at the $R_{100}$ and using the 40 mm applicator. The short-term stability of the LINAC system (i.e., the stability of charge collected in 10 consecutive irradiations) and the long-term stability (i.e., stability of the ratio between collected charge and the registered MU over a period of 3 days) were checked to be within tolerance (2% and 5%, respectively).

The proportionality between the output and the pulse duration (from 0.5 up to 4 μs) and the linearity between the output and the number of pulses were also evaluated. The linearity between the output and the registered MU was checked. This was performed with a 100 mm applicator after MU calibration (at the value 1 cGy/MU at the build-up region) for the same applicator. The proportionality ratio between the output and PRF, ranging from 5 to 245 Hz, was also checked by measuring the standard deviation of the charge collected for the same number of pulses delivered with different PRF. A summary table indicating the boundary tolerance for each measurement is provided in the Supplementary Materials.

## 3.2 LINAC flexibility and performance

The percentage depth dose curves obtained at 9 MeV with a fixed beam current of 4 mA for all available applicators are shown in Figure 4. The beam parameters and the maximum measured variation are listed in Table 2, with the uncollimated beam data reported separately. It is worth noting that all PDD curves, except for the uncollimated beam, exhibit a semi-flat region of approximately 10 mm for the 97% isodose, allowing for flexibility in the placement of devices or specimen. The impact of the different applicators on the PDD can be deemed relatively insignificant.

Figure 5 displays the variation of the 9 MeV PDD curves in response to changes in the beam current, while Table 3 provides a summary of their characteristics: in particular it can be observed

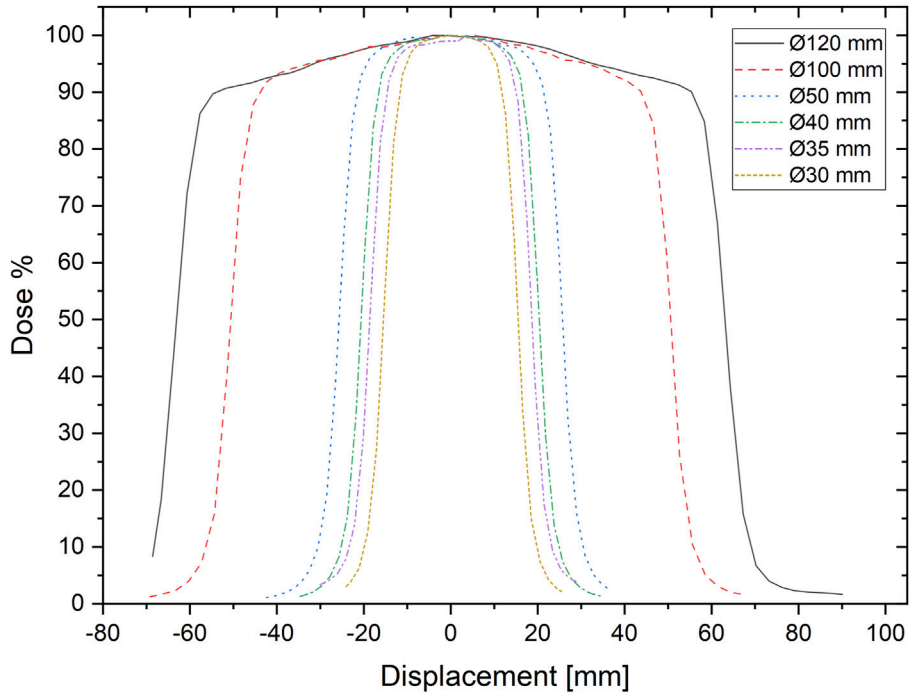


FIGURE 6
Beam profiles for all the applicators.

**TABLE 4 Profile data for various applicators.**

| Applicator diameter [mm] | Flatness [%] | Symmetry [%] | Diameter of 95% isodose [mm] |
|---|---|---|---|
| 120 | 4.65 | 1.49 | 70 |
| 100 | 4.03 | 1.02 | 60 |
| 50 | 3.79 | 0.69 | 36 |
| 40 | 5.02 | 1.25 | 30 |
| 35 | 5.97 | 2.05 | 26 |
| 30 | 7.20 | 1.50 | 20 |

that therrent, the maximum variation observed in the $R_{50}$ parameter is less than 1 mm. The differences in PDDs resulting from changes in the beam current are not critical when positioning samples at the $R_{100}$, thanks to a fairly large zone of uniformity of the dose around the depth of maximum dose ($d_{max}$) observed in all three PDDs.

The results of the analogous studies with the 7 MeV beam are reported in the Supplementary Materials.

The beam profiles obtained at $R_{100}$ with 9 MeV energy for all applicators are displayed in Figure 6, normalized to the maximum dose. Table 4 presents the corresponding Flatness, Symmetry, and the diameter of the 95% isodose for each profile. Additionally, Figure 7 depicts the gaussian profile for the uncollimated beam. Notably, the 120 mm and 100 mm applicators exhibit a sufficiently large useful field, making them suitable for accommodating various sizes of cell culture multiwell plates, thereby facilitating *in vitro* experiments. The smaller applicators are more suitable for irradiating individual dishes with more extreme irradiation parameters.

The linearity of the dose with respect to the number of delivered pulses was verified through a linear fit ($y = 0.877x$, $R^2 = 0.999$). These measurements also revealed a pulse variability of less than 2%, which can be corrected by the ACCT reading.

The investigation of the LINAC output dependence on different PRF, as shown in Figure 8, resulted in a variation of less than ±1.5% relative to the average value measured when scanning various PRF. This variation was adjusted for the beam output variability monitored by the ACCT.

The effect of pulse width on the dose per pulse was studied by measuring the effective pulse duration, determined as the full width at half maximum (FWHM) of the ACCT signal recorded using an oscilloscope. Figure 9 shows different pulse waveforms along with their corresponding effective durations. The measurements demonstrated high reproducibility, with relative differences of

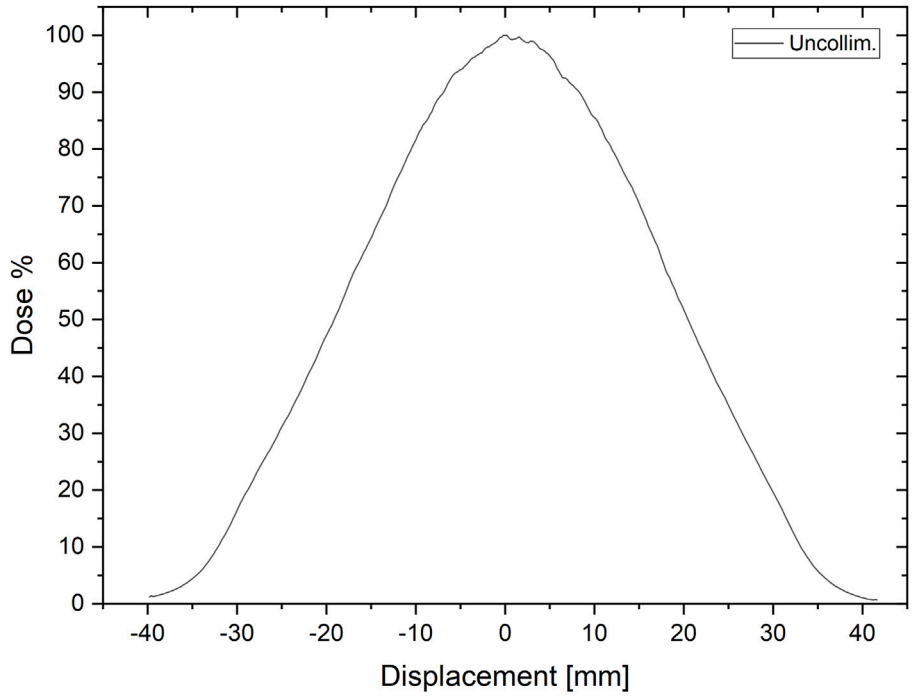


FIGURE 7
Beam profile for the uncollimated beam.

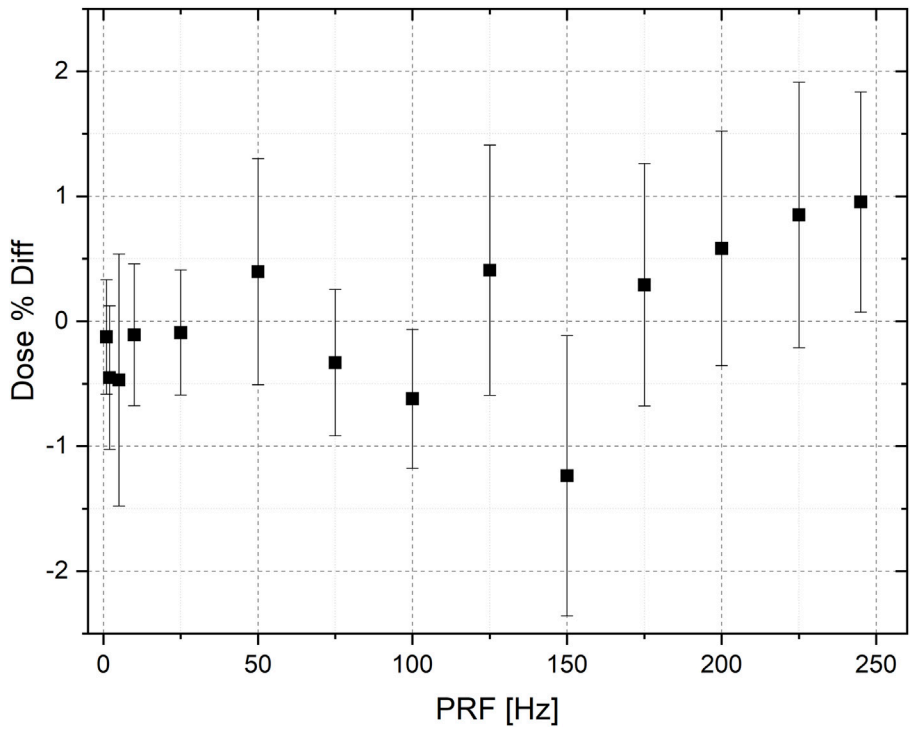


FIGURE 8
Relative differences from the mean dose value of dose measured at different PRFs.

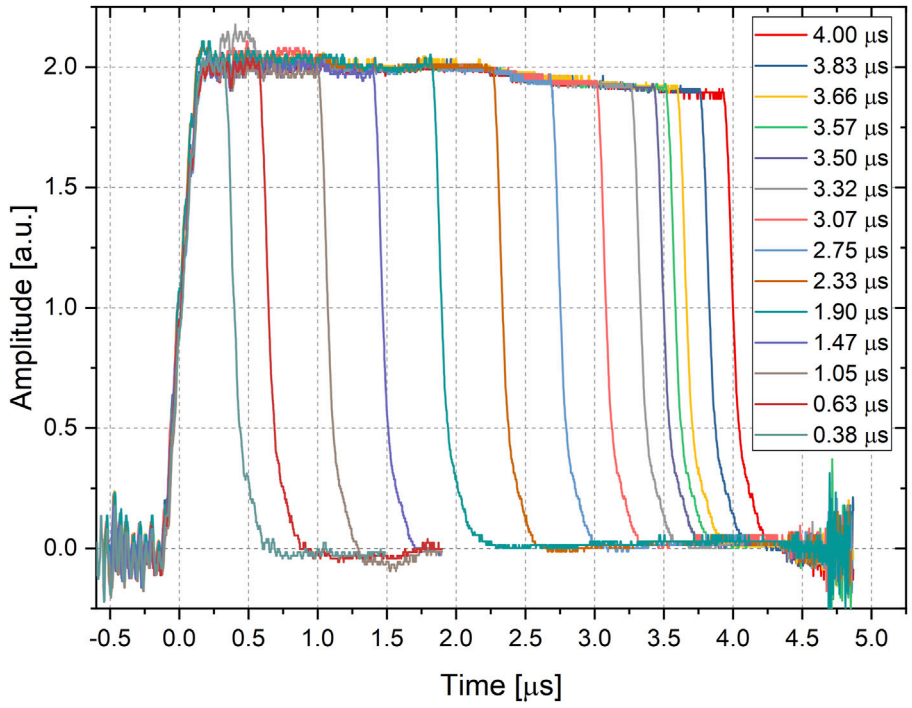


FIGURE 9
Pulse waveform for different pulse duration.

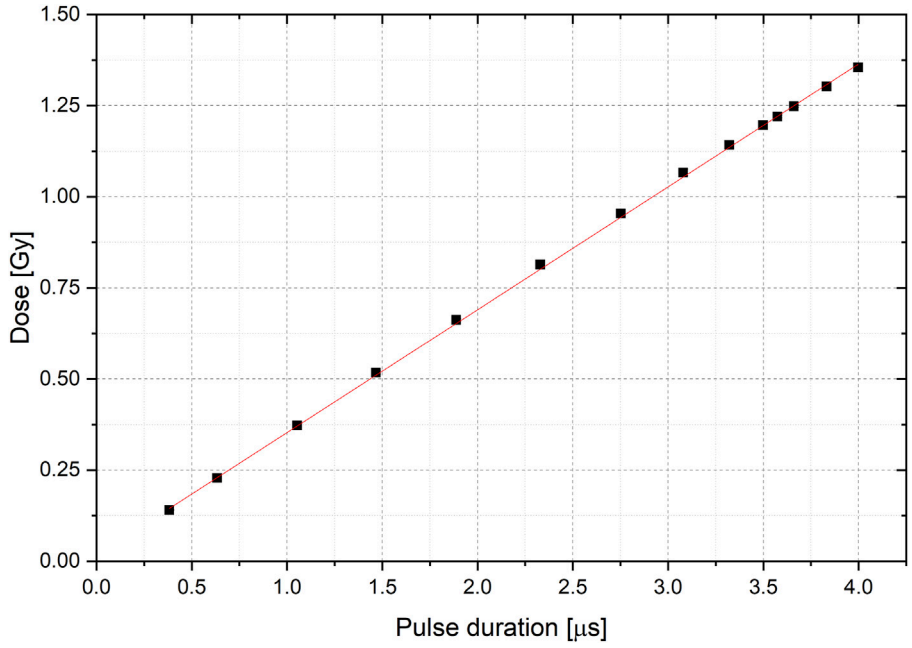


FIGURE 10
Linear fit (red) to the Dose value with respect of the pulse duration. Errorbars are on the order of graph point size.

less than 0.3% observed for the same pulse duration setting. To analyze the relationship between pulse width and dose, a linear regression was performed on the dose values associated with each pulse width, as shown in Figure 10. The results revealed a clear linear trend with a slope of 0.343 and an excellent goodness of fit ($R^2$ = 0.999).

Additionally, we calculated the ranges of irradiation parameters available at $R_{100}$ for each applicator and the maximum pulse

**TABLE 5 Irradiation parameters available at R100. The interval extremes are reported for all but the 100 mm applicator diameter where all the available dose per pulses are listed.**

| Applicator diameter [mm] | Normalized average dose rate ADRN [Gy/s] | Dose per pulse [Gy] | Average dose rate within the pulse [kGy/s] |
|---|---|---|---|
| 120 | [0.023, 330] | [0.023, 1.36] | [5.8, 340] |
| 100 | [0.035, 500] | 0.035, 0.069, 0.36, 0.54, 0.85, 1.16, 1.42, 1.66, 1.85, 2.05 | [8.8, 513] |
| 50 | [0.097, 1390] | [0.097, 5.67] | [24.2, 1418] |
| 40 | [0.116, 1660] | [0.116, 6.79] | [28.9, 1696] |
| 35 | [0.131, 1880] | [0.131, 7.67] | [32.7, 1918] |
| 30 | [0.132, 1900] | [0.132, 7.75] | [33.1, 1937] |
| Uncollimated | [0.33, 4890] | [0.33, 19.95] | [82.5, 4988] |

duration using the collected data. These ranges are presented in Table 5, where the available dose per pulse values at 9 MeV are explicitly listed for the 100 mm applicator, while for the other applicators, only the minimum and maximum values are provided. Intermediate values can be obtained by scaling the values of the 100 mm applicator. Furthermore, since the ADR depends on the number of pulses, even when the PRF is fixed, in the table we normalized such dependency reporting the normalized $ADR_n$, obtained by dividing the ADR by n/(n-1), where n is the number of pulses.

## 3.3 Discussion

In this study, we described the unique architecture of the ElectronFlash, a triode gun electron LINAC specifically developed for investigating the FLASH effect. The dosimetric characterization of the ElectronFlash system was also described in detail. This LINAC allows independent control of three key beam parameters relevant to the FLASH effect: average dose rate, dose per pulse, and instantaneous dose rate. The flexibility to vary these parameters within a wide range, spanning from conventional radiotherapy values to extreme FLASH conditions, is a significant advantage. Importantly, these parameter changes can be achieved without modifying the experimental setup, reducing uncertainty in dosimetric and radiobiological experiments.

The ElectronFlash system is equipped with two dedicated ACCTs that enable online monitoring of output variability, allowing adjustments to account for small output variations, which have been measured to be below 2%. The availability of various applicators further enhances the versatility of the LINAC. Larger applicators enable simultaneous irradiation of multiple samples under FLASH conditions (>1 Gy per pulse) with a useful field diameter (>95%) of 70–60 mm. Smaller applicators can be used to gradually transition to extreme irradiation values at the cost of a reduced useful irradiation area. Additionally, the LINAC offers two nominal energies, 7 and 9 MeV, providing further flexibility in experimental setups.

Given the challenges of using commercial active dosimeters for FLASH irradiation, the dosimetric characterization was performed using a specially designed detector, the flashDiamond detector. The linearity of the flashDiamond detector was verified through measurements at 9 MeV using NPL's secondary standard calorimeter and alanine pellets, traceable to UK's primary standard electron and photon calorimeters, respectively. Calibrated EBT-XD gafchromic films were used to obtain beam profiles. The results confirmed that changes in applicators or beam current had negligible effects on the percentage depth dose (PDD) curves. Furthermore, the 9 MeV PDD curves exhibited a wide near-flat region near the maximum dose (97% isodose), allowing for flexibility in the types of specimens to be irradiated. The linearity of output with respect to the number of pulses, pulse duration, and independence on the pulse repetition frequency were also successfully verified.

Based on the dosimetric measurements, the maximum range of beam parameter excursions was determined: average dose rate ranging from ~2 cGy/s to ~4800 Gy/s, dose per pulse ranging from ~2 cGy to ~20 Gy, and average dose rate within the pulse ranging from ~5.8 kGy/s to ~4800 kGy/s.

To showcase the remarkable versatility of the ElectronFlash system, we propose three different irradiation setups that can be utilized to independently investigate the irradiation parameters. The first setup involves irradiating samples under FLASH conditions ($D_p$ > 1 Gy/pulse, ADR >100 Gy/s) with a fixed number of pulses. Subsequently, the experiment can be repeated under conventional irradiation conditions, delivering the exact same dose with a difference of less than 1%. This can be easily achieved by utilizing the lowest beam current settings, which allow precise delivery of very small doses. Additionally, the real-time monitoring provided by the ACCT system ensures accurate adjustment for any output variation. Furthermore, dose escalation experiments can be conducted by fixing the ADR and adjusting the pulse repetition frequency (PRF) accordingly, considering the ADR's dependency on the number of pulses, which is particularly relevant in high dose per pulse conditions such as FLASH. The second type of experiment, designed to test the ADR dependency, can be readily implemented by fixing the beam current, the number of pulses, and varying the PRF. With the availability of numerous beam currents, a wide range of ADR values can be explored while keeping the dose per pulse ($D_p$) and average dose rate within the pulse ($ADR_p$) constant. Lastly, by fixing the PRF and maintaining

a constant product of the beam current and pulse duration, a setup can be established where both the ADR and $D_p$ remain fixed while the $ADR_p$ varies.

Considering all the aforementioned features, the ElectronFlash system proves to be an ideal instrument for investigating the FLASH effect, providing extensive flexibility in experimental setups and allowing for precise control of irradiation parameters.

Establishing FLASH-RT as a viable clinical technique requires further research to determine the radiobiological mechanism underlying the FLASH effect and to investigate the dependence of the effect on various beam parameters and irradiated tissues. Advances in accelerator technology and dosimetry may provide a way to overcome the current limitations and enable researchers to obtain quantitative radiobiological data from *in vivo* experiments. The proposed design of a new research LINAC provides a promising avenue for further research into FLASH-RT, essential to study the response of dosimeters to UHDP beams, the quantitative dependence of the effect on the beam parameters and the mechanisms underlying the effect itself. All this is essential for the development of specific dosimetric protocols, to understand the optimal characteristics of clinical FLASH LINACs and, in general, to arrive at the optimal clinical implementation of the FLASH effect in the shortest possible time.

## Data availability statement

The raw data supporting the conclusion of this article will be made available by the authors, without undue reservation.

## Author contributions

FD: Writing–original draft, Writing–review and editing. DD: Writing–original draft, Writing–review and editing. GB: Writing–review and editing. SC: Writing–review and editing. MC: Writing–review and editing. DC: Writing–review and editing. AD: Writing–review and editing. MMari: Writing–review and editing. MMarr: Writing–review and editing. LM: Writing–review and editing. GM: Writing–review and editing. MMon: Writing–review and editing. FP: Writing–review and editing. JP: Writing–review and editing. LR: Writing–review and editing. FR: Writing–review and editing. AS: Writing–review and editing. ET: Writing–review and editing. GV: Writing–review and editing. GF: Writing–original draft, Writing–review and editing.

## Funding

The author(s) declare financial support was received for the research, authorship, and/or publication of this article. This work was funded by Piano Nazionale di Ripresa e Resilienza (PNRR), Missione 4, Componente 2, Ecosistemi dell'Innovazione–Tuscany Health Ecosystem (THE), Spoke 1 "Advanced Radiotherapies and Diagnostics in Oncology"—CUP I53C22000780001.

## Acknowledgments

The Authors would like to thank Ilaria D'Amico and Veronica De Liso for their experimental support. We also thank Fondazione Pisa for funding CPFR with the grant "prog. n. 134/2021"

## Conflict of interest

Author DC and ET were employed by Bergoz Instrumentation and LM, JP, and GF were employed by SIT Sordina IORT Technologies.

The remaining authors declare that the research was conducted in the absence of any commercial or financial relationships that could be construed as a potential conflict of interest.

## Publisher's note



## Supplementary material

The Supplementary Material for this article can be found online at: https://www.frontiersin.org/articles/10.3389/fphy.2023.1268310/full#supplementary-material

## References

1. Favaudon V, Caplier L, Monceau V, Pouzoulet F, Sayarath M, Fouillade C, et al. Ultrahigh dose-rate FLASH irradiation increases the differential response between normal and tumor tissue in mice. *Sci translational Med* (2014) 6(245):245ra93. doi:10.1126/scitranslmed.3008973

2. Montay-Gruel P, Acharya MM, Petersson K, Alikhani L, Yakkala C, Allen BD, et al. Long-term neurocognitive benefits of FLASH radiotherapy driven by reduced reactive oxygen species. *Proc Natl Acad Sci* (2019) 116(22):10943–51. doi:10.1073/pnas.1901777116

3. Vozenin M-C, De Fornel P, Petersson K, Favaudon V, Jaccard M, Germond JF, et al. The advantage of FLASH radiotherapy confirmed in mini-pig and cat-cancer patients. *Clin Cancer Res* (2019) 25(1):35–42. doi:10.1158/1078-0432.ccr-17-3375

4. Vozenin M-C, Hendry JH, Limoli CL. Biological benefits of ultra-high dose rate FLASH radiotherapy: sleeping beauty awoken. *Clin Oncol* (2019) 31(7):407–15. doi:10.1016/j.clon.2019.04.001

5. Friedl AA, Prise KM, Butterworth KT, Montay-Gruel P, Favaudon V. Radiobiology of the FLASH effect. *Med Phys* (2022) 49(3):1993–2013. doi:10.1002/mp.15184

6. Schüler E, Acharya M, Montay-Gruel P, Loo BW, Vozenin M, Maxim PG. Ultra-high dose rate electron beams and the FLASH effect: from preclinical evidence to a new radiotherapy paradigm. *Med Phys* (2022) 49(3):2082–95. doi:10.1002/mp.15442

7. Ursino S, Gadducci G, Giannini N, Gonnelli A, Fuentes T, Di Martino F, et al. New insights on clinical perspectives of FLASH radiotherapy: from low-to very high electron energy. *Front Oncol* (2023) 13:1254601. doi:10.3389/fonc.2023.1254601

8. Atkinson J, Bezak E, Le H, Kempson I. The current status of FLASH particle therapy: a systematic review. *Phys Eng Sci Med* (2023) 46:529–60. doi:10.1007/s13246-023-01266-z

9. Marcu LG, Bezak E, Peukert DD, Wilson P. Translational research in FLASH radiotherapy—from radiobiological mechanisms to *in vivo* results. *Biomedicines* (2021) 9(2):181. doi:10.3390/biomedicines9020181

10. Eggold JT, Chow S, Melemenidis S, Wang J, Natarajan S, Loo PE, et al. Abdominopelvic FLASH irradiation improves PD-1 immune checkpoint inhibition in preclinical models of ovarian cancer. *Mol Cancer Ther* (2022) 21(2):371–81. doi:10.1158/1535-7163.mct-21-0358

11. Liljedahl E, Konradsson E, Gustafsson E, Jonsson KF, Olofsson JK, Ceberg C, et al. Long-term anti-tumor effects following both conventional radiotherapy and FLASH in fully immunocompetent animals with glioblastoma. *Scientific Rep* (2022) 12(1):12285. doi:10.1038/s41598-022-16612-6

12. Levy K, Natarajan S, Wang J, Chow S, Eggold JT, Loo PE, et al. Abdominal FLASH irradiation reduces radiation-induced gastrointestinal toxicity for the treatment of ovarian cancer in mice. *Scientific Rep* (2020) 10(1):21600. doi:10.1038/s41598-020-78017-7

13. Del DEBBIOF, Bertilacchi MS, Gonnelli A, Da Pozzo E, Tozzini V, Martini C, et al. An insight into hypothesized biological mechanisms contributing to the Flash effect. *Front Phys* (2023) 11:396. doi:10.3389/fphy.2023.1201708

14. Limoli CL, Kramár EA, Almeida A, Petit B, Grilj V, Baulch JE, et al. The sparing effect of FLASH-RT on synaptic plasticity is maintained in mice with standard fractionation. *Radiother Oncol* (2023) 2023:109767. doi:10.1016/j.radonc.2023.109767

15. Konradsson E. *Radiotherapy in a FLASH: towards clinical translation of ultra-high dose rate electron therapy*. Doctoral thesis. Lund, Sweden: Lund University (2023).

16. Zou W, Zhang R, Schüler E, Taylor PA, Mascia AE, Diffenderfer ES, et al. Framework for quality assurance of ultra-high dose rate clinical trials investigating FLASH effects and current technology gaps. *Int J Radiat Oncology* Biology* Phys* (2023) 116:1202–17. doi:10.1016/j.ijrobp.2023.04.018

17. Wilson JD, Hammond EM, Higgins GS, Petersson K. Ultra-high dose rate (FLASH) radiotherapy: silver bullet or fool's gold? *Front Oncol* (2020) 9:1563. doi:10.3389/fonc.2019.01563

18. Rahman M, Trigilio A, Franciosini G, Moeckli R, Zhang R, Böhlen TT. FLASH radiotherapy treatment planning and models for electron beams. *Radiother Oncol* (2022) 175:210–21. doi:10.1016/j.radonc.2022.08.009

19. Schwarz M, Traneus E, Safai S, Kolano A, van de Water S. Treatment planning for Flash radiotherapy: general aspects and applications to proton beams. *Med Phys* (2022) 49(4):2861–74. doi:10.1002/mp.15579

20. Esplen N, Mendonca MS, Bazalova-Carter M. Physics and biology of ultrahigh dose-rate (FLASH) radiotherapy: a topical review. *Phys Med Biol* (2020) 65(23):23TR03. doi:10.1088/1361-6560/abaa28

21. Romano F, Bailat C, Jorge PG, Lerch MLF, Darafsheh A. Ultra-high dose rate dosimetry: challenges and opportunities for FLASH radiation therapy. *Med Phys* (2022) 49(7):4912–32. doi:10.1002/mp.15649

22. Di Martino F, Del Sarto D, Giuseppina Bisogni M, Capaccioli S, Galante F, Gasperini A, et al. A new solution for UHDP and UHDR (Flash) measurements: theory and conceptual design of ALLS chamber. *Physica Med* (2022) 102:9–18. doi:10.1016/j.ejmp.2022.08.010

23. Subiel A, Romano F. Recent developments in absolute dosimetry for FLASH radiotherapy. *Br J Radiol* (2023) 96:20220560. doi:10.1259/bjr.20220560

24. Lourenço A, Subiel A, Lee N, Flynn S, Cotterill J, Shipley D, et al. Absolute dosimetry for FLASH proton pencil beam scanning radiotherapy. *Scientific Rep* (2023) 13(1):2054. doi:10.1038/s41598-023-28192-0

25. Schüller A, Heinrich S, Fouillade C, Subiel A, De Marzi L, Romano F, et al. The European Joint Research Project UHDpulse–Metrology for advanced radiotherapy using particle beams with ultra-high pulse dose rates. *Physica Med* (2020) 80:134–50. doi:10.1016/j.ejmp.2020.09.020

26. Szpala S, Huang V, Zhao Y, Kyle A, Minchinton A, Karan T, et al. Dosimetry with a clinical linac adapted to FLASH electron beams. *J Appl Clin Med Phys* (2021) 22(6):50–9. doi:10.1002/acm2.13270

27. Petersson K, Adrian G, Butterworth K, McMahon SJ. A quantitative analysis of the role of oxygen tension in FLASH radiation therapy. *Int J Radiat Oncology* Biology* Phys* (2020) 107(3):539–47. doi:10.1016/j.ijrobp.2020.02.634

28. Boscolo D, Scifoni E, Durante M, Krämer M, Fuss MC. May oxygen depletion explain the FLASH effect? A chemical track structure analysis. *Radiother Oncol* (2021) 162:68–75. doi:10.1016/j.radonc.2021.06.031

29. Di Martino Fabio Barone S, Bortoli E, Borgheresi R, De Stefano S, et al. FLASH radiotherapy with electrons: issues related to the production, monitoring, and dosimetric characterization of the beam. *Front Phys* (2020) 8:570697. doi:10.3389/fphy.2020.570697

30. Faillace L, Barone S, Battistoni G, Di Francesco M, Felici G, Ficcadenti L, et al. Compact S-band linear accelerator system for ultrafast, ultrahigh dose-rate radiotherapy. *Phys Rev Acc Beams* (2021) 24(5):050102. doi:10.1103/physrevaccelbeams.24.050102

31. Webstore. IEC 60601-2-1:2020, Medical electrical equipment - Part 2-1: particular requirements for the basic safety and essential performance of electron accelerators in the range 1 MeV to 50 MeV (2020). https://webstore.iec.ch/publication/31388 (Accessed July 20, 2023).

32. Bergoz . ACCT (2023). https://www.bergoz.com/products/acct/ (Accessed July 20, 2023).

33. Oesterle R, Gonçalves Jorge P, Grilj V, Bourhis J, Vozenin M, Germond J, et al. Implementation and validation of a beam-current transformer on a medical pulsed electron beam LINAC for FLASH-RT beam monitoring. *J Appl Clin Med Phys* (2021) 22(11):165–71. doi:10.1002/acm2.13433

34. Liu K, Palmiero A, Chopra N, Velasquez B, Li Z, Beddar S, et al. Dual beam-current transformer design for monitoring and reporting of electron ultra-high dose rate (FLASH) beam parameters. *J Appl Clin Med Phys* (2023) 24(2):e13891. doi:10.1002/acm2.13891

35. Leggieri A, Passi D, di Paolo F, Ciccotelli A, De Stefano S, Marangoni F, et al. Real-time beam monitor for charged particle medical accelerators. *IEEE Trans Nucl Sci* (2016) 63(2):869–77. doi:10.1109/tns.2015.2504403

36. Gonçalves JORGEP, Grilj V, Bourhis J, Vozenin M, Germond J, Bochud F, et al. Technical note: validation of an ultrahigh dose rate pulsed electron beam monitoring system using a current transformer for FLASH preclinical studies. *Med Phys* (2022) 49(3):1831–8. doi:10.1002/mp.15474

37. Niroomand-Rad A, Chiu-Tsao S, Grams MP, Lewis DF, Soares CG, Van Battum LJ, et al. Report of AAPM task group 235 radiochromic film dosimetry: an update to TG-55. *Med Phys* (2020) 47(12):5986–6025. doi:10.1002/mp.14497

38. Jain S, Cetnar A, Woollard J, Gupta N, Blakaj D, Chakravarti A, et al. Pulse parameter optimizer: an efficient tool for achieving prescribed dose and dose rate with electron FLASH platforms. *Phys Med Biol* (2023) 68:19NT01. doi:10.1088/1361-6560/acf63e

39. Di Martino F, Del Sarto D, Barone S, Giuseppina Bisogni M, Capaccioli S, Galante F, et al. A new calculation method for the free electron fraction of an ionization chamber in the ultra-high-dose-per-pulse regimen. *Physica Med* (2022) 103:175–80. doi:10.1016/j.ejmp.2022.11.001

40. Gómez F, Gonzalez-Castaño DM, Fernández NG, Pardo-Montero J, Schüller A, Gasparini A, et al. Development of an ultra-thin parallel plate ionization chamber for dosimetry in FLASH radiotherapy. *Med Phys* (2022) 49(7):4705–14. doi:10.1002/mp.15668

41. Romano F, Milluzzo G, Di Martino F, D'Oca MC, Felici G, Galante F, et al. First characterization of novel silicon carbide detectors with ultra-high dose rate electron beams for FLASH radiotherapy. *Appl Sci* (2023) 13(5):2986. doi:10.3390/app13052986

42. Verona RINATIG, Barna S, Georg D, Hamad Y, Magrin G, Marinelli M, et al. Application of a novel diamond detector for commissioning of FLASH radiotherapy electron beams. *Med Phys* (2022) 49(8):5513–22. doi:10.1002/mp.15782

43. Bass GA, Shipley DR, Flynn SF, Thomas RAS. A prototype low-cost secondary standard calorimeter for reference dosimetry with ultra-high pulse dose rates. *Br J Radiol* (2023) 96(1141):20220638. doi:10.1259/bjr.20220638

44. Ashland. EBT-XD (2023). https://www.ashland.com/industries/medical/radiotherapy-films/ebtxd (Accessed July 20, 2023).

45. Vienna International Atomic Energy Agency. *Absorbed dose determination in external beam radiotherapy: an International Code of Practice for Dosimetry based on standards of absorbed dose to water*. Vienna, Austria: Vienna International Atomic Energy Agency (2000).

frontiers | Frontiers in Physics

TYPE Original Research
PUBLISHED 26 February 2024
DOI 10.3389/fphy.2024.1258832



OPEN ACCESS

EDITED BY
Marco Borghesi,
Queen's University Belfast, United Kingdom

REVIEWED BY
Pedro M. M. Correia,
University of Aveiro, Portugal
Consuelo Guardiola,
Spanish National Research Council (CSIC), Spain

*CORRESPONDENCE
Arianna Ferro,
arianna.ferro767@edu.unito.it

†These authors have contributed equally to this work and share first authorship

‡These authors share last authorship

RECEIVED 14 July 2023
ACCEPTED 02 February 2024
PUBLISHED 26 February 2024

CITATION
Medina E, Ferro A, Abujami M, Camperi A, Centis Vignali M, Data E, Del Sarto D, Deut U, Di Martino F, Fadavi Mazinani M, Ferrero M, Ferrero V, Giordanengo S, Martì Villarreal OA, Hosseini MA, Mas Milian F, Masturzo L, Montalvan Olivares DM, Montefiori M, Paternoster G, Pensavalle JH, Sola V, Cirio R, Sacchi R and Vignati A (2024), First experimental validation of silicon-based sensors for monitoring ultra-high dose rate electron beams.
*Front. Phys.* 12:1258832.
doi: 10.3389/fphy.2024.1258832



# First experimental validation of silicon-based sensors for monitoring ultra-high dose rate electron beams

Elisabetta Medina[1,2†], Arianna Ferro[1,2*†], Mohammad Abujami[1,2], Aurora Camperi[2], Matteo Centis Vignali[3], Emanuele Data[1,2], Damiano Del Sarto[4,5], Umberto Deut[1,2], Fabio Di Martino[4,5,6], Mohammad Fadavi Mazinani[2], Marco Ferrero[2], Veronica Ferrero[2], Simona Giordanengo[2], Oscar A. Martì Villarreal[3], Mohammad Amin Hosseini[1,2], Felix Mas Milian[2,7], Luigi Masturzo[5,6,8,9], Diango M. Montalvan Olivares[1,2], Marco Montefiori[6,8], Giovanni Paternoster[3], Jake Harold Pensavalle[5,6,8,9], Valentina Sola[1,2], Roberto Cirio[1,2], Roberto Sacchi[1,2‡] and Anna Vignati[1,2‡]

[1]Università degli Studi di Torino, Dipartimento di Fisica, Torino, Italy, [2]National Institute of Nuclear Physics (INFN), Sezione di Torino, Torino, Italy, [3]Fondazione Bruno Kessler, Center for Sensors and Devices, Trento, Italy, [4]Fisica Sanitaria, Azienda Ospedaliera Universitaria Pisa AOUP, Pisa, Italy, [5]Centro Pisano ricerca e implementazione clinica Flash Radiotherapy (CPFR@CISUP), Università di Pisa, Pisa, Italy, [6]National Institute of Nuclear Physics (INFN), Sezione di Pisa, Pisa, Italy, [7]Universidade Estadual de Santa Cruz, Department of Exact and Technological Sciences, Ilhéus, Brazil, [8]Università di Pisa, Dipartimento di Fisica, Pisa, Italy, [9]Sordina IORT Technologies S p A, Research and Development, Aprilia, Italy

Monitoring Ultra-High Dose Rate (UHDR) beams is one of the multiple challenges posed by the emergent FLASH radiotherapy. Technologies (i.e., gas-filled ionization chambers) nowadays used in conventional radiotherapy are no longer effective when applied to UHDR regimes, due to the recombination effect they are affected by, and the time required to collect charges. Exploiting the expertise in the field of silicon sensors' applications into clinics, the medical physics group of the University and INFN Torino is investigating thin silicon sensors as possible candidates for UHDR beam monitoring, exploiting their excellent spatial resolution and well-developed technology. Silicon sensors of 30 and 45 µm active thicknesses and 0.25, 1 and 2 $mm^2$ active areas were tested at the SIT ElectronFlash machine (CPFR, Pisa) on 9 MeV electron beams, featuring a pulse duration of 4 µs, a frequency of 1 Hz, and a dose-per-pulse ranging from 1.62 to 10.22 Gy/pulse. The silicon sensors were positioned at the exit of the ElectronFlash applicator, after a solid water build-up slab, and were readout both with an oscilloscope and with a multi-channel front-end readout chip (TERA08). A response linearity extending beyond 10 Gy/pulse was demonstrated by comparison with a reference dosimeter (FlashDiamond), thus fulfilling the first requirement of a potential application in UHDR beam monitoring.

KEYWORDS

**FLASH radiotherapy, ultra-high dose rate electron beams, beam monitoring, silicon sensors, TERA chip**

# 1 Introduction

In recent preclinical studies, Ultra-High Dose Rate (UHDR) beams have demonstrated a tumoricidal effect comparable to the one of conventional radiotherapy (RT), with an increased sparing effect on surrounding healthy tissue (FLASH effect) [1]. This led to the concept of FLASH RT: an emerging irradiation approach that involves delivering an average dose rate of more than 40 Gy/s in a total time of less than 200 m, with extremely high instantaneous dose rates (above $10^6$ Gy/s in microsecond-long pulses). FLASH RT could then represent a breakthrough in the field of cancer treatment, if confirmed by *in vivo* biological validations. Most preclinical studies performed up to now have relied on passive dosimeters, which implies a time delay before the readout of the delivered dose. However, the role of detectors capable of real-time monitoring UHDR beams is crucial to allow fine tuning of the dose delivery, improving the study of irradiation parameters (e.g., average dose rate, instantaneous dose rate, dose-per-pulse, beam time structure), and unfolding their contribution in triggering the FLASH effect [2]. Standard ionization chambers cannot withstand the requirements of FLASH RT, since the amount of ions generated per unit volume and unit time leads to high recombination rates, and the typical charge collection time (30–300 μs for air gaps of 0.5–5 mm) cannot resolve in time-pulsed beam timing structures. Besides modifications and optimizations of the ionization chambers themselves (e.g., by reducing the active gap distance, increasing the bias voltage [3, 4], filling the chamber gap with helium [5], filling the cavity of the chamber with a suitably depressurized noble gas [6], or by using two consecutive chambers [7]), new technologies are being investigated to monitor FLASH beams, such as beam current transformers (BCTs) [8–10], scintillators [11, 12], approaches based on air fluorescence measurement [13], and solid state detectors [14–16]. Preliminary results have already been obtained with SiC sensors on high dose rate beams [14] and promise to take advantage of the excellent temporal and spatial resolution. The latter is gaining interest in the realm of Very High Electron Energy (VHEE) beams, whenever a pencil-beam-like scanning modality is considered [17, 18]. Based on the experience gained in applying innovative silicon sensors for beam monitoring in charged particle therapy [19–21], the University and INFN of Torino are contributing to the INFN FRIDA project by studying the response linearity with dose-per-pulse, the recombination effect and the radiation resistance of silicon sensors in order to investigate their applicability in beam monitoring in FLASH therapy. This work shows the results of the test of thin silicon sensors on UHDR electron beams delivered by the SIT ElectronFLASH (EF) machine of the Centro Pisano Multidisciplinare sulla Ricerca e Implementazione Clinica della Flash Radiotherapy (CPFR) in Pisa (Italy). The successful integration of the sensors with the TERA08 front-end readout is also reported, thus providing a possible framework for developing a multi-channel readout system for large area segmented silicon sensors.

# 2 Materials and methods

## 2.1 ElectronFlash accelerator

The EF LINAC (Figure 1) of the CPFR in Pisa was funded by Fondazione Pisa and manufactured by the Italian company SIT-Sordina [22]. The system can produce and accelerate electron pulsed beams of 7 and 9 MeV and employs a radial focusing technique in its accelerating waveguide. The electron beam at the exit window has a gaussian shape of around 1 cm FWHM. The uniformity of the dose profile at the surface of a patient or water phantom is obtained by means of special PMMA plastic applicators of different lengths and diameters, directly attached to the radiant head. For a fixed beam current, the size of the applicator (from 1 to 12 cm diameter) changes the dose-per-pulse values at the irradiation point. Maintaining the energy spectrum unchanged (i.e., keeping the same experimental setup), it is possible to choose among twelve values of beam current (in the range 1–100 mA at the exit window), and change the pulse duration (in the range 0.5–4 μs) and the pulse frequency (in the range 1–249 Hz). This allows varying each beam parameter of interest for the FLASH effect investigation, such as dose-per-pulse, pulse duration, average dose rate, instantaneous dose-per-pulse in a wide range, one independently from the others, minimizing the setup uncertainties. Real-time beam monitoring of the fluence is performed by a beam current transformer (BCT), a toroid positioned in the proximity of the exit window, and by a pickup in the resonant cavity for real-time verification of the beam energy [23]. During the experiment the electron beam energy of 9 MeV and the applicator of 30 mm diameter and 15 cm length were used. The pulse duration was set at 4 μs, and 10 pulses were delivered in each shot of the accelerator at a frequency of 1 Hz. A trigger signal, provided by the accelerator control, was used to synchronize the data acquisition with the beam pulse delivery. Measurements performed with the FlashDiamond (FD) [24] set in the same position of the silicon sensors were considered as reference.


FIGURE 1
SIT ElectronFlash (EF) accelerator of the Centro Pisano Multidisciplinare sulla Ricerca e Implementazione Clinica della Flash Radiotherapy (CPFR) in Pisa, Italy. The experimental setup positioned on the table is shown.

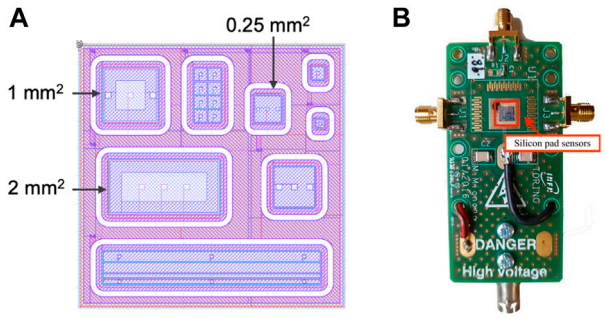


FIGURE 2
**(A)** Technical drawing of the sensors used in the experiment. Among the different implanted pads, the arrows point out the ones tested (0.25, 1, and 2 mm$^2$). **(B)** The sensor mounted on the HV distribution board is represented.

## 2.2 Planar silicon sensors

The use of silicon sensors of small sensitive thickness reduces the generation of charge carriers in the active volume and the charge collection time, thus limiting the recombination and saturation effects. In addition, by etching the support wafer, sensor with a total thickness smaller than 100 microns can be obtained which would reduce the beam perturbation as required for an ideal beam monitor device. The samples chosen for the experiment are PiN silicon sensors, manufactured within the FBK [25] EXFLU1 production batch [26, 27]. Two silicon square devices (4.5 mm side length) were selected from two wafers featuring different active thickness (30 µm and 45 µm) and a total thickness of 655 and 570 µm, respectively. Each device hosts six different pad sensors of different active areas, and three of them from both wafers were tested, featuring areas of 2, 1, and 0.25 mm$^2$ (Figure 2). The active thickness is epitaxially grown (Epi) over a thick low-resistivity handling wafer. The sensors were preliminary characterized in our department lab to verify their electrical properties. Through the analysis of the I-V curves, it was verified that they fully deplete at 10 V and the breakdown voltage occurs over 300 V of reverse bias. The sensors were mounted with conductive glue on high-voltage distribution boards, shown in Figure 2, allowing simultaneous reading of the three chosen pads connected to the output channels through wire-bonding. The guard ring of each pad was grounded.

## 2.3 TERA08 front-end

The readout system used is based on the TERA08 integrated circuit, designed for medical applications by the INFN group of Torino [28]. Initially developed as a front-end electronic readout for gas monitor chambers, TERA08 performs a conversion from the instantaneous current to a digital pulse frequency, where each digital pulse corresponds to a fixed input charge quantum. It implements 64 identical channels, each featuring a converter followed by a 32 bit counter. The maximum conversion frequency is 20 MHz and the charge quantum can be selected in a range extending up to 1.115 pC [29]. For all measurements presented in this work, the value of the charge quantum was measured to be (211 ± 1) fC, in accordance with the chosen nominal setting of 200 fC. The counters were read out using a NI FlexRIO FPGA module at a frequency of 100 Hz. A data acquisition program, developed using LabView, allowed to display online the count rates of each channel and to store the data for the offline analysis.

## 2.4 Experimental setup

The silicon device was aligned along the beamline, at the exit of the EF applicator, at the center of the beam spot and it was mounted on a fixed motor system positioned on a table in the EF room (Figure 3). This configuration allowed moving the silicon sensors and the FD, used to provide the reference dose measurements, in and out of the beam in the same experimental conditions. All the measurements were performed at the maximum of the depth-dose distribution in water for the 9 MeV electron beam, obtained by placing a 12 mm thick solid water slab sandwiched between the applicator and the detector holder. Both silicon sensors and FD were enclosed in 3D-printed PLA boxes with an opening window in front of the active sensor surface to ensure the same air-gap distance (7 mm) between the sensors and the 12 mm thick solid water slab. For twelve values of the beam current at the exit window in the available range (1–100 mA), several EF parameters, such as magnetron power and bias of the cathode, have been optimized in order to have a constant energy spectrum. These twelve "working points" have been named according to the dose values measured in water at the build-up depth, using the 10 cm diameter applicator during the commissioning procedure. The "working points" labels (WPlabels) need to be converted into the actual dose related to the specific irradiation point and applicator considered. Table 1 reports the correspondence between the nine (out of the twelve possible) WPlabels considered in the test and the corresponding values measured by the FD for the 30 mm diameter applicator. The reference setup for measurements with the FD relies in positioning it in a cylindrical PMMA phantom of 120 mm diameter (*ref setup*), while in the experimental setup considered in this test the FD was positioned in the already described 3D-printed PLA box (test setup). Therefore, in order to obtain the values of effective dose-in-water, the discrepancy in the response of the FD in the *ref* or *test setup* was studied by means of Geant4 Monte Carlo simulations. More specifically, the Monte Carlo simulations included the support structure of the sensor, the 3D-printed PLA box and the 12 mm thick build-up slab for the *test setup*, the PMMA cylindrical water equivalent holder and the build-up slab for the *ref setup*. All the components were positioned at the applicator exit. In both cases, simulations were based on the "eFLASH radiotherapy" example code, available in Geant4 11.0, which includes the EF accelerator and different applicator geometries. The energy spectrum of the primary electrons was measured, showing a slight decrease in the beam's mean energy due to the low-energy tail presence. The lateral scattering contribution due to the presence of the FD holder was quantified. The Geant4 simulations were run with "G4EmStandardPhysics_option4," "G4RadioactiveDecayPhysics," and "G4DecayPhysics" physics list, while cut-offs for all particle productions were set to 0.01 mm. The electron dose was scored along a 1.9 × 1.9 × 10 cm$^3$ water volume in a grid with 1.9 ×

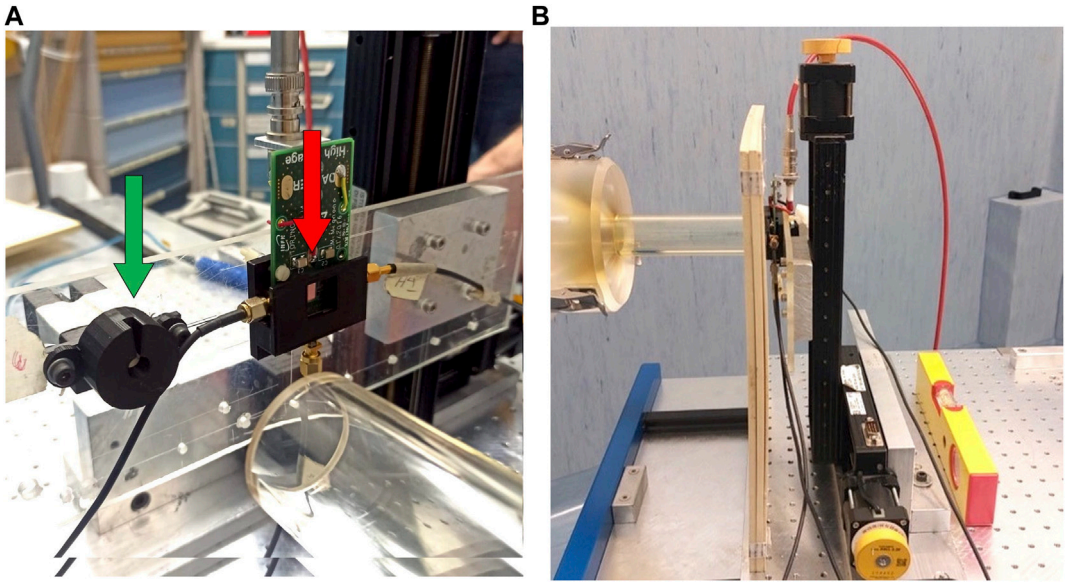


FIGURE 3
**(A)** The silicon sensor (right arrow) and the FlashDiamond (left arrow) mounted on the same supporting structure. The two 3D printed boxes (in black) in which the sensors are positioned are visible. **(B)** The EF applicator, in contact with the solid water slab, adjacent to the sensor support box is shown.

**TABLE 1** Reference dose-per-pulse (DPP) values measured by the FlashDiamond at nine increasing beam current values, identified by the corresponding nine "working points" labels (WPlables), for the irradiation point and the EF applicator considered in the test experimental setup. One measurement was performed for each WPlabel. The values measured with the FlashDiamond are reported with the corresponding error (± 3%).

| Reference dose-per-pulse values | | | | | | | | | |
|---|---|---|---|---|---|---|---|---|---|
| WPlabels (Gy/pulse) | 0.3 | 0.6 | 0.9 | 1.2 | 1.5 | 1.8 | 2.0 | 2.3 | 2.8 |
| $DPP_{ref}$ (Gy/pulse) ± ERR% | 1.62 ± 0.05 | 2.55 ± 0.08 | 3.9 ± 0.1 | 5.3 ± 0.2 | 6.6 ± 0.2 | 7.4 ± 0.2 | 7.7 ± 0.2 | 9.4 ± 0.3 | 10.2 ± 0.3 |

1.9 × 1 $mm^3$ resolution, with and without a 10 × 10 × 10 $cm^3$ water phantom all around to simulate the contribution of the cylindrical PMMA phantom. The simulations were performed with $10^8$ particles. In these conditions, a 3.9% increase in the deposited dose was found when considering the cylindrical PMMA phantom. The values reported in the following table were corrected for this effect. A maximum dose-per-pulse of 10.2 ± 0.3 Gy was reached.

For part of the test, a sensor pad of 2 $mm^2$ active area from the device of 45 µm thickness was connected to the TERA08 chip. Since the latter can read a maximum current of 4 µA per channel before saturation, the sensor signal was split into 64 channels. As reported in a previous publication [29], such an arrangement allows to extend the current range up of 256 µA preserving a linearity better than 1% in the whole range. A specific fan-in board was used to allow the splitting of the input into the TERA08 channels. Moreover, in order to cope with the large instantaneous input current during each pulse, an RC circuit was added between the sensor output and the TERA08 input such that the charge produced by each pulse is stored in the capacitor, which discharges into the TERA08 input with a time constant much larger than the pulse duration. A series resistance value of 156 kΩ and a capacitance value of 470 nF, connected to the reference voltage of the TERA08 input, were used. Figure 4A shows a typical signal consisting of 10 pulses at a frequency of 5 Hz after software acquisition. In Figure 4B, the value of the time constant τ, determined by fitting an exponential curve to a single-pulse discharge data, is reported and is found to be in good agreement with the product RC.

A second part of the beam time was dedicated to the test of three sensor pads of active areas 2, 1 and 0.25 $mm^2$ from the 45 µm active thickness wafer connected directly to three input channels of an oscilloscope (Keysight Infiniium S-series DSOS254, 20 G/s sampling rate), with input impedance of 50 Ω. Through the oscilloscope, it was possible to visualize and store the voltage signal generated from the pulses delivered by the EF and its temporal structure. An example of an acquisition with the oscilloscope of one single pulse of 4 µs duration is shown in Figure 5, where three waveforms corresponding to each output channel are represented with three different colors. The shapes of the signals, characterized by an initial spike followed by an increase up to a broad maximum at the center of the pulse, were found to be perfectly compatible with those recorded by the machine's internal BCTs. The total charge of each pulse was obtained by dividing the integral of the acquired waveforms by the input impedance of the oscilloscope.

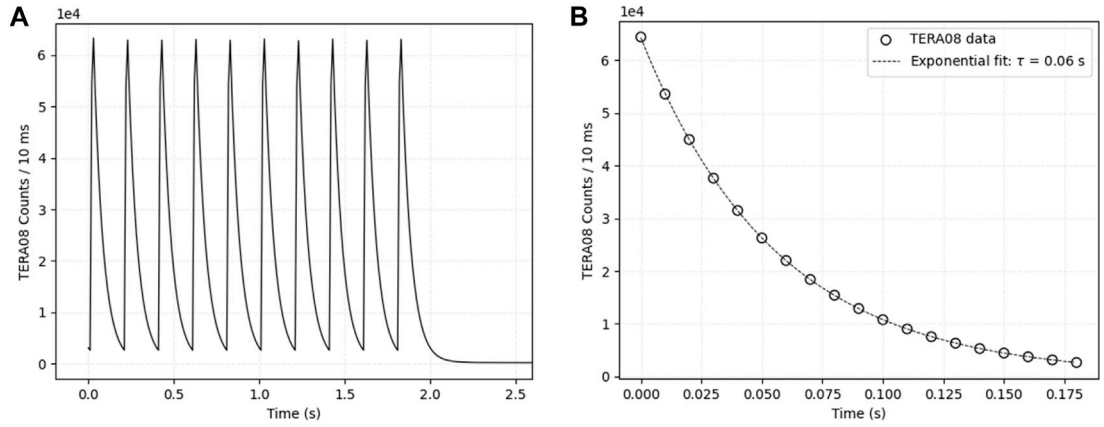


FIGURE 4
Example of acquisition with the TERA08 chip. **(A)** TERA08 counts as a function of acquisition time for an entire run, where 10 pulses with a frequency of 5 Hz are clearly distinguishable. **(B)** Zoom on a single signal of the discharge of the capacitor. The exponential fit results for the τ value is reported in the figure legend.

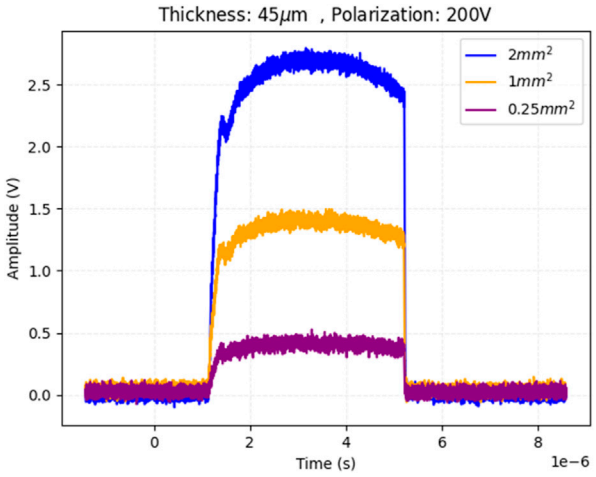


FIGURE 5
Waveforms acquired by the oscilloscope for a 4 μs pulse delivered by the EF at 3.89 Gy/pulse dose-per-pulse. Three sensors of different active areas (2, 1, and 0.25 mm$^2$) were connected to 3 channels of the oscilloscope, represented in different colors in the plot. The data correspond to the 45 μm thick sensor inversely biased at 200 V.

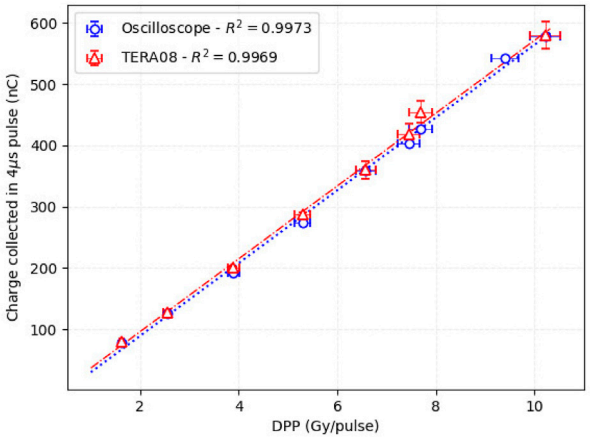


FIGURE 6
The charge produced in one pulse of 4 μs duration as a function of the dose-per-pulse is represented for both TERA08 and oscilloscope data. A coefficient of determination $R^2 > 0.99$ was obtained in both cases. The data correspond to the pad of 2 mm$^2$ area and 45 μm active thickness, inversely polarized at 200 V.

## 3 Results

The charge per pulse measurements acquired with a silicon pad of 2 mm$^2$ area and 45 μm active thickness, using both TERA08 and the oscilloscope, are shown in Figure 6 as a function of the dose-per-pulse up to ~10 Gy/pulse. The sensor was reverse-biased at 200 V, well above his depletion voltage, to ensure operating the sensor under saturated drift velocity of charge carriers. Each point represents the average charge of the ten pulses used for the measurement. The charges measured with TERA08 and using the oscilloscope are found to be compatible within the uncertainties. Both data sets show very good linearity, resulting in a coefficient of determination of a linear fit $R^2 > 0.99$.

Figure 7 shows the charge collected in the six different pads considered (2, 1, and 0.25 mm$^2$ active areas for both 45 and 30 μm thicknesses), where the bias voltage in the case of the thinner device was set to 133.34 V to achieve the same internal electric field (~4.44 V/μm) and thus saturation of the charge carriers drift velocity. For all the pads, the collected charge showed a very linear behavior as a function of the dose-per-pulse. At the same dose per pulse, the collected charge varies proportionally to the pad area and to the sensor thickness. In addition, the ratio between charges collected in different pads is found to be independent of the dose-per-pulse, indicating that volume-dependent effects of recombination of charge carriers are playing a negligible effect.

The energy deposited in the active layer of silicon sensors of different geometries and the corresponding total charge produced

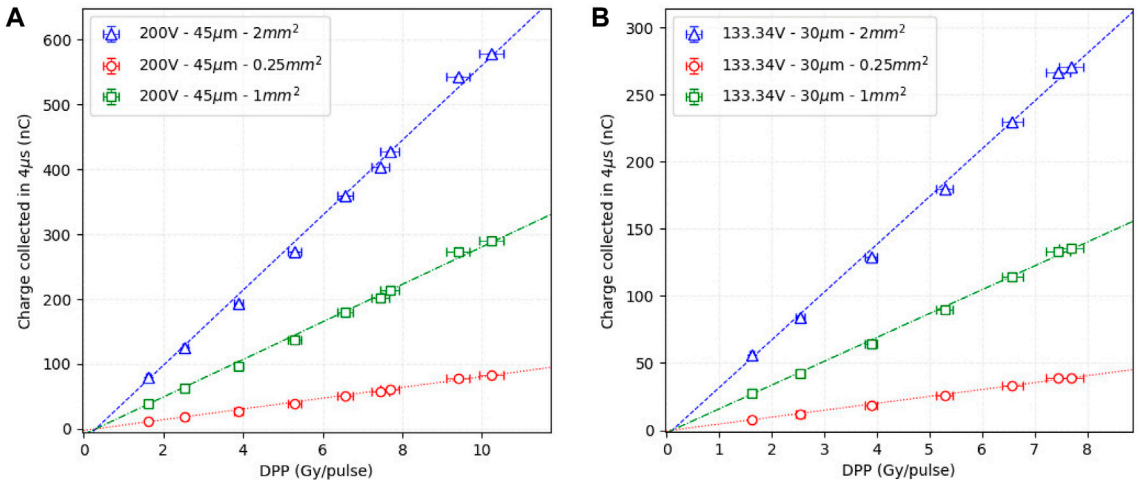


FIGURE 7
The results of the charge collected in each pulse for the 3 sensor pads of the 45 μm device are shown in **(A)**, while the ones of the 30 μm macro-sensor in **(B)**. In order to have the same electric field condition within the active thickness, the first sensor was inversely polarized at 200 V, while the second one at 133.34 V.

was simulated with Allpix Squared framework (v 2.4.0) [30]. The electron source was defined with a radius of 2 mm and the energy spectrum was set as the one obtained at the applicator exit from the "eFLASH radiotherapy" Geant4 example. The deposited charges have been assumed to be equal to the propagated charges at the readout electronics.

For both sensor thicknesses $10^7$ events have been simulated. Assuming a linear increase of the charge with the number of initial particles, the collection of charge can be estimated for a larger number of initial particles. In the case of 30 μm thick sensors, the simulation results are compatible with all those obtained experimentally within 2.0% for the 2 $mm^2$ area, 6.2% for the 1 $mm^2$ one, and 4.1% for the 0.25 $mm^2$ one. In the case of 45 μm thick sensors, the simulation results are compatible with the experimental ones within 8.1% for the 2 $mm^2$ area, 13.5% for the 1 $mm^2$ area, and 17.6% for the 0.25 $mm^2$ area. Although the grounded guard ring, a slight broadening of the depletion region into the silicon could explain the higher value of the charge collected in respect to the simulated one, and this has a larger impact in the 45 μm case. Further studies are ongoing to investigate and verify this effect.

As previously reported, data acquired at 200 V bias voltage show perfect linearity for the whole range of dose-per-pulse values investigated. However, by decreasing the bias voltage, a saturation effect of the charge collected was observed from values of dose-per-pulse >3.89 Gy/pulse. This effect is illustrated in Figure 8 which shows the charge collected in a 4 μs pulse in a 2 $mm^2$ area pad, 45 μm thick, as a function of the dose-per-pulse for different polarization voltages.

To further investigate the effect, Figure 9A shows the waveforms of a pulse as a function of the dose-per-pulse for 200 V polarization, as acquired with the oscilloscope. As expected, the signal amplitude increases as the dose-per-pulse increases, while keeping the pulse duration constant (4 μs). A peak is present at the beginning of the pulse, which is more evident at higher dose-per-pulse, and was also present in the BCT signal, thus not relying on the internal effects of the sensor. On the other hand, the waveforms for the measurements taken at 50 V (Figure 9B) show a distortion of the signal shape for dose-per-pulse values >3.89 Gy/pulse. The signal duration is shorter

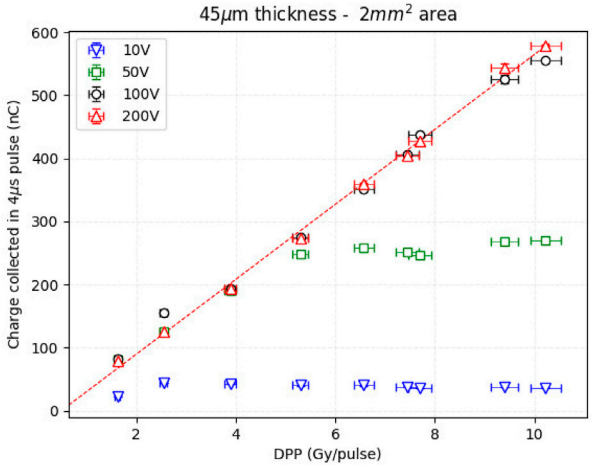


FIGURE 8
Charge produced in 4 μs pulses as a function of the dose in each pulse in a 2 $mm^2$ area and 45 μm active thickness pad inversely polarized at 10, 50, 100, and 200 V. The data were acquired with the oscilloscope.

than 4 μs, and the integrated value reaches a constant value. The detector continues to be irradiated but the e/h pairs created are no longer collected. The hypothesis that the high density of charge carriers generates an opposing electric field that cancels the drift field, inhibiting charge collection, is currently under study by models and simulations.

## 4 Discussion

The UHDR scenario poses challenges, mainly related to ion recombination effects, for radiation detectors dedicated to both real-time beam monitoring and reference dosimetry. However, beam monitors are characterized by supplementary specifications with

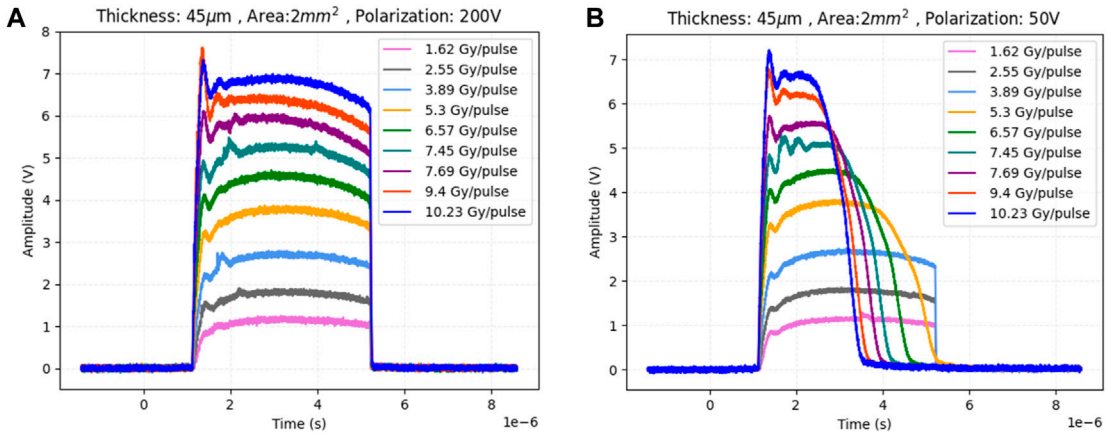


FIGURE 9
Waveforms acquired with the oscilloscope for pulses at nine different dose-per-pulse conditions. The data correspond to the pad with 2 mm$^2$ area and 45 μm active thickness, inversely polarized at 200 V **(A)** and 50 V **(B)**.

respect to dosimeters, which are more demanding when dealing with FLASH beams: high spatial and temporal resolution to measure the beam profile and provide a feedback/interlock signal to the acceleration system, beam transparency, large response dynamic range, large sensitive area to enclose the entire beam cross-section and radiation hardness.

In this study, the results of the test of different silicon sensor geometries exposed to 9 MeV electron beams from the EF machine of the CPFR (Pisa, Italy) were presented. The main advantages of using silicon sensors as beam monitoring devices lie in the possibility of a) polarizing them up to very high voltages, larger than 300 V, to overcome the problem of charge saturation and signal distortion, b) reducing the active area and thickness to lower the amount of charge produced in the device and to increase the beam transparency and c) exploiting the excellent spatial resolution. The latter does not represent a priority when a low energy dedicated FLASH LINAC, like the Pisa EF, is considered, since BCTs are perfectly suited to provide current measurements, while beam uniformity and flatness measurements are performed moving a point-like dosimeter (e.g., FD) in the irradiation field. However, even in this experimental setup, a silicon sensor able to cover the entire diameter of the EF applicator exit could provide a measure of the beam profile in a unique beam shot, reducing the number of spots needed to scan the field with a point-like detector and thus cutting down the delivered dose. In addition, the availability of detectors with excellent spatial resolution gains attention in the realm of Very High Electron Energy (VHEE) research. Recently, the idea of investigating the use of VHEE beams (50–200 MeV) aims at investigating and exploiting the FLASH effect of electrons at penetration depths larger than the superficial ones reached by low energy beams. Small diameter VHEE beams can be scanned in a pencil-beam-like modality and focused, producing finer resolution for intensity modulated treatments than photon beams, and accelerators may be constructed at significantly lower cost compared to the current installations required for protons beams [17, 18].

## 5 Conclusion

Silicon pads of 30/655 μm or 45/570 μm active/total thickness and areas 2, 1, 0.25 mm$^2$ were investigated as potential solutions for monitoring UHDR beams. Future tests will be performed with thinner active thicknesses (10 and 20 μm, also available within the same batch) and with thinned down sensors (100 or 120 μm total thickness) to verify beam transparency. The charge collected by the sensors during irradiation was measured with an oscilloscope and the TERA08 chip. Several measurements were made up to very high dose rates of $2.5{\cdot}10^6$ Gy/s, corresponding to ~10 Gy in pulses of 4 μs duration and a good linearity ($R^2 > 0.99$) was verified for both readout systems, as well as a very good compatibility of the two measurements. This work aimed at studying the response linearity of silicon sensors as a first step towards their possible application in UHDR electron beams. However, it also allowed verifying that no sign of signal degradation, e.g., depletion voltage or leakage current increase [31], appeared after a total cumulative dose of more than 9 kGy. The cumulative dose a beam monitor needs to withstand to comply with the UHDR requirements is still difficult to be estimated, but the radiation hardness is obviously a critical characteristic for solid-state sensors in this realm. Although the larger bandgap and e-h pair production energy of SiC and diamond compared to silicon make them more suitable for applications in UHDR beams [14, 32], it is interesting to evaluate the limits in terms of radiation hardness of silicon sensors, which could benefit of a greater technological maturity in respect to SiC and diamonds.

Simulation tools (Geant4 Monte Carlo and Allpix Squared) were implemented, and the simulation results were in good agreement with the experimental data, opening the possibility to simulate the performance of different silicon geometries and experimental setups configurations. Further studies and simulations with Sentaurus TCAD are ongoing to better understand the distortion of the signal occurring at lower bias voltages.

The results obtained by splitting the sensor output in all 64 chip channels of the TERA08 chip open the way to the chip adaptation towards the readout of multiple silicon pads/strips, aiming at enlarging the sensitive area of the beam monitoring device. Taking into account the maximum current that a single channel of the TERA08 can sustain (4 μA), the total number of chip channels (64), and the charge measured by the chip under high dose rate conditions (about 600 nC at the maximum 10.2 Gy/pulse dose rate

value), more than one chip can be considered to measure the charge collected in an hypothetical multiple strip/pad silicon sensor. Keeping constant the signal readout circuit (R ≃ 156 kΩ and C ≃ 470 nF) and the silicon pad characteristics (2 $mm^2$, 45 μm thickness) used in the described test and by computing the maximum of the function describing the number of counts read by TERA08 chip ($N(t) = N_{tot}$ (1—exp (t/τ))), splitting the sensor output in only 3 TERA08 channels (instead of the all 64 channels, as done in the test) would be sufficient to avoid reaching electronic saturation. This would then allow to simultaneously readout ~20 sensors with the same chip. These estimations would improve with the use of sensors thinner than those presented in this work and with the use of an upgraded version of TERA08 with a higher current range (TERA09, 12 μA of maximum instantaneous current per channel using a charge quantum of 200 fC).

In conclusion, this preliminary work demonstrates the response linearity of thin silicon sensors' prototypes in UHDR electron beam irradiation. Further studies will be performed to test the sensors radiation hardness, to enlarge the sensitive area of the detector, to develop the proper readout electronics, to test adapted prototypes to other beam types, such as UHDR proton beams.

## Data availability statement

The raw data supporting the conclusions of this article will be made available by the authors, without undue reservation.

## Author contributions

EM: Conceptualization, Data curation, Formal Analysis, Investigation, Methodology, Software, Visualization, Writing–original draft, Writing–review and editing. AF: Conceptualization, Data curation, Formal Analysis, Investigation, Methodology, Software, Visualization, Writing–original draft, Writing–review and editing. MA: Investigation, Validation, Writing–review and editing. AC: Conceptualization, Data curation, Formal Analysis, Investigation, Methodology, Software, Writing–original draft. MC: Investigation, Methodology, Resources, Supervision, Validation, Writing–review and editing. ED: Investigation, Validation, Writing–review and editing. DD: Investigation, Methodology, Resources, Supervision, Validation, Writing–review and editing. UD: Conceptualization, Data curation, Formal Analysis, Investigation, Methodology, Software, Writing–original draft. FD: Investigation, Methodology, Resources, Supervision, Validation, Writing–review and editing. MFM: Investigation, Validation, Writing–review and editing. MF: Investigation, Methodology, Resources, Supervision, Validation, Writing–review and editing. VF: Investigation, Validation, Writing–review and editing. SG: Conceptualization, Funding acquisition, Investigation, Methodology, Project administration, Supervision, Validation, Writing–review and editing. OM: Conceptualization, Data curation, Formal Analysis, Investigation, Methodology, Software, Writing–original draft. MAH: Investigation, Validation, Writing–review and editing. FM: Conceptualization, Funding acquisition, Investigation, Methodology, Project administration, Supervision, Validation, Writing–review and editing. LM: Investigation, Methodology, Resources, Supervision, Validation, Writing–review and editing. DM: Conceptualization, Data curation, Formal Analysis, Investigation, Methodology, Software, Writing–original draft. MM: Investigation, Methodology, Resources, Supervision, Validation, Writing–review and editing. GP: Investigation, Methodology, Resources, Supervision, Validation, Writing–review and editing. JP: Investigation, Methodology, Resources, Supervision, Validation, Writing–review and editing. VS: Investigation, Methodology, Resources, Supervision, Validation, Writing–review and editing. RC: Conceptualization, Funding acquisition, Investigation, Methodology, Project administration, Supervision, Validation, Writing–review and editing. RS: Conceptualization, Funding acquisition, Investigation, Methodology, Project administration, Supervision, Validation, Writing–review and editing. AV: Conceptualization, Funding acquisition, Investigation, Methodology, Project administration, Supervision, Validation, Writing–review and editing.

## Funding

The author(s) declare that financial support was received for the research, authorship, and/or publication of this article. This research was supported by INFN CSN5 funded project "FRIDA" and by the VIGA_S1921_EX-POST_21_01 (Compagnia di San Paolo). Part of the EXFLU1 batch has been funded by the European Union's Horizon 2020 Research and Innovation programme under Grant Agreement No 101004761.

## Acknowledgments

We thank INFN CSN5 funded project "eXFlu" for the collaboration and "Fondazione Pisa" for funding CPFR with the grant "prog. n. 134/2021".

## Conflict of interest

The authors declare that the research was conducted in the absence of any commercial or financial relationships that could be construed as a potential conflict of interest.

## Publisher's note

# References


1. Farr J, Grilj V, Malka V, Sudharsan S, Schippers M. Ultra-high dose rate radiation production and delivery systems intended for FLASH. *Med Phys* (2022) 49(7): 4875–911. doi:10.1002/MP.15659

2. Romano F, Bailat C, Jorge PG, Lerch MLF, Darafsheh A. Ultra-high dose rate dosimetry: challenges and opportunities for FLASH radiation therapy. *Med Phys* (2022) 49(7):4912–32. doi:10.1002/MP.15649

3. Gómez F, Gonzalez-Castaño DM, Fernández NG, Pardo-Montero J, Schüller A, Gasparini A, et al. Development of an ultra-thin parallel plate ionization chamber for dosimetry in FLASH radiotherapy. *Med Phys* (2022) 49(7):4705–14. doi:10.1002/MP.15668

4. Zou W, Diffenderfer ES, Ota K, Boisseau P, Kim MM, Cai Y, et al. Characterization of a high-resolution 2D transmission ion chamber for independent validation of proton pencil beam scanning of conventional and FLASH dose delivery. *Med Phys* (2021) 48(7): 3948–57. doi:10.1002/MP.14882

5. Tinganelli W, Sokol O, Quartieri M, Puspitasari A, Dokic I, Abdollahi A, et al. Ultra-high dose rate (FLASH) carbon ion irradiation: dosimetry and first cell experiments. *Int J Radiat Oncol Biol Phys* (2022) 112(4):1012–22. doi:10.1016/J.IJROBP.2021.11.020

6. Di Martino F, Del Sarto D, Giuseppina Bisogni M, Capaccioli S, Galante F, Gasperini A, et al. A new solution for UHDP and UHDR (Flash) measurements: theory and conceptual design of ALLS chamber. *Physica Med* (2022) 102:9–18. doi:10.1016/J.EJMP.2022.08.010

7. Giordanengo S, Guarachi LF, Braccini S, Cirrone GAP, Donetti M, Fausti F, et al. Fluence beam monitor for high-intensity particle beams based on a multi-gap ionization chamber and a method for ion recombination correction. *Appl Sci* (2022) 12(23):12160. doi:10.3390/APP122312160

8. Gonçalves Jorge P, Grilj V, Bourhis J, Vozenin MC, Germond JF, Bochud F, et al. Technical note: validation of an ultrahigh dose rate pulsed electron beam monitoring system using a current transformer for FLASH preclinical studies. *Med Phys* (2022) 49(3):1831–8. doi:10.1002/MP.15474

9. Liu K, Palmiero A, Chopra N, Velasquez B, Li Z, Beddar S, et al. Dual beam-current transformer design for monitoring and reporting of electron ultra-high dose rate (FLASH) beam parameters. *J Appl Clin Med Phys* (2023) 24(2):e13891. doi:10.1002/ACM2.13891

10. Oesterle R, Gonçalves Jorge P, Grilj V, Bourhis J, Vozenin MC, Germond JF, et al. Implementation and validation of a beam-current transformer on a medical pulsed electron beam LINAC for FLASH-RT beam monitoring. *J Appl Clin Med Phys* (2021) 22(11):165–71. doi:10.1002/ACM2.13433

11. Ashraf MR, Rahman M, Zhang R, Williams BB, Gladstone DJ, Pogue BW, et al. Dosimetry for FLASH radiotherapy: a review of tools and the role of radioluminescence and cherenkov emission. *Front Phys* (2020) 8:570033. doi:10.3389/fphy.2020.00328

12. Levin DS, Ferretti C, Ristow N, Tecchio M, Friedman PS, Litzenberg DW, et al. A scintillator beam monitor for real-time FLASH radiotherapy. ArXiv (2023).

13. Trigilio A, De Gregorio A, Fischetti M, Franciosini G, Garbini M, Lippa G, et al. The FlashDC project: development of a beam monitor for FLASH radiotherapy. *Nucl Instr Methods Phys Res Section A: Acc Spectrometers, Detectors Associated Equipment* (2022) 1041:167334. doi:10.1016/J.NIMA.2022.167334

14. Romano F, Milluzzo G, Di Martino F, D'Oca MC, Felici G, Galante F, et al. First characterization of novel silicon carbide detectors with ultra-high dose rate electron beams for FLASH radiotherapy. *Appl Sci* (2023) 13(5):2986. doi:10.3390/APP13052986

15. Vignati A, Giordanengo S, Fausti F, Martì Villarreal OA, Mas Milian F, Mazza G, et al. Beam monitors for tomorrow: the challenges of electron and photon FLASH RT. *Front Phys* (2020) 8:375. doi:10.3389/fphy.2020.00375

16. Fausti F, Olave J, Giordanengo S, Ali OH, Mazza G, Rotondo F, et al. A single ion discriminator ASIC prototype for particle therapy applications. *Nucl Instr Methods Phys Res Section A: Acc Spectrometers, Detectors Associated Equipment* (2021) 985:164666. doi:10.1016/J.NIMA.2020.164666

17. Ronga MG, Cavallone M, Patriarca A, Maia Leite A, Loap P, Favaudon V, et al. Back to the future: very high-energy electrons (VHEEs) and their potential application in radiation therapy. *Cancers* (2021) 13(19):4942. doi:10.3390/CANCERS13194942

18. Sarti A, De Maria P, Battistoni G, De Simoni M, Di Felice C, Dong Y, et al. Deep seated tumour treatments with electrons of high energy delivered at FLASH rates: the example of prostate cancer. *Front Oncol* (2021) 11:777852. doi:10.3389/FONC.2021.777852

19. Marti Villarreal OA, Vignati A, Giordanengo S, Abujami M, Borghi G, Centis Vignali M, et al. Characterization of thin LGAD sensors designed for beam monitoring in proton therapy. *Nucl Instr Methods Phys Res Section A: Acc Spectrometers, Detectors Associated Equipment* (2023) 1046:167622. doi:10.1016/J.NIMA.2022.167622

20. Vignati A, Abujami M, Bersani D, Borghi G, Centis Vignali M, Data E, et al. Monitoring therapeutic proton beams with LGAD silicon detectors. *J Instrumentation* (2022) 17(11):C11001. doi:10.1088/1748-0221/17/11/C11001

21. Vignati A, Giordanengo S, Milian FM, Ganjeh ZA, Donetti M, Fausti F, et al. A new detector for the beam energy measurement in proton therapy: a feasibility study. *Phys Med Biol* (2020) 65(21):215030. doi:10.1088/1361-6560/ABAB58

22. SIT. *S.I.T. Sordina IORT technologies S.P.A* (2023). Available at: https://www.soiort.com/ (Accessed on July 12, 2023).

23. Di Martino F, Barca P, Barone S, Bortoli E, Borgheresi R, De Stefano S, et al. FLASH radiotherapy with electrons: issues related to the production, monitoring, and dosimetric characterization of the beam. *Front Phys* (2020) 8:570697. doi:10.3389/fphy.2020.570697

24. Marinelli M, Felici G, Galante F, Gasparini A, Giuliano L, Heinrich S, et al. Design, realization, and characterization of a novel diamond detector prototype for FLASH radiotherapy dosimetry. *Med Phys* (2022) 49(3):1902–10. doi:10.1002/MP.15473

25. FBK. *FBK center for sensors and devices* (2023). Available at: https://sd.fbk.eu/en/ (Accessed on July 12, 2023).

26. Croci T, Morozzi A, Sola V, Asenov P, Fondacci A, Giordanengo S, et al. TCAD optimization of LGAD sensors for extremely high fluence applications. *J Instrumentation* (2023) 18(01):C01008. doi:10.1088/1748-0221/18/01/C01008

27. Sola V, Paternoster G, Arcidiacono R, Asenov P, Borghi G, Boscardin M, et al. *Advances in LGAD technology for high radiation environments* (2023). doi:10.1088/1748-0221/6/06/P06013

28. La Rosa A, Mazza G, Donetti M, Marchetto F, Luetto L, Attili A, et al. Design and test of a 64-channel charge measurement ASIC developed in CMOS 0.35 µm technology. *Nucl Instr Methods Phys Res Section A: Acc Spectrometers, Detectors Associated Equipment* (2007) 583(2–3):461–8. doi:10.1016/J.NIMA.2007.09.024

29. Cirio R, Fausti F, Fanola Guarachi L, Giordanengo S, Marchetto F, Mazza G, et al. A simple method to increase the current range of the TERA chip in charged particle therapy applications. *Nucl Instr Methods Phys Res Section A: Acc Spectrometers, Detectors Associated Equipment* (2015) 798:107–10. doi:10.1016/J.NIMA.2015.07.013

30. Allpix Squared. *Semiconductor detector Monte Carlo simulation framework* (2023). Available at: https://allpix-squared.docs.cern.ch/ (Accessed on July 12, 2023).

31. Radu R, Fretwurst E, Klanner R, Lindstroem G, Pintilie I. Radiation damage in n-type silicon diodes after electron irradiation with energies between 1.5 MeV and 15 MeV. *Nucl Instr Methods Phys Res Section A: Acc Spectrometers, Detectors Associated Equipment* (2013) 730:84–90. doi:10.1016/j.nima.2013.04.080

32. Medina E, Sangregorio E, Crnjac A, Romano F, Milluzzo G, Vignati A, et al. Radiation hardness study of silicon carbide sensors under high-temperature proton beam irradiations. *Micromachines* (2023) 14(1):166. doi:10.3390/mi14010166

# Frontiers in Physics

**Investigates complex questions in physics to understand the nature of the physical world**

Addresses the biggest questions in physics, from macro to micro, and from theoretical to experimental and applied physics.

---

## Discover the latest Research Topics

See more →

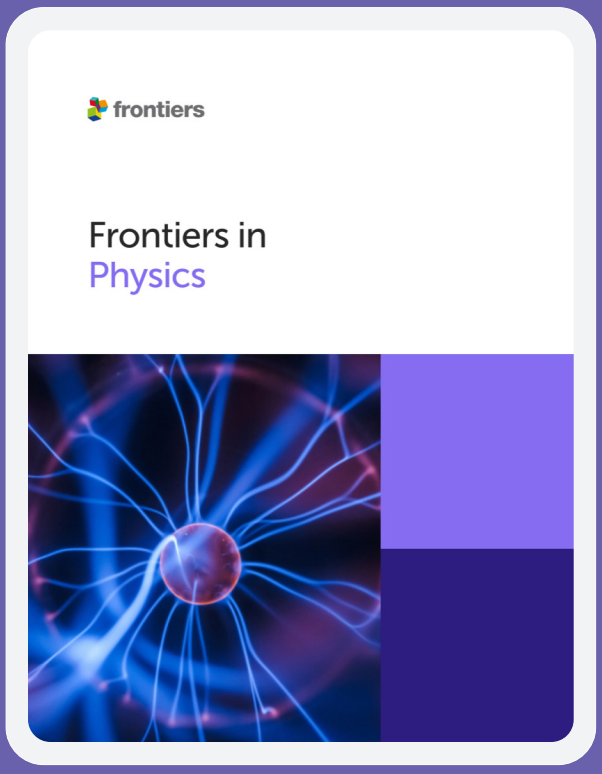


**Frontiers**

Avenue du Tribunal-Fédéral 34
1005 Lausanne, Switzerland
frontiersin.org

**Contact us**

+41 (0)21 510 17 00
frontiersin.org/about/contact